LMU Ludwig-Maximilians-Universität

Sigillum Universitatis Ludovici Maximiliani

The Kinematics of the Intracluster Light in the Core of the Hydra I Cluster

Dissertation der Fakultät für Physik
Dissertation of the Faculty of Physics

der Ludwig-Maximilians-Universität München
at the Ludwig Maximilian University of Munich

für den Grad des
for the degree of

Doctor rerum naturalium

vorgelegt von Giulia Ventimiglia
presented by

aus Catania, Italien
from

München, 22. Dezember 2010

Sigillum Universitatis Ludovici Maximiliani

1. Gutachter: PD Dr. Ortwin E. Gerhard

referee:

2. Gutachter: Prof. Dr. Hans Böhringer

referee:

Tag der mündlichen Prüfung: 18. Februar 2011

Date of the oral exam:

To my father

Contents

List of Figures

List of Tables

Zusammenfassung

Dem aktuellen kosmologischen Modell nach wachsen Galaxienhaufen – die größten virialisierten Systeme des Universums – durch die Akkretion kleinerer Objekte aus der umgebenden, wabenartigen kosmischen Massenverteilung. Die entsprechenden Galaxien kommen dabei in Wechselwirkung sowohl mit anderen Galaxien als auch mit dem heißen Röntgengas (ICM) und dem Gravitationsfeld des Galaxienhaufens, und verändern in der Folge ihre Struktur. Einige der dabei auftretenden Prozesse sind ’tidal stripping’ (Massenverlust durch Gezeitenkräfte), die Verschmelzung mit anderen Galaxien und ’ram pressure stripping’ (Gasverlust durch den Staudruck des Röntgengases im Haufen). Diese Prozesse spielen nicht nur für die weitere Entwicklung der Galaxien eine Rolle, sondern sind auch verantwortlich für die Entstehung des sog. ’intracluster light’ (ICL). Beim ICL handelt es sich um Sterne, die nicht mehr an einzelne Haufengalaxien gebunden sind. Numerische Simulationen sagen voraus, dass alle Wechselwirkungsprozesse der Galaxien im Haufen Sterne ins ICL übergehen lassen, aber insbesondere jene, die mit der Bildung der hellsten Haufengalaxie (BCG) im Zusammenhang stehen.

Gegenstand dieser Arbeit ist die Untersuchung des ICL im Zentrum des Galaxienhaufens Hydra I. Hydra I gehört zur südlichen Hemisphäre, ist etwa 50 Mpc entfernt und von mittlerer Kompaktheit. Im Röntgenlicht erscheint der Galaxienhaufen als ein relaxiertes System, das von zwei nicht in Wechselwirkung stehenden elliptischen Galaxien beherrscht wird: NGC3311 (cD) und NGC3309 (E3). Wir wollen herausfinden, wie die Kinematik des ICLs mit der im Halo der cD Galaxie NGC3311 zusammenhängt, und was man an der Photometrie und Kinematik des ICLs über die Entwicklung des Haufens insgesamt ablesen kann.

Um das Zentrum von Hydra I genauer zu untersuchen, wurden drei unterschiedliche Datensätze verwendet. Die Absorptionslinienkinematik von NGC3311 wurde mit Hilfe von Langspalt-Spektren (gewonnen mit FORS2 am UT1) untersucht. Mit ’multislit imaging spectroscopy’ (MSIS; Daten vom gleichen Instrument) haben wir die Kinematik von Planetarischen Nebeln (PNe) gemessen, welche Teil der Sternverteilung des Haufens in den innersten 100x100 kpc^2 um NGC3311 sind, und mit Photometrie vom WFI-ESOS2.2 Teleskop haben wir um die cD Galaxie die Lichtverteilung und ihre Unterstruktur untersucht.

Die Absorptionslinienkinematik von NGC3311 zeigt, dass der Halo dieser Galaxie von den inneren Sternen des Galaxienhaufens selbst beherrscht wird. Die Dominanz der Haufensterne beginnt in etwa 4-12 kpc Entfernung vom Galaxienzentrum, während die Sterne weiter innen an die Galaxie gebunden sind. Das ICL im Hydra Haufen ist dynamisch noch nicht durchmischt. In der projizierten Geschwindigkeitsverteilung (LOSVD) der PNe findet man mehrere Maxima, die Unterstrukturen im Haufenzentrum anzeigen. Mittels V-Band Photometrie haben wir entdeckt, dass das Licht im Halo von NGC3311 nicht symmetrisch um die Galaxie verteilt ist, sondern dass der nord-östliche Teil heller ist. Die Geschwindigkeit in diesem Halobereich passt zu einem Maximum der PN LOSVD bei 5000 km/s Geschwindigkeit, und außerdem zu der einer Gruppe von Zwerggalaxien im Zentrum von Hydra I. Das asymmetrische Licht könnte von der kleinen Gruppe von Zwerggalaxien stammen, wenn diese während eines kürzlichen Durchgangs durch das Haufenzentrum teilweise zerrieben wurden

und sich nun hinter NGC 3311 befinden. Die stellare Population und die Strukturparameter einer dieser Zwerggalaxien, HCC 26, sind konsistent mit denen anderer zwergelliptischer Galaxien.

Zusammengefasst, obwohl der Hydra I Haufen in Röntgenbeobachtungen als Prototyp eines relaxierten und dynamisch entwickelten Haufens erscheint, schreitet die Bildung des diffusen ICL und des Halos der zentralen cD Galaxie NGC 3311 immer noch voran.

Abstract

In the current cosmological scenario clusters, that are the biggest virialized systems of the Universe, are formed through accretion of smaller objects from the *cosmic web* in which they are embedded. During these events the galaxies involved are modified due to interaction with other galaxies, the cluster hot X-ray emitting gas and the cluster potential well. Some of mechanisms acting in dense environments are tidal stripping, mergers and ram pressure stripping, just to name a few. These mechanisms involved in galaxy evolution are also responsible for the formation of what is called the intracluster light (ICL). ICL consists of stars in clusters that are not bound to any cluster member. Numerical simulations predict that the stars contributing to the ICL component are unbound by the processes that are involved in galaxy evolution and in the formation of the brightest cluster cD galaxies in particular.

The aim of this work is to study the ICL component in the central core of Hydra I. Hydra I is a medium compact cluster in the Southern Hemisphere at a distance of $\sim$50 Mpc. The cluster, a relaxed system from X-ray observations, is dominated by two non interacting elliptical galaxies, NGC 3311 (cD) and NGC 3309 (E3). We are interested in the kinematic relation between the ICL component and the cD halo of NGC 3311 and in exploring what can be understood from the photometric and kinematic characteristics of the ICL about the evolutionary history of the cluster as a whole.

We studied the core of Hydra I using three different kinds of data. With UT1-FORS2 long-slit spectroscopy we investigated the absorption line kinematics of NGC 3311. With UT1-FORS2 multislit-imaging spectroscopy we probed the kinematics of the Planetary Nebulas (PNs) tracing the stellar light in the central 100×100 kpc^2 of the cluster, around NGC 3311. Finally, with WFI-ESO2.2m telescope photometry we studied the light distribution around the cD galaxy and its substructures.

The absorption line kinematics of NGC 3311 shows that the stellar halo of NGC 3311 is dominated by the central intracluster stars of the cluster. The transition from predominantly galaxy-bound stars to cluster stars occurs in the radial range from 4 to 12 kpc from the center of the galaxy. The diffuse light in the Hydra I cluster is still un-mixed. The PN line-of-sight velocity distribution (LOSVD) shows a multi-peaked structure and reveals the presence of subcomponents in the cluster core. From V-band photometric data we discovered an excess of light, with respect to a symmetric distribution, in the North-East part of the halo of NGC 3311. The excess has a velocity compatible with the velocity of the PNs contributing to a high-velocity peak in the PN LOSVD and a group of dwarf galaxies populating the central core of the Hydra I cluster. The excess of light could have formed from stars unbound from the small group of dwarf galaxies that were partially disrupted during a recent close passage through the dense cluster core and which are now behind NGC 3311. The stellar population and structural properties of one of the DWs, HCC 26, are consistent with those of other dwarf elliptical galaxies.

We conclude that even if from X-rays Hydra I appears to be the prototype of a relaxed and dynamically evolved cluster, the build up of the diffuse light and halo of its central cD galaxy, NGC 3311, is still ongoing.

Chapter 1

Introduction

This thesis is dedicated to the study of the kinematics of the intracluster light (ICL) in the core of the Hydra I cluster.

In the introduction I describe the main physical characteristics of galaxy clusters in the X-ray and optical ranges and I give a general overview on the mechanisms that drive the evolution of galaxies in dense cluster environments. Then I go on to define ICL, discussing its characteristics and its importance for the study of galaxy clusters, with a short review of several techniques used for its detection and investigation. A brief paragraph on the physics of the Planetary Nebulas (PNs), post-AGB stars at the end of their lives, follows, highlighting in particular the relevance of these stars for the study of the ICL. The Multi-Slit Imaging Spectroscopy technique for the PNs detection is introduced and an overview is given of the principal characteristics of the Hydra I cluster. Finally, the main results from the subsequent chapters are summarized.

1.1 Clusters of Galaxies

According to the Concordance Cosmological model we live in an expanding Universe that formed about $\sim$ 13.7 billions years ago in the Big Bang after a plasma phase at very high density and temperature. Structure formation started about 300,000 years later, due to the growth of cosmological perturbations, with a typical comoving scale of $\sim 10\ h^{-1}$Mpc, through gravitational instability. The driver of this gravitational instability is dark matter, a weakly interacting form of matter whose nature is not yet completely understood. The Universe observed today appears as a net, commonly called *cosmic web*, consistent of high density regions populated by galaxies and voids. In the formation scenario mentioned above, the structures aggregate in a hierarchical *bottom-up* way, with small mass virialized systems forming first and then enlarging by accretion and merging events (Peebles, 1993; Peacock, 1999).

Galaxy clusters are the most massive virialized systems in the Universe and the last structures to form. They are part of the cosmic web, occurring at the intersection of filaments and they keep accreating material from infalling galaxies or groups of galaxies. The masses of clusters are in the range from 10^{13} to 10^{15} $M_{\odot}$, while their extension is of the order of some 10s Mpc. As the densest regions in the Universe, clusters are very important both (i) as physical laboratories, for the study of the mechanisms leading to the evolution of galaxies (Böhringer, 2004) and (ii) as probes of cosmological models. Constraints on cosmological parameters can be obtained by the study of a) the cluster baryonic content, b) the cluster abundance and its evolution with redshift, c) the spatial distribution of the clusters (Kofman et al., 1993; White et al., 1993; Eke et al., 1998; Borgani, 2006, for a review).

80-87% of the total cluster mass is made of dark matter, which determines the depth of their potential wells. The remaining 13-20% is in the form of baryonic matter. N-body simulations predict that the dark matter density profile is well described by the Navarro, Frenk and White profile:

$$\frac{\rho(r)}{\rho_{cr}} = \frac{\delta_c}{(r/r_s)(1+r/r_s)^2} \tag{1.1}$$

where $\rho_{cr} = 3H^2/8\pi G$ is the critical cosmic density, r_s is the scale radius and $\delta_c(c) = \frac{200}{3}c^3/[ln(1+c-c/(1+c))]$ is a characteristic dimensionless density (Navarro et al., 1997). H is the Hubble constant, G the gravitational constant and c is called concentration parameter. It is proportional to r_{200}/r_s, where r_{200} is defined as the radius at which the cluster density is 200 times the mean density of the Universe. From Eq. 1.1 it is possible to derive the corresponding integrated mass profile:

$$M(<R) = 4\pi\rho_{cr}r_s^3\delta_c(c)[\ln(1+\tilde{R}) - \tilde{R}/(1+\tilde{R})] \tag{1.2}$$

where $\tilde{R} = R/r_s$. This quantity can be directly measured in a reliable way from X-ray and lensing observations in relaxed clusters (Pratt and Arnaud, 2002; Lewis et al., 2003). Both in low mass and massive systems the measured mass profile is found to be well described by a NFW model, indicating that simulations properly reproduce the dark matter halo density structure (Allen et al., 2001; Buote and Lewis, 2004; Pointecouteau et al., 2005; Pratt and Arnaud, 2005).

The baryonic matter is mostly in the form of hot, X-ray emitting gas permeating the cluster potential - the so called intracluster medium (ICM). Only $\sim$3% of the baryonic mass is in the form of stars and galaxies. Roughly 10-20% of the stars in a cluster contribute to what we call intracluster light (ICL). The ICL is therefore a very small component in galaxy clusters and its study has developed only in the last 10-15 years. However, as I will discuss later in this introduction, the ICL plays a major role in the understanding of the formation history and dynamical status of clusters.

1.1.1 Substructures in clusters of galaxies

An important consequence of the hierarchical structure formation scenario is that clusters are often not-relaxed systems and present, instead, subcluster components. This is a direct effect of the accretion events. The identification and analysis of such substructures is important not only to test cosmological models, but also for understanding galaxy evolution. In the last decades substructure components have been identified in ∼40% of the observed cluster (Geller and Beers, 1982; Dressler and Shectman, 1988). The identification of these subcomponents is possible with different methods: (i) by using the projected phase-phase distribution of galaxies (Biviano et al., 2006), (ii) by studying the irregularities in the hot X-ray emitting gas, tracing the potential well of the cluster (Briel et al., 1992; Böhringer et al., 2010), or by (iii) gravitational lensing (Abdelsalam et al., 1998). In the fifth chapter of this thesis we will show how the investigation of the kinematics of the intracluster light component in Hydra I, a cluster in the local Universe, contributed to the identification of one of the substructures of the cluster in its central region.

1.1.2 Clusters of galaxies: X-ray observations

Clusters of galaxies are the most common bright extragalactic X-ray sources. In this band they are relatively easy to identify because they stand as single extended sources. The first cluster X-ray survey was done at the beginning of the 70s, with the launch of the the *Uhuru* satellite (see Sarazin, 1988, for a review on the first X-ray surveys). The new X-ray satellites, *ROSAT*, *Newton-XMM*, *Chandra* and *SUZAKU* continue to give us an increasingly detailed picture of the galaxy clusters (see Fabian, 1994; Borgani and Guzzo, 2001; Rosati et al., 2002; Böhringer and Werner, 2010 for some reviews). With the next generation missions, for example *IXO* and *ASTRO-H*, more and more exhaustive information will be accessible.

The Intracluster medium and the physics of the X-ray emission

When clusters are formed, the primordial gas trapped in the dark matter potential is heated due to adiabatic compression, reaching very high temperatures of the order of $10^7 - 10^8$K. The gas has an extremely low density, $n_e = 10^{-3}\mathrm{cm}^{-3}$; it is mainly composed of fully ionized hydrogen (∼75%) and helium (∼24%). The remaining ∼1% consists of heavier elements. The hydrogen and helium concentrations are similar to the cosmic abundances, confirming that the ICM is primarily constituted by primordial gas that has been trapped by the cluster potential. The metal abundance is related to the star-formation history of the galaxy cluster and models predict that the ICM is enriched with heavy elements coming from supernovae explosions or stellar winds in the member galaxies (Matteucci and Vettolani, 1988; Böhringer et al., 2005b; Ettori, 2005).

Observations have shown that the ICM has a radial density profile well fitted by a β-model:

$$\rho(r) = \rho(0)\left[1 + \left(\frac{r}{r_c}\right)^2\right]^{3\beta/2} \tag{1.3}$$

where r_c is the so called core radius, defined as the radius where the density projected on the sky is half of the central value (Cavaliere and Fusco-Femiano, 1976). The ICM emits Bremsstrahlung radiation, with luminosity of the order of 10^{43-45}erg s^{-1}, plus a series of emission line features due to the presence of heavy elements (Felten et al., 1966). Among these, the strongest is the 7 KeV iron line (Sarazin, 1988). The typical metal abundance in nearby galaxy clusters is $0.3\,Z_\odot$ (Mushotzky and Loewenstein, 1997; Ettori et al., 2001).

The Bremsstrahlung radiation at frequency ν is given by the formula:

$$\epsilon_\nu = \frac{2^5 \pi e^6}{3 m_e c^3} \left(\frac{2\pi}{3 m_e k} \right)^{1/2} Z^2 n_e n_i g(Z, T_g, \nu) T_g^{-1/2} \exp(-h\nu/kT_g) \tag{1.4}$$

where n_e and n_i are the ion and electron densities, e is the elementary charge and the ion charge number. T_g is the temperature of the gas, m_e is the electron mass, k is the Boltzmann constant, h the Planck constant and $g(Z, T_g, \nu)$ is the Gaunt factor, a dimensionless quantity related to the scatter mean distance between electrons and ions (Sarazin, 1988, and references therein). This formula shows a linear dependence of the Bremsstrahlung emissivity on both ion and electron densities, so as all $n_i \propto n_e$ for fixed T and metallicity the emission is proportional to n_e^2. The exponential cutoff of Eq. 1.4 is sensitive to the gas temperature T_g. The Bremsstrahlung emission and the line emissions can be fitted with different models (Liedahl et al., 1995; Kaastra and Mewe, 2000) that allow us an estimation of the temperature and abundance of heavy elements of the observed ICM.

From the measurement of the ICM density and temperature, in the hypothesis of hydrostatic equilibrium (a hypothesis that is reasonably justified in the central core of a cluster) it is possible to calculate the mass distribution of the cluster:

$$M = -\frac{kTr}{\mu_p G} \left(\frac{\Delta ln\rho_g}{\Delta lnr} + \frac{\Delta lnT_g}{\Delta lnr} \right) \tag{1.5}$$

The cooling flow problem and the feedback mechanism

One of the most important open questions regarding the study of the ICM is the cooling flow problem. As mentioned above, the gas forming the ICM emits in the X-ray range. In this way it looses energy. The time scale of this cooling process for pure Bremsstrahlung emission is given by:

$$t_{cool} = 8.5 \times 10^{10} yr \left(\frac{n_p}{10^{-3} cm^{-3}} \right)^{-1} \left(\frac{T_g}{10^8 K} \right)^{1/2} \tag{1.6}$$

This time scale is in general larger that the age of the Universe. As a consequence, the cooling should be a negligible effect. But already the first observations carried out with the *Uhuru* satellite in the 70s (Giacconi et al., 1972; Forman et al., 1978) showed very bright X-ray SB values at the center of a large fraction of clusters. These, associated with a temperature drop and an increase of the gas density in the same regions, demonstrated that for some clusters the cooling time can drop below the cluster age. Observations have confirmed that 50-70% of the clusters have a cooling core. These are more frequent in more relaxed and dynamically evolved systems (Fabian, 1994 and references therein). The most luminous cluster cooling core was discovered by Böhringer et al. (2005a) in the X-ray-luminous galaxy cluster, RXC J1504.1-0248. Models have been developed to explain the cooling flow mechanism (Fabian and Nulsen, 1977). These models predict a drop of the central temperature in the cool core clusters and a gas density increase, with a mass deposition rate of the order of 100-1000 $M_\odot$/yr. The *cooling flow problem* consists in the fact that both the temperature drop and the mass deposition rates predicted are larger than those observed (Böhringer et al., 2002; Edge and Frayer, 2003; Bauer et al., 2005). The observations can be explained if some heating mechanism acts to balance the cooling (Böhringer et al., 2007). At present, supernovae explosions are considered likely candidate heat sources (Kravtsov and Yepes, 2000; Menci and Cavaliere, 2000), as well as the so called active galactic nucleus (AGN) feedback (Peterson and Fabian, 2006). This last mechanism is observationally supported by strong interaction seen in the local Universe between black holes (BH) and the gas surrounding their host elliptical galaxies or BCGs. This gas often contains X-ray *bubbles* filled with relativistic plasma inflated by relativistic jets launched from their central AGN BH (Fabian et al., 2006). Models predict that the energy output from AGNs should be sufficient to compensate the cooling rate (Voit, 2005).

1.1.3 Clusters of galaxies: optical observations

In optical surveys, clusters appear as enhancements of the surface density of galaxies on the plane of the sky. One of the most extensive, and still used cluster catalog was obtained by Abell at the end of the 50s (Abell, 1958). In this catalog clusters were classified as objects with at least 50 galaxies concentrated within a radius of $R = 1.7/\mathrm{z}$ arcmin, where z is the measured cluster redshift, and within a well established magnitude range ($m_3 < m_{galaxy} < m_{3+2}$, where m_3 is the magnitude of the third brightest galaxy of the cluster). From the morphological point of view many different classifications have been proposed. Zwicky et al. (1961) classified clusters as compact, medium compact and open, based on the presence of one, more than one or no single pronounced concentration of galaxies in the cluster. Bautz and Morgan (1970) divided clusters in Type I-II-III according to the presence of one (Type I), more than one (Type II) or no (Type III) dominant brightest cluster galaxies. Alternatively Rood and Sastry (1971) proposed a classification relative to the spatial distribution of the ten brightest galaxies in the cluster, from cD clusters, dominated by one central brightest galaxy to Irregular cluster, in which the ten brightest galaxies of the cluster are distributed in an irregular way. Based only on photometric images the identification of clusters can be very difficult. If spectroscopic data are not available, it is often impossible to establish if a galaxy is a cluster member or not due to projection effects. Many different techniques and algorithms have been developed in the last decades to solve this problem, since spectroscopy follow-up is highly desirable, but can be very time consuming (Rosati et al., 2002 for a review). Among others, one of the techniques that has proved to be very efficient also at $z \geq 1$, if multi-band photometric images of the sky are available, is that of the identification of the so called red sequence. This is formed by a population of red, early-type galaxies (see next Section), present in clusters but not in the field, lying on a well defined sequence in the galaxy color-magnitude plane (Stanford et al., 1997; Gladders and Yee, 2000; Koester et al., 2007).

Galaxies: a morphological classification

If sorted according to their morphology, galaxies can be divided in a relative small number of classes. The most widely used classification is the Hubble sequence (Hubble and Rosseland, 1936; Sandage and Bedke, 1994). This sequence is populated from left to right by four different types of galaxies: ellipticals (E), lenticulars (S0), spirals (S) and irregulars (Irr). Ellipticals, in first approximation, have a surface brightness (SB) profile that can be described by a Sersic law:

$$\Sigma(r) \propto \Sigma_e \exp(r/r_e)^{1/n} - 1 \tag{1.7}$$

where r_e is called effective radius and is defined so that half of the luminosity of the galaxy falls inside this radius and n is an index that is inversely related to the concentration of the light profile in the galaxy (Sersic, 1968). In the particular case in which n=4 Eq. 1.7 is called de Vaucouleurs law (de Vaucouleurs, 1948).

On the other end of the Hubble sequence there are spiral galaxies. These can be divided into barred and non-barred systems. In the middle, between ellipticals and spirals, there are the lenticular galaxies. Both spirals and lenticulars are characterized by a central region, often called bulge, whose SB profile, similarly to ellipticals, can be described by a Sersic law. In addiction to the bulge, they have a rotating disk. But, while spirals are so called because they present spiral structures in the disk, in the S0 galaxies these structures are not visible. The SB of this disk structure is, in general, well described by an exponential law:

$$\Sigma(r) = \Sigma_0 \exp(-r/r_s) \tag{1.8}$$

where Σ_0 is the central SB. In the Hubble sequence, lenticulars are between ellipticals and spirals because they show intermediate properties between these two classes of galaxies. From a morphological point of view they have a structure more similar to disk galaxies, but like ellipticals they are characterized by an older stellar population, they are red, more massive and they do not show a lot of star formation activity. Ellipticals and lenticulars are often referred to as early-type galaxies. Spirals on the other hand are blue, they have a younger stellar population, they often show sites of ongoing star formation, and are also called late-type galaxies.

Another class of systems very common in the Universe but not contained in the Hubble sequence, is that of dwarf galaxies (DWs). These are morphologically similar to ellipticals, but with much lower SBs (Mateo, 1998). These galaxies, in general, do not contain young stars.

Galaxy Luminosity Function (LF)

How galaxies are distributed in luminosity is described by the luminosity function, $\Phi(L)$. The law that better fits observations is the Schechter function (Schechter, 1976):

$$\Phi(L) = (\Phi^*/L^*)(L/L^*)^{\alpha} \exp(-L/L^*) \tag{1.9}$$

where $\Phi(L)dL$ gives the number of galaxies in the luminosity range $L + dL$, L^* is the characteristic luminosity above which the number of galaxies sharply falls, Φ^* is a normalization factor and α is the slope of the luminosity function at the faint end. It is well known that the Schechter law is only an approximation to the real luminosity function of galaxies, since this depends both on the galaxy type and the environment (Dressler, 1978; Jerjen and Tammann, 1997; Hansen et al., 2005). The study of the LF for different systems is, in fact, a way to investigate the influence of environment on galaxy formation and evolution (Garilli et al., 1999; De Propris et al., 2003).

Analyzing a sample of galaxies in the Virgo cluster and in the field, Binggeli et al. (1988) found evidence suggesting that the luminosity function of the individual morphological types differs from type to type, but for a give type is instead invariant with environment, with just the amplitude changing in different host systems. The difference observed between the LF of galaxies in the field and in clusters arises as a consequence of the morphology density relation (see following Sections) (Lugger, 1986). The slopes of the LFs are very similar at the bright end because spiral galaxies and ellipticals have comparable characteristic luminosities. The main difference is observed at the faint end. The slope of the LF of galaxies in clusters is significantly steeper than that of the galaxies in the field. This is due to dwarfs galaxies which are much more frequent in clusters than in the field (Pracy et al., 2004).

The Fundamental plane (FP)

For ellipticals and bulges of spiral and S0 galaxies a relation exists between their morphological and dynamical properties. In the three-dimensional space given by velocity dispersion, effective SB Σ_e and effective radius r_e, ellipticals and bulges fall on a plane, called the *Fundamental plane* (FP) (Dressler et al., 1987; Faber et al., 1987; Bender et al., 1992) given by:

$$log(r_e) = a\, log(\sigma_0) + b\, \Sigma_e + c \tag{1.10}$$

where a, b, c are constants. The projection of the FP on Σ_e vs r_e plane is known as the Kormendy relation (Kormendy, 1977) and on the Σ_e vs σ_0 plane is called Faber-Jackson relation (Faber and Jackson, 1976). Dwarf ellipticals also lie on a plane in this 3D space, but not the same as the one defined by the ellipticals and bulges.

An alternative way to define the FP is the via the κ-space formulation (Bender et al., 1992):

$$\mathrm{k}_1 = \frac{1}{\sqrt{2}}\log(r_e\sigma_0^2);\ \mathrm{k}_2 = \frac{1}{\sqrt{6}}\log\left(\frac{\Sigma_e\sigma_0^2}{r_e}\right);\ \mathrm{k}_3 = \frac{1}{\sqrt{3}}\log\left(\frac{\sigma_0^2}{\Sigma_e r_e}\right) \tag{1.11}$$

In this case k_1 is proportional to the considered system mass, k_2 depends on its SB and k_3 on its M/L ratio. DWs lie on a distribution perpendicular to those formed by ellipticals and bulges in the $\mathrm{k}_1 - \mathrm{k}_2$ plane (de Rijcke et al., 2005). This evidence suggests a different origin and/or evolution history for these systems with respect to ellipticals. Even if DWs are the most common objects in the Universe, their formation is still debated. The most likely mechanisms responsible for their formation are: (i) gravitational collapse of primordial density fluctuations, similarly to ellipticals (Dekel and Silk, 1986); (ii) ram-pressure stripping from low-mass irregular galaxies (Boselli et al., 2008); (iii) galaxy-galaxy or galaxy-cluster potential well tidal interactions from more massive galaxies (Mastropietro et al., 2005).

Brightest cluster galaxies (BCGs)

A particular class of objects of which we have not yet talked about is that of the brightest cluster galaxies (BCGs). Morphologically they are similar to ellipticals, but apart from being, by definition, the most luminous galaxies in clusters, from an observational point of view they are particular for several reasons. (i) They are special for their positions being located near the centers of galaxy clusters, close to the peak of X-ray emission (Lin and Mohr, 2004; Rafferty et al., 2008), at the bottom of the potential well. (ii) They usually show small offsets in velocity in comparison to their host cluster systemic velocity (Zabludoff et al., 1990). (iii) They are larger and have higher velocity dispersions (von der Linden et al., 2007) and masses with respect to other ellipticals. They, in fact, lie off standard relations for *normal* early-type galaxies (Bernardi et al., 2007). Their Faber-Jackson relation, for example, is steeper than for the brightest non-BCG ellipticals. This is consistent with significant growth of BCGs via dry mergers (Desroches et al., 2007). (iv) Their SB profiles are special, since BCGs often present faint and extended cD halos around them in the form of an excess of light with respect to a de Vaucouleurs law (Binggeli et al., 1988). (v) BCGs also seem to be brighter than expected from the bright end of the luminosity function of galaxies in clusters (Bernstein and Bhavsar, 2001) and (vi) they are more likely to host AGNs than other ellipticals of the same stellar mass (Best et al., 2007).

Since BCGs are different from *normal* early-type galaxies, studying their characteristics is important in particular to understand the physics acting in cores of clusters. Their peculiar position indicates, in fact, that their formation is tightly related to that of clusters as a whole (Brough et al., 2005). In the next section we discuss some of the processes that are thought to be involved in the evolution of BCGs and galaxies in general.

How galaxies populate clusters

Many studies have been done to investigate the characteristics of galaxies in clusters and the existence of a strong relation between galaxy properties and the density of their host environment is known since many decades (Hubble and Rosseland, 1936). This dependence affects most of the characteristics of galaxies from their mass to their star-formation history. Some of the most important observed relations are: the Butcher-Oemler (BO) effect, the morphology-density relation and the downsizing effect. Butcher and Oemler (1978a,b) were the first to notice that the number of blue galaxies in the cores of clusters increases with increasing redshift. Later Dressler et al. (1994), using Hubble space telescope images, showed that these galaxies are seen in clusters at high redshift but not in the local Universe, and are star-forming spiral galaxies. The morphology density (MD) relation relates the frequency of the various galaxy types and the local environment density (Oemler, 1974; Dressler, 1980). What is observed is that elliptical galaxies are more frequent in the dense cores of the clusters, while there is an inverse trend with density (i.e. distance from the cluster center) for the population of lenticular and spiral galaxies. These tend to be more frequent in the outskirts of clusters. This relation seems to hold at all redshifts (Dressler et al., 1997), but while at high redshift the fraction of spiral galaxies is high, as redshift decreases spiral galaxies seem to be substituted by S0 galaxies (Fasano et al., 2000). Finally the downsizing effect is related to galaxy star-formation and mass. From observations it appears that galaxies with lower mass have longer star-formation histories. That means that blue, low mass spiral galaxies have more star-formation activity than bright massive ellipticals. This has two effects: (i) since as we have already noticed the number of spiral galaxies decreases with decreasing redshift, then also the star-formation activity decreases with redshift in an anti-hierarchical way (Smail et al., 1998; De Lucia et al., 2004; Poggianti et al., 2004); (ii) as a consequence of the MD relation the outskirts of clusters show more star-formation than the cores and the field (Balogh et al., 1999). The truncation of star-formation in clusters can be due to evolution of galaxies in dense environments, for example due to gas loss in the interaction with the cluster ICM. This is supported by the observational evidence that the fraction of star-forming galaxies is also anti-correlated with cluster mass (Poggianti et al., 2006).

1.1.4 Mechanisms causing galaxy evolution in clusters

There has been much discussion in the last decades about the formation of the Hubble sequence. The origin of the MD and downsizing effects or the formation processes involved in the formation of BCGs are not yet completely understood. It is not clear if the observed correlations are due to mechanisms acting in dense environments or are imprinted during structure formation. Attempting to summarize the work that has been done to try to find an answer to these questions is beyond the purpose of this introduction, but, since many of the mechanisms involved in galaxy evolution are also important for the formation of the intracluster light component, I give here a brief overview of the proposed processes. The most accredited mechanisms proposed to cause galaxy evolution involve galaxy-galaxy, galaxy-ICM and galaxy-cluster potential well interactions.

Mergers result from strong and direct galaxy-galaxy collisions (Mihos, 2004, for a review). There are different types of mergers, major and minor mergers and wet and dry mergers. The first two classes refer to the dimensions of the galaxies involved. In a major merger the two involved galaxies have comparable masses, in a minor merger one is much bigger than the other. The second two classes are related to the presence of gas in the involved galaxies. Wet are those mergers in which gas is involved and dry are those in which gas is not involved. Mergers are considered to be rare events and numerical simulations predict that during their lifetime galaxies with a mass $M \leq 10^{11} M_{\odot}$ experience at most one merger event. Only more massive galaxies, like BCGs, have an evolution tree that involves a higher number of mergers up to ~5 (De Lucia et al., 2006; De Lucia, 2007). Numerical simulations demonstrated that mergers can also change the morphology of galaxies from spirals to early-type galaxies (Toomre and Toomre, 1972; Gerhard, 1981; Naab and Burkert, 2003). Dry mergers between two ellipticals are often responsible for the formation of BCGs, while encounters between an elliptical and a spiral galaxy produce less massive ellipticals. Very low luminous ellipticals can be generated by wet mergers between spirals (Khochfar and Burkert, 2003). Mergers are more efficient if they happen between galaxies that move at a relative low velocity (Merritt, 1985). For this reason they are expected to be more efficient in groups of galaxies than in galaxy clusters.

Actually, recent observations demonstrated that mergers happen both in groups and clusters. Studying a sample of 515 clusters in the redshift range $0.03 \leq z \leq 0.12$ Liu et al. (2009) discovered 18 ongoing major dry mergers involving BCG galaxies. From this they calculated that 3.5% of BCGs in the local Universe are involved in merger events. At $z \leq 0.12$ McIntosh et al. (2008) investigated the formation of massive early-type galaxies analyzing a sample of 845 groups and clusters of galaxies. They identified 38 pairs of merging galaxies and found that dry mergers are more likely at the center of massive groups. At intermediate redshift, $z = 0.39$, Rines et al. (2007) reported, in the very massive cluster CL 0958+4702, the detection of one of the biggest major merger events ever observed. They predicted that the process will lead to the formation of the BCG of the cluster. At higher redshift, $z \sim 0.83$, Tran et al. (2005) identified six merging pairs of galaxies in the MS 1054-03 cluster. They calculated that galaxies in bound subsystems make up 15.7% of the cluster population at this redshift.

Tidal stripping and harassment can be classified into two main mechanisms: galaxy-galaxy tidal stripping and galaxy-cluster potential well interactions. Tidal fields, produced by massive galaxies (Gnedin, 2003) or by the global cluster halo (Merritt, 1984), can lead strong dynamical evolution in galaxies that happen to pass close enough to them. In this case the satellite galaxies are distorted by the tidal fields and can lose material beyond a certain radius called tidal radius. Numerical simulations showed that the tidal radius in general is a function of the potential of the two interacting galaxies or the galaxy and the cluster, and of the orbit of the satellite galaxy (Barnes, 1988; Read et al., 2006). These encounters, apart from distorting the shape of satellite galaxies can truncate their dark matter halos and quench star-formation. They can also be responsible for the transformation of spiral galaxies into S0, and in the case of a very low mass satellite galaxy they can also completely destroy it. During these events the formation of tidal tails and debris is very common (Toomre and Toomre, 1972).

Harassment is similar to tidal stripping, but is related to faster encounters. At high speed (of the order of the cluster velocity dispersion) close interactions can cause impulsive gravitational shocks that can severely damage galaxies. In particular, this mechanism could be responsible for the transformation of very low luminosity disk galaxies into dwarfs (Moore et al., 1996; Mayer et al., 2006).

Ram pressure stripping is related to galaxy-ICM interactions. On the one hand, its effect consists in the loss of intergalactic gas from a galaxy that crosses at high velocity the central core of a cluster, due to the friction with the hot, X-ray emitting ICM (Gunn and Gott, 1972). This effect helps explaining the deficiency of gas observed in the S0 galaxies in the densest regions of clusters and star-formation quenching. On the other hand, the interaction of a galaxy with the ICM can compress the galaxy gas inducing star formation (Dressler and Gunn, 1983). Observations of the clusters A1689 at $z \sim 0.18$ and A2667 at $z \sim 0.23$ indeed confirmed these scenarios. Cortese et al. (2007) detected in these clusters infalling galaxies with bright blue star formation knots. They explained the morphology and the star formation of the galaxies as a consequence of both tidal interactions with the cluster potential well and of the ram pressure experienced by them while being accreted on the clusters.

1.2 The Intracluster Light

Intracluster light (ICL) consists of stars that are born in galaxies but have been lost by them during the interaction they undergo in the cluster environment with other galaxies or the cluster potential well. Even if diffuse light represents only a relatively small fraction of the light emitted by clusters, its study is important to understand the dynamical status of the cluster to which it belongs and the physics involved in galaxy formation and evolution. Once this component has formed it will not be able to lose energy and/or angular momentum and will remain on the orbit on which it was formed, conserving the chemical characteristics of the objects from which it has been lost. This makes ICL a good probe of the mechanisms acting in the build up of structures and explains why the study of this component is fundamental to understand the dynamical state of a cluster and cluster evolution in general.

The existence of the ICL is suspected since the 50s. Zwicky in a paper of 1951 on the Coma cluster wrote: *"vast and often very irregular swarms of stars and other matter exist in the spaces between the conventional spiral, elliptical and irregular galaxies"* (Zwicky, 1951). Unfortunately, due to very low surface brightness of this component, which is less than 1% of the brightness of the night sky (Vílchez-Gómez, 1999), a systematic study of ICL has been possible only in the last decade, with the advent of CCDs.

Since then the main questions that the astronomers have tried to answer are: where, in a cluster, ICL is mainly formed? Is there a preferential time during cluster evolution in which it is formed? Which are the mechanisms that contribute more to the formation of the ICL and is there any relation between the cluster mass and the amount of ICL? Do all galaxies contribute to the formation of ICL or only the most massive ones?

To answer these questions different approaches have been used. On the one side the increasing resolution of numerical simulations has given the possibility to predict the origin and behavior of ICL in more detail (see Sec. 1.2.1). On the other side, from the observational point of view, deep photometry has allowed to understand the spatial distribution of the ICL, to study its color in relation to the color of the galaxies in the cluster and to estimate its amount in relation to the global properties of the hosting system (see Sec. 1.2.2). In parallel in some cases, the study of single intracluster stars, like red-giant stars and supernovae and globular clusters, has allowed to derive an estimate of the age and metallicity for the ICL (see Sec. 1.2.3). And finally, this is the framework in which the presented thesis is embedded, the study of Planetary Nebulas (see Sec. 1.2.5) has also allowed to study the kinematic properties of this component.

In the next sections, I give a brief summary of the most recent results on ICL, both from simulations and observations.

1.2.1 Formation mechanisms and numerical simulations

Today the existence of ICL is well known, but the physics involved in its production is still subject of debate. The main candidate mechanisms to produce ICL are: (i) galaxy mergers; (ii) fast encounters between galaxies (*galaxy harassment*); (iii) tidal interactions between two galaxies or between a galaxy and the cluster potential; (iv) stripping of groups of galaxies falling into a bigger structure; (v) stripping of stars from galaxies in the initial collapse of clusters (see Sec. 1.1.4 for more detailed physical description of these mechanisms). Reasonably all of these mechanisms contribute to the formation of ICL, but it is not clear yet in which measure they contribute and in which phase of the cluster formation they mainly play a role. It is likely that there is not a common path for all the clusters, but that the formation of the ICL strongly depends on the dynamical evolution history of the particular systems and that generalized conclusion cannot always be drawn (Merritt, 1984; Dubinski, 1998; Willman et al., 2004). However, in general we expect more massive and evolved systems to have a higher amount of ICL than dynamically younger and less massive systems.

Numerical simulations were performed and studied to understand the formation of the diffuse light component and to put it in relation to the global characteristics of the host structure. Napolitano et al. (2003) performed a ΛCDM dark matter simulation with tracer particles of a Virgo like cluster, and more recently hydro-dynamical simulations comprising cooling and heating mechanisms, star formation and stellar evolution have been analyzed. In accordance to observations (see next paragraphs), most of the simulations found that the amount of ICL in the simulated clusters at z=0 comprises of the order from 10 to 30% of the total optical light emitted by the clusters (Willman et al., 2004; Sommer-Larsen et al., 2005; Purcell et al., 2007), even if in some cases a bigger amount was observed (Murante et al., 2007; Puchwein et al., 2010). Simulations suggest that the ICL evolves in parallel to cluster, with the increase of ICL strongly related to the accretion of groups onto the system (Rudick et al., 2006). Most is formed at $z < 1$ (Murante et al., 2007; Dolag et al., 2009). The morphology of the ICL changes with the dynamical status of the cluster. Tidal streams are more present in dynamically young systems. These substructures are generally colder that the galaxies in the system and present unmixed stellar populations (Napolitano et al., 2003; Rudick et al., 2009). Their predicted color is comparable to the color of elliptical galaxies with metallicities that decrease from near solar at the cluster core, to metal-poor in the outer regions (Sommer-Larsen et al., 2005). Their formation is mainly due to the stripping in close passages near the central cluster galaxy of both massive and small galaxies, with the stars mainly stripped from the outer, lower-metallicity parts of the galaxies (Willman et al., 2004). As clusters evolve, ICL evolves in parallel and a more diffuse and homogeneous ICL envelope forms (Rudick et al., 2009).

Simulations agree that massive galaxies mainly contribute to the formation of intracluster stars (Murante et al., 2007; Puchwein et al., 2010). Murante et al. (2007), analyzing a sample of 117 clusters, showed that most of the ICL is produced during the merger history that lead to the formation of the BCG or other massive galaxies in the cluster, while smaller galaxies and tidal stripping mechanisms are responsible only for a minor fraction of the ICL in the outskirt of the cluster. Debated remains the role of dwarf galaxies (DWs) in the formation of ICL. Wetzel and White (2010), studying the fate of satellite galaxies in galaxy cluster, found that most of them are disrupted by tidal stripping into the ICL. Baria et al. (2009) found that during cluster evolution DW galaxies are mainly destroyed by mergers with massive galaxies, but that in the case of destruction by tidal fields of other galaxies, the light released is sufficient to explain the ICL observed in clusters.

1.2.2 Amount and morphology

ICL is a common component in all structures, from massive clusters to groups (Feldmeier et al., 2002, 2004), but the amount of diffuse light as a function of host system mass and other main characteristics remains a controversial issue. Observations of the Leo group showed that only a few percent of the optical light in these systems is in the form of intragroup light (IGL) (Castro-Rodríguez et al., 2003). On the other side, HGC 15, HGC 35 and HGC 51 have a detected IGL component that emits from 15% to 30% of the total light of the group (Da Rocha et al., 2008) and as an extreme case the compact group HGC 90 has an IGL component that is 45% of the total group light (White et al., 2003). In galaxy clusters recent studies have shown that ICL comprises of the order of 10-30% (Gonzalez et al., 2000; Zibetti et al., 2005) of the total optical light emitted by a cluster, but in young systems like Virgo its fraction can be very low (Aguerri et al., 2005) while it can reach values of about 50% at the center of very massive clusters like Coma (Bernstein et al., 1995).

Several deep photometry multi-band campaigns have been carried out in clusters in the nearby and intermediate redshift Universe. These studies have shown that the ICL is present in the form of diffuse component among galaxies or extended halos around BCGs, and also in the form of plumes and tidal tails. The extended halos are thought to built-up by the accretion of material onto the central BCG galaxy of the cluster, while tidal debris is the sign of recent interaction of galaxies in the dense cluster environment.

However, the spatial distribution of ICL is, in general, very different from cluster to cluster. The presence of a cD galaxy often corresponds to both centrally concentrated galaxy profiles and centrally concentrated ICL profiles (Gonzalez et al., 2005; Krick and Bernstein, 2007). Studying a sample of 683 BCG clusters in the SDSS survey, Zibetti et al. (2005) found that the ICL fraction is 30-40% of the total optical light of the cluster within the central 100 kpc and that this fraction dramatically decreases to a value of $< 5\%$ at a galactic distance of $600 - 700h_{70}^{-1}$ kpc. This is consistent with ICL either forming from galaxy interactions at the center or forming at earlier times in groups and later combining in the center. The spatial distribution of ICL in dynamically young and non-cD galaxy clusters is less regular and reveals the ongoing formation of ICL by galaxy-galaxy interactions (Feldmeier et al., 2004). Therefore, there seems to be a tight bond between ICL and BCG galaxies. The two components remain difficult to disentangle and several authors speak about a BCG+ICL as a single component (Gonzalez et al., 2007) (see Sec. 1.2.4 for a more detailed discussion).

A well studied system is the Virgo cluster. Very deep imaging, covering a large area, obtained with the Burrell Schmidt Telescope, revealed a complex network of diffuse light and extended tidal features in the core of this cluster (Mihos et al., 2005; Rudick et al., 2010). In Fig. 1.1 the upper panel shows an DSS image of the Virgo cluster and the lower panel a very deep photometric image of the same area obtained by Mihos et al. (2005). It is evident in this second image how the space between the galaxies is filled with light distributed in a very complicated way. The study of the color of the ICL around M 87, out to a radius of 2000″ showed that the diffuse light component becomes bluer from the center to larger radii. A similar color for the BCG galaxy halo and most of the observed streams was found (Rudick et al., 2010).

An interesting case is also that of the Centaurus cluster. Deep images revealed the presence of an arc of diffuse light that stretches for over 100 kpc South of NGC 4079, one of the galaxies in the cluster (see upper left panel of Fig. 1.2). Comparison with simulations support the hypothesis that such feature is what remains from a galaxy that was disrupted by a close passage with this elliptical galaxy (Calcáneo-Roldán et al., 2000).

Multi-wavelength analysis of the Coma cluster showed a similar situation in the Coma cluster, where several different concentrations of diffuse light around the central galaxies of the cluster, NGC 4874 and NGC 4889, were detected (Bernstein et al., 1995; Adami et al., 2005). Most of the ICL has a red color, compatible with old non star forming material lost from elliptical galaxies, while one of the light concentrations has a bluer color, and is probably due to the recent disruption of a spiral galaxy near the two main galaxies of the cluster.

At higher redshift, i.e. $z \sim 0.3$, Pierini et al. (2008) analyzed a sample of three X-ray luminous clusters selected from the REFLEX cluster survey. Two of them are relaxed clusters, the other is a merging cluster dominated by two subclusters, each dominated by a pair of BCGs. From the color study they found a consistency between the color of the BCGs and the ICL component in the clusters that from the X-rays are classified as relaxed. The color of the diffuse light observed around the BCGs galaxies in the non-relaxed systems is significantly bluer than that of the BCGs themselves. This result suggests again that the mechanisms leading to the formation of the ICL depend on the dynamical status of the cluster. In the un-relaxed system, for example, the bluer color of the diffuse light could be due to the recent disruption of star-forming, low metallicity dwarf galaxies.

A systematic study of ICL characteristics as a function of redshift remains for the moment a difficult task to implement. A first attempt in this direction was done by Krick and Bernstein (2007). They detected ICL for all the groups and clusters in their sample up to a redshift of $z=0.3$. They found that ICL is present both in cD and non-cD clusters, with ICL not centralized in non-cD ones. Unfortunately, this result is not conclusive due to the biases in the used cluster sample which contains

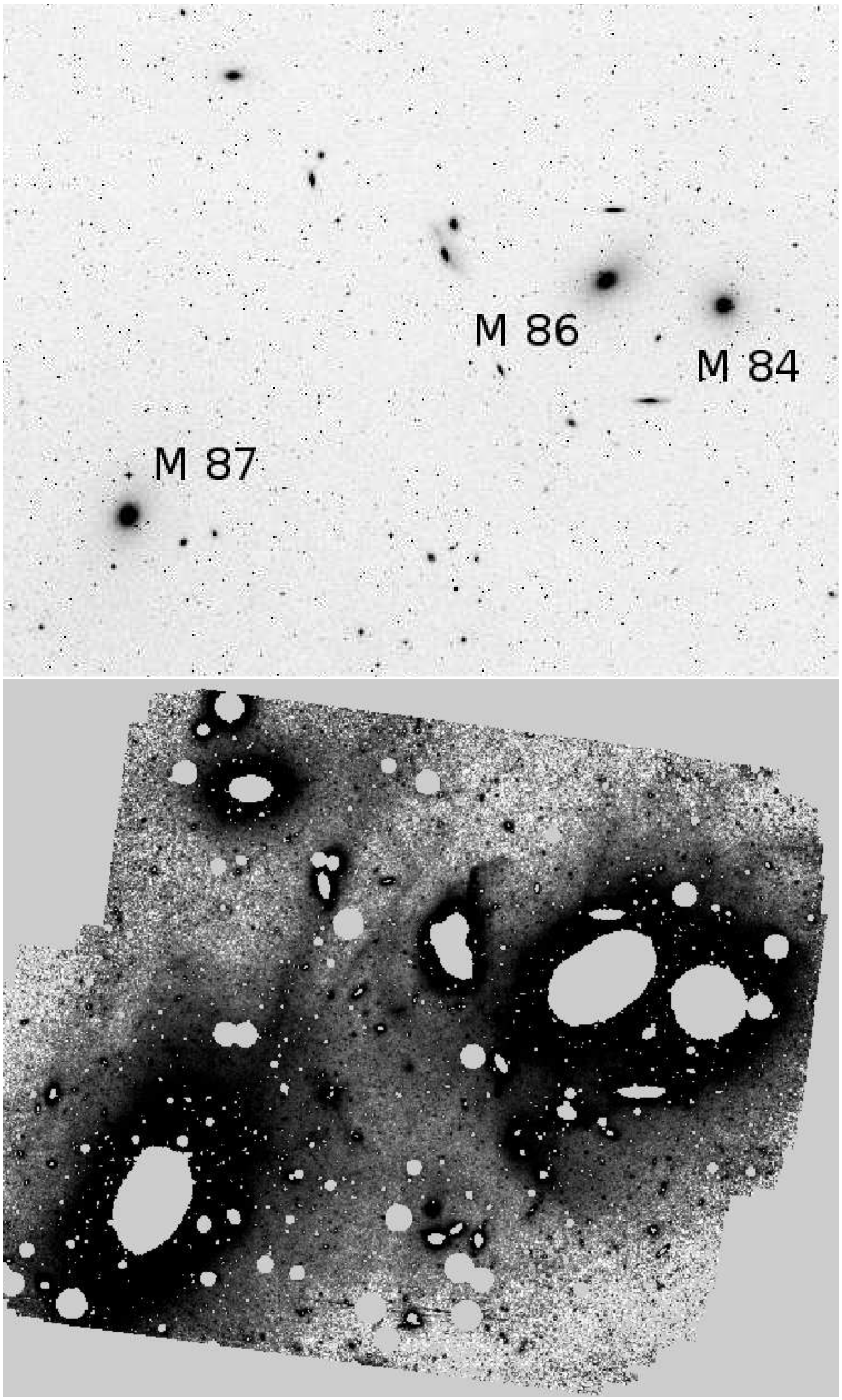

Figure 1.1: *Upper panel*: DSS image of the core of the Virgo cluster. *Lower panel*: Deep V band image of the core of the Virgo cluster showing the diffuse light (Mihos et al., 2005). The black levels saturate at $\mu_V \sim$26.5, while the faintest features visible have a surface brightness of $\mu_V \sim$28.5. North is up; East is to the left.

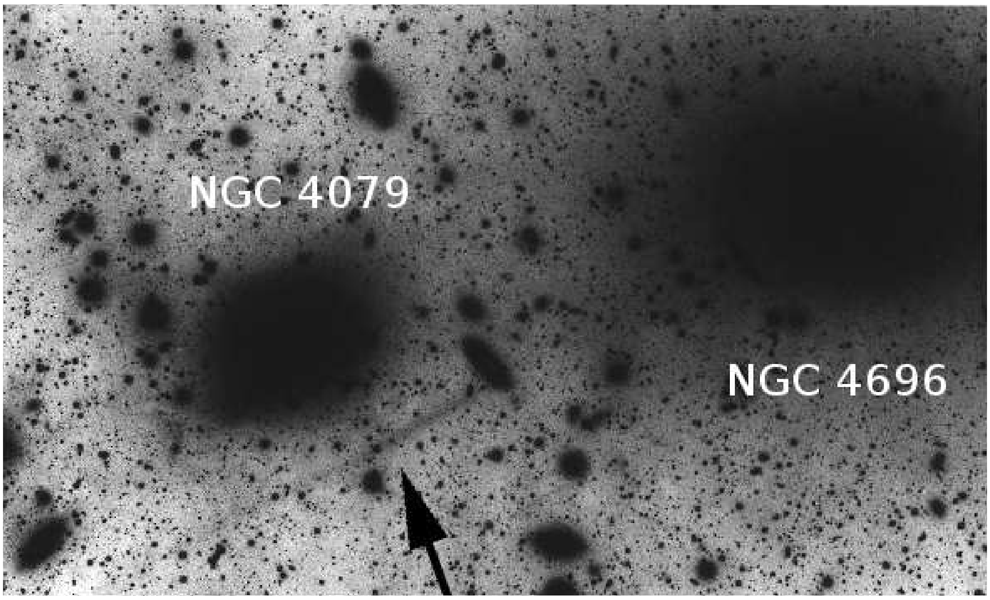

Figure 1.2: High-contrast image of the core of the Centaurus galaxy cluster with NGC 4696, the brightest galaxy in the cluster (upper right). Under NGC 4079 (lower left) the extremely faint jet-like feature extending towards the lower left corner is visible.

no low-luminosity high-redshift clusters and no high flux low-redshift clusters.

A further important issue to mention is the relevance of the IGL and ICL to address the problem of the missing baryon mass. The inclusion of the diffuse component in the calculation of the baryonic mass fraction may help to fill the gap between the values measured by WMAP (Spergel et al., 2007) and direct measurements of baryons in groups and clusters. Gonzalez et al. (2007) found, in particular, that the importance of the BCG+ICL component in the baryon budget is inversely proportional to system mass and velocity dispersion and that its contribution is more fundamental at the center of the groups and clusters and less in the outskirts.

1.2.3 Metallicity: individual stars as diffuse light tracers

The study of the age and metallicity of the ICL is possible by the detection of individual stars and globular clusters (GCs) lost by galaxies which now belong to the diffuse ICL component.

Among others giant branch (RGB) stars are particularly good for this purpose, both because they are bright and therefore relatively easy to detect, and because the absolute magnitude of the tip of their luminosity function is related to the age and metallicity of their parent stellar population. Durrell et al. (2002) using the Wide Field Planetary Camera 2 on the *Hubble Space Telescope*, detected a sample of intracluster RGB stars in a field 41’ North-West of the cD galaxy M 87 in the Virgo cluster. From the LF of the detected stars they calculated the age of the parent diffuse stellar population to be greater than 2 Gyrs, and found it moderately metal-rich. This result supports the hypothesis that this diffuse component has been stripped from intermediate luminosity galaxies. Williams et al. (2007), using the

Advanced Camera for Surveys on the *Hubble Space Telescope*, detected a sample of ~ 5300 stars in another field of Virgo, half-way between M 86 and M 87. They found that the age of this population is mostly older that 10 Gyrs. More interestingly, they discovered that the detected stars span a wide range in metallicity. This indicates that the ICL component has originated from different galaxies and is not well mixed yet.

In parallel also intracluster supernovae (SNe) have been observed. Already in 1998 Reiss (Reiss and Hola, 1998; Reiss et al., 1998) talked about Supernovae in *"anonymous galaxy"*, but at the time the lack of a spectroscopic follow-up of these objects precluded the possibility of assigning the object to a cluster. The first confirmed intracluster SNe were observed by Gal-Yam et al. (2003) in a sample of clusters at $0.06 < z < 0.2$. They found in these clusters a couple of SNe of Type Ia that are in projection on top of the halo of the cD galaxies of the clusters, but with a velocity offset of 750-2000 km s^{-1} relative to those galaxies themselves. They calculated that 20% of the SNe generated in clusters derive from an intracluster stellar population. Analyzing a sample of 1401 low-redshift groups McGee and Balogh (2010) discovered 19 new intracluster SNe Ia. From this they calculated an amount of IGL in the observed groups equal to ~47% of their total stellar mass. This supports the hypothesis that mechanisms like tidal stripping are very efficient in the production of diffuse light in low mass systems.

Also globular clusters are good tracers of the intracluster stellar population, both because of their abundance and their brightness. It is not very clear yet how well they follow light. In fact, in general they seem to follow a different distribution than the stars. However, there is evidence suggesting that blue GCs trace ICL better than red GCs. Intracluster GCs were observed both in Coma and in Virgo (Jordán et al., 2009; Takamiya et al., 2009). An excess of blue, metal poor GCs with respect to a red, metal rich population was detected in the Hydra I and in the Centaurus clusters (Richtler et al., 2004; Misgeld et al., 2009).

1.2.4 The ICL and the BCGs

We have already seen that BCG galaxies have characteristics that are different from that of their elliptical counterparts in the field. It was observed that many of them emit more light at lager radii than expected for a $R^{1/4}$ profile, often referred to as the cD halo of BCG galaxies.

cD halos of BCG galaxies have been subjects of many studies in the last decades. The aim of such studies was to understand the origin of the cD halo, the mechanisms leading its formation and also to understand the relation to the BCG itself and the ICL. A particularly interesting open question is, in fact, the dynamical status of the cD halo. Is it dynamically bound to the BCG or is it made of stars floating in the cluster potential?

Gonzalez et al. (2005) studied the photometric characteristics for a sample of 24 BCG clusters at $0.03 < z < 0.13$, out to a radius ~ 300 kpc. They found that in most cases the surface brightness of the BCG galaxies is best fitted by a double $R^{1/4}$ model with independent scale lengths, ellipticity and orientations. They showed that the inner profile has properties typical of giant elliptical galaxy, while the outer profile has a scale lengths of the order of 10-40 times larger. They interpreted this second component as due to a population of intracluster stars tracing the cluster potential. Moreover, they interpreted the misalignment of the two light profiles, strong in about 60% of the clusters, as an evidence of the different physical nature of the BCG and the ICL. Zibetti et al. (2005) considered a sample of more than 683 BCGs galaxies at $0.2 < z < 0.3$, selected from the Sloan Digital Sky Survey. By stacking images they were able to measure light out to $\sim$ 700 kpc from the cluster center. As in the previously mentioned case, the light profile measured shows an excess with respect to a simple $R^{1/4}$ profile. This excess was interpreted as the presence of an ICL component.

On the one hand, this hypothesis is supported by numerical simulations. Willman et al. (2004) observed that in simulated clusters the halos of cD galaxies also show, in accordance with observations (Zibetti et al., 2005), an excess of light in comparison to a de Vaucouleur profile and that their formation is tightly related to the formation of the ICL component. Dolag et al. (2010) found that the kinematics of the BCGs in their simulated clusters identify two distinct populations. There is a more spatially concentrated cD component gravitationally bound to the galaxy, and an additional diffuse component that traces the cluster potential. The velocity dispersion of the diffuse component is comparable to the velocity dispersion of the member galaxies in the cluster and its age is $\sim$1.5 Gyrs, significantly older that the cD component. On the other hand, in a recent study on the structure of all ellipticals and spheroidal galaxies in Virgo Kormendy et al. (2009) showed that to have Sersic index $n > 4$ is common not only for BCGs, but also for many giant elliptical galaxies, mainly due to their merger origin. Therefore, the hypothesis that the excess with respect to a $R^{1/4}$ profile is related to ICL needs to be demonstrated by studying the kinematics and stellar population of this light. Only a kinematic study can really explain if the excess is bound to the BCG, as seen in the Dolag et al. (2010) simulations, and the stellar population can give hints on the most likely formation scenario. The problem with such studies is unfortunately related to the very low surface brightness of the halo component. Therefore it has been very difficult till now to study these galaxies beyond one effective radius (i.e. $\sim 5 - 10$ kpc Carter et al. (1999); Loubser et al. (2008, 2009)) to reach the regions dominated by the halo light.

Coccato et al. (2010a) presented the kinematics of the central two galaxies of the Coma cluster out to a radius of $\sim$ 65 kpc for NGC 4889 and $\sim$ 50 kpc for NGC 4874 along their respective major axis. They used very deep long-slit spectroscopic (LSS) data obtained with the SUBARU telescope with FOCAS. In this case the velocity dispersion of both the galaxies shows a flat profile, that indicates that the stars also at $R \sim 4R_e$ are still bound to the central BCGs and that there is no measurable contribution of ICL in the halo of these cD galaxies. However, in accordance with what is suggested by Kormendy et al. (2009), the study of the stellar population of NGC 4889 reveals that the stellar population of the galaxy within $1R_e$ have been formed in a timescale significantly shorter than the stars in the halo (Coccato et al., 2010b). This is compatible with a scenario in which the halo has a completely different evolution history and has formed by later accretion of stars from old systems with different star formation rates.

A different velocity dispersion profile was measured for the cD galaxy NGC 6166 in the Abell 2199 cluster (Kelson et al., 2002). This is the only case known, for which the kinematics of the ICL in the halo of a BCG has been measured. The velocity dispersion profile of the galaxy, in fact, first decreases, from a value of 300 km/s at the center to 200 km/s within a few kpc, and then rises up to the cluster velocity dispersion at R=60 kpc, showing that at this radius the halo of the galaxy is dominated by intracluster stars, floating in the cluster potential and not bound to the BCG anymore.

An alternative and efficient way of studying the kinematics of the halo of BCG galaxies at low SBs, i.e. large radii, and also the ICL in general is to explore the characteristics of the Planetary Nebulas (PNs). Why PNs are particularly suitable for this aim and how they have been studied till now is the main topic of the next section.

1.2.5 Kinematics

After what we have learned about ICL it is clear that a study of the kinematics of this diffuse component is very important to better explore its physical characteristics. The kinematic study of the observed structures in the ICL can, in fact, give very important hints on the origin of the diffuse component. It is also fundamental to study the kinematic status of the halo of cD galaxies, giving the opportunity to disentangle if the cD halo is dynamically linked to central BCG or it is dynamically distinct and part of the ICL component as suggested by photometric studies of BCGs systems (Zibetti et al., 2005; Gonzalez et al., 2007).

As already seen, due to the very low surface brightness of the ICL component, the study of ICL kinematics with absorption line spectroscopy is very hard due to variable sky background and sky noise (see section 1.2.4). Moreover, absorption line spectroscopy gives information only on the integrated light along the line of sight, and the identification of substructures, if possible, is very challenging. A valid alternative is to study single stars tracing the underlying stellar population and kinematics.

The Planetary Nebulas and their physical characteristics

The best known discrete tracers are Planetary Nebulas (PNs). A star becomes a PN, after its post-AGB phase, if at this point of its evolution its core mass is in the range $1M_{\odot} < M_{core} < 8M_{\odot}$ (Richer et al., 2010). The star becomes unstable, its atmosphere is ejected and the resulting PN consists of a central white dwarf star, surrounded by low density ionized gas. Due to the extreme rarefaction of the gas, PNs re-emit up to 15% of their light in the [OIII] λ5007 Å (Dopita et al., 1992). It is because of this bright and narrow emission line that PNs are relative easy to detect. The typical spectrum of a PN is shown in Fig. 1.3. It is characterized by many emission lines. Among these, apart from the [OIII] λ5007 Å other strong lines are [OIII] λ4959Å and Hα.

The PN luminosity function (PNLF), measured as the distribution of the [OIII] λ5007Å emission line fluxes, is characterized by a very sharp cutoff on its bright end. The PNLF is empirically well

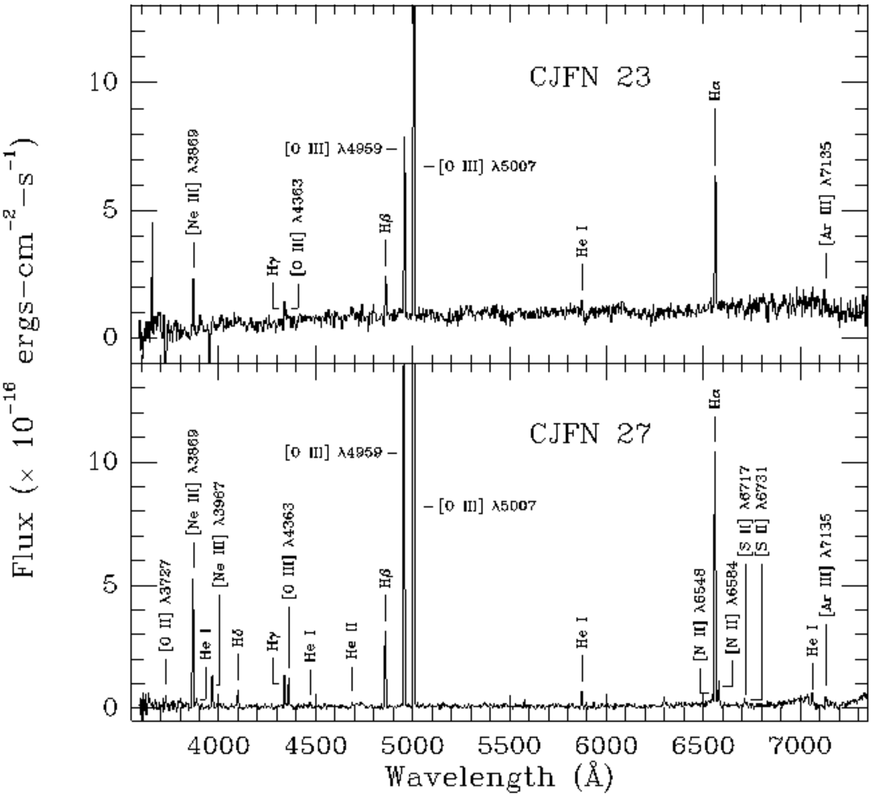

Figure 1.3: Example of two PNs' spectra from Jacoby and Ciardullo (1999).

described by the formula:

$$N_{(m_{5007})} = e^{0.307 m_{5007}}[1 - e^{3(m^*_{5007} - m_{5007})}] \tag{1.12}$$

where m^*_{5007} is the observed bright cutoff magnitude (Ciardullo et al., 1989). Different observations of the PNLF in numerous galaxies of the local Universe and comparison with other distance estimators have demonstrated that the bright cutoff corresponds to an intrinsic magnitude of $M^*_{5007} = -4.51$ mag, independent from the characteristics of the parent stellar population (Ciardullo et al., 1989; Jacoby, 1989; Jacoby et al., 1992; Ciardullo, 2003). This makes the PNLF bright cutoff a strong distance indicator. Unfortunately, theories have till now failed in explaining, from a theoretical point of view, the physical reason for such behavior. They predict, on the contrary, the bright cutoff to be dependent on the age and metallicity of the parent stellar population (Mendez and Soffner, 1997; Marigo et al., 2004). In particular, from the models the bright cutoff should be fainter for early type galaxies than for late type galaxies. A possible partial solution to the problem could lie in the presence of blue stragglers formed by coalescence of binary stars (Ciardullo et al., 2005). These rejuvenated stars could have sufficient mass to be the cause of the observed bright PNs in early type galaxies (Ciardullo et al., 2005).

An interesting relation exists between the number density of PNs and the total luminosity of their parent stellar population. This relation is given by the luminosity-specific planetary nebula number, the so called α parameter, defined as

$$\alpha = \frac{N_{PN}}{L_{tot}} \tag{1.13}$$

where N_{PN} is the number of PNs and L_{tot} is the bolometric total luminosity of the sampled light. Simple stellar population (SSP) models (Renzini and Buzzoni, 1986) predict that the α parameter is physically related to the so called specific evolutionary flux, β, that is linked to the rate to which stars turn from the main sequence (MS) to the post-AGB phase, and to the visibility lifetime of a PN, i.e. the time in which its [OIII] emission is visible: $\alpha = \beta * \tau_{PN}$. An exhaustive description of this issue is beyond the purpose of this introduction, but what is important to remember is that empirically a relation between the α parameter and the color of observed light exists. A list of values is given in table 6 of Buzzoni et al. (2006). Therefore it is possible, knowing the color, and consequently the α parameter, and the total bolometric luminosity L_{tot} emitted by the sampled light, to predict the number of observed PNs and vice versa.

Summarizing the reasons why PNs are good to study are:

- the envelope of a PNs re-emit about 15% of the total light emitted by the central white dwarf in only one emission line, the green [OIII] λ5007Å forbidden emission line. This makes PNs relatively easy to detect. Moreover, the [OIII] λ5007Å emission line is narrow ($\sim$ 30 km/s), therefore the PNs' velocities can be measured with medium resolution spectroscopy;
- the PNLF is a standard candle distance indicator due to its bright cutoff;
- from the number count of PNs is possible to predict the SB of the parent stellar population, via the α parameter.

Moreover, recent studies on a sample of galaxies in the local Universe demonstrated that

- the PNs trace light, because they follow the same spatial distribution and kinematics of stars (Coccato et al., 2009).

PN surveys for $D < 25$ Mpc

At low redshift the most widely used technique to detect PNs is the on/off-band technique (Ciardullo et al., 1989). It consists in taking two images of the sky. One is obtained through a narrow band filter, centered around the redshifted [OIII] λ5007Å emission line at the distance of the observed object and the other is obtained through a broader filter (V or R band most frequently). PNs are distinguishable from other sources because they have a very faint continuum level. For this reason they are visible in the narrow band filter image because of their bright [OIII] λ5007Å emission line, but not in the broad band image. The technique allows to measure with two exposures both flux and position for the detected sources. Possible contamination to the sample from [OII] regions and Lyα background galaxies have been taken under control by the use of blank field surveys used for comparison (Freeman et al., 2000), the additional observations of the PNs via a Hα narrow band filter (Okamura et al., 2002; Arnaboldi et al., 2003) and by spectroscopic-follow up of subsamples of the detected objects.

Surveys of PNs were done in M 81 (Jacoby, 1989) and in the Leo group (Castro-Rodríguez et al., 2003), but the Virgo cluster has been the most observed system in the local Universe. Since 1998 a considerable number of PN surveys have been carried out. At the present time a total of 18 different fields spread all over the cluster have been observed, reaching regions at a distance larger that $\sim 3°$ from the cluster center (Arnaboldi et al., 2002; Feldmeier et al., 2003, 2004; Aguerri et al., 2005; Castro-Rodriguéz et al., 2009). The PN samples were used both to infer, from the α parameter, the SB of the parent ICL stellar population, and by the analysis of the bright cut-off of the PNLF the distance of the light in the cluster.

The overall picture that comes from the analysis of the characteristics of the detected PNs is that the distribution of ICL is not uniform in the cluster (Castro-Rodriguéz et al., 2009). The ICL is more concentrated at the center of the cluster, where the galaxy density is higher and lower elsewhere. In the core, no significant trend of the SB of the parent stellar population was observed in the different surveyed fields with increasing distance from M 87 (Aguerri et al., 2005). Feldmeier et al. (2004), from studying a sample of more than 300 PNs (Feldmeier et al., 2003), calculated an amount of ICL for this cluster of the order of 10% in its core, a result confirmed by the photometric study of Mihos et al. (2005). Moreover, several evidence contributed to give an image of the cluster as dynamically young and now on the point of forming: (i) the observed inhomogeneity of the spatial distribution of the ICL on scales of $30' - 90'$ (Aguerri et al., 2005), (ii) the study of the PNLF as distance indicator, in a region in the North with respect to the cluster center where no big galaxies are visible (Arnaboldi et al., 2002), suggesting that the front end of the cluster may be closer to us by about $\sim 14 - 18\%$ with respect to the cD galaxy M 87, and (iii) the α parameter suggesting that many observed PNs come from late-type galaxies (Feldmeier et al., 2004).

In parallel, very interesting results were obtained from the study of the kinematics of the PNs for which a spectroscopic follow-up was done. Velocities were obtained for a sample of 40+12 PNs in the Virgo core (Arnaboldi et al., 2004; Doherty et al., 2009). The spectra were obtained with the FLAMES spectrograph on UT2. The velocity distribution of the whole sample shows an unmixed kinematics that confirm the young dynamical status of the cluster. The study of the spatial distribution and kinematics of the PNs bound to M 87 as a function of the distance from the center of galaxy, together with results suggested by dynamical models, reveals a truncation of the halo of the galaxy at ~ 160 kpc and a decreasing velocity dispersion profile with increasing distance from the galaxy center.

Méndez et al. (2001) and Teodorescu et al. (2005) measured the velocity of 531 and 195 PNs in two Fornax cluster galaxies, respectively NGC 4697 and NGC 1344. To do that they used the classical on/off band technique, but combined with a dispersed image obtained during the same observing run. In this way they were able to study the kinematics of these galaxies up to three effective radius from their center.

An alternative technique to detect PNs in galaxies in the nearby Universe is the so called counter-dispersed slitless spectroscopy technique. The technique consists in observing each field twice, the first time with a dispersed image and the second time with a dispersed image obtained with the spectrograph rotated 180 degrees with respect to the previous observation. The technique allows us to measure flux, position and velocity of the detected sources. The velocity of the detected emission lines is proportional to the separation between their positions in the two spectral images. A dedicated instrument for the detection of PNs with the counter-dispersed technique is the PN Spectrograph (Douglas et al., 2002). The instrument is build so that the light coming through the telescope is split in two opposite arms at the end of which two identical spectrographs are located.

McNeil et al. (2010) used the counter-dispersed technique with FORS1 on the VLT to study the PN population in a five field survey around NGC 1399, a cD galaxy in the Fornax cluster. Of the 187 detected PNs McNeil et al. (2010) showed that 146 are bound to NGC 1399. Of the remaining 44, some are bound to NGC 1404, another galaxy in the cluster and the rest reveals the presence of a substructure at low velocity. The superposition of these various components highlight the complexity of the cluster core structures and the importance of discrete components as PNs, to detect them.

Multi-Slit Imaging Spectroscopy technique: PN surveys for $D > 25$ Mpc

The techniques described till now are suitable to detect PNs up to a distance of ~25 Mpc. At a distance of ~ 100 Mpc, the flux from the [OIII] λ5007 Å emission line of a PN at the bright cutoff of the PNLF is of the order of a few 10^{-18} erg $\text{cm}^{-2}\text{s}^{-1}$. In a window of 40-50 Å (the typical FWHM of a narrow band filter), the level of the sky noise is of the same order of magnitude. To detect PNs at these distances it is necessary to reduce substantially the noise from the night sky. This is possible by using the Multi-Slit Imaging Spectroscopy technique (MSIS, Gerhard et al., 2005). The MSIS is a blind search technique. It combines the use of a mask of parallel slits (see Fig.1.4), a narrow band filter centered at the redshifted [OIII] λ5007Å emission line, and a dispersing element. With the use of the mask of slits and the dispersing element the sky noise is reduced by a factor of 5-10, depending on the instrumental resolution. The technique allows us to detect all the emission line objects that happen to lie behind the mask slits, and to measure their fluxes, positions and velocities with only one exposure. To survey as much surface as possible, the mask is stepped along the dispersion direction in order to cover the distance between two adjacent slits of the mask.

The technique was pioneered at the SUBARU telescope, where a field South of the cD galaxy NGC 4874, the second brightest galaxy in the Coma cluster, was observed with the FOCAS spectrograph. The velocity distribution of 37 ICPNs detected has a main peak at a systemic velocity ~700 km/s bluer than the systemic velocity of the nearby galaxy NGC 4874, but coincident with the redshift of the other cD galaxy, NGC 4889. These ICPNs are therefore not bound to NGC 4874, and have been probably stripped from the halo of NGC 4889 during a close passage to NGC 4874. Combined with galaxy redshifts and X-ray data the PN line of sight velocity distribution (LOSVD)

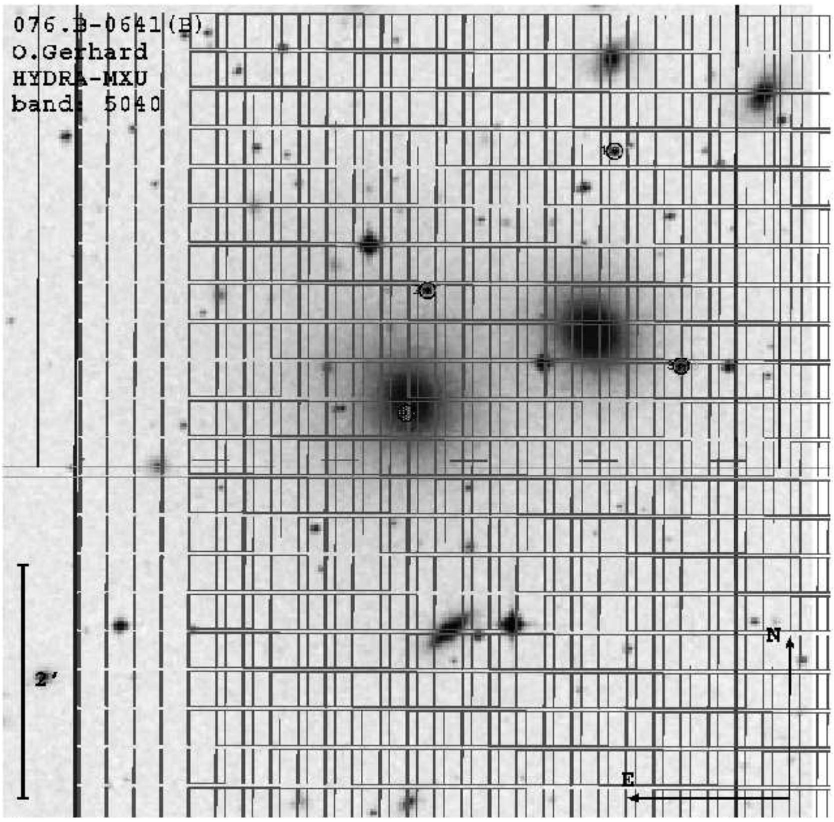

Figure 1.4: Multi-Slit mask used in the observations carried out in the Hydra I cluster, with FORS2 on UT1-VLT, using the MSIS technique. The mask has 21 horizontal × 24 vertical slits. Each is $\sim 17''.5$ long and $0''.8$ wide. The dispersion direction is horizontal and the spatial direction is vertical

suggests that the cluster is currently in the midst of a subcluster merger, where the two subcluster cores around the supergiant galaxies NGC 4874 and NGC 4889 are presently beyond their first and second close passage, during which the elongated distribution of intracluster light has been created (Gerhard et al., 2007).

Another two fields in the Coma cluster have been observed with FOCAS at the SUBARU telescope and other surveys have been realized with FORS2 on UT1. One of these is analyzed in this work, covering the core of the Hydra I cluster around its central cD galaxy NGC 3311. Moreover, two fields have been observed, one East and one South of the central galaxy of the Centaurus cluster, NGC 4696, and in the summer of this year, also the central core of the compact group HGC 90 has been observed.

1.3 The Thesis

The work presented in this thesis is dedicated to the study of the kinematics of the ICL component in the core of the Hydra I cluster. Hydra I is a medium compact cluster in the Southern hemisphere at a distance of ~50 Mpc. The cluster is dominated by two central non interacting elliptical galaxies, NGC 3311 and NGC 3309. It has a systemic velocity of $\sim$ 3683 $\mathrm{km\,s^{-1}}$ with a velocity dispersion of $\sim$ 724 $\mathrm{km\,s^{-1}}$ (Christlein and Zabludoff, 2003; Misgeld et al., 2008). A complete description of the characteristics of the cluster is presented in Sec. 5.2 of this thesis. The goal of our study is, by analyzing the Hydra I case, to address in particular to two questions: (i) Which is the relation between the ICL and the halo of BCGs galaxies: are these two physically distinct? Does the BGCs' halo smoothly blend into the ICL light or do the two form two kinematically different components? (ii) How does the study of the kinematics of the ICL help us in understanding the dynamical status of a cluster as a whole? Does it help us in the identification of the cluster substructure, if any is present? We have chosen Hydra I to answer these questions, because from X-ray observations, the cluster appears to be the prototype of a relaxed system. The study of the interaction of the halo of NGC 3311 with the intracluster light component should therefore be relatively easy to investigate in this system. To reach this aim we study the core of the cluster, the central $\sim$ 100 kpc^2, by using different data sets. First we analyze deep Gemini GMOS-South archive long-slit data and UT1-VLT FORS2 long-slit (LSS) data to study the absorption line kinematics of NGC 3311 along its major axis. Then using the Multi-Slit Imaging Spectroscopy (MSIS, see Sec. 1.2.5) technique with FORS2 on UT1 we detect the Planetary Nebulas (PNs) (see Sec 1.2.5) populating the core of the cluster. PNs trace light and we use them as single tracers to study the kinematics of the light in the core of the cluster. The MSIS mask used for the Hydra I observations is shown in Fig. 1.4 superposed on a DSS image of the cluster itself. The two galaxies are NGC 3311 at the center of the image and NGC 3309 on the upper right. Finally we use photometric K band 2MASS archive data and V band WFI data to study the distribution of light around NGC 3311 and NGC 3309.

The thesis is organized as follows: in Chapter 2 we present the measurements of the velocity and velocity dispersion profiles of NGC 3311 along its major axis as published in Ventimiglia et al. (2010b). These are obtained from the study of the LSS data and show the kinematics of the galaxy out to a radius of ~25 kpc. The velocity dispersion profile turns out to be particularly interesting. As in the case of NGC 6166 (see Sec. 1.1.3), it shows an increase, from a value of $\sim$ 150 $\mathrm{km\,s^{-1}}$ at the center of the galaxy to $\sim$ 450 $\mathrm{km\,s^{-1}}$ at a radius of ~12 kpc. Further out, to a distance of ~25 kpc, the velocity dispersion remains constant. The outer velocity dispersion is about 65% of the velocity dispersion of the cluster. We conclude that the stellar halo of NGC 3311 is dominated by intracluster stars and that the passage from galaxy-bound to intracluster stars happens in the radial range from 4 to 12 kpc.

Chapter 3 and 4 are dedicated to the MSIS technique. Here we describe the data reduction and the selection criteria used to classify the detected emission line objects. With the MSIS technique with the setup used for the Hydra I cluster, in fact, we detect two classes of objects: PNs at the distance of Hydra I and background galaxies. These are [OII] emitters at z~0.37 and Lyα galaxies at z~ 3.1. PNs are identified as unresolved emission line sources both spatially and in wavelength, with no continuum. Background galaxies are resolved emission line sources with or without continuum and unresolved emission lines sources with continuum. In Chapter 3 we present the evidence for the objects classified as PNs to be really stars associated to the Hydra I cluster and show their distribution in the velocity-magnitude plane (Ventimiglia et al., 2008). In Chapter 4 we describe the main characteristics of the background galaxies, their redshift, observed flux and equivalent width distribution (Ventimiglia and Arnaboldi, 2010).

In Chapter 5 we concentrate on the kinematics of the PNs detected with the MSIS in the central $100 \times 100\,\mathrm{kpc}^2$ of the cluster (Ventimiglia et al., 2010a). We find that the line-of-sight velocity distribution (LOSVD) of the 56 detected PNs is highly non-Gaussian and has a multi-peaked structure. The distribution is dominated by a broad central component at around the average velocity of the cluster. By simulating a sample of PNs at the distance of Hydra I, observed with the MSIS and distributed in velocity according to a Gaussian centered at the systemic velocity of NGC 3311 and with a velocity dispersion of $\sim 460\,\mathrm{km\,s^{-1}}$ (i.e. the velocity dispersion of the halo of NGC 3311 at $R \geq 12$ kpc), we are able to demonstrate that the central peak observed in the PN LOSVD is compatible with PNs tracing the hot halo of NGC 3311. This confirms the LSS results described in Chapter 2. The other two detected peaks, one at $\sim 1800\,\mathrm{km\,s^{-1}}$ and the second one at $\sim 5000\,\mathrm{km\,s^{-1}}$, reveal the presence of real substructures in the core of the Hydra I cluster. From this we conclude that the ICL component in the core of the cluster is still unmixed. This suggests that the build-up of the halo of NGC 3311 is on-going. From the comparison of the spatial and velocity distribution of the detected PNs with the phase-space distribution of the galaxies in the cluster we find that the redder of the two peaks in the PN LOSVD is consistent both spatially and in velocity with a group of DWs populating the core of the cluster.

In Chapter 5 we also present the study of the luminosity function of the detected PNs used as a distance indicator and their number density in relation to the light in the cluster. We find that the luminosity function is consistent with that expected at a distance of ~ 50 Mpc, while the PN number density is ~ 4 times lower than expected. A possible explanation for this evidence is that the PNs lifetime in the central core of NGC 3311 is significantly shortened by ram pressure effects.

Chapter 6 is dedicated to the study of the light distribution in the core of the cluster. We perform a complete photometric study for the two central galaxy of Hydra I, NGC 3311 and NGC 3309, both in Ks and V bands. We find that the SB profile of NGC 3309 is well described by a de Vaucouleurs law, while NGC 3311 is described by a de Vaucouleurs law for $R \leq 12$ kpc and with a Sersic law with $n \sim 6.9$ for $R \geq 12$ kpc. This evidence confirms again the LSS results. Moreover, from the study of the 2D photometry of the cluster core we find that there is an excess of light in the North-East part of the halo of NGC 3311 with respect to a symmetric distribution of light. We measure the velocity of this excess. The excess is shown to be correlated both spatially and in velocity with the PNs contributing to the redder peak in the PN LOSVD and to the group of DWs in the core of the cluster.

In Chapter 7 we discuss the characteristics of these DWs, concentrating on one of them, HCC 26. For this object we study the stellar population and the structural properties. We discuss the possibility that the group of DWs was partially disrupted during a recent close passage through the dense cluster core.

Finally, in Chapter 8 the main conclusions of this thesis and a summary of its results are presented and future work and prospectives are discussed.

Chapter 2

The dynamically hot stellar halo around NGC 3311: a small cluster-dominated central galaxy

Giulia Ventimiglia, Ortwin Gerhard, Magda Arnaboldi, Lodovico Coccato

Astronomy & Astrophysics, 2010, 520, L9[1]

Abstract

An important open question is the relation between intracluster light and the halos of central galaxies in galaxy clusters. Here we report results from an on going project with the aim to characterize the dynamical state in the core of the Hydra I (Abell 1060) cluster around NGC 3311. We analyze deep long-slit absorption line spectra reaching out to $\sim$ 25 kpc in the halo of NGC 3311. We find a very steep increase in the velocity dispersion profile from a central $\sigma_0 = 150$ km s^{-1} to $\sigma_{out} \simeq 450$ km s^{-1} at $R \simeq 12$ kpc. Farther out, to $\sim$ 25 kpc, σ appears to be constant at this value, which is $\sim$ 60% of the velocity dispersion of the Hydra I galaxies. With its dynamically hot halo kinematics, NGC 3311 is unlike other normal early-type galaxies. These results and the large amount of dark matter inferred from X-rays around NGC 3311 suggest that the stellar halo of this galaxy is dominated by the central intracluster stars of the cluster, and that the transition from predominantly galaxy-bound stars to cluster stars occurs in the radial range 4 to 12 kpc from the center of NGC 3311. We comment on the wide range of halo kinematics observed in cluster central galaxies, depending on the evolutionary state of their host clusters.

---

[1] FCQ8 fits were preformed by L. Coccato.

2.1 Introduction

An important open question is the physical and evolutionary relation between the intracluster light (ICL) and the extended halo of the brightest cluster galaxies (BCGs), whether they are truly independent components or whether the former is a radial extension of the latter. Using a sample of 683 SDSS clusters Zibetti et al. (2005) found a surface brightness excess with respect to an inner $R^{1/4}$ profile that characterizes the mean profile of the BCGs, but it is not yet known whether this cD envelope is simply the central part of the cluster's diffuse light component, or whether it is distinct from the ICL and part of the host galaxy (Gonzalez et al., 2005).

In the Southern hemisphere, the cD galaxy NGC 3311 and the giant elliptical NGC 3309 dominate the central region of the Hydra I cluster, an X-ray bright, non-cooling flow, medium compact cluster with a velocity dispersion $\sigma_{HydraI} = 784$ km s^{-1} (Misgeld et al., 2008). The X-ray observations show that the hot intracluster medium centered on NGC 3311 has a fairly uniform distribution of temperature and metal abundance from a few kpc out to a radius of 230 kpc (Tamura et al., 2000; Yamasaki et al., 2002; Hayakawa et al., 2004, 2006). Given the overall regular X-ray emission and temperature profile, the Hydra I cluster is considered as a prototype of an evolved and dynamically relaxed cluster; it is therefore a suitable candidate for a dynamical study of a relaxed extended stellar halo around a BCG.

The primary goal of this work is to establish the dynamical state of the stellar halo of NGC 3311. We use long-slit spectra to uncover the kinematics in the halo region of NGC 3311 out to ~ 25 kpc from its center. In Sect. 2.2 we present observations with FORS2 at VLT and the GEMINI GMOS archive data, which we reanalyze. We describe the data reduction and the kinematic measurements in Sect. 2.3. The newly measured halo kinematics and their implications are discussed in Sect. 2.4, and our conclusions are summarized in Sect. 2.5.

We adopt a distance to NGC 3311 of 51 Mpc (NED), equivalent to a distance modulus of 33.54 mag. Then $1''$ corresponds to 0.247 kpc.

2.2 Observations and archive data

VLT FORS2 long slit spectra - The long-slit spectra were obtained during the nights of 2009 March 25-28, with FORS2 on VLT-UT1. The instrumental setup had a long-slit $1''.6$ wide and $6'.8$ long, Grism 1400V+18, with instrumental dispersion of 0.64 Å pixel^{-1} and spectral resolution $\sigma = 90$ km s^{-1}, and a spatial resolution along the slit of $0''.252$ pixel^{-1}. The seeing during observations ranged from $0''.7$ to $1''.2$. The wavelength coverage of the spectra is from 4655 Å to 5965 Å, including absorption lines from H_β, MgI ($\lambda\lambda 5167, 5173, 5184$ Å) and Fe I ($\lambda\lambda 5270, 5328$ Å). We obtained eight spectra of 1800 sec each, for a total exposure time of 4 hrs. In the FORS2 observations, the long slit is centered on the dwarf galaxy HCC 26 at α = 10h36m45.85s and $\delta = -27$d31m24.2s (J2000), with a position angle of P.A.=142°; HCC 26 is seen in projection onto the NGC 3311 halo. The position of

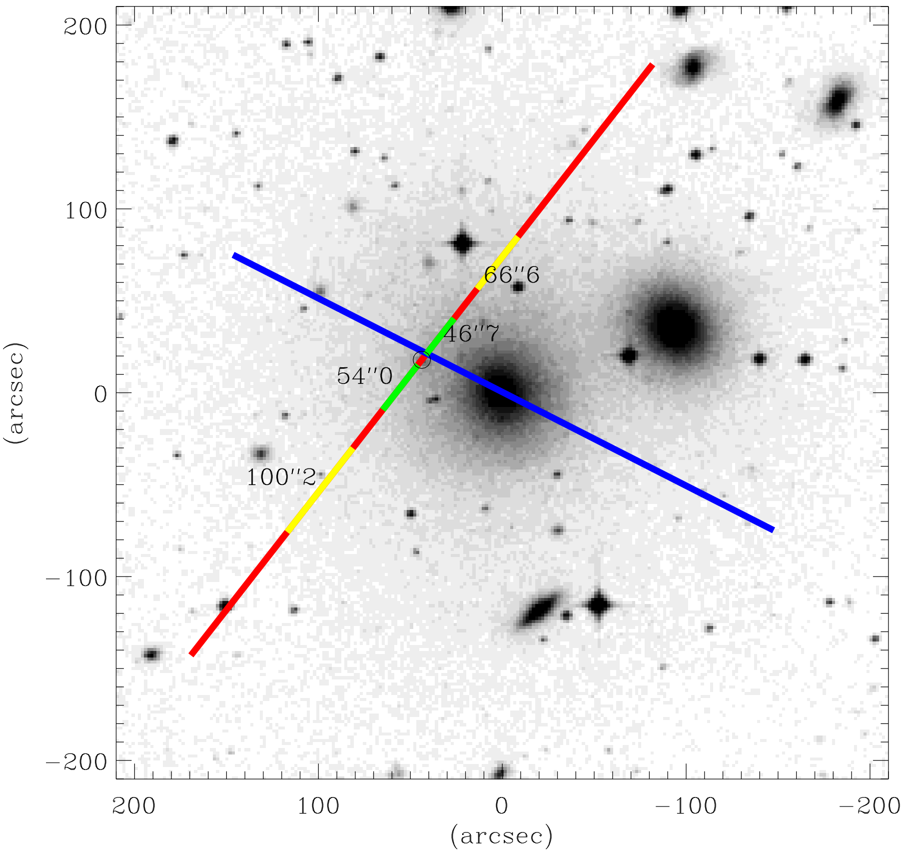

Figure 2.1: Optical DSS 7′ × 7′ image centered on NGC 3311 in the Hydra I cluster. The relative positions of the GMOS slit (5′.5, blue line) and FORS2 slit (6′.8, red line) are illustrated. Green and yellow sections on the FORS2 slit indicate regions where average spectra are extracted. The adjacent numbers specify the radial distances of their light-weighted mean positions from the center of NGC 3311. The center of the FORS2 slit coincides with the position of the dwarf galaxy HCC 26 and is marked by a black circle. North is up and East to the left.

the FORS2 long slit is shown in Fig. 2.1. Its center is located at P.A.=64° with respect to NGC 3311, approximately along the major axis of the galaxy.

Gemini GMOS-South long slit spectra - We use Gemini archive long-slit spectra in the wavelength range from 3675 Å to 6266 Å observed with the B600 grating, a dispersion of 0.914 Å pixel^{-1}, a spectral resolution of σ = 135 km s^{-1}, and a spatial scale of 0″.146 pixel^{-1}; a detailed description of the instrumental setup is presented in Loubser et al. (2008). The seeing was typically in the range from 0″.6 to 1″.2. We target the same absorption lines as for the FORS2 spectra, i.e. H_β, MgI ($\lambda\lambda$5167, 5173, 5184 Å) and Fe I ($\lambda\lambda$5270, 5328 Å). The 0″.5 wide and 5′.5 long Gemini slit is centered on NGC 3311, at α = 10h36m42.74s and $\delta = -$27d31m41.3s (J2000), along P.A. = 63°, the direction of the galaxy major axis. Its position is shown in Fig. 2.1.

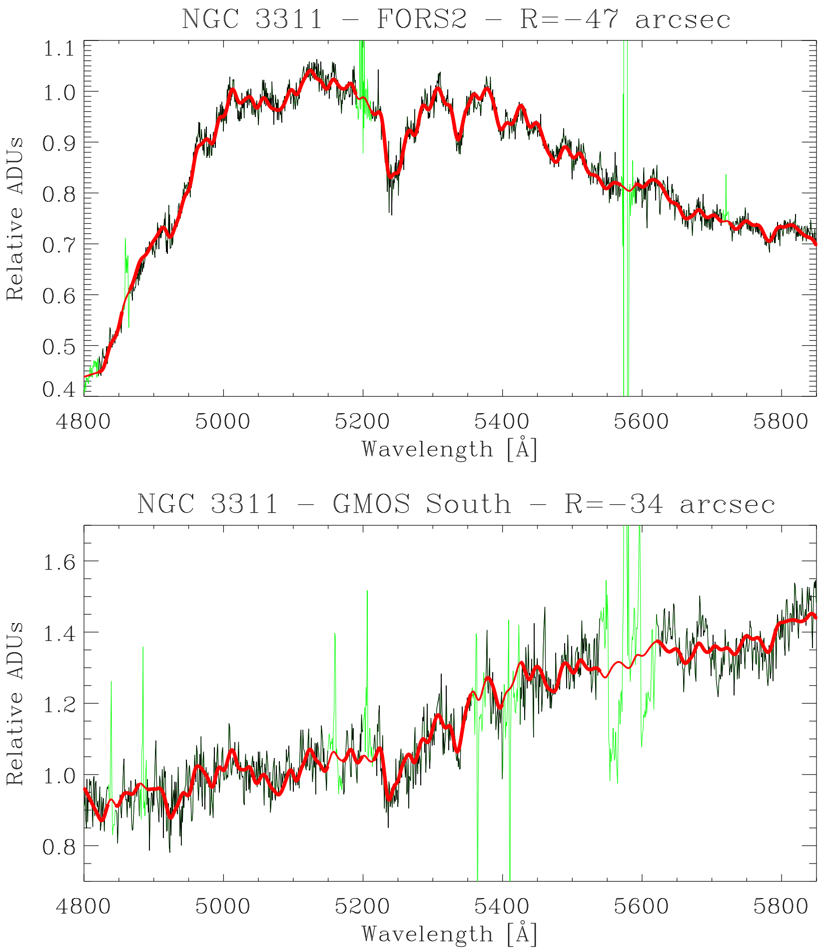

Figure 2.2: Kinematic fits with PPXF of the spectra extracted at $-47''$ (VLT FORS2) and at $-34''$ (Gemini GMOS). In *black* we display the galaxy spectra, in *green* the wavelength range excluded from the fit because of sky residuals, and in *red* the best-fit-broadened template model. All spectra are normalized to the value of the best-fit model at 5100 Å.

2.3 Data reduction

The data reduction of the FORS2 long slit spectra is carried out in *IRAF*. After the standard operations of bias subtraction and flat-fielding, the spectra are registered, co-added and wavelength calibrated. The edges of the FORS2 slit reach well into sky regions, which are then used to interpolate the sky emission in the regions covered by the stellar spectra.

In the low surface brightness regions, spectra are summed along the spatial direction in order to produce one-dimensional spectra with an adequate S/N ratio ($\geq$ 20 per Å). Four independent one-dimensional spectra are extracted along the slit where the light is dominated by the halo of NGC 3311; of these, two are from regions North and two from regions South of HCC 26, respectively. We extract spectra from slit regions of $\sim 31'' \times 1''.6$ and $\sim 25'' \times 1''.6$ at distances of about 54” and 47” from the center of NGC 3311, and of $\sim 58'' \times 1''.6$ and $\sim 36'' \times 1''.6$ at central distances of about 100” and

67”. We properly mask the spectra of foreground stars in those areas.

The data reduction for the GMOS long slit spectra is carried out independently here, also in *IRAF* and with the standard tasks in the Gemini package. The procedure is described in Loubser et al. (2008) for the wavelength calibration and background subtraction; also in this case the edges of the slit are used to interpolate the sky emission in the regions covered by the stellar continuum. Because our goal is to sample the kinematics well into the halo, the one-dimensional spectra for the absorption line measurements are summed along the slit direction so that a minimum S/N $\sim$ 20 per Å is obtained in each radial bin, out to a radial distance of about 40” from the center of NGC 3311.

Stellar kinematics - The stellar kinematics is measured from the extracted 1D spectra in the wavelength range 4800 Å$< \lambda <$ 5800 Å, using both the “penalized pixel-fitting” method (PPXF, Cappellari and Emsellem (2004)) and the Fourier correlation quotient (FCQ) method (Bender, 1990), in order to account for possible systematic errors and template mismatch.

In the PPXF method, stellar template stars from the MILES library (Sanchez-Blazquez et al., 2007) are combined to fit the one-dimensional extracted spectra; the rotational velocity, the velocity dispersion and Gauss-Hermite moments (e.g. Gerhard (1993)) are measured simultaneously. Fig. 2.2 shows two of the extracted spectra and the broadened templates fit by PPXF. In the FCQ method, the rotational velocity and velocity dispersion are derived for each extracted one-dimensional spectrum by assuming that the LOSVD is described by a Gaussian plus third- and fourth- order Gauss-Hermite functions. Before to the fitting procedure the MILES template spectra are smoothed to the GMOS and FORS2 spectral resolution with the measured broadening offsets. While FCQ provides error estimates along with the measured kinematics, errors for the PPXF kinematic parameters are calculated with a series of Monte Carlo simulations adopting the appropriate S/N for each bin.

Because the stellar populations in cD halos may have different metal abundances and ages from those of the inner regions (Coccato et al., 2010a,a), systematic effects caused by template mismatch must be evaluated and accounted for. We therefore extract kinematic measurements with PPFX and FCQ as follows:

1. fit with PPFX the best stellar template from the MILES library in the central regions with the highest S/N, and extract v and σ at all radii, using the same stellar template;

2. simultaneously fit the best stellar template, v and σ in each radial bin with PPFX;

3. adopt the respective best-fit PPXF stellar template to derive the LOSVD with FCQ for all radial bins;

4. finally, average rotational velocities v and velocity dispersions σ are computed as weighted means of the three values extracted in each radial bin as detailed above. Errors for these weighted average values are computed from those of the three measurements, but if the reduced $\chi^2 = \frac{1}{(n-1)} \sum_{i=1}^{n} \frac{(x_i-\bar{x})^2}{\epsilon_i^2}$ is greater than one, they are increased by $\sqrt{\chi^2}$ in order to take into account systematic differences. I.e., $\epsilon_{\bar{x}}^2 = \frac{1}{\sum_{i=1}^{n} 1/\epsilon_i^2} \times \chi^2$ where ϵ_i, $\epsilon_{\bar{x}}$ are the errors on the individual measurements x_i and the weighted mean $\bar{x}$, respectively.

Mean velocities and velocity dispersions in all radial bins are listed in Table 2.1, and the profiles are shown in Fig. 2.3 together with the previous measurements from Loubser et al. (2008). Table 1, which is available in electronic form, contains the following information: source of data (Col. 1), distance from galaxy center (Col. 2), P.A. (Col. 3), v,σ with errors for each of the procedures 1.-4. described in the text, in Col. (4-5), (6-7), (8-9), and (10-11), respectively. Heliocentric and relativistic corrections have been applied to the mean velocities. The systemic velocity is 3800 kms and has been subtracted.

In the central region of NGC 3311, our new velocity dispersion profile marginally agrees with that of Loubser et al. (2008). The new mean line-of-sight velocity measurements agree with the systemic

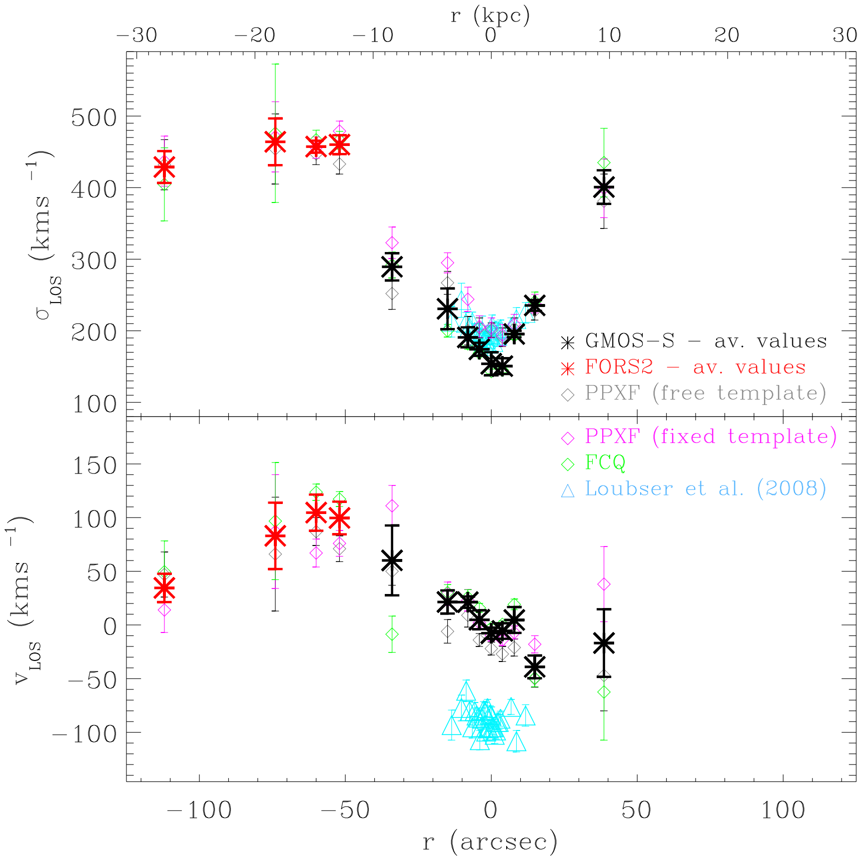

Figure 2.3: Major axis line-of-sight velocity and velocity dispersion profiles for NGC 3311 (P.A. = 63°). The open light blue triangles are the values published by Loubser et al. (2008), based on Gemini-South GMOS data. The black asterisks are our independent measurements from these GMOS (archival) spectra, and the red asterisks show measurements from the new VLT-FORS2 spectra. These are weighted averages of three independent measurements which are obtained with PPXF and FCQ as described in Sec. 2.3 and shown separately as the gray, magenta and green diamonds. The FORS2 data points are obtained from averages over ∼ 25″ and ∼ 31″ in the inner regions and over ∼ 36″ and ∼ 58″ in the outer regions of the slit; see Fig. 2.1. These off-axis measurements are plotted at their light-weighted average radii, corrected for projection onto the major axis of NGC 3311 with an isophotal flattening of 0.89. Positive distances are South-West from the center of NGC 3311 and negative values are North-East, along P.A.=63°.

velocity of NGC 3311 obtained by Misgeld et al. (2008), but have a systematic offset from the v data of Loubser et al. (2008), by about 91 km s^{-1}. The agreement between the new FORS2 measurements at -47" and the revised value at -34" from archive GMOS data gives us confidence that the systematic effects from wavelength calibration offsets, template mismatch, etc., are sufficiently small in the new, independent data reductions. However, several tests have convinced us that the data do not allow us to reliably determine full line-of-sight distributions (e.g., h_3, h_4), which could be used to test for subcomponents, which one would expect in particular at radii $\sim 30" - 40"$.

2.4 The kinematics of the NGC 3311 stellar halo

The combined new velocity dispersion profile for NGC 3311 reaches to $R_{mj} = 39'' \simeq 10$ kpc from the center of NGC 3311 along the galaxy's major axis (P.A.=63°), and to an off-axis distance of $R = 100'' \simeq 25$ kpc along the FORS2 slit. It shows a very unusual steep rise with increasing radial distance from the galaxy center: from a central value $\sigma_0 = 150\,\mathrm{km\,s^{-1}}$, to $\sigma = 231$ $\mathrm{km\,s^{-1}}$ at $R = 15'' \simeq 3.7$ kpc, and then on to a flat $\sigma_{out} \simeq 450\,\mathrm{km\,s^{-1}}$ outside $R = 47'' = 12$ kpc. The steep outward gradient is supported by two independent data sets and data reductions. The measurements of Loubser et al. (2008) near the galaxy center had already hinted at a positive gradient from 190 km s^{-1} at $R = 5''$ to ~ 240 km s^{-1} at a radius of $R = 10''$, and data shown in Fig. 1 of (Hau et al., 2004) reach $\simeq 300\,\mathrm{km\,s^{-1}}$ at ~ 25". With the new data we now have very clear evidence of a dynamically hot stellar halo in NGC 3311.

To put the extremely rapid rise of the velocity dispersion profile of NGC 3311 in context, we compare its kinematic properties with those of early-type galaxy (ETG) halos mapped using planetary nebula data (Coccato et al., 2009) and with the halos of the two Coma BCG galaxies NGC 4889, NGC 4874 from deep absorption line spectroscopy (Coccato et al., 2010b). Fig. 2.4 shows the mean $< V/\sigma >$, X-ray luminosity, and total absolute B-band magnitude for these galaxies versus their outermost halo velocity dispersion. For NGC 3311, we use a bolometric X-ray luminosity within $50'' \simeq 12$ kpc, $L_X = 2.75 \times 10^{40}$ erg s^{-1} (based on the flux in the 0.5-4.5 keV energy range from Yamasaki et al. (2002) and corrected to bolometric L_X according to Table 1 of O'Sullivan et al. (2001)), and the total extinction corrected B-band magnitude (12.22) from de Vaucouleurs et al. (1991). For the velocity dispersion of NGC 3311, we use the values at the center, at 15" ($\simeq 3.7$ kpc) and at $47''$ ($\simeq 12$ kpc). Only the central σ_0 puts NGC 3311 in the middle of the ETG distribution; σ(47") deviates strongly, with a much larger σ than expected for the given L_X, B_T.

The natural interpretation for these results is that the outer stellar halo of NGC 3311 is dominated by the central intracluster star component of the Hydra cluster. This is supported by several pieces of evidence: (i) The steep rise of the σ-profile; more isolated ETGs all have slightly or even steep falling σ-profiles (Coccato et al., 2009). (ii) The saturation of σ at $\simeq 12$ kpc, outside of which the dynamically hot component dominates completely. σ(47") is $\sim 60\%$ of the galaxy velocity dispersion in the cluster core. (iii) The large amount of dark matter inferred from X-ray observations around

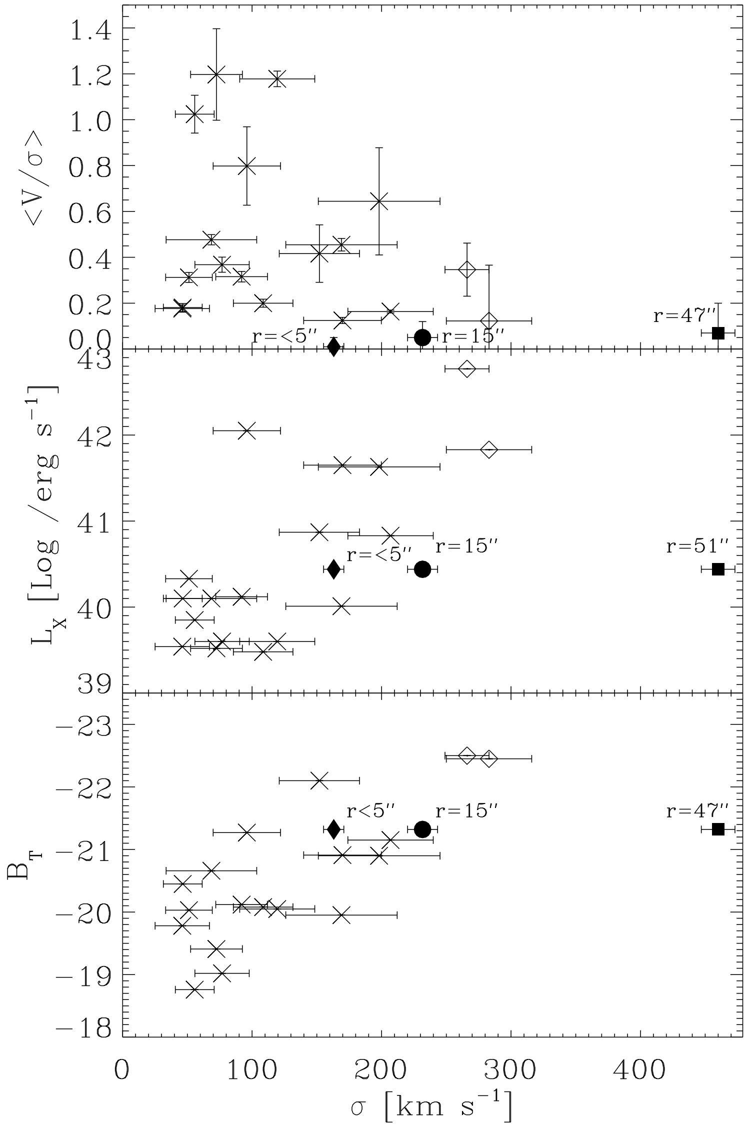

Figure 2.4: Properties of the stellar halo of NGC 3311 compared with other early-type galaxy halos: mean $< V/\sigma >$ (*upper panel*), total X-ray luminosity (*central panel*), and B-band total magnitude (lower panel) against stellar velocity dispersion σ. Solid diamond, circle, and square show the measured σ of NGC 3311 at the center, 15” ($\simeq$ 3.7 kpc), and 47” ($\simeq$ 12 kpc). Crosses show outermost velocity dispersions from Coccato et al. (2009), and open diamonds for NGC 4889/4874 from Coccato et al. (2010b).

NGC 3311 ($\sim 10^{12}$ $M_\odot$ within 20 kpc, Hayakawa et al. (2004)).

In recent cosmological hydrodynamic simulations of cluster formation, Dolag et al. (2010) applied a kinematic decomposition to the stellar particles around cD galaxies. With a double Maxwellian fit to the velocity histogram of star particles centered on a simulated cD, they were able to separate an inner, colder Maxwellian distribution associated with the central galaxy, and an outer, hotter component of stars that orbit in the cluster potential. For both components they derived radial density profiles and, fitting Sersic profiles, found that the inner stellar component is much steeper than the outer diffuse stellar component. A comparison with these simulations indicates that the steep velocity dispersion gradient in the halo of NGC 3311 traces the transition from central galaxy stars to the diffuse intracluster stellar component. In the NGC 3311 halo, the transition between the two occurs at smaller radii than in other BCGs in nearby clusters, in the range between 4 and 12 kpc.

NGC 3311 appears to have a similar halo as the cD galaxy NGC 6166 in the Abell 2199 cluster (Kelson et al., 2002), whose σ-profile rises to cluster values at $R \sim 60$ kpc. But NGC 3311 is even more extreme; it is a fairly small galaxy, based on its central $\sigma_0 = 150$ km s^{-1}, and it is already dominated by the surrounding cluster component at $R \sim 12$ kpc. Presumably, this is because the core of the “relaxed” Hydra cluster has had time to collapse onto the galaxy. For comparison, the two BCG galaxies in the Coma cluster core, which have a nearly constant σ-profile (Coccato et al., 2010b), may be in the middle of an ongoing merger (Gerhard et al., 2007), so that their previous subcluster halos would have been stripped and a new cluster halo could have been built only after the merger was completed; and in the outer halo of the more isolated M87, the velocity dispersion appears to drop (Doherty et al., 2009) towards the edge.

2.5 Conclusions

Based on two independent long-slit data sets and reductions, we find a steep gradient in the velocity dispersion profile of the central galaxy NGC 3311 in the Hydra I cluster, from $\sigma_0 \simeq 150$ km s^{-1} to $\sigma_{out} \simeq 450$ km s^{-1} outside 12 kpc (60% of the velocity dispersion of the galaxies in the surrounding cluster).

The new data provide evidence that NGC 3311 is a fairly small galaxy dominated by a large envelope of intracluster stars already beyond $R \sim 12$ kpc, whose orbits are dominated by the cluster dark matter potential. Comparison with other BCG galaxies shows a wide range of dynamical behavior in their halos.

2.6 Acknowledgements

The authors wish to thank the ESO VLT staff for their support during the observations and the referee for a constructive report. This research has made use of the Gemini archive data, the NASA/IPAC Extragalactic Database (NED), which is operated by the Jet Propulsion Laboratory, California Institute of Technology, under contract with the National Aeronautics and Space Administration.

Table 2.1: Measured mean velocities and velocity dispersions for NGC 3311. For details see text. The galaxy's systemic velocity V_{sys} = 3800 km s^{-1} has been obtained by a linear fit to the velocities in the central 20″ and has then been subtracted from the measurements. This value includes heliocentric and relativistic corrections. The calculated correction to the velocity in heliocentric system are ∼ −25 km/s and ∼ −5 km/s for the Gemini-South and FORS2 spectra, respectively.

Instr. (1)	R (arcsec) (2)	P.A. (3)	$V_{\rm ppxf1}$ (km s^{-1}) (4)	$\sigma_{\rm ppxf1}$ (km s^{-1}) (5)	$V_{\rm ppxf2}$ (km s^{-1}) (6)	$\sigma_{\rm ppxf2}$ (km s^{-1}) (7)	$V_{\rm FCQ}$ (km s^{-1}) (8)	$\sigma_{\rm FCQ}$ (km s^{-1}) (9)	$< V >$ (km s^{-1}) (10)	$< \sigma >$ (km s^{-1}) (11)
GMOS-S	38.6	63°	38 ± 33	399 ± 38	−47 ± 33	381 ± 38	−62 ± 45	435 ± 48	−17 ± 31	401 ± 23
GMOS-S	14.89	63°	−18 ± 8	238 ± 13	−50 ± 8	228 ± 13	−49 ± 8	241 ± 14	−39 ± 11	235 ± 8
GMOS-S	7.88	63°	−7 ± 8	209 ± 15	−21 ± 8	203 ± 15	19 ± 5	193 ± 5	5 ± 12	195 ± 5
GMOS-S	3.8	63°	−14 ± 7	194 ± 13	−27 ± 7	191 ± 13	1 ± 3	145 ± 3	−5 ± 7	151 ± 11
GMOS-S	0	63°	−10 ± 6	204 ± 10	−22 ± 6	201 ± 10	−3 ± 3	143 ± 3	−8 ± 5	154 ± 16
GMOS-S	−4.09	63°	2 ± 6	206 ± 14	−14 ± 6	204 ± 14	16 ± 4	169 ± 4	5 ± 9	174 ± 9
GMOS-S	−8.05	63°	23 ± 11	244 ± 20	9 ± 11	200 ± 20	26 ± 7	182 ± 8	21 ± 5	191 ± 14
GMOS-S	−15	63°	29 ± 11	295 ± 16	−6 ± 11	267 ± 16	30 ± 7	200 ± 9	22 ± 11	231 ± 28
GMOS-S	−34	63°	111 ± 13	323 ± 22	50 ± 13	252 ± 22	−8 ± 17	292 ± 18	60 ± 33	289 ± 19
FORS2	−47	45°	76 ± 12	479 ± 14	71 ± 12	433 ± 14	117 ± 7	466 ± 12	100 ± 15	460 ± 13
FORS2	−54	83°	67 ± 13	456 ± 15	87 ± 13	447 ± 15	124 ± 8	467 ± 14	105 ± 17	457 ± 8
FORS2	−67	6°	87 ± 53	471 ± 49	66 ± 53	454 ± 49	97 ± 55	476 ± 97	83 ± 31	464 ± 33
FORS2	−100	114°	14 ± 21	437 ± 35	47 ± 21	432 ± 35	50 ± 29	405 ± 51	35 ± 13	429 ± 22

Notes – Col. 1: Instrument. Col. 2: Radial distance from center of NGC 3311. Col. 3: Position angle of data with respect to NGC 3311's center. Col. 4: Velocity measured with PPXF (using template determined at R = 0"), relative to the galaxy systemic velocity. Col. 5: Velocity dispersion measured with PPXF (using template determined at R = 0"). Col. 6: Velocity measured with PPXF (free template), relative to the galaxy systemic velocity. Col. 7: Velocity dispersion measured with PPXF (free template). Col. 8: Velocity measured with FCQ, relative to the galaxy systemic velocity. Col. 9: Velocity dispersion measured with FCQ. Col. 10: Weighted average velocity. Col. 11: Weighted average velocity dispersion.

Chapter 3

Intracluster Planetary Nebulas in the Hydra I Cluster

Giulia Ventimiglia, Magda Arnaboldi, Ortwin Gerhard

Astronomische Nachrichten, 2008, 329, 1057 [1]

Abstract

Using the Multi-Slit Imaging Spectroscopy (MSIS) technique at the FORS2 spectrograph on VLT-UT1, we have identified 60 Intracluster Planetary Nebula (ICPN) candidates associated with the Intracluster Light (ICL) in the central region of the Hydra I cluster. Hydra I is a medium compact, relatively near (~ 50 Mpc), rich cluster in the Southern hemisphere. Here we describe the criteria used to select emission sources and present the evidence for these PN candidates to be associated with the ICL in the Hydra I cluster.

3.1 Introduction

Diffuse intracluster light (ICL) has been observed both in nearby and intermediate redshift clusters (Feldmeier et al., 2004; Mihos et al., 2005). Observations show that the diffuse light in galaxy clusters amounts to ~ 10% of the total light emitted by the cluster galaxies (Aguerri et al., 2005; Zibetti et al., 2005).

Cosmological simulations of structure formation predict intracluster stars to be lost from galaxies in interactions during the assembly of galaxy clusters (Napolitano et al., 2003; Murante et al., 2004; Willman et al., 2004; Sommer-Larsen et al., 2005). Simulations suggest that most of the diffuse light in galaxy cluster cores originates from mergers that lead to the formation of the brightest cluster

---

[1] Last section of this proceeding and references in the text to this section are omitted because a more accurate comparison of the number of detected PNs with that expected from the luminosity and stellar population of NGC 3311 is presented in Sec. 5.7.3 of this thesis.

galaxy and of the other massive galaxies, while the tidal stripping mechanism dominates the formation of the ICL at larger radii (Murante et al., 2007).

The study of the properties of this diffuse component has then an important role in understanding the mechanisms relevant for the evolution of galaxies in high density environments, and the formation history, dynamics and merging status of clusters.

Wide field imaging has already shown the morphological complexity of the ICL: studies of the Virgo and Coma cluster ICL have shown that it is characterized by tidal features like streamers and extended galaxy halos (Adami et al., 2005; Mihos et al., 2005). Due to its intrinsically low surface brightness, $\mu_V > 28.5$ mag arcsec^{-2} (Feldmeier et al., 2004; Mihos et al., 2005), the kinematics of ICL can only be studied using the *Intracluster Planetary Nebulas* (ICPNs) associated with this stellar component (Arnaboldi et al., 2004; Gerhard et al., 2007; Doherty et al., 2009). ICPNs are relatively easy to detect because their spectra are characterized by two strong emission lines: [OIII]λ4959Å and [OIII]λ5007Å, with relative flux ratio 1 : 3.

The goal of our project is to measure the velocity distribution of the PNs associated with the diffuse light in the central region of the nearby Hydra I cluster (Abell 1060, D ∼ 50 Mpc, z ∼ 0.0126), a medium compact, non-cooling flow, rich cluster in the Southern hemisphere. This will be presented in a forthcoming paper. Here we present the selection criteria and the evidence for the detection of PNs associated with the ICL in Hydra I.

At the distance of the Hydra I cluster, the flux of the O[III] λ5007Å emission line of a PN is less than 8×10^{-18} erg s^{-1}cm^{-2}, therefore we need to reduce substantially the noise from the night sky in order to detect these lines. This is possible by using the Multi-Slit Imaging Spectroscopy technique (MSIS: Gerhard et al. (2005); Arnaboldi et al. (2007). In what follows we define $m_{5007} = -2.5 \log F_{5007} - 13.74$ (the Jacoby formula, Jacoby (1989)), where F_{5007} is the integrated flux in the [OIII] λ5007Å emission line, and we assume a distance of 50 Mpc for the Hydra I cluster implying 1” ∼ 0.24 kpc.

In the next section we present the MSIS observations carried out with FORS2 on UT1. In Section 3 we summarize the data reduction. We present the adopted selection criteria to identify the emission sources and the evidence for PNs associated with the ICL in the Hydra I cluster in Section 4. In Section 5 we show that the number density of PN candidates detected is consistent with that expected for the stellar population associated with the central cD galaxy of the cluster, NGC 3311. In Section 6 we summarize our results.

3.2 Observations

3.2.1 The Multi-Slit Imaging Spectroscopy technique

The MSIS technique consists of the combined use of a mask of parallel slits, a narrowband filter centered around the redshifted [OIII] λ5007Å line, and a dispersing element. It is a blind search technique and allows one to obtain spectra of all PNs (and other emission line objects) that happen to lie behind the mask slits. Because the [OIII] emission lines from PNs are only ~ 30 km/s wide (Arnaboldi et al., 2008), when dispersed at spectral resolution $R = \lambda/\Delta\lambda \sim 6000$, their entire flux falls into a small number of pixels in the two-dimensional spectrum, determined by the slit width and seeing. By dispersing the sky noise on many pixels, the technique allows measurement of very faint fluxes. We can detect PNs with magnitudes ~ 1.2 mag below the bright cut-off of the Planetary Nebulas Luminosity Function (PNLF; Ciardullo et al. (1998)) and their positions and radial velocities can be measured at the same time.

3.2.2 Observational set up

Data were collected in visitor mode during 2006 March 26-28, using the FORS2 spectrograph on UT1. The observed area covers the central region of the Hydra I cluster, around NGC 3311, at α = 10h36m42.8s, $\delta = -27$d31m42s (J2000).

The FORS2 field of view (FoV) is $6'.8 \times 6'.8$ wide, corresponding to (~ 100 kpc)^2, and is imaged onto a mosaic of two CCDs, rebinned 2×2 in the readout. We used two narrow band filters, one centered at λ = 5045Å and a second one at λ = 5095Å, both with a FWHM of 60Å. We cover, in this way, the whole range of cluster line-of-sight (LOS) velocities and, for fast, $v_{LOS} \geq 4000$ km s^{-1}, and bright PNs, $m_{5007} \leq 29.3$, the [OIII] λ5007Å emission line falls in the red filter and the [OIII] λ4959Å line in the blue filter. Spectra were obtained with the GRIS-600B grism, which has a spectral resolution of 0.75 Å/pixel at 5075 Å. The MSIS mask is made of 24×21 slits, each of them 0".8 wide and 17".5 long. Each slit is projected along the dispersion axis onto ~ 40 rebinned pixels. The effective area imaged by the slits is ~ 7056 arcsec^2, that is ~ 4.5% of the whole FORS2 FoV. In order to cover the whole field the MSIS mask was stepped 15 times on the sky to cover the region between two adjacent slits. For each mask position 3 exposures, of 1200 sec each, were taken, ensuring a proper cosmic ray subtraction. The seeing during the three observing nights was in the range from 0".6 to 1".5.

Arclamp calibration frames were acquired for the wavelength calibration, as well as flats and bias images. The flux calibration was done using long slit observations of the standard star LTT7379 with narrow band filter plus Grism.

3.3 Data reduction

Data reduction was carried out following the procedure described in Arnaboldi et al. (2007). After bias subtraction, the images were properly co-added and the continuum light from the two main galaxies was subtracted, with an fmedian filtering using a window of 19×35 pixels.

Then we extracted and rectified the 2D spectra (fig. 3.1) of the emission sources and performed the wavelength and flux calibration. The total number of emission sources detected is 95. On the basis of the flux calibration the 1σ limit on the continuum is $\sim 7 \times 10^{-20}$ erg cm^{-2} s^{-1} Å^{-1}.

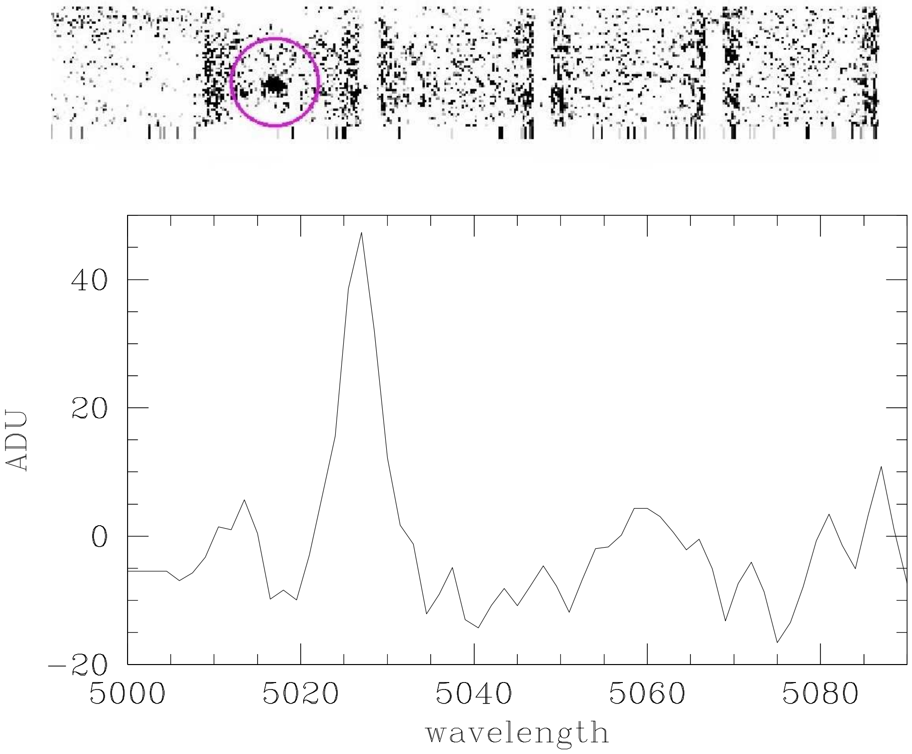

Figure 3.1: *Upper panel*: 2-D spectrum of a PN candidate. The dispersion axis is along the vertical direction. The emission line falls onto about 6 pixels both in the spatial and spectral direction. *Lower panel*: 1-D spectrum of the same PN candidate. The emission line has the same FWHM as the arc lamp lines, showing that the observed emission line is unresolved in wavelength.

A first classification of the emission line objects can be carried out according to the following criteria:

- PN candidates: unresolved emission line objects, both in space and in wavelength, with no continuum;

- background objects candidates: continuum sources with unresolved or resolved emission line.

Of the 95 emission lines sources identified, 60 were classified as possible PN candidates, the remaining sources as background object candidates. Monochromatic point like emissions appear in the final images as unresolved sources with a width of ~ 6 pixels both in the spatial and in the wavelength direction. The final spectral resolution is ~ 4.5 Å, or 140 km s^{-1}. Magnitudes for the PN candidates were computed using the Jacoby formula.

3.4 Selection Criteria for the PN population: the wavelength-magnitude plane

We now describe the physical properties of PNs belonging to the Hydra I ICL in a two dimensional wavelength-magnitude space, as shown in fig. 3.2.

A PN population is characterized by a bright cut-off of the PNLF, which according to Ciardullo et al. (1998) has absolute magnitude of the [OIII] λ5007Å emission line of $M^* = -4.48$. At the Hydra I cluster distance ($m - M = 33.49$), this corresponds to an apparent magnitude of $m_{5007} = 29.1$ (plotted as the dotted horizontal line in fig. 3.2). The apparent magnitude for the [OIII] λ4959Å emission line is 1.2 mag fainter.

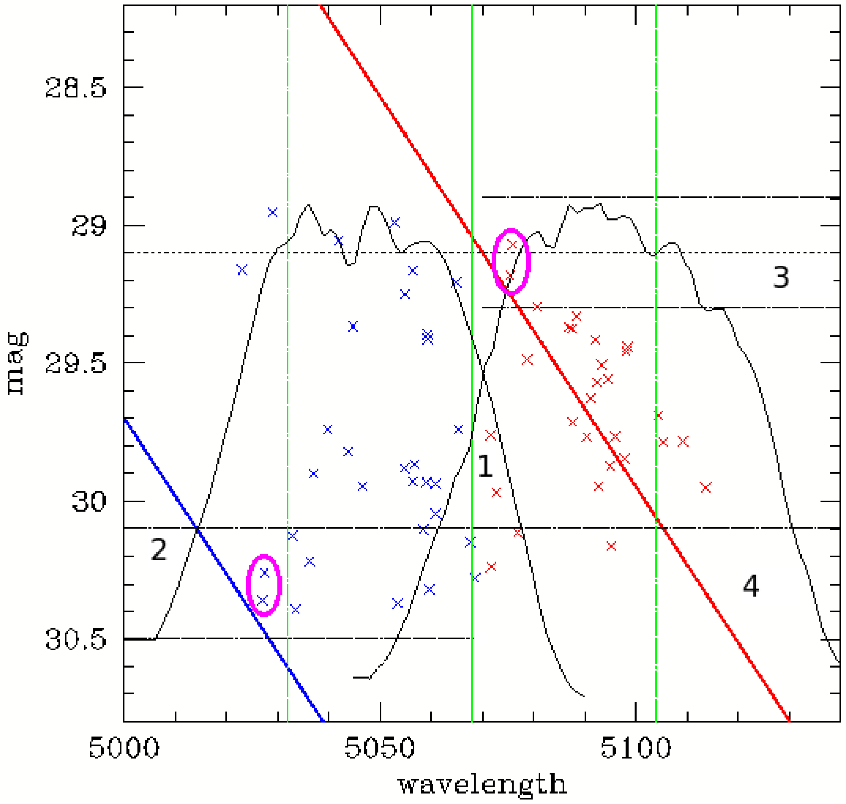

Figure 3.2: The plot shows the wavelength vs magnitude space in which we describe the physical properties of a PN population at 50 Mpc and bound to the Hydra I cluster. Blue and red crosses are the PN candidates detected in the MSIS images. The various lines and the characteristics of the 4 regions identified in the plot are explained in the text.

The red inclined line in fig. 3.2 shows the apparent magnitude of a PN at the PNLF bright cutoff, as a function of the Hubble flow distance, and the blue line shows the same dependence for the [OIII] λ4959Å emission line. If the line-of-sight velocity corresponded only to the Hubble flow, then the magnitude of the two emission lines, [OIII] λ4959Å and [OIII] λ5007Å of a PN fainter than the bright cut-off would fall on the left side of the blue and red line, respectively.

The systemic velocity of the Hydra I cluster $v_{Hydra\ I} = 3683$ km s^{-1} and its velocity dispersion $\sigma_{Hydra\ I} = 724$ km s^{-1} (Christlein & Zabludoff 2003) identify a wavelength range in which [OIII] emissions from objects orbiting in the Hydra I cluster potential can be observed. At the systemic velocity of the cluster, the [OIII] emission lines are redshifted to $\lambda = 5068$Å and $\lambda = 5020$Å, respectively. In fig. 3.2 the central green line is at $\lambda = 5068$Å where the [OIII] λ5007Å line is redshifted to the cluster systemic velocity. The other two vertical green lines are at the wavelengths bounding the $\pm 3\sigma$ velocity range, respectively at $\lambda = 5032$Å and $\lambda = 5104$Å.

The black continuous lines in fig. 3.2 show the measured profiles of the narrow band filters, T(λ), normalized so that the maximum transmission is at the PNLF bright cutoff. They are centered respectively at $\lambda = 5045$Å and $\lambda = 5095$Å and have a FWHM of ~ 60Å.

Considering the magnitude limit and wavelength range specified, we can identify different areas in this wavelength-magnitude space, separated by black horizontal lines:

- **Region #1** According to their velocity and magnitude all emission lines are [OIII] λ5007Å.
- **Region #2** It is the region where, considering the flux and wavelength, we can find both faint [OIII] λ5007Å or [OIII] λ4959Å emission lines.
- **Region #3** Here we have high flux and red wavelengths so that we can see the bright [OIII] λ5007Å emissions. For such emissions we expect to detect the corresponding [OIII] λ4959Å in region #2.
- **Region #4** Here the emissions are most likely [OIII] λ5007Å. In principle, we may find both [OIII]λ4959Å and [OIII]λ5007Å; however, if an emission were identified as [OIII] λ4959Å its LOS velocity would be about 8600 km s^{-1} which is more than 6σ away from the cluster systemic velocity. This PN would then not be bound to Hydra I and its velocity driven by the Hubble flow. Then its [OIII] λ4959Å magnitude should fall on the left side of the blue line. Therefore [OIII] λ4959Å emission lines in this region are ruled out.

We can now populate the wavelength-magnitude plane with the PN candidates detected in the MSIS spectra. This gives us important information to validate the PNs catalogue. In the plot the blue and red crosses are the PN candidates detected in the wavelength ranges covered by the blue and red filters respectively.

The first result is that the fluxes of these candidates are all consistent with those of PNs at the distance of the Hydra I cluster, in the range from 1.7×10^{-18} to 8.4×10^{-18} erg s^{-1}cm^{-2}, i.e. $30.7 > m_{5007} > 28.9$.

The second is that for the two bright [OIII] λ5007Å emission sources identified in region #3, the corresponding [OIII] λ4959Å have been identified in region #2: these objects are encircled in magenta. All others emission sources in the plot are [OIII] λ5007Å if in the cluster.

Moreover, we know that the 1σ continuum upper limit flux in both filters is $\sim 7 \times 10^{-20}$ erg cm^{-2}s^{-1}Å^{-1}. Considering that the compact HII regions detected in the Virgo cluster (Gerhard et al., 2002) have a V-band continuum flux of $\sim 8.2 \times 10^{-19}$ erg cm^{-2}s^{-1}Å^{-1}, corresponding to $\sim 9.6 \times 10^{-20}$ erg cm^{-2}s^{-1}Å^{-1} at the distance of the Hydra I cluster, this allows us to rule out from our sample compact HII regions such as or brighter than those observed in Virgo. Also, from the continuum upper limit flux we calculate that the Equivalent Width (EW) of the most luminous candidates is EW > 90Å. This value is larger than those of [OII] emitting background galaxies at z = 0.37, which have $EW_{[OII]} < 50$ (Hogg et al., 1998). Therefore, we can rule out all contaminations to our sample except a few background Lyα galaxies.

In summary, from analysing the PN candidates in the wavelength-magnitude plane we learn that:

- fluxes are consistent with PNs at the distance of the Hydra I cluster; the only possible contaminants are Lyα emitters at high redshift;
- objects in magenta circles can reliably be classified as PNs because we are able to see both their [OIII] λ5007Å and [OIII] λ4959Å emission lines;
- for all other PNs we have detected the [OIII] λ5007Å at the LOS velocity expected for objects bound to the Hydra I cluster.

3.5 Conclusions

In this work, we have presented MSIS observations of PN candidates associated with the diffuse light around the central cD galaxy NGC 3311 in the Hydra I cluster. We have discussed criteria used for selecting these emission sources and have analyzed their properties in the wavelength-magni- tude plane. In total, we have identified 60 PN candidates around NGC 3311.

In the next steps of our analysis we will focus on the kinematics of the diffuse stellar population in the halo of NGC 3311. We will study the histogram of the LOS velocity distribution of the PNs candidates to obtain information about possible substructures in the ICL and the merging status of the cluster. Together with the X-ray temperature profile (Yamasaki et al., 2002) and the surface brightness profiles of the stellar light this will give us constraints on the orbit distribution in the halo of this cD galaxy.

3.6 Acknowledgements

G. Ventimiglia is supported by an ESO studentship.

Chapter 4

A Lyα survey of background galaxies at z ∼ 3.12

Giulia Ventimiglia, Magda Arnaboldi, Ortwin Gerhard

2010, accepted for publication in VA

Abstract

We describe the results of a deep survey for Lyα emission line galaxies at z ∼ 3.1, carried out with the Multi-Slit Imaging Spectroscopy (MSIS) technique, with the FORS2 spectrograph on VLT-UT1. We discuss the criteria used to select the emission line galaxies and present the main physical characteristics of the sample: redshift, observed flux and equivalent width distributions.

4.1 Introduction

In the last decades our knowledge of the high redshift ($z > 2$) Universe has significantly increased. The observational technique that allowed such galaxies to be found, in a significant number, is the dropout technique (Giavalisco, 2002). It detects Lyman Break galaxies by the flux discontinuity due to their Lyman limit absorption (Steidel et al., 1996a,b). Since 1998, narrow band surveys reported the detection of Lyα emission from objects in the redshift range $2.4 < z < 6.5$ (Hu et al., 1998; Ciardullo et al., 2002; Ajiki et al., 2003; Ouchi et al., 2005, 2008; Gronwall et al., 2007; Schaerer, 2007). The Lyα emission not only allows galaxies to be detected at very high redshifts, but also gives a valuable star formation diagnostic and facilitates the study of large scale structures at high redshift. With spectroscopic surveys the Lyα emission line profiles can be studied (Kudritzki et al., 2000; Shapley et al., 2003; Martin et al., 2008; Rauch et al., 2008). This, in turn, provides the possibility of testing models of the physical parameters of the Lyα emitters and to derive constraints on their stellar populations and their gas and dust content (Verhamme et al., 2008).

Here we present the results of a survey at z ~ 3.1 carried out with the Multi-Slit Imaging Spectroscopy technique (MSIS, Gerhard et al., 2005) with FORS2 on UT1.

4.2 The Multi-Slit Imaging Spectroscopy technique

MSIS is a blind search technique that consists of the combined use of a mask of parallel slits, a narrowband filter, and a dispersing element. It obtains the spectra of all emission line objects that happen to lie behind the mask slits. Our main purpose is to detect the [OIII] λ5007 line emission for Planetary Nebulas (PNs), in order to study the kinematic properties of the Intracluster light (ICL) in the central regions of nearby (< 100 Mpc) clusters of galaxies (Gerhard et al., 2007; Ventimiglia et al., 2008). By dispersing the sky noise on many pixels, the technique enables measurements of very faint fluxes. Thus MSIS surveys are also suitable for the detection of the redshifted 1216 Å emission line from high-redshift Lyα galaxies.

4.3 Observational set up

Data were collected in visitor mode during 2006 March 26-28, using the FORS2 spectrograph on UT1. The observed area covers the central region of the Hydra I cluster, around NGC 3311, at $\alpha = 10^h 36^m 42.8^s$, δ= -$27^d 31^m 42^s$ (J2000). The FORS2 field of view (FOV) is $6'.8 \times 6'.8$ wide, corresponding to ~ 10000 kpc^2, and it is imaged onto a mosaic of two CCDs, rebinned 2×2 in the readout. We used two narrow band filters, one centered at $\lambda = 5045$ Å and a second one at $\lambda = 5095$ Å, both with a FWHM of 60 Å. In this way we are able to detect Lyα emission lines in the redshift range $3.12 < z < 3.21$. Spectra were obtained with the GRIS-600B grism, which has a spectral resolution of 0.75 Å/pixel at 5075 Å. The MSIS mask is made of 24×21 slits, each of them 0".8 wide and 17".5 long. Each slit is projected along the dispersion axis onto ~ 40 rebinned pixels. The effective area imaged by the slits is ~ 7056 arcsec^2, that is ~ 4.5% of the whole FORS2 FOV. In order to cover the whole field, the MSIS mask was stepped 15 times on the sky to fill the region between two adjacent slits. For each mask position 3 exposures, of 1200 sec, were taken, ensuring a proper cosmic ray subtraction. The seeing during the three observing nights was in the range from 0".6 to 1".5. We can detect emission line objects with a flux completeness limit of ~ 3.4×10^{-18} erg cm^{-2}s^{-1}, and their positions and radial velocities can be measured at the same time. With this instrumental set up and total exposure time, monochromatic point like emissions appear in the final images as unresolved sources with a width of ~ 6 pixels both in the spatial and in the wavelength direction. Therefore, the FWHM spatial resolution is 1".1 and the FWMH spectral resolution is 450 km s^{-1}.

4.4 Data reduction

Data reduction was carried out following the procedure described in Arnaboldi et al. (2007); Ventimiglia et al. (2008). After bias subtraction, the images were co-added and the continuum light from the two Hydra I galaxies was subtracted, with an fmedian filtering using a window of 19×35 pixels. The 2D stacked spectra of the emission sources were then extracted, rectified, wavelength and flux calibrated. The total number of emission sources detected is 86. On the basis of the flux calibration the 1σ limit on the continuum is $\sim 7{\times}10^{-20}$ erg cm^{-2} s^{-1}Å^{-1}. Continuum fluxes were calculated in the 60 Å wavelength range covered by the filter in which the emission line was detected.

In a first classification, all objects with unresolved emission lines and no continuum were classified as PN candidates; the remaining as background galaxy candidates. The PN candidate sample likely contains a fraction of unresolved Lyα emitters without continuum which are not included in the present study.

4.5 Lyα candidates and their physical characteristics

In the background galaxy sample 6 objects are classified as [OII] emitters; they are characterized by an emission line with a clearly visible continuum at all wavelengths. The remaining 20 objects are classified as candidate Lyα galaxies. They include sources with resolved emission lines, either spatially or in wavelength or both, without continuum, and sources with resolved/unresolved emission lines and continuum only to the red side of the spectrum. This classification is supported by spectroscopic follow up of similar sample of background galaxies in previous PN surveys (Freeman et al., 2000; Arnaboldi et al., 2002; Kudritzki et al., 2000), and by the fact that the deep sample of $2.7 < z < 3.7$ Lyα galaxies of Rauch et al. (2008) contains few foreground [OII] emitting galaxies, contrary to higher redshift samples (Martin et al., 2008).

The redshift distribution of the Lyα candidates (LACs) is shown in Figure 4.1. The emission lines of all objects were fitted by simple Gaussian profiles, both in the spatial and in the dispersion direction. For all the LACs, Fig.4.1 (upper left panel) shows the FWHM of the Gaussian profiles along the spatial direction vs. the FWHM of the Gaussian profiles along the dispersion direction. About 65% of the sample has an emission line which is spatially unresolved; the rest is spatially resolved. About 60% of the sample is unresolved in velocity and the rest is resolved.

Based on this information we adopt a simple morphological classification of the candidates: unresolved objects both spatially and in wavelength (PS), resolved objects in both directions (EXT) and resolved objects only in the spatial or wavelength direction, respectively (EXTs, EXTv). A proper morphological classification is beyond the purpose of the current work. More detailed discussion about morphology and the related physics of LACs can be found in Rauch et al. (2008); Verhamme et al. (2008).

The fluxes were measured in apertures of 0”.8 × 2” × 755 km/s centred around the emission lines

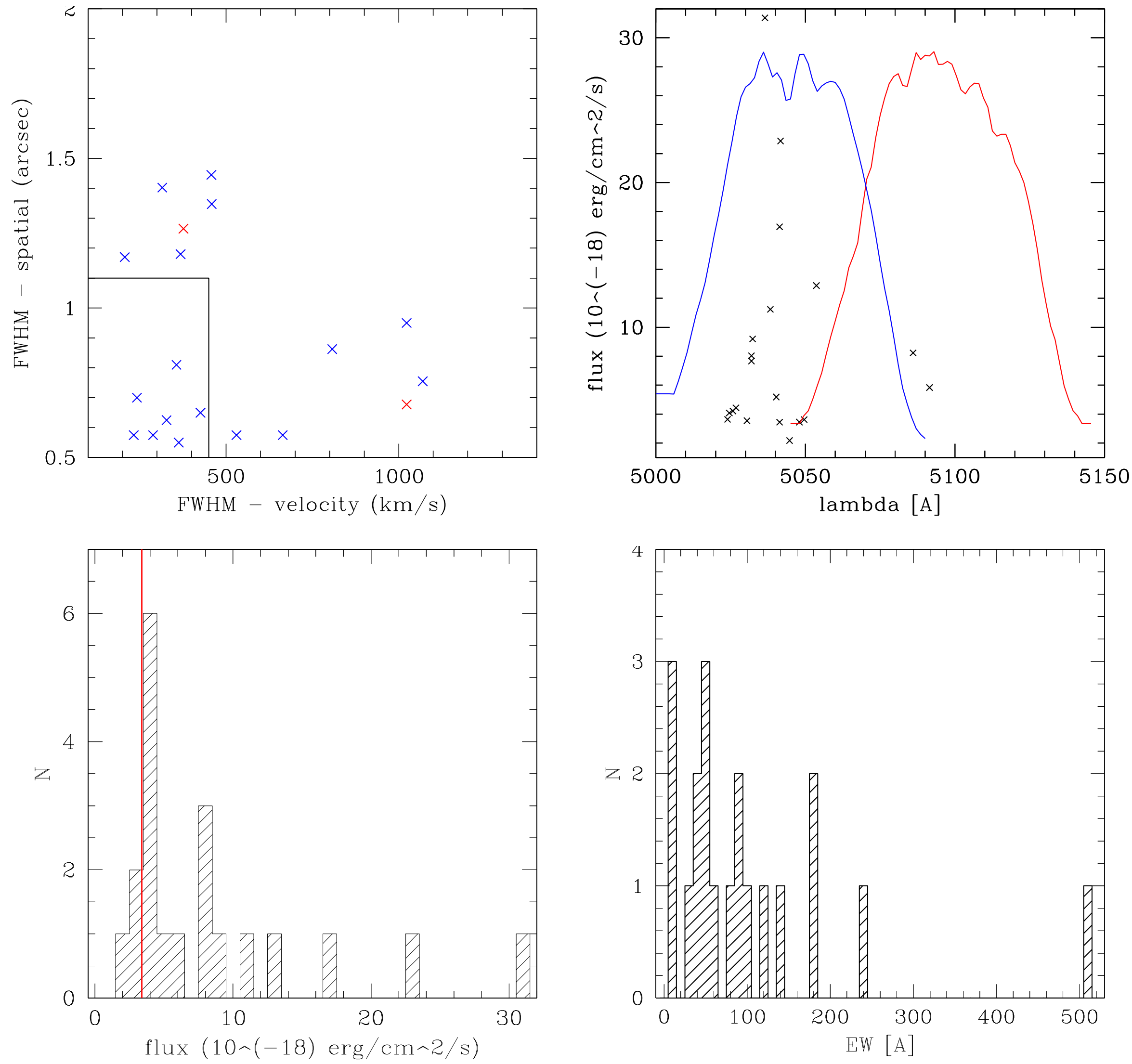

Figure 4.1: Physical characteristics of all emission line sources in the survey classified as Lyα candidate galaxies (LACs). *Upper left panel*: Distribution of the Gaussian FWHM along the spatial direction vs. the Gaussian FWHM along the dispersion direction. One extended object in velocity could not be fitted by a Gaussian and is omitted. In the rectangle on the lower left are LACs whose emission line is unresolved both spatially and in wavelength. Blue crosses are objects detected in the wavelength range covered by the blue filter and red crosses are those detected in the wavelength range covered by the red filter. *Upper right panel*: Flux vs. wavelength for the LACs (black crosses) detected in the MSIS field. The blue and the red lines show the normalized measured profiles of the blue and red filters, respectively. *Lower left panel*: Histogram of the LACs emission line flux distribution. The red vertical line defines the flux completeness limit. *Lower right panel*: Histogram of LACs EW distribution.

and corrected for the filter response. Fig.4.1 shows the fluxes of the LACs as a function of wavelength (upper right panel), and their flux distribution (lower left panel). The latter is peaked at $\sim 3\times10^{-18}$ erg cm^{-2}s^{-1} and is truncated at faint fluxes, because our survey is flux limited. The completeness limit of the sample is $\sim 3.4\times10^{-18}$ erg cm^{-2}s^{-1}, while the detection limit is $\sim 2\times10^{-18}$ erg cm^{-2}s^{-1}. The most luminous objects have fluxes greater than 20×10^{-18} erg cm^{-2}s^{-1}.

The equivalent width (EW) distribution is also shown in Fig.4.1 (lower right panel). The continuum fluxes go from the limit on the 1σ continuum value of 7×10^{-20} erg cm^{-2}s^{-1} to $\sim 7\times10^{-19}$ erg cm^{-2}s^{-1}. Most of the objects have an observed EW < 200 Å.

A study of the luminosity function and a comparison of the number densities with results from previous surveys at redshift ~ 3.1 will be the subject of a forthcoming paper.

4.6 Acknowledgements

G. Ventimiglia is supported by an ESO studentship.

Chapter 5

The unmixed kinematics of intracluster stars in the core of the Hydra I cluster

Giulia Ventimiglia, Magda Arnaboldi, Ortwin Gerhard

2010, accepted for publication in A&A[1]

Abstract

Diffuse intracluster light (ICL) and cD galaxy halos are believed to originate from galaxy evolution and disruption in clusters.

The processes involved may be constrained by studying the dynamical state of the ICL and the galaxies in the cluster core. Here we present a kinematic study of diffuse light in the Hydra I (Abell 1060) cluster core, using planetary nebulas (PNs) as tracers.

We use Multi-Slit Imaging spectroscopy with FORS2 on VLT-UT1 to detect 56 PNs associated with diffuse light in the central 100×100 kpc^2 of the Hydra I cluster, at a distance of $\sim$ 50 Mpc. We measure their [OIII] m_{5007} magnitudes, sky positions, and line-of-sight velocity distribution (LOSVD), and compare with the phase-space distribution of nearby galaxies.

The luminosity function of the detected PNs is consistent with that expected at a distance of $\sim$ 50 Mpc. Their number density is $\sim$ 4 times lower for the light seen than expected, and we discuss ram pressure stripping of the PNs by the hot intracluster medium as one of the possible explanations. The LOSVD histogram of the PNs is highly non-Gaussian and multi-peaked: it is dominated by a broad central component with $\sigma \sim 500\,\mathrm{km\,s^{-1}}$ at around the average velocity of the cluster, and shows two additional narrower peaks at $1800\,\mathrm{km\,s^{-1}}$ and $5000\,\mathrm{km\,s^{-1}}$. The main component is broadly consistent with the outward continuation of the intracluster halo of NGC 3311, which was earlier shown to have a velocity dispersion of $\sim 470\,\mathrm{km\,s^{-1}}$ at radii of $\geq 50''$. Galaxies with velocities in this range are

---

[1] In Sec. 5.7.1 the through-slit convolution of the PNLF, the photometric error convolution and the completeness correction were performed with a code written by O. Gerhard. - The analysis of Sec. 5.7.3 was done by M.Arnaboldi and O. Gerhard.

absent in the central 100×100 kpc^2 and may have been disrupted earlier to build this component. The PNs in the second peak in the LOSVD at 5000 km s^{-1} are coincident spatially and in velocities with a group of dwarf galaxies in the MSIS field. They may trace the debris from the on-going tidal disruption of these galaxies.

Most of the diffuse light in the core of Abell 1060 is still not phase-mixed. The build-up of ICL and the dynamically hot cD halo around NGC 3311 are on-going, through the accretion of material from galaxies falling into the cluster core and tidally interacting with its potential well.

5.1 Introduction

Intracluster light (ICL) consists of stars that fill up the cluster space among galaxies and that are not physically bound to any galaxy cluster members. For clusters in the nearby Universe, the morphology and quantitative photometry of the ICL have been studied with deep photometric data or by detection of single stars in large areas of sky.

Deep large field photometry shows that ICL is common in clusters of galaxies and it has morphological structures with different angular scales. The fraction of light in the ICL with respect to the total light in galaxies is between 10% and 30%, depending on the cluster mass and evolutionary status (Feldmeier et al., 2004; Adami et al., 2005; Mihos et al., 2005; Zibetti et al., 2005; Krick and Bernstein, 2007; Pierini et al., 2008). The detection of individual stars associated with the ICL, such as PNs (Arnaboldi et al., 2004; Aguerri et al., 2005; Gerhard et al., 2007; Castro-Rodriguéz et al., 2009), globular clusters (GCs) (Hilker, 2002; Lee et al., 2010), red giants stars (Durrell et al., 2002; Williams et al., 2007), and supernovae (Gal-Yam et al., 2003; Neill et al., 2005) is a complementary approach to deep photometry for studying the ICL, enabling also kinematic measurements for this very low surface brightness population.

An important open question is the relation between the ICL and the extended outer halos of brightest cluster galaxies (BCGs), whether they are independent components, or whether the former is a radial extension of the latter. Using a sample of 683 SDSS clusters, Zibetti et al. (2005) found a surface brightness excess with respect to an inner $R^{1/4}$ profile used to describe the mean profile of the BCGs, but it is not known yet whether this cD envelope is simply the central part of the cluster's diffuse light component, or whether it is distinct from the ICL and part of the host galaxy (Gonzalez et al., 2005).

Both the ICL and the halos of BCGs are believed to have formed from stars that were tidally dissolved from their former host galaxies, or from entirely disrupted galaxies. A number of processes have been discussed, starting with early work such as Richstone (1976); Hausman and Ostriker (1978). Contributions to the ICL are thought to come from weakly bound stars generated by interactions in galaxy groups, subsequently released in the cluster's tidal field (Rudick et al., 2006, 2009; Kapferer et al., 2010), interactions of galaxies with eachother and with the cluster's tidal field (Moore et al., 1996; Gnedin, 2003; Willman et al., 2004), and from tidal dissolution of stars from massive galaxies prior to mergers with the BCG (Murante et al., 2007; Puchwein et al., 2010). Stars in BCG halos may have originated in both such major mergers as well as through minor mergers with the BCG. Which of these processes are most important is still an open issue.

Kinematic studies of the ICL and the cD halos are instrumental in answering these questions. The kinematics of the ICL contains the fossil records of past interactions, due to the long dynamical timescale, and thus helps in reconstructing the processes that dominate the evolution of galaxies in clusters and the formation of the ICL (Rudick et al., 2006; Gerhard et al., 2007; Murante et al., 2007; Arnaboldi and Gerhard, 2010). The kinematics in the cD halos can be used to separate cluster from galaxy components, as shown in simulations (Dolag et al., 2010); so far, however, the observational results are not unanimous: in both NGC 6166 in Abell 2199 (Kelson et al., 2002) as well as NGC 3311 in Abell 1060 (Ventimiglia et al., 2010b) the velocity dispersion profile in the outer halo rises to nearly cluster values, whereas in the Fornax cD galaxy NGC 1399 (McNeil et al., 2010) and in the central Coma BCGs (Coccato et al., 2010b) the velocity dispersion profiles remain flat, and in M87 in Virgo (Doherty et al., 2009) it appears to fall steeply to the outer edge. Evidently, more work is needed both to enlarge the sample and to link the results to the evolutionary state of the host clusters.

The aim of this work is to further study the NGC 3311 halo, how it blends into the ICL, and what is its dynamical status. NGC 3311 is the cD galaxy in the core of the Hydra I (Abell 1060) cluster. Based on X-ray evidence, the Hydra I cluster is the prototype of a relaxed cluster (Tamura et al., 2000; Furusho et al., 2001; Christlein and Zabludoff, 2003). Surface photometry is available in the Johnson B, Gunn g and r bands (Vasterberg et al., 1991), and the velocity dispersion profile has been measured out to $\sim$ 100” (Ventimiglia et al., 2010b), showing a steep rise to $\sim 470\,\mathrm{km\,s^{-1}}$ in the outer halo. Here we use the kinematics of Planetary Nebulas (PNs) from a region of $100 \times 100\ \mathrm{kpc}^2$ centered on NGC 3311, to extend the kinematic study to larger radii and characterize the dynamical state of the outer halo and of the cluster core.

In Section 5.2 we summarize the properties of the Hydra I cluster from X-ray and optical observations. In Section 5.3 we discuss PNs as kinematical and distance probes, and the “Multi-Slit Imaging Spectroscopy - MSIS” technique for their detection in clusters in the distance range 40 – 100Mpc. We present the observations, data reduction, identification, and photometry in Sections 5.4 and 5.5. In Section 5.6 we describe the spatial distribution, line-of-sight (LOS) velocity distribution (LOSVD), and magnitude-velocity plane of the PN sample. In Section 5.7 we use the properties of the Planetary Nebulas luminosity function (PNLF) and a kinematic model for the PN population to predict its LOSVD in MSIS observations. The simulation allows us to interpret the observed LOSVD and also to determine the α parameter for the halo of NGC 3311. In Section 5.8 we correlate the velocity subcomponents in the PN LOSVD with kinematic substructures in the Hydra I galaxy distribution and discuss implications for galaxy evolution and disruption in the cluster core. Finally, Section 5.9 contains a summary and the conclusions of this work.

5.2 The Hydra I cluster of galaxies (Abell 1060)

The Hydra I cluster (Abell 1060) is an X-ray bright, non-cooling flow, medium compact cluster in the Southern hemisphere, whose central region is dominated by a pair of non-interacting giant elliptical galaxies, NGC 3311 and NGC 3309. NGC 3309 is a regular giant elliptical (E3) and NGC 3311 is a cD galaxy with an extended halo (Vasterberg et al., 1991).

X-ray properties of Hydra I - Except for two peaks associated with the bright elliptical galaxies NGC 3311 and NGC 3309, the X-ray emission from the hot intracluster medium (ICM) in the Hydra I (A 1060) cluster is smooth and lacks prominent spatial substructures. The center of the nearly circularly symmetric emission contours roughly coincides with the center of NGC 3311 (Tamura et al., 2000; Yamasaki et al., 2002; Hayakawa et al., 2004, 2006). A faint extended emission with angular scale $< 1'$ trailing NGC 3311 to the North-East, overlapping with an Fe excess, could be due to gas stripped from NGC 3311 if the galaxy moved towards the South-West with velocity $\geq 500\,\mathrm{km\,s^{-1}}$, according to Hayakawa et al. (2004, 2006). The total gas mass and iron mass contained in this region are $\sim 10^9\,\mathrm{M_\odot}$ and $2\times10^7\,\mathrm{M_\odot}$, respectively (Hayakawa et al., 2004, 2006). The emission components of NGC 3311 and NGC 3309 themselves are small, extending to only $\sim$ 10” $\simeq$ 2.5 kpc, suggesting that both galaxies lost most of their gas in earlier interactions with the ICM. In both galaxies, the X-ray gas is hotter than the equivalent temperature corresponding to the central stellar velocity dispersions, and in approximate pressure equilibrium with the ICM (Yamasaki et al., 2002).

On cluster scales the X-ray observations show that the hot ICM has a fairly uniform temperature distribution, ranging from about 3.4 KeV in the center to 2.2 KeV in the outer region, and constant metal abundances out to a radius of 230 kpc. Deviations from uniformity of the hot gas temperature and metallicity distribution in Hydra I are in the high metallicity region at $\sim$ 1.5 arcmin North-East of NGC 3311, and a region at a slightly higher temperature at 7 arcmin South-East of NGC 3311 (Tamura et al., 2000; Furusho et al., 2001; Yamasaki et al., 2002; Hayakawa et al., 2004, 2006; Sato et al., 2007). Based on the overall regular X-ray emission and temperature profile, the Hydra I cluster is considered as the prototype of an evolved and dynamically relaxed cluster, with the time elapsed since the last major subcluster merger being at least several Gyr. From the X-ray data the central distribution of dark matter in the cluster has been estimated, giving a central density slope of $\simeq -1.5$ and a mass within 100 kpc of $\simeq 10^{13}\,\mathrm{M_\odot}$ (Tamura et al., 2000; Hayakawa et al., 2004). Given these properties, the Hydra I cluster is an interesting target for studying the connection between the ICL and the extended halo of NGC 3311.

The cluster average velocity and velocity dispersion - From a deep spectroscopic sample of cluster galaxies extending to $\mathrm{M}_R \leq -14$, Christlein and Zabludoff (2003) derive the average cluster redshift (mean velocity) and velocity dispersion of Hydra I. We adopt their values here: $\bar{v}_{\mathrm{Hy}} = 3683 \pm 46\,\mathrm{km\,s^{-1}}$, and $\sigma_{\mathrm{Hy}} = 724 \pm 31\,\mathrm{km\,s^{-1}}$. The sample of measured galaxy spectra in Hydra I is extended to fainter magnitudes $\mathrm{M}_V > -17$ through the catalog of early-type dwarf galaxies published by Misgeld et al. (2008); their values for the average cluster velocity and velocity dispersion are

$\bar{v}_{\rm Hy} = 3982 \pm 148\,{\rm km\,s^{-1}}$ and $\sigma_{\rm Hy} = 784\,{\rm km\,s^{-1}}$, with the average cluster velocity at somewhat larger value with respect to the measurement by Christlein and Zabludoff (2003). Both catalogues cover a radial range of $\sim 300\,$kpc around NGC 3311. Close to NGC 3311, a predominance of velocities redshifted with respect to $\bar{v}_{\rm Hy}$ is seen, but in the radial range $\sim 50 - 300\,$kpc, the velocity distribution appears well-mixed with about constant velocity dispersion.

Distance estimates - The distance to the Hydra I cluster is not well constrained yet, as different techniques provide rather different estimates. The cosmological distance to Abell 1060 based on the cluster redshift is $51.2 \pm 5.7\,$Mpc assuming $H_0 = 72 \pm 8{\rm km^{-1}\,Mpc^{-1}}$ (Christlein and Zabludoff, 2003), while direct measurements using the surface brightness fluctuation (SBF) method for 16 galaxies give a distance of 41 Mpc (Mieske et al., 2005).

The relative distance of NGC 3311 and NGC 3309 along the line of sight is also controversial. Distance measurements based on the globular cluster luminosity function locate NGC 3311 about 10 Mpc in front of NGC 3309, which puts NGC 3309 at 61 Mpc (Hilker, 2003), while SBF measurements suggest the opposite, with NGC 3311 now at shorter distance of about 41 Mpc and NGC 3309 even closer at 36 Mpc, 5 Mpc in front of NGC 3311 (Mieske et al., 2005).

In this work we assume a distance for NGC 3311 and the Hydra I cluster of 51 Mpc, corresponding to a distance modulus of 33.54. Then 1” corresponds to 0.247 kpc. The systemic velocity for NGC 3311 and its central velocity dispersion are $v_{\rm N3311} = 3825\ (3800)\ \pm 8\,{\rm km\,s^{-1}}$ (heliocentric; without and in brackets with relativistic correction), and $\sigma_0 = 154 \pm 16\,{\rm km\,s^{-1}}$ (Ventimiglia et al., 2010b). The systemic velocity of NGC 3309 is $v_{\rm N3309} = 4099\,{\rm km\,s^{-1}}$ (Misgeld et al., 2008). The velocities of the other Hydra I galaxies are extracted from the catalogs of Misgeld et al. (2008) and Christlein and Zabludoff (2003).

5.3 Probing the ICL kinematics using Planetary Nebulas

5.3.1 Planetary Nebulas as kinematical probes and distance indicators

Planetary Nebulas (PNs) occur as a brief phase during the late evolution of solar-type stars. In stellar populations older than 2 Gyrs, about one star every few million is expected to be in the PN phase at any one time (Buzzoni et al., 2006). Stars in the PN phase can be detected via their bright emission in the optical [OIII]λ 5007 Å emission line, because the nebular shell re-emits $\sim$ 10% of the UV photons emitted by the stellar core in this single line (Ciardullo et al., 2005). When the [OIII] emission line is detected, the line-of-sight velocity of the PN can be easily measured.

The number density of PNs traces the luminosity density of the parent stellar population. According to single stellar population theory, the luminosity-specific stellar death rate is independent of the precise star formation history of the associated stellar population (Renzini and Buzzoni, 1986; Buzzoni et al., 2006). This property is captured in a simple relation such that

$$N_{PN} = \alpha L_{gal} \tag{5.1}$$

where N_{PN} is the number of all PNs in a stellar population, L_{gal} is the bolometric luminosity of that parent stellar population and α is the luminosity-specific PN number. The predictions from stellar evolution theory are further supported by empirical evidence that the PN number density profiles follow light in late- and early-type galaxies (Herrmann et al., 2008; Coccato et al., 2009), and that the luminosity-specific PN number α stays more or less constant, with (B-V) color. The empirical result that the rms scatter of α for a given colour is about a factor 2-3 remains to be explained, however (Buzzoni et al., 2006).

The planetary nebula luminosity function (PNLF) technique is one of the simplest methods for determining extragalactic distances. This is based on the observed shape of the PNLF. At faint magnitudes, the PNLF has the power-law form predicted from models of uniformly expanding shells surrounding slowly evolving central stars (Henize and Westerlund, 1963; Jacoby, 1980). However, observations and simulations have demonstrated that the bright end of the PNLF dramatically breaks from this relation and falls to zero very quickly, within ~ 0.7 mag (Ciardullo et al., 1998; Mendez and Soffner, 1997). It is the constancy of the cutoff magnitude, $M^* = -4.51$, and the high monochromatic luminosity of PNs, that makes the PNLF such a useful standard candle.

5.3.2 The Multi-Slit Imaging Spectroscopy technique

At the distance of the Hydra I cluster, the brightest PNs at the PNLF cutoff have an apparent m_{5007} magnitude equal to 29.0, corresponding to a flux in the [OIII]λ5007Å line of $\sim 8 \times 10^{-18}$ erg s^{-1}cm^{-2} according to the definition of m_{5007} by Jacoby (1989). To detect these faint emissions we need a technique that substantially reduces the noise from the night sky. This is possible by using a dedicated spectroscopic technique named “Multi-Slit Imaging Spectroscopy” (MSIS, Gerhard et al., 2005; Arnaboldi et al., 2007).

MSIS is a blind search technique that combines the use of a mask of parallel slits, a dispersing element, and a narrow band filter centered at the redshifted [OIII]λ5007Å emission line. With MSIS exposures, PNs and other emission objects in the filter’s wavelength range which happen to lie behind the slits are detected, and their velocities, positions, and magnitudes can be measured at the same time. The [OIII] emission line from a PN is $\sim 30\,\mathrm{km\,s^{-1}}$ wide (Arnaboldi et al., 2008), so if dispersed with a spectral resolution $R \sim 6000$, it falls on a small number of pixels, depending on the slit width and seeing.

In this work we use MSIS to locate a sample of PNs in the core of the Hydra I cluster and measure their velocities and magnitudes. Our aim is to infer the dynamical state of the diffuse light in the cluster core, as described below in Sections 5.7 and 5.8.

5.4 Observations

MSIS data for Hydra I were acquired during the nights of March 26-28, 2006, with FORS2 on UT1, in visitor mode. The FORS2 field-of-view (FoV) is $\sim 6.8 \times 6.8\,\mathrm{arcmin}^2$, corresponding to

$\sim$ 100 kpc $\times$ 100 kpc at the distance of the Hydra I cluster. The effective field area in which it was possible to position slits with the grism used here is 44.6 square arcmin. The FoV was centered on NGC 3311 at α = 10h36m42.8s, δ = −27d31m42s (J2000) in the core of the cluster. The FoV is imaged onto two 2×2 rebinned CCDs, with spatial resolution $0''.252$ per rebinned-pixel. The mask used has 24×21 slits, each $0''.8$ wide and $17''.5$ long. The area covered with the mask is about 7056 arcsec^2, corresponding to about 4.4 % of the effective FoV. To cover as much of the field as possible, the mask was stepped 15 times so as to fill the distance between two adjacent slits in the mask. The total surveyed area is therefore 29.4 arcmin^2, i.e., 66 % of the effective FoV. Three exposures of 800 sec were taken at each mask position to facilitate the removal of cosmic rays during the data reduction process.

The dispersing element was GRISM-600B with a spectral resolution of 0.75 Å pixel^{-1} (or 1.5 Å rebinned-pixel^{-1}) at 5075 Å. With the adopted slit width, the measured spectral resolution is 4.5 Å or 270 km s^{-1}. Two narrow band filters were used, centered at 5045 Å and 5095 Å, respectively, both with 60 Å FWHM. This ensures the full coverage of the Hydra I cluster LOS velocity range. Each illuminated slit in the mask produces a two-dimensional spectrum of 40 rebinned pixels in the spectral direction and 70 rebinned pixels in the spatial direction.

The seeing during the observing nights was in the range from $0''.6$ to $1''.5$. For the average seeing ($0''.9$) and with the spectral resolution of the set-up, monochromatic point-like sources appear in the final spectra as sources with a total width of $\sim$ 5 pixels in both the spatial and wavelength directions.

Biases and through-mask flat field images were also taken. Arc-lamp calibration frames with mask, grism and narrow band filter were acquired for the extraction of the 2D spectra, their wavelength calibration and distortion correction. Long slit data for the standard star LTT 7379 with narrow band filter and grism were acquired for flux calibration.

5.5 Data reduction and analysis

The data reduction is carried out in *IRAF* as described in Arnaboldi et al. (2007) and Ventimiglia et al. (2008). The frames are registered and co-added after bias subtraction. The continuum light from the bright galaxy halos is subtracted using a median filtering technique implemented in the *IRAF* task *.images.imfilter.median*, with a rectangular window of 19×35 pixels. Then emission line objects are identified, and 2D-spectra around the emission line positions are extracted, rectified, wavelength and flux calibrated, and background subtracted. Finally the wavelength of the redshifted [OIII]λ 5007Å emission line for all the identified sources is measured via a Gaussian fit. The heliocentric correction for the PN velocities is −5.44 km s^{-1}.

5.5.1 Identification of Emission-Line Objects

All emission line objects found are classified according to the following criteria as

- PN candidates: unresolved emission line objects, both in wavelength and in the spatial direction, with no continuum;
- background galaxy candidates: unresolved emission line objects with continuum, or resolved emission line objects both with and without continuum.

The total number of detected emission line sources in our data set is 82, of which 56 are classified as PN candidates and 26 as background galaxy candidates, of which 6 are classified as [OII] emitters and the remaining 20 as candidate Lyα galaxies [2].

For details on the background galaxy candidates see Ventimiglia and Arnaboldi (2010). Note that the background galaxy classification is independent of luminosity and that these objects have a broad equivalent width distribution. Therefore, the fact that the PN candidates (unresolved emission line objects without detectable continuum) have a luminosity function as expected for PNs observed with MSIS at a distance of $\sim$ 50 Mpc (see Section 5.7.1), implies that the large majority of these PN candidates must indeed be PNs. In addition, Fig. 1 of Ventimiglia and Arnaboldi (2010) shows that all of the background galaxy candidates but two fall in the blue filter in the velocity range between 1000 $\mathrm{km\,s^{-1}}$ and 2800 $\mathrm{km\,s^{-1}}$, blue-shifted with respect to the Hydra I cluster. Several of the *unresolved* background galaxies in this blue-shifted velocity range have a continuum level just above the detectability threshold, suggesting that the PN candidate sample may contain a few background galaxy contaminants in this velocity range whose continuum is too faint to detect.

The two background galaxies seen in the red filter are both extended and have medium bright emission fluxes; one has a very bright continuum, the other no detectable continuum. From this we conclude that the residual contamination of the PN candidate sample at velocities > 3000 $\mathrm{km\,s^{-1}}$ must be minimal. With this in mind, we will in the following simply refer to the PN candidates as PNs.

5.5.2 Photometry

Magnitudes of the PN candidates are computed using the m_{5007} definition by Jacoby (1989), $m_{5007} = -2.5 \log F_{5007} - 13.74$, where F_{5007} is the integrated flux in the line computed in circular apertures of radius $0''.65 - 0''.85$ in the 2D spectra, measured using the $IRAF$ task $.noao.digiphot.aphot.phot$. The 1σ limit on the continuum in these spectra is $7.2 \times 10^{-20} \mathrm{erg\,cm^{-2}s^{-1}\AA^{-1}}$.

Photometric errors and completeness function

The photometric errors are estimated using simulations on a sample of 2D wavelength, flux calibrated and background subtracted spectra. For each simulation 100 artificial PN sources are generated using the $IRAF$ task $.noao.artdata.mkobject$. The adopted PSF is a Gaussian with a dispersion obtained

---

[2] Note that the equivalent widths (EWs) of the PN candidates are mostly distributed between 30 Å $< EW <$ 100 Å, similar to the EWs of the background galaxy candidates, and cannot therefore be used to discriminate between both types of emission sources. This is because these distant PNs are faint and the continuum level in the MSIS images is given by the 1σ limit from the sky noise; see Section 5.2.

by fitting a 2D Gaussian to the profile of a detected PN candidate with adequate signal-to-noise. The σ value is 1.1 pixels, i.e., FWHM $\sim 0''.7$, and the FWHM in wavelength is $\sim 4\,\text{Å}$. The simulated PN samples have luminosity functions (LFs) given by a delta function at one of five different input magnitudes (29.3, 29.7, 30.1, 30.5 and 30.9 mag). The output magnitudes on the 2D spectra are measured with *.noao.digiphot.aphot.phot* using circular apertures, in the same way as for real PN candidates. In these experiments, no significant systematic shift in the magnitudes was found, and the standard deviation of the retrieved magnitude distribution is adopted as the measured error at the respective *output* magnitude.

On the basis of these simulations, we thus model the errors for the MSIS m_{5007} photometry, which increase approximately linearly towards fainter magnitudes, by

$$\epsilon \simeq 0.25(\mathrm{m}_{5007} - 28.5) \;\; [29.0, 30.4]. \tag{5.2}$$

We then evaluate a completeness correction function, using the fraction of objects retrieved at each magnitude as these become fainter. This fraction is nearly 100% at 29.0 mag, the apparent magnitude of the PNLF bright cutoff at 51 Mpc, and decreases linearly down to 10-20% at 30.4 mag, the detection limit magnitude of our observations. We model this dependence by

$$f_c \simeq \begin{cases} 1 & \text{if } \mathrm{m}_{5007} \leq 29.0, \\ 0.64(-\mathrm{m}_{5007} + 30.55) & \text{if } 29.0 < \mathrm{m}_{5007} \leq 30.4, \\ 0 & \text{if } \mathrm{m}_{5007} > 30.4. \end{cases} \tag{5.3}$$

The error distribution and the completeness function are used in Section 5.7 below to perform simulations of the LOSVD for the PN sample.

5.6 The PN sample in Hydra I

Our PN catalog for the central $(100\,\mathrm{kpc})^2$ of the Hydra I cluster contains 56 candidates, for which we measure v_{LOS}, x_{PN}, y_{PN} and m_{5007}. The detected PN velocities cover a range from $970\,\mathrm{km\,s^{-1}}$ to $6400\,\mathrm{km\,s^{-1}}$ with fluxes from $2.2\times10^{-18}\mathrm{erg\,cm^{-2}s^{-1}}$ to $7.6\times10^{-18}\mathrm{erg\,cm^{-2}s^{-1}}$. The detected sample of objects have a magnitude distribution compatible with the PNLF at the distance of Hydra I; see also Section 5.7.1.

The magnitude-velocity plane - The properties of the PN sample in the velocity-magnitude plane are shown in the left panel of Fig. 5.1[3]. In this plot, the apparent magnitude of the PNLF bright cutoff at the distance of the Hydra I cluster corresponds to a horizontal line at 29.0 mag. The blue and red lines are the filter transmission curves, as measured from the spectra, normalized so that the maximum transmission occurs near the PNLF bright cutoff. The PNs are indeed all fainter than $m_{5007} = 29.0$ and

---

[3] This plot is based on more accurate photometry than and updates Fig.1 of Ventimiglia et al. (2008).

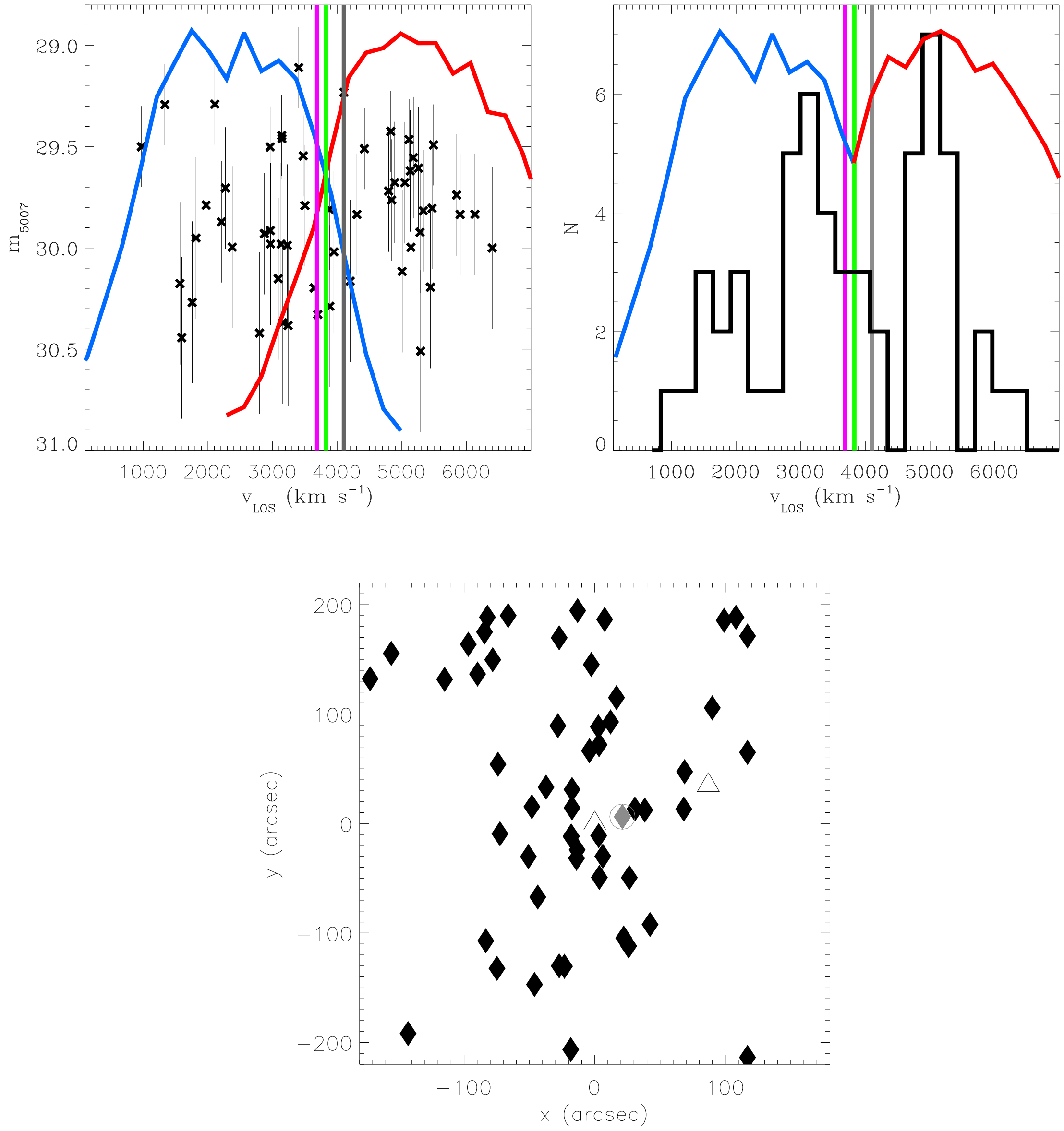

Figure 5.1: PNs in the Hydra I cluster core. *Left upper panel*: the PN velocity-magnitude distribution. The black crosses show the entire sample of 56 PN candidates. The blue and red lines are the measured transmission curves of the blue and the red filter, respectively, normalized so that the maximum transmission is near the theoretical bright cutoff of the PNLF at the distance of Hydra I. *Right upper panel*: the PN LOSVD (black histogram). The bins in velocity are 270 km s^{-1} wide. The blue and the red solid lines show again the suitably normalized transmission curves of the blue and red filters. The vertical magenta, green and gray lines in both panels mark the systemic velocity of Hydra I, NGC 3311 and NGC 3309, respectively. *Lower panel*: Spatial distribution of the PNs (black diamonds) in the MSIS field. The field is centered on NGC 3311 and has size ~ 100 × 100 kpc^2; North is up and East to the left. The two open triangles indicate the positions of NGC 3311 (center) and NGC 3309 (upper right). The PN indicated by the gray symbol is the only object compatible with a PN bound to NGC 3309, based on its position on the sky and LOS velocity, $v_{\rm grayPN}$ = 4422 km s^{-1}.

extend to the detection limit magnitude, $\mathrm{m_{dl}}$. This is slightly different for the two filters; the faintest PNs detected through the blue filter have $\mathrm{m_{B,dl}} = 30.45$, and those detected with the red filter have $\mathrm{m_{R,dl}} = 30.3$.

The PN LOSVD - The measured LOSVD of the PN sample is shown by the black histogram in the central panel of Fig. 5.1. The velocity window covered by the two filters is also shown and the systemic velocities of Hydra I, NGC 3311 and NGC 3309 (see Section 5.2) are indicated by the magenta, green and gray vertical lines, respectively. These velocities fall in the middle of the velocity window allowed by the filters, where both filters overlap. The mean velocity of all PN candidates is $\bar{\mathrm{v}}_{PNs} = 3840\,\mathrm{km\,s^{-1}}$ and the standard deviation is $\mathrm{rms}_{PNs} = 1390\,\mathrm{km\,s^{-1}}$. The distribution is highly non Gaussian and dominated by several individual components. The main peak appears in the range of velocities from 2400 to $4400\,\mathrm{km\,s^{-1}}$ and its maximum is at $\sim\, 3100\,\mathrm{km\,s^{-1}}$, within $1\sigma_{\mathrm{Hy}}$ of the systemic velocity of the Hydra I cluster. In the blue filter velocity range there is a secondary peak at $\sim 1800\,\mathrm{km\,s^{-1}}$ that falls $2-3\sigma_{\mathrm{Hy}}$ from the systemic velocity of Hydra I. This blue peak may contain a few background galaxy contaminants, as discussed in Section 5.5.1 above. Finally a red peak at $\sim\, 5000\,\mathrm{km\,s^{-1}}$ within $\sim\, 2\sigma_{\mathrm{Hy}}$ of the cluster mean velocity is detected in the velocity interval from 4600 to $5400\,\mathrm{km\,s^{-1}}$, and there are some PNs with even larger LOS velocities.

The spatial distribution of the PNs - The locations of the detected PNs on the sky are shown in the right panel of Fig. 5.1. Their spatial distribution can be characterized as follows:

- most PNs follow an elongated North-South distribution approximately centered on NGC 3311;
- there is no secondary high density concentration around NGC 3309. Only one PN, indicated by the gray symbol in the right plot of Fig. 5.1, has a combination of velocity and position that are compatible with a PN bound to the halo of NGC 3309;
- a possibly separate concentration of PNs is present in the North-East corner of the field.

We summarize our main results so far:

1. The PN candidates detected in the MSIS field have luminosities consistent with a population of PNs at the distance of the Hydra I cluster.
2. The distribution of PNs in the MSIS field is centered on NGC 3311. Only one candidate is consistent with being bound to NGC 3309, even though NGC 3309 is of comparable luminosity to NGC 3311 and, on account of the X-ray results (see Section 5.2), is likely located in the inner parts of the cluster within the dense ICL, at similar distance from us as NGC 3311.
3. There is no evidence for a single, well-mixed distribution of PNs in the central 100 kpc of the Hydra I cluster, contrary to what one would expect from the dynamically relaxed appearance of the X-ray emission. Instead, the observed PNs separate into three major velocity components.

5.7 Kinematic substructures and α parameter for the observed PN sample in Hydra I: comparison with a simulated MSIS model

At this point, we would like to reinforce the last point by comparing the observed velocity distribution with a simple model. The model is obtained by assuming a phase-mixed PN population placed at the distance (51 Mpc) and mean recession velocity of NGC 3311, and simulating its line-of-sight velocity distribution by convolving with the MSIS instrumental set up. The velocity dispersion of the PN population is taken to be 464 km s^{-1}, the hightest value measured from the long-slit data in Ventimiglia et al. (2010b). In this way we can test more quantitatively whether the observed multi-peaked LOSVD for PNs in our field is biassed by the MSIS observational set-up, or whether it provides evidence for un-mixed components in the Hydra I cluster core.

5.7.1 Predicting the luminosity function and LOSVD with MSIS for a model PN population

We first characterize the model in terms of the intrinsic luminosity function and LOSVD of the PN population. Then we describe the steps required to predict the corresponding m_{5007} magnitude vs. LOS velocity diagram and LOSVD that would be measured with the MSIS set up. In the next subsection we compare the results obtained with the observed Hydra I PN sample.

Model for the intrinsic PN population - The intrinsic PN luminosity function can be approximated by the analytical function given by Ciardullo et al. (1989):

$$N(m) = C\, e^{0.307\, m} \left[1 - e^{3(m^{*}-m)}\right] \tag{5.4}$$

where m is the observed magnitude, $m^{*} = 29.0$ is the apparent magnitude of the bright cutoff at the adopted distance of NGC 3311, and C is a multiplicative factor. The integral of $N(m)$ from m^{*} to $m^{*} + 8$ gives the total number of PN associated with the bolometric luminosity of the parent stellar population (N_{PN} in Eq. 5.1), and the C parameter can be related to the luminosity-specific PN number α (Buzzoni et al., 2006). For our model we distribute the magnitudes of a PN population according to a very similar formula fitted by Méndez to the results of Mendez and Soffner (1997).

Next we assume that this PN population is dynamically phase-mixed and that its intrinsic LOSVD is given by a Gaussian centered on the systemic velocity of NGC 3311, $\overline{\mathrm{v}}$,

$$\mathrm{G(v)} = \frac{1}{\sigma_{\mathrm{core}}\sqrt{2\pi}} \exp\left[\frac{(\mathrm{v} - \overline{\mathrm{v}})^{2}}{2\sigma^{2}_{\mathrm{core}}}\right] \tag{5.5}$$

where here we adopt $\overline{\mathrm{v}} = 3830$ km s^{-1} (Ventimiglia et al., 2010b, corrected to the filter frame), and for the velocity dispersion we take $\sigma_{\mathrm{core}} = 464$ km s^{-1}, the hightest value measured from the long-slit data in this paper. This approximates the velocity dispersion for the intracluster component in the outer halo of NGC 3311, at central distances $\sim 20 - 30$ kpc (Ventimiglia et al., 2010b). We will consider the magnitude-velocity diagram and the LOSVD as histograms in velocity; then in each velocity bin $\Delta\mathrm{v}_i$, the number of PNs is

$$LF(\mathrm{v}_i) \simeq N(m)\, G(\mathrm{v}_i)\, \Delta\mathrm{v}_i \tag{5.6}$$

where G(v) is normalized so that $\sum_i \mathrm{G}(\mathrm{v}_i)\,\Delta\mathrm{v}_i = 1$.

Simulating the MSIS observations - The magnitude-velocity diagram for such a model population is modified by a number of effects in the MSIS observations, which we simulate as described below. The MSIS simulation procedure implements the following steps:

- the through-slit convolution of the PNLF;
- the convolution with the filter transmission;
- the photometric error convolution;
- the completeness correction;
- the computation of the LOSVD.

The through-slit PNLF - The MSIS technique is a blind survey technique. Therefore the positions of the slits on the sky are not centered on the detected objects, and the further away an object is from the center of its slit, the fainter it becomes. This effect is a function of both seeing and slit width, and it modifies the functional form of the PNLF, which needs to be accounted for when using the LF from MSIS PN detected samples.

In principle, some PNs may be detected in two adjacent slits of the mask, and this would need to be corrected for. However, at the depth of the present Hydra I survey this effect is not important for the predicted PNLF, and indeed no such object has been found in the sample.

Given a “true” PNLF LF(m), the “*through slit PNLF*” sLF(m) can easily be computed, and depends on slit width and seeing; for further details see Gerhard et al. (2010, in preparation). The effect of the through-slit correction is to shift the sLF(m) faintwards in the observable bright part, compared to the ”true” PNLF.

Convolution with filter transmission - When the filter transmission T(v_i) is less then 1 (100%), it shifts the through-slit PNLF to fainter magnitudes. The Δm depends on the value of the filter transmission curve at the wavelength λ or equivalent binned velocity v_i, and is equal to $\Delta m(\mathrm{v}_i) = -2.5 \log \mathrm{T}(\mathrm{v}_i)$. The resulting *instrumental PNLF*, the distribution of source magnitudes before detection, becomes velocity dependent, i.e., iLF(m, v_i).

For the present MSIS Hydra I observations, the combined filter transmission curve from both filters is defined as

$$\mathrm{T}(\mathrm{v})_i = \max[\mathrm{T_B}(\mathrm{v}_i), \mathrm{T_R}(\mathrm{v}_i)], \tag{5.7}$$

where B and R denote the blue and red filters. It is 1 where the transmission is 100%, approximately from $\sim 1500\,\mathrm{km\,s^{-1}}$ to $\sim 3300\,\mathrm{km\,s^{-1}}$ and from $\sim 4200\,\mathrm{km\,s^{-1}}$ to $\sim 6300\,\mathrm{km\,s^{-1}}$; it is < 1 in the filter gap around $\sim 3800\,\mathrm{km\,s^{-1}}$ and at the low and high velocity ends of the observed range.

Photometric error convolution - Once the instrumental LF iLF(m, v_i) is computed, it must be convolved with the photometric errors which, for the case of the Hydra I observations, are given by the linear function in Eq. 5.2. Because of the photometric errors, PNs that are intrinsically fainter than the detection limit (here mag $\sim$ 30.4) may be detected if they happen to fall on a positive noise peak on the CCD image, and PNs that are intrinsically brighter than mag $\sim$ 30.4 may be lost from the sample. Generally, because the through-slit PNLF sLF(m) increases towards fainter magnitudes, the photometric errors scatter more faint objects to brighter magnitudes than vice-versa; so the effect of the convolution is to shift the PNLF to brighter magnitudes again.

Completeness correction - The completeness correction at a given observed magnitude is a multiplicative function which accounts for the decreasing fraction of PNs at fainter magnitudes detected against the noise on the MSIS image. For the case at hand it is given in Eq. 5.3. After the last two steps, we arrive at the final “MSIS PNLF”, MSLF(m) for short.

Computation of the simulated LOSVD - For each velocity bin the MSLF(m, v_i) is integrated between the apparent magnitude of the PNLF bright cut off ($m^* = 29.0$ for Hydra I) and the detection limit magnitude in the relevant filter, $m_{\mathrm{f,dl}}$ (see Section 5.6), to obtain the “observed” cumulative number of PNs in each velocity bin:

$$N_{\mathrm{MSIS}}(\mathrm{v}_i) = \int_{m^*}^{m_{\mathrm{f,dl}}} \mathrm{MSLF}(m, \mathrm{v}_i) dm. \tag{5.8}$$

The most cumbersome step in this procedure is the correction for the filter transmission, because it makes the final MSLF(m, v_i) velocity-dependent. It must correctly be applied *before* the convolution with the photometric errors, because the latter depend on the flux measured at certain positions on the CCD. So the errors on the through-slit magnitudes depend on the filter transmission values of the PNs.

However, we have found that the observed MSLF for the Hydra I PN sample, when obtained from wavelength regions where the filter transmission is $\sim$ 100%, is very similar to the one obtained by summing over the entire filter bandpass. The effect of the velocity dependence on the overall MSLF must therefore be small, and for the comparison of simulated and measured LOSVDs below we have therefore applied the filter transmission only after the error convolution and completeness correction.

Before we discuss the LOSVD obtained from the complete model, we show in Fig. 5.2 the predicted cumulative luminosity function resulting from error convolution, completeness correction, and filter transmission correction of the through-slit luminosity function, weighting by the number of observed PNs in each velocity bin. Also shown in Fig. 5.2 is the cumulative histogram of the m_{5007} magnitudes for the 56 observed PNs in the MSIS field. With a cutoff magnitude of 29.0 the model fits the observed histogram fairly well; however, this is not a formal best fit to the distance. The important point shown by Fig. 5.2 is that the observed MSIS luminosity function of the PN emission sources in the Hydra cluster core is evidently consistent with a population of PNs at $\sim$ 50 Mpc distance.

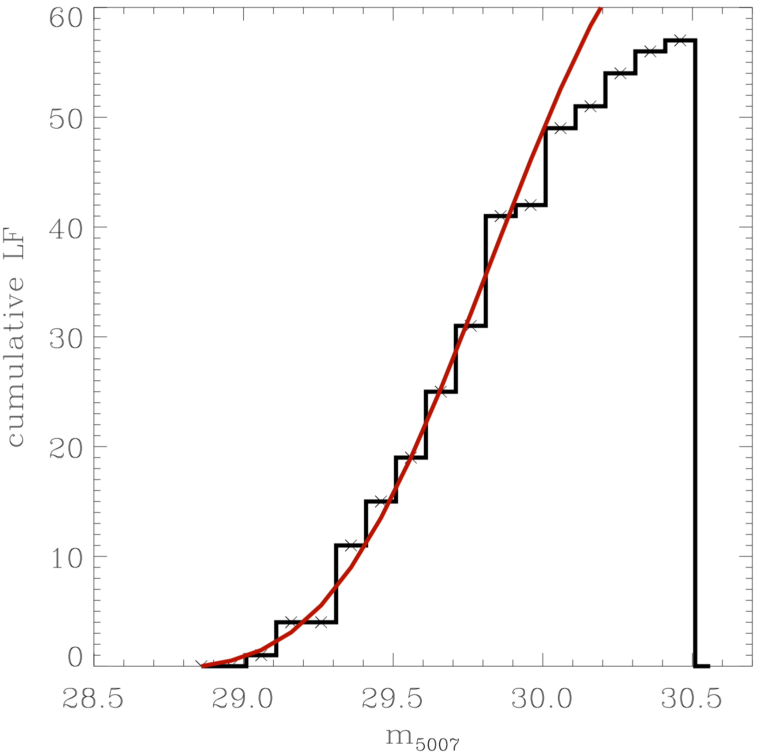

Figure 5.2: Cumulative luminosity function predicted for the present MSIS observations and the nominal cutoff magnitude of the Hydra I cluster, 29.0 (full red line, see text), compared with the cumulative histogram of the observed m_{5007} magnitudes.

5.7.2 Reality of observed kinematic substructures

The simulated MSIS LOSVD given by $N_{\mathrm{MSIS}}(\mathrm{v}_i)$ for the simple Gaussian velocity distribution model and luminosity function of Eq. 5.4 is shown as the green histogram in Fig. 5.3, with the observed PN LOSVD overplotted in black. The simulated MSIS LOSVD is scaled to approximately match the observed Hydra I sample in the central velocity bins.

The comparison between the simulated LOSVD and the Hydra I PN LOSVD in Fig. 5.3 identifies the central peak at about 3100 km s^{-1} in the observed PN LOSVD with that of the PN population associated with the stellar halo around NGC 3311 in the cluster core, with $\sigma_{\mathrm{core}} \sim 500\,\mathrm{km\,s^{-1}}$. The mean $\bar{\mathrm{v}}_{\mathrm{core}}$ and σ_{core} of this component are approximately consistent with those of the intracluster light halo of NGC 3311 derived from the long-slit kinematic analysis in Ventimiglia et al. (2010b). However, the asymmetry and offset of the peak of the observed histogram (by several 100 km s^{-1}) relative to the MSIS convolved model centered at the systemic velocity of NGC 3311 appear significant ($\sigma_{\mathrm{core}}/\sqrt{N_{\mathrm{core}}} \simeq 100\,\mathrm{km\,s^{-1}}$), arguing for some real asymmetry of the central velocity component. We shall refer to the central peak in the Hydra I PN LOSVD in Fig. 5.3 as the central ICL component.

Two additional velocity peaks are seen in the LOSVD in Fig. 5.3, one near 1800 km s^{-1} and one

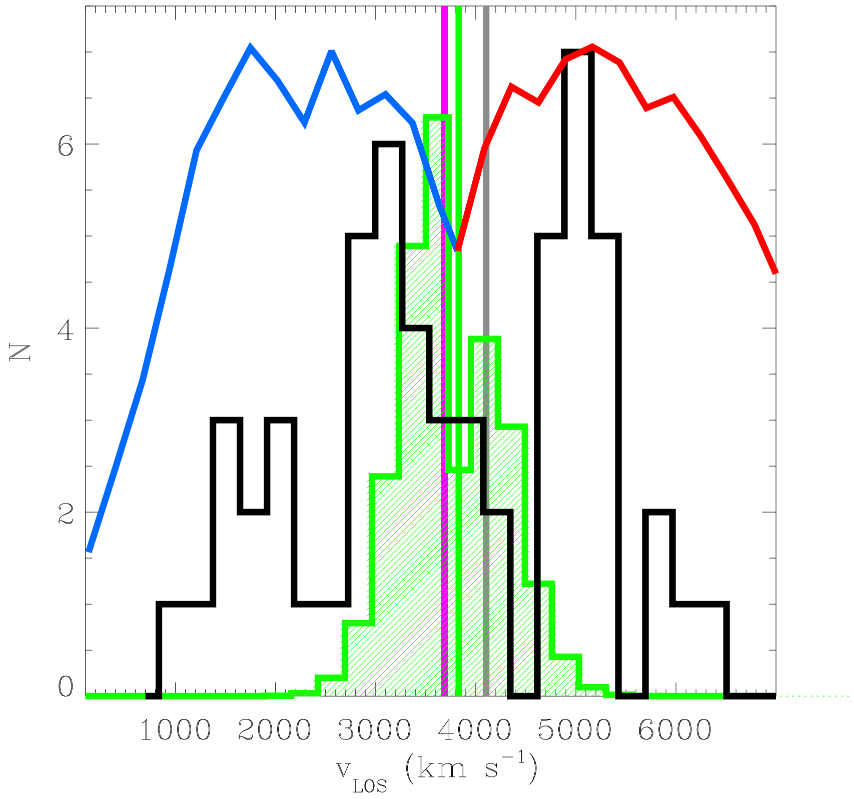

Figure 5.3: LOSVD for the Hydra I PN sample from Fig. 5.1 (black histogram), compared with a simulated MSIS LOSVD (green histogram) for a Gaussian velocity distribution with $\sigma_{\rm core} = 464\,{\rm km\,s^{-1}}$; see text for further details. The blue-red solid line shows the combined filter transmission curve as given in Eq. 5.7. The vertical magenta, green and gray lines mark the systemic velocity of Hydra I, NGC 3311 and NGC 3309, respectively.

at $\sim$ 5000 km s^{-1}, which do not have any correspondence with the velocity distribution derived for the simulated MSIS model. These velocity components cannot be explained as artifacts of the MSIS set up, in particular, the filter gap in the B+R filter combination. We will refer to these two velocity components as secondary blue and red peaks, respectively. They reveal the possible presence of two kinematical substructures in the core of Abell 1060, whose origins must be investigated further; see Section 5.8.

5.7.3 Low α-parameter in the core of Hydra I

We now compare the number of observed PNs with the expectations from the luminosity distribution and kinematics in and around NGC 3311. One issue is the absence of a clear subcomponent of PNs with velocity dispersion $\sim$ 150 – 250 km s^{-1}, as would be expected from the central $\sim$ 25” of NGC 3311 (Ventimiglia et al., 2010b). It is known that PN samples in elliptical galaxies are generally not complete in the central regions because of the increasing surface brightness profile; PNs are hard to detect against the image noise in the bright centers. E.g., in observations with the Planetary Nebula Spectrograph, the threshold surface brightness is typically in the range $\mu_V = 20 - 22\,\mathrm{mag\,/\,arcsec^2}$ (Coccato et al., 2009). In the current Hydra I data, the PN sample is severely incomplete at $\mu_V = 21.0\,\mathrm{mag\,/\,arcsec^2}$ (only two PNs are seen at $\mu_V \sim 21.0\,\mathrm{mag\,/\,arcsec^2}$, and six at $\mu_V \geq 21.5\,\mathrm{mag\,/\,arcsec^2}$). Referring to Fig. 13 of Méndez et al. (2001), we estimate that the current sample is not complete for $\mu_V \leq 22.0\,\mathrm{mag\,/\,arcsec^2}$, which is reached at a distance of $\simeq$ 30" from the center of NGC 3311 (Arnaboldi et al. 2010, in prep.). At this radius, the projected velocity dispersion has risen to $\sigma_{N3311}(30") \simeq 300 - 400\,\mathrm{km\,s^{-1}}$ (Ventimiglia et al., 2010b). Thus the PNs detected in this paper almost exclusively sample the hot (intracluster) halo of NGC 3311. The cold inner galaxy component is not sampled.

The second issue is the observed total number of PNs, given the detection limit, the instrumental set up and the light in NGC 3311 and NGC 3309. Integrating the simulated MSIS luminosity function down to the detection limit of 30.4 mag, we obtain an effective α parameter for our observations of $\alpha_{\mathrm{MSIS,Hy}} = 0.012\alpha_{\mathrm{tot}}$, where α_{tot} quantifies the total number of PNs 8 mag down the PNLF[4]. This value is similar to $\alpha_{0.5}$, the integrated value 0.5 mag down the PNLF. It is consistent with Fig. 5.1, even though in this figure PNs are seen up to 1.5 mag fainter than the nominal cutoff magnitude, because of (i) the shift towards fainter magnitudes due to the slit losses, and (ii) the completeness correction (Eq. 5.3).

We can estimate the bolometric α_{tot} for NGC 3311 from its (FUV-V) colour, the relation between (FUV-V) and $\log\alpha_{1.0}$ shown in Fig. 12 of Coccato et al. (2009), and correcting to $\log\alpha_{tot}$ by using Fig. 8 of Buzzoni et al. (2006). The (FUV-V) colour is determined from the Galex FUV magnitude and the V band magnitude from RC3, both corrected for extinction, as described in Coccato et al. (2009). The resulting value, (FUV-V)=6.7, corresponds to $\log\alpha_{1.0} = 1.1$ and $\log\alpha_{tot} = -7.34$. This is very similar to the value of $\log\alpha_{tot} = -7.30$ found for the Fornax cluster cD galaxy NGC 1399 (Buzzoni et al., 2006). Using the V band light profile of NGC 3311 measured in Arnaboldi et al. (2011, in preparation), and a bolometric correction of 0.85 mag, we can then predict the expected cumulative number of PNs within radius R from the center of NGC 3311. This is shown as the red curve in Figure 5.4, after subtracting the luminosity within 20" which is not sampled by our MSIS observations. Also shown are the cumulative histograms of the observed number of PNs in the MSIS data, both for all PNs in the field, and for PNs with velocities in the central velocity component only.

Fig. 5.4 shows that the total number of PNs detected in the field falls short of the number predicted from the luminosity profile by a factor $\sim$ 4. Outside $\sim$ 100", the number of PNs with velocities consistent with the central ICL halo of NGC 3311 is a factor $\sim$ 2 lower than the number of all PNs. Clearly therefore, some of the light at these radii is in a component different from the phase-mixed central ICL halo, but the amount is uncertain because we do not know whether the luminosity-specific α-parameter of this component is similarly low as for the NGC 3311 ICL halo. For example, agreement between observed and predicted PN numbers could be achieved by scaling only the NGC 3311 halo component by a factor $\sim$ 6. On the other hand, scaling only an outer

---

[4] This value includes the light between adjacent slits for the normalisation.

component will not work, because the discrepancy in Fig. 5.4 is already seen at small radii. Thus we can conclude that the α-parameter of the NGC 3311 ICL halo is low by a factor 4–6.

Such an anomalous specific PN number density requires an explanation. One possibility is that the stellar population in the halo of NGC 3311 is unusually PN poor; this will need studying the stellar population in the galaxy outskirts. A second possibility is that the ram pressure against the hot X-ray emitting gas in the halo of NGC 3311 is sufficiently large to severely shorten the life-time of the PNs (Dopita et al., 2000; Villaver and Stanghellini, 2005). In their simulations, Villaver and Stanghellini (2005) consider a gaseous medium of density $n = 10^{-4}\,\mathrm{cm}^{-3}$ and a relative velocity of $1000\,\mathrm{km\,s}^{-1}$. They find that the inner PN shell is not significantly affected by the ram pressure stripping during the PN life-time, and because the inner shell dominates the line emission in their model, the PN visibility life-time is therefore not shortened relative to an undisturbed PN. However, with a density of the ICM inside $5'$ around NGC 3311 of $\sim 6{\times}10^{-3}\,\mathrm{cm}^{-3}$, and a typical velocity of $\sqrt{3}{\times}450\,\mathrm{km\,s}^{-1} \simeq 800\,\mathrm{km\,s}^{-1}$ the ram pressure on the NGC 3311 is $\sim$ 40 times larger than in their simulated case, so the ram pressure effects could be much stronger. Unfortunately, simulations of the evolution of PNs in such dense media are not yet available, to our knowledge.

If this explanation is correct, PNs should be most efficiently ram pressure stripped in the innermost, densest regions of the ICM. Hence in this case we would expect most of the observed PNs to be located in the outermost halo of NGC 3311, even those projected onto the inner parts of our MSIS field. At these outer radii, dynamical time-scales are longer, and phase-mixing should be less complete. This would fit well with the unmixed kinematics and spatial distribution of the observed sample (see also next Section).

The third issue is that we do not see a concentration of PNs around NGC 3309. As shown in Section 5.6, only one PN in the sample, shown by the gray symbol in the right panel of Fig. 5.1, has both position and LOS velocity compatible with being bound to NGC 3309. Whereas using the relative total luminosities of NGC 3309 and NGC 3311 to scale the number of PNs associated with the main LOS velocity component for NGC 3311 in Fig. 5.3 (i.e., 27 PNs), we would expect about 11 PNs associated with the light of NGC 3309 if both galaxies were at the same distance. There are two possible explanations for this fact. One is that NGC 3309 is at significantly larger distance than NGC 3311, such that even PNs at the bright cutoff would be difficult to see. However, a simple calculation shows that then NGC 3309 would be put at $\sim$ 70 Mpc well outside the cluster, at variance with X-ray observations finding that its gas athmosphere is confined by the ICM pressure (see Section 5.2). The second possibility is that, similarly as for NGC 3311, also the PNs in NGC 3309 may be severely ram pressure stripped by the galaxy's motion through the dense ICM in the cluster core. This would require that NGC 3309 moves rapidly through the cluster core, and is physically rather close to NGC 3311. Again simulations would be needed to check this quantitatively.

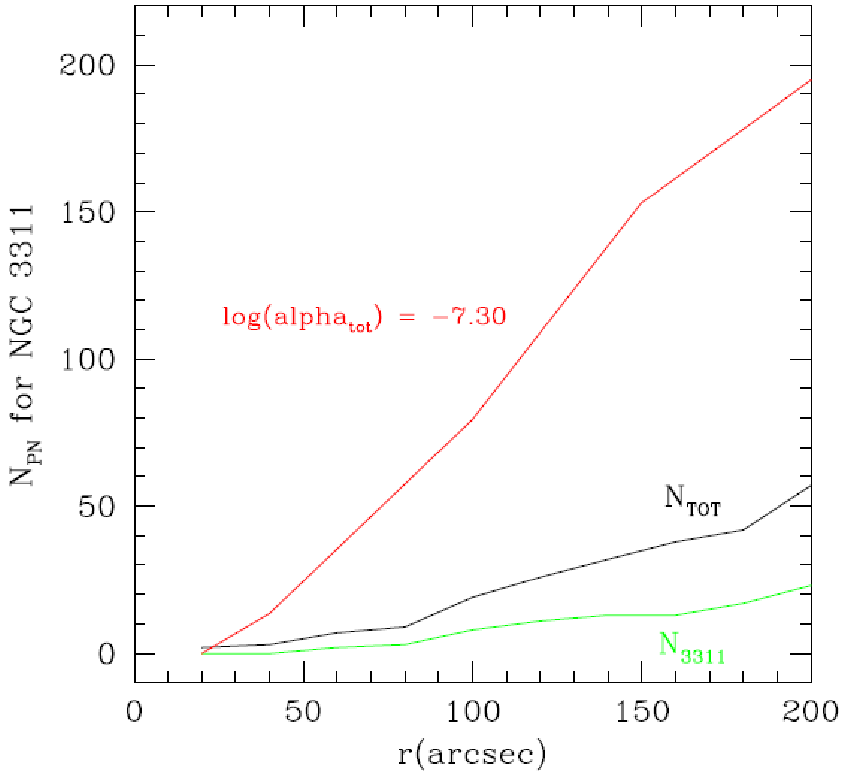

Figure 5.4: Observed and predicted cumulative PN numbers, as a function of radial distance from the center of NGC 3311. The green line shows the cumulative number of PNs associated with the central ICL halo of NGC 3311, based on their velocities. The black line shows the cumulative number of all PNs, without velocity selection. The red curve shows the predicted cumulative number of PNs computed using the luminosity-specific parameter α estimated in the text, the MSIS observational set-up, and the integrated bolometric luminosity in increasing circular apertures centred on NGC 3311.

5.8 The substructures in the Hydra I cluster core

We now turn to a more general discussion of the spatial distribution and kinematics of PNs and galaxies in the central region of the cluster. ICL is believed to originate from galaxies, so it is interesting to ask whether the phase-space substructures seen in the distribution of the PNs that trace the ICL has some correpondence to similar structures in the distribution of cluster galaxies. Thus we want to investigate the spatial distributions of the PNs associated with the velocity subcomponents in the PN LOSVD discussed earlier, and compare them with the spatial distribution of Hydra I galaxies in similar velocity intervals. In this way, we may obtain a better understanding of the dynamical evolution of the galaxies in the cluster core, and of the relevance of cluster substructures for the origin of the diffuse cluster light.

5.8.1 Spatial distributions of the PN velocity components

We first consider the spatial distribution of the PNs associated with the different velocity components in the PN LOSVD. This is shown in the three panels of Fig. 5.5, divided according to the classification in Sect. 5.7.2. Each panel covers a region of $6.8 \times 6.8\,\mathrm{arcmin}^2 \simeq 100 \times 100\,\mathrm{kpc}^2$ centered on NGC 3311.

PNs associated with the central ICL component (middle panel of Fig. 5.5) can be divided into two spatial structures. There is a prominent PN group concentrated, as expected, around NGC 3311, and an elongated East-West distribution in the Northern part of the FoV. By contrast, we see a low PN density region in the Southern part of the MSIS field.

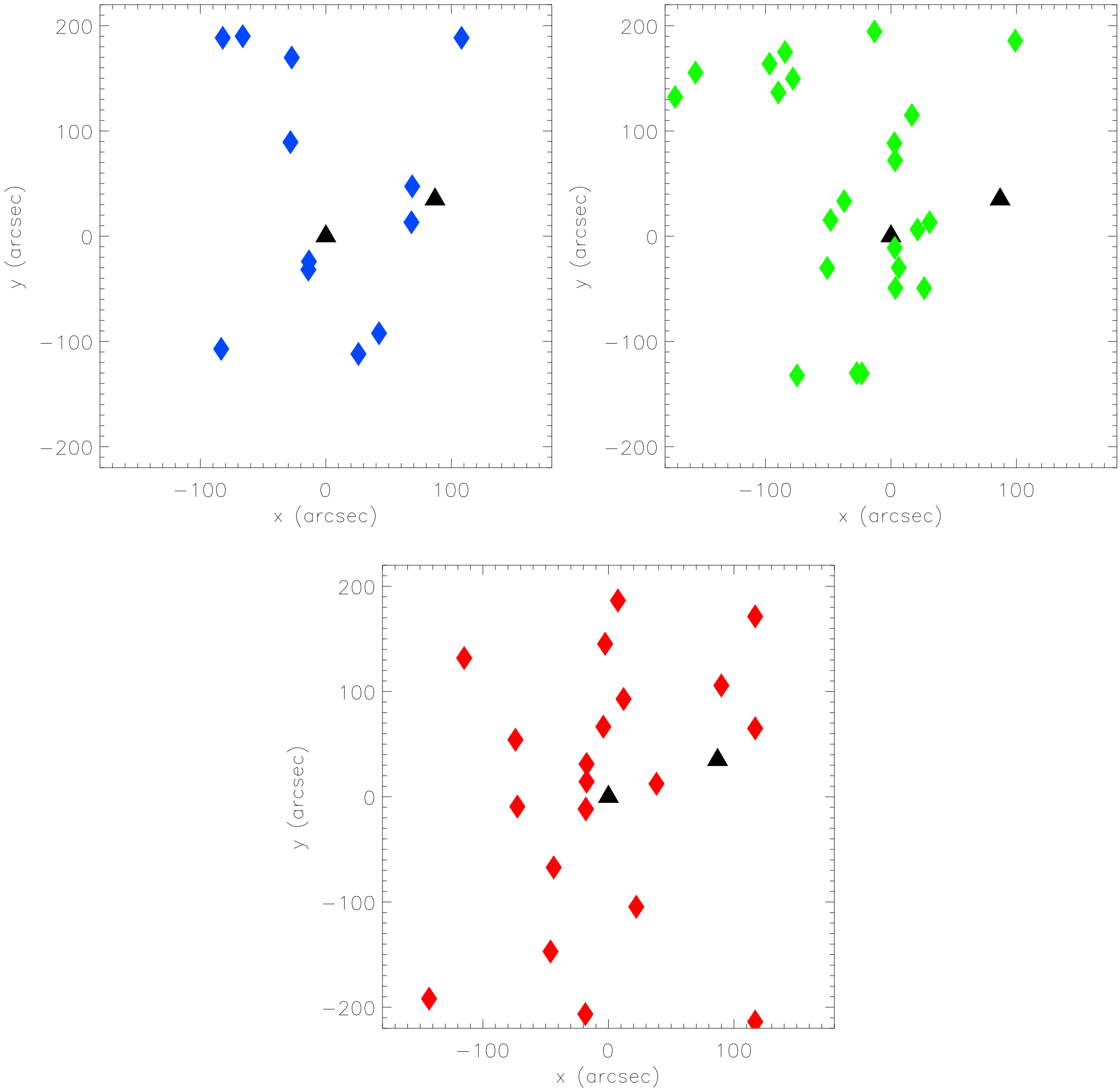

Figure 5.5: *Left upper panel*: Spatial distribution of the PNs associated with the blue secondary peak in the PN LOSVD ($< 2800\,\mathrm{km\,s^{-1}}$). *Right upper panel*: Spatial distribution of the PNs associated with the central ICL component ($2800\,\mathrm{km\,s^{-1}}$ to $4450\,\mathrm{km\,s^{-1}}$). *Lower panel*: Spatial distribution of the PNs associated with the secondary red peak at $> 4450\,\mathrm{km\,s^{-1}}$ in the PN LOSVD. The black triangles indicate NGC 3311 (center) and NGC 3309 (North-West of center), respectively. North is up and East is to the left.

Such a North/South asymmetry is seen also in the spatial distribution of the galaxies. Fig. 5.7 displays a larger area, $20 \times 20\,\mathrm{arcmin}^2$, which includes the MSIS field studied in this work, as indicated by the orange square. We can see from the two panels (foto, and schematic) that NGC 3311 and NGC 3309 dominate the center of the MSIS field, that there is a high density of bright galaxies in the Northern part of the field, but a deficit of galaxies to the South of NGC 3311.

The spatial distribution of the PNs associated with the secondary red peak in the PN LOSVD is shown in the right panel of Fig. 5.5. It has a North/South elongation, apparently extending further towards the South of NGC 3311 than the central ICL component, with a high density region North/East of NGC 3311.

Finally, the spatial distribution of the PNs associated with the secondary blue component at $1800\,\mathrm{km\,s^{-1}}$ (left panel of Fig. 5.5) also appears elongated along the North/South direction, but the smaller number of objects in this subsample makes inferring their spatial structure more difficult.

In summary, there is little evidence for a spherically symmetric well-mixed distribution of PNs in the outer halo of NGC 3311 in the cluster core. Several velocity components are seen, and even the central ICL component centered on NGC 3311 shows signs of spatial substructures.

5.8.2 Spatial and velocity distribution of Hydra I galaxies: comparison with the PNs sample

The spatial distribution of the galaxies from Christlein and Zabludoff (2003); Misgeld et al. (2008) in the central $20 \times 20\,\mathrm{arcmin}^2$ centered on NGC 3311 is shown in Fig. 5.7. We would like to analyze their phase-space distribution by dividing into the same velocity components as identified in the PN LOSVD. Therefore, in the image on the left the bright galaxies are encircled with the colours of the PN components in Fig. 5.5, and in the right panel all galaxies in the field are shown schematically as squares and crosses with the same color code for these velocity bins. NGC 3311 and NGC 3309 are marked in the center of the MSIS field (orange square).

In Fig. 5.6, the left panel shows the velocity distribution of all the galaxies in the $20 \times 20\,\mathrm{arcmin}^2$ region centered on NGC 3311. In the right panel, the velocity histograms for the bright galaxies ($m_R < 15.37$, violet color) and dwarf galaxies ($m_R > 15.37$, green color) are shown separately.

The LOSVD for the Hydra I galaxies covers the same velocities as for the PN sample. If we select only galaxies in the range of velocities of the PNe in the central ICL component, from $2800\,\mathrm{km\,s^{-1}}$ to $4450\,\mathrm{km\,s^{-1}}$, their LOSVD is consistent with a Gaussian distribution centered at a velocity of $3723\pm100\,\mathrm{km\,s^{-1}}$ with a dispersion of $542\pm80\,\mathrm{km\,s^{-1}}$. This confirms results from long-slit kinematics in the outer halo of NGC 3311 (Ventimiglia et al., 2010b), where the velocity dispersion was found to increase to $\sim 465\,\mathrm{km\,s^{-1}}$ at $\sim 70''$ radius, 64% of the velocity dispersion of all cluster galaxies.

This subsample of galaxies also has an interesting spatial distribution: the central $6.8\times6.8\,\mathrm{arcmin}^2$ region of the cluster (the MSIS field), while dominated by NGC 3311 and NGC 3309, contains no other Hydra I galaxies with these velocities. Whereas outside this region, they appear uniformly distributed over the field (see the green squares and crosses in the right panel of Fig. 5.7). NGC 3311 is at the center of the distribution of these galaxies both in space and in velocity. The distribution of these galaxies, as well as the similarity of their velocity dispersion with that measured in the halo of NGC 3311, supports the interpretation of Ventimiglia et al. (2010b) that the halo of NGC 3311 is dominated by intracluster stars that have been torn from galaxies disrupted in the cluster core: galaxies that passed through the central 100 kpc of the cluster core at modest velocities have all been disrupted.

By contrast, the galaxies with LOS velocities $> 4450\,\mathrm{km\,s^{-1}}$ as in the secondary red peak of the PN LOSVD are mostly located *within* the central 100×100 kpc^2 region of the cluster (red squares and crosses in the right panel of Fig. 5.7). In this subsample, there are 14 galaxies in total, 5 are classified as bright galaxies and 9 are dwarfs, and 3 bright galaxies and 6 dwarfs fall within the MSIS FORS2 field. These 6 dwarfs are concentrated in the North-Eastern part of the halo of NGC 3311, in the same region occupied by many PNs associated with the secondary red peak.

Finally, in this region there are only a few galaxies with a LOS velocity lower than $2800\,\mathrm{km\,s^{-1}}$, compatible with the secondary blue peak in the PNs. They are 8 in total (blue squares and crosses in the right panel of Fig. 5.7). Only one of these falls on the boundary of the central $100{\times}100\,\mathrm{kpc}^2$ region around NGC 3311. One of these galaxies is the giant spiral NGC 3312, South-East of NGC 3311. The others, including the spiral galaxy NGC 3314, are located at larger distances from NGC 3311.

5.8.3 Galaxy evolution and presence of substructures in the core of the Hydra I cluster

The distribution of galaxy properties in clusters holds important information on galaxy evolution and the growth of galaxy clusters. In Sect. 5.8.2, we have discovered an apparent lack of galaxies in the central $100 \times 100\,\mathrm{kpc}^2$ region of the cluster core with velocities in the same range as covered by the cD halo. A similar result has been found in the NGC 5044 group (Mendel et al., 2009). A possible explanation is the tidal disruption of galaxies at small cluster-centric radii. Galaxies with LOS velocities in the range of the central ICL component of the Hydra I cluster are no longer seen in the central region of the cluster, because they were all disrupted in the past during close encounters with the luminous galaxy and the dark matter distribution at the cluster center (Faltenbacher and Mathews, 2005). Their former stars now contributes to the diffuse stellar component in the Hydra I core.

Differently from the NGC 5044 group, however, we have found a number of dwarf galaxies *with high velocities* in the Hydra I core, with small cluster-centric radii (< 100 kpc). These dwarfs have LOS velocities larger than $4400\,\mathrm{km\,s^{-1}}$ and seem to form a well defined substructure both in velocity and spatial distribution. We speculate that these galaxies are falling through the cluster core and are not yet disrupted by the tidal interaction with NGC 3311. The PNLF of the subsample of PNs associated spatially and in velocity with this substructure places it almost at the same distance as the central ICL component of the cluster: this group of galaxies may indeed now be on the point of close encounter with NGC 3311 in the cluster center.

Finally, we have found a correlation between the PNs contributing to the secondary blue peak of PN LOSVD, and 8 galaxies with a LOS velocity lower than $2800\,\mathrm{km\,s^{-1}}$. Among these galaxies is

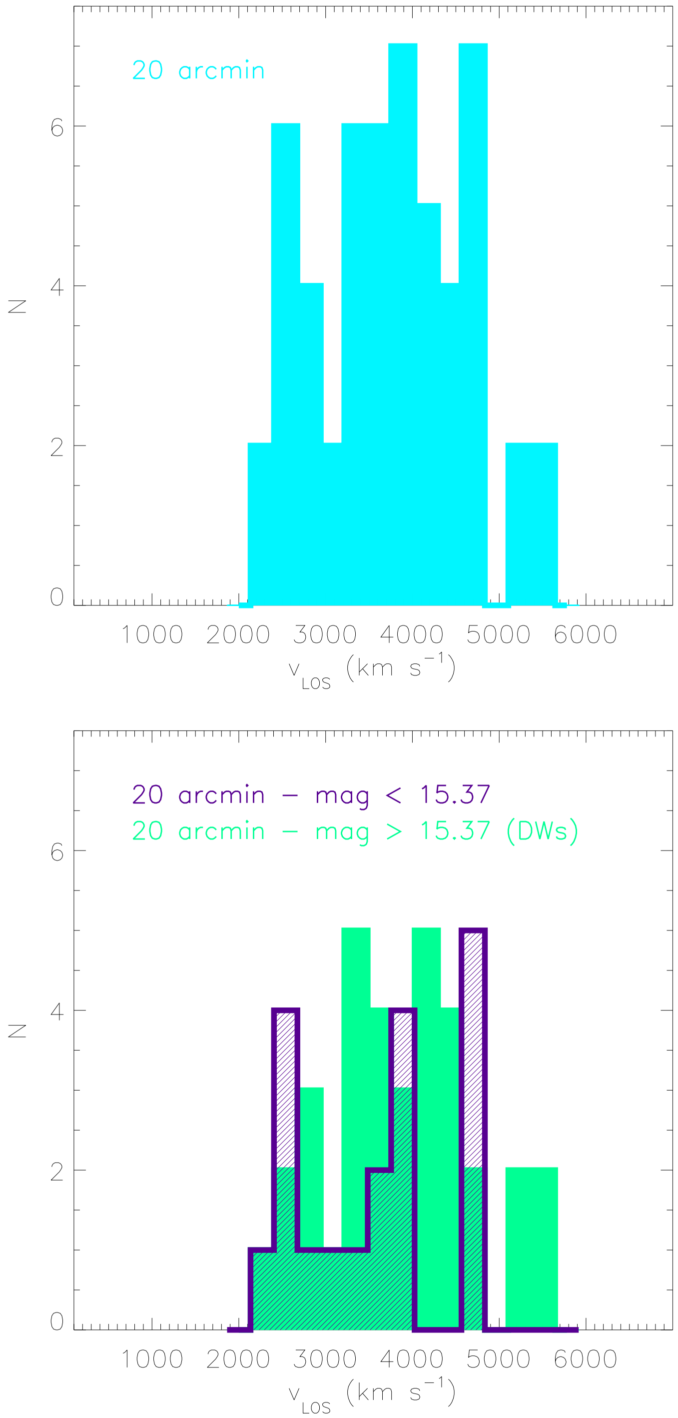

Figure 5.6: *Left panel*: Histogram showing the LOSVD of all galaxies from the catalog of Christlein and Zabludoff (2003) within an area of 20 arcmin in size centered around NGC 3311. *Right panel*: The purple histogram indicates the LOSVD for the bright galaxies in this field, and the light green histogram the LOSVD for all dwarf galaxies from the catalog of Misgeld et al. (2008) in the same area.

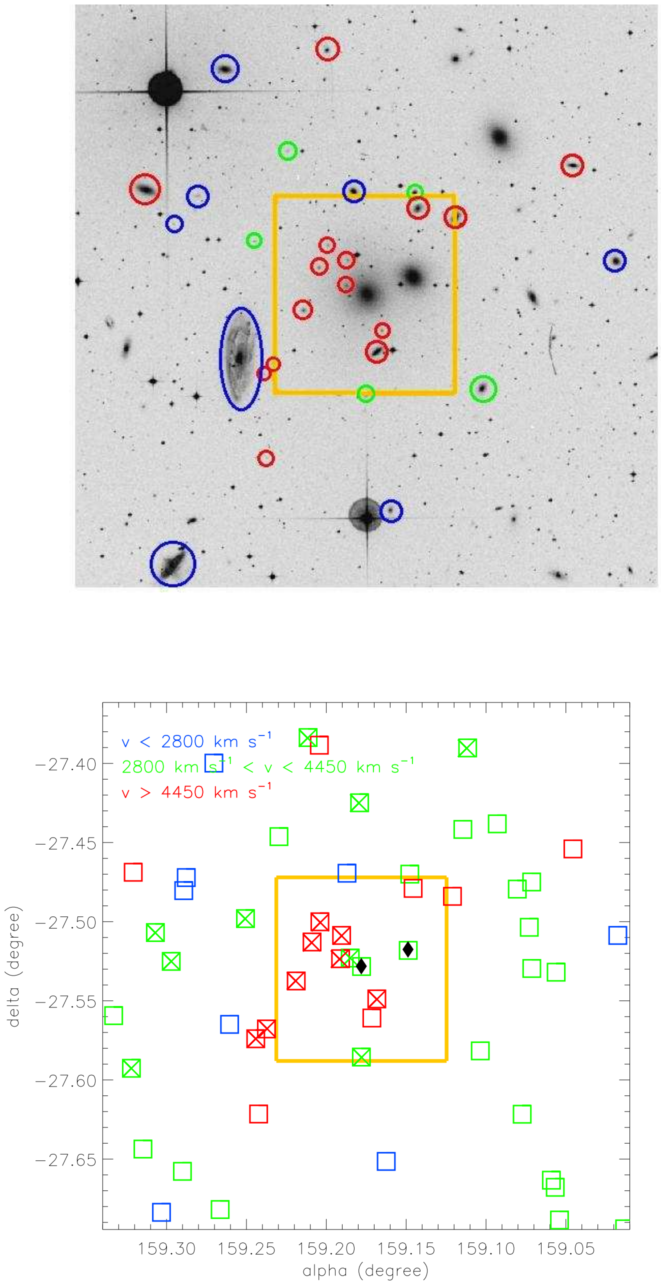

Figure 5.7: *Upper panel*: 20 × 20 arcmin^2 DSS image of the Hydra I cluster. The two bright galaxies at the field center are NGC 3311 (center) and NGC 3309 (North-West of center). The blue circles indicate galaxies with $v_{sys} < 2800\,\mathrm{km\,s^{-1}}$, the green circles galaxies with $2800\,\mathrm{km\,s^{-1}} < v_{sys} < 4450\,\mathrm{km\,s^{-1}}$ (only those within 10 arcmin around NGC 3311 and with $m_R > 15.37$), and the red circles galaxies with $v_{sys} > 4450\,\mathrm{km\,s^{-1}}$. *Lower panel*: Spatial distribution of Hydra I galaxies in the same area of 20 arcmin^2 centered on NGC 3311. Squares indicate galaxies from the catalog of Christlein and Zabludoff (2003) and crosses indicate galaxies from Misgeld et al. (2008). The color of the symbols refers to the velocity components in the PN LOSVD as described in Fig. 5.5. The two diamonds locate NGC 3311 and NGC 3309. The orange square shows the FoV used in the FORS2 MSIS observations.

the large spiral galaxy NGC 3312 ($v_{sys} = 2761\,km\,s^{-1}$) as well as NGC 3314 ($v_{sys} = 2795\,km\,s^{-1}$). Fitchett and Merritt (1988) and McMahon et al. (1992) have claimed the presence of a foreground group of galaxies associated with these spirals. Unfortunately due to the small area covered by the current MSIS survey, it is difficult to determine unambiguously whether the low velocity PNs (which from their PNLF are at the distance of the cluster) are associated with these galaxies. A PN survey covering the region between NGC 3311 and NGC 3312 may provide a definite answer to this question.

5.9 Summary and Conclusions

Using Multi-Slit Imaging Spectroscopy with FORS2 on VLT-UT1, we have studied a sample of 56 planetary nebula candidates in the Hydra I cluster at 50Mpc distance, targeting a region $100\times100\,kpc^2$ centered on the cluster cD galaxy, NGC 3311. The MSIS technique allows us detect these emission sources and measure their velocities, positions and magnitudes with a single observation.

PN candidates are defined as unresolved emission sources without measurable continuum. Emission sources that are either resolved spatially or in wavelength or have a detected continuum are classified as background galaxies; see Ventimiglia and Arnaboldi (2010). We show that the luminosity function of the PN candidates is as expected for a population of PNs at the distance of Hydra I. Moreover, almost all the detected background galaxies occur in the velocity range between $1000\,km\,s^{-1}$ and $2800\,km\,s^{-1}$, blue-shifted by $\geq 900\,km\,s^{-1}$ with respect to the mean recession velocity of the Hydra I cluster. From these facts we conclude that any residual contamination of the PN sample by background galaxies with undetectable continuum must be small and restricted to the velocity range given.

The luminosity-specific number density α inferred from the PN sample and the luminosity of diffuse light around NGC 3311 is is a factor ~ 4 smaller than expected, even if we compare with the low α value determined from the (FUV-V) colour which is one of the lowest for elliptical galaxies. A possible interpretation is that ram pressure stripping by the dense, hot X-ray emitting intracluster medium in the center of the cluster core around NGC 3311 dramatically shortens the life-time of the PN phase. This also seems the most likely explanation for the observed lack of PNs bound to NGC 3309, the other giant elliptical galaxy in the Hydra I core.

The line-of-sight velocity distribution (LOSVD) of the observed PNs shows at least three separate peaks, and their phase-space distribution is inconsistent with a single well-mixed intracluster distribution. One peak, which we term the central intracluster component, is broadly consistent with the outward continuation of the intracluster halo of NGC 3311, which was earlier shown to have a velocity dispersion of $\sim 470\,km\,s^{-1}$ at radii of $\geq 50''$ (Ventimiglia et al., 2010b). Simulating MSIS observations for a Gaussian intrinsic LOSVD with $\sim 470\,km\,s^{-1}$ centered on the systemic velocity of NGC 3311 has additionally shown significant residual asymmetries, suggesting that also this central component is not completely phase-mixed in the central cluster potential.

Many cluster galaxies are found in the LOS velocity range associated with this central intracluster component ($2800\,\mathrm{km\,s^{-1}}$ to $4450\,\mathrm{km\,s^{-1}}$), but *none* in the central $100 \times 100\,\mathrm{kpc}^2$ around NGC 3311. We suggest that the missing galaxies have been disrupted by the gravitational field of NGC 3311 and the surrounding cluster dark matter, and that their light has been added to the diffuse intracluster halo of NGC 3311 which is traced by the PNs.

The second main peak in the PN LOSVD is centered at $5000\,\mathrm{km\,s^{-1}}$, some $1200\,\mathrm{km\,s^{-1}}$ to the red of the main component. In the same velocity range, a number of dwarf galaxies are seen, which *are* projected onto the central $100 \times 100\,\mathrm{kpc}^2$ around NGC 3311 where also the PNs are located. We suggest that the PNs and the galaxies in this red peak of the LOSVD are linked, i.e., on similar orbits through the cluster core, indicating that the galaxies have been partially disrupted and the tidal debris is traced by the PNs. This will be the subject of a further study based on deep photometry (Arnaboldi et al. 2010, in preparation).

Finally, a third, blue peak in the PN LOSVD is seen at $\sim 1800\,\mathrm{km\,s^{-1}}$. The spatial distribution of these PNs is elongated in the same sense as for the other two components in the cluster core, but the number of sources with these velocities is smaller and a few of them might be unresolved background galaxies. This makes it difficult to establish a robust association between these PNs and cluster galaxies, such as the group related to the spiral NGC 3312. A larger survey area would be needed to establish such a link.

In summary, from this study of the kinematics of diffuse light in the Hydra I cluster core with PNs, and the comparison with the projected phase-space distribution of galaxies, we infer that: (1) The intracluster stellar population in the Hydra I cluster is not well-mixed, even though this cluster is believed to be the prototype of an evolved and dynamically relaxed cluster based on X-ray indicators. (2) The build-up of diffuse intracluster light and of the cD halo of NGC 3311 are on-going, through the accretion of material from galaxies falling into the cluster core and tidally interacting with its potential well.

5.10 Acknowledgements

The authors thank the ESO VLT staff for their support during the MSIS observations. They also thank L. Coccato, K.C. Freeman and E. Iodice for useful discussions. This research has made use of the Gemini data archive and the NASA/IPAC Extragalactic Database (NED) operated by the Jet Propulsion Laboratory, California Institute of Technology.

Chapter 6

Disrupted galaxies in the Hydra I cluster. Deep photometry and spectroscopy of galaxies' debris in Hydra I core.

Magda Arnaboldi, Giulia Ventimiglia, Ortwin Gerhard, Enrica Iodice, Lodovico Coccato

2010, to be submitted to A&A[1]

Abstract

The aim of this work is to reach a better understanding of the relevance of cluster substructures for the origin of the diffuse light. We compare the structures of the surface brightness distribution in the core of the Hydra I cluster and their line-of-sight velocities with substructures in the planetary nebulas (PNs) and galaxy distributions.

In this work we perform surface brightness photometry in Ks and V band for the giant elliptical galaxies NGC 3311 and NGC 3309 to derive their structural parameters (Sersic index n, R_e, a/b and P.A.) and quantify the presence of additional light, with respect to an axisymmetric two-dimensional model. We then use deep long slit spectroscopy to establish a link among the light excess, the substructures in the galaxy distribution and PN line-of-sight (LOS) velocity distribution.

There is an light excess in the North-East quadrant of NGC 3311. Such light excess is at the same position on the sky and velocity-space as the PNs associated with the red velocity component discovered at 5000 km s^{-1}, and the dwarf galaxies at 5000 km s^{-1} average velocity within a region of 100 kpc radius centred on NGC 3311. These observational results are consistent with a scenario where the contribution to the light in the intracluster component and extended halos around brightest cluster galaxies is an on-going process facilitated by the infall of substructures and tidal disruption by

---

[1] My part in this work was to perform the data reduction of the photometry and the measurement of the velocity of the excess of light.

the overall cluster potential.

This study of the Hydra I cluster provides evidence that diffuse light is associated with infalling substructures, it can be deposited in the cluster cores, and that such mechanisms take place at zero redshift.

6.1 Introduction

Galaxy clusters are the most massive overdensity structures in the Universe, and they may be formed by thousands of galaxies. One of the most interesting open fields in modern cosmology is the understanding of the mechanisms leading to the formation of such systems and the evolution of galaxies in these massive clusters. The hierarchical model predicts that structure formation and evolution occur by the merging of smaller units into larger systems (De Lucia and Blaizot, 2007), and this model has been supported by many observational evidences. Merges, cannibalism, harassment, gas stripping and tidal forces are only some of the most accredited mechanism acting on galaxies as they experience infall into dense environments (Poggianti, 2004; De Lucia, 2007; Moore et al., 1998). Which mechanism takes a leading role under which conditions for a given galaxy morphological type is still to be clearly understood.

In the nearby Universe those questions concerning the evolution of clusters as a whole and the mechanisms leading the evolution of galaxies in clusters can be addressed with the study of the physics of the intracluster light (ICL). The ICL is the diffuse light in galaxy clusters emitted by stars which are not bound to any specific galaxy; for a review on the subject see Arnaboldi and Gerhard (2010). Wide field surface brightness photometry shows structures in the ICL on all scales, from few arcminutes to degrees on the sky (Thuan and Kormendy, 1977; Mihos et al., 2005; Rudick et al., 2009). Recent studies have shown that ICL provides direct evidence for the dynamical status of galaxy cluster cores (Gerhard et al., 2007; Doherty et al., 2009; Ventimiglia et al., 2010a), because it contains the fossil record of past interactions, due to its long dynamical time.

Cosmological hydro-dynamical simulations predict that the ICL is formed by stars that are unbound from galaxies during the interactions they experience as they fall in the cluster potential well and interact with other cluster galaxies. In these simulations the ICL shows significant substructures on all scales in its spatial and velocity distribution (Napolitano et al., 2003; Murante et al., 2004; Willman et al., 2004; Sommer-Larsen et al., 2005). At early times the ICL morphology is dominated by long, linear features like streams that become more diffuse and spread out as envelopes within the cluster volume at later times (Rudick et al., 2009). Murante et al. (2007) predict that most of the intracluster stars become unbound from their parent galaxies during the merging history leading to the formation of the brightest cluster galaxies (BCGs) in the cluster cores, and that other mechanism like tidal stripping becomes more important at large radii.

In this paper we perform surface photometry and long slit spectroscopy measurements of the ICL in the Hydra I cluster, a medium compact cluster at a distance of $\sim$ 50 Mpc, in the Southern hemisphere. The aim is to compare the structures in the surface brightness distribution in the core of the Hydra I cluster and their LOS velocities around its central cD galaxy NGC 3311 with the kinematic of the Intracluster Planetary Nebulas (ICPNs) detected in Ventimiglia et al. (2008, 2010a). The study of the kinematics of the ICL in nearby clusters like the Hydra I cluster is possible using ICPNs, because these objects are relatively easy to detect due to their strong O[III] emission line (Jacoby, 1989; Ciardullo et al., 1989) and trace the light distribution of the parent stellar population (Coccato et al., 2009).

Ventimiglia et al. (2010a) measured the LOS velocity distribution of the ICPNs associated with the diffuse light within 100 kpc distance from the NGC 3311 center. They detected the presence of discrete velocity components at $\sim$ 1800 km s^{-1} (blue peak) and $\sim$ 5000 km s^{-1} (red peak), in addition to a broad component with $\sigma \simeq 500$ km s^{-1} at the systemic velocity of the Hydra I cluster. The presence of the broad velocity component in the ICPN LOSVD and a steep positive velocity gradient in the halo of NGC 3311 (Ventimiglia et al., 2010b), led Ventimiglia et al. (2010a) to conclude that the core of the Hydra I cluster is not relaxed, with sub-components being accreted and infalling through its core.

The core of the Hydra I cluster is dominated by two giant elliptical galaxies, NGC 3311 and NGC 3309. Early CCD surface photometry showed that both NGC 3311 and NGC 3309 are fitted by an $R^{1/4}$ law within 30″ distance from their center (Vasterberg et al., 1991). On the basis of the large $R_e = 98''$ value from the $R^{1/4}$ fit, Vasterberg et al. (1991) classified NGC 3311 as a cD galaxy.

In the center of NGC 3311, there is a complex dust lane, and the observed surface brightness profile is less luminous than the best fit $R^{1/4}$ interpolation in the center. Both the dust lane and the core central profile are confirmed by the HST WFPC2 imaging carried out by Laine et al. (2003). NGC 3309 does not have a dust lane in its core (Vasterberg et al., 1991). Clearly, any two-dimensional models of the light distribution in NGC 3311 may be affected by the dust lane in the optical band; for an appropriate decomposition of the surface brightness profile in the central regions, near infrared (NIR) images are therefore required.

This paper is structured as follows: in Sect. 6.2 we present the optical V band and 2MASS Ks band images for the Hydra I cluster core. The isophote fitting, the analysis of the surface brightness radial profiles, the two-dimensional models and the evaluation of the residuals with respect to the symmetric models are illustrated in Sect. 6.3. The long slit spectroscopy data and the measurements of the recession velocity of the light excess in the halo of NGC 3311 are presented and discussed in Sect. 6.4. In Sect. 6.5 we investigate the association among the ICPN component at the 5000 km s^{-1} velocity peak, the dwarf galaxies within 100 kpc radius of NGC 3311 center, and the excess of light in the North-East quadrant of the NGC 3311 halo. Summary and conclusions are drawn in Sect. 6.6. We assume a distance to the Hydra I cluster of $D = 50$ Mpc, so $1'' = 0.247$ kpc.

6.2 Optical and Near Infrared imaging of the Hydra I core

6.2.1 V band photometry - Observations and data reduction

Johnson V band imaging of the Hydra I cluster was acquired in service mode on the night of January 12, 2006 at the Wide Field Imager (WFI) on the ESO/MPI 2.2 m telescope, at the La Silla observatory. The WFI is a mosaic of 4×2 CCDs (2k×4k), with an angular scale of $0''.238$ pixel^{-1}. The field-of-view (FoV) of $34' \times 33'$ was centered at α = 10h36m51s, $\delta = -27$d31m35s. 13 exposures of 300 sec each were obtained for a total observing time of $\sim$ 0.5 hr. The average seeing in the combined median image is $FWHM \sim 0''.7$.

Standard calibrations, bias, sky flats and dark skies, were acquired. Several Landolt standard stars in the Rubin 149 field were observed in V band for the photometric calibration. The zero point for the V band photometry is $ZP_V = 24.018 \pm 0.002$.

Data reduction is carried out with standard IRAF tasks for pre-reduction and calibration. After bias subtraction and flat fielding, the average background emission is measured in several regions of the FoV far from the galaxy light and the final average value is subtracted off each single frame. The IRAF task *NOAO.NPROTO.IRMOSAIC* is used to obtain a mosaic of the CCDs. Finally, the mosaic images are registered and combined in the final co-added image.

As the first step in the study of the light distribution in NGC 3311, we determine the extension of the dust lane in its central region. We use the *FMEDIAN* task in IRAF with a smoothing box of 15×15 pixels, and compute the ratio of the V band image with the *FMEDIAN* smoothed version; the V band unsharped image is shown in Figure 6.1.

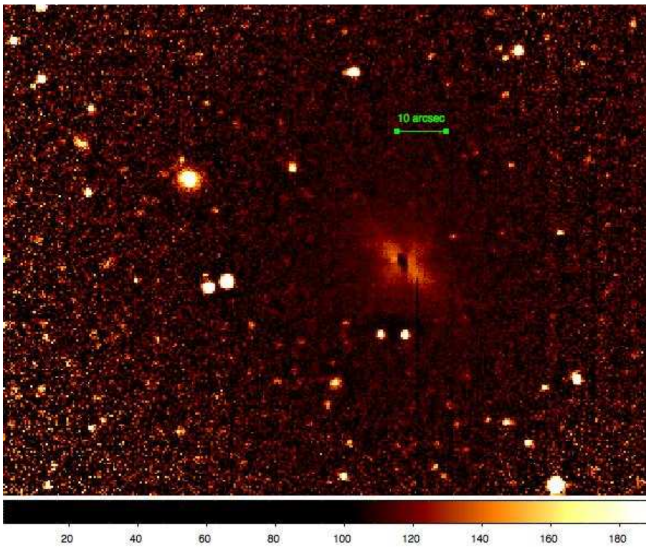

Figure 6.1: Unsharp masked V band image obtained from optical data acquired at the ESO/MPI 2.2m telescope with the WFI; North is up, and East to the left. The green bar indicates 10″ length. The inner dust lane at the center of NGC 3311 is about 2″ wide (Laine et al., 2003) and it is embedded within a central light excess of about 10″ in diameter, which is also visible in the HST image (see Laine et al., 2003).

This image illustrates the complex structure at the center of NGC 3311, where the dust lane is embedded within a brighter central region. A complex dust lane crosses the galaxy center in the direction North-South and extends to about $2''$ in radius, see the high angular resolution image in Laine et al. (2003). Bright regions are seen East, at the center and SW of the galaxy center, within and around the dust lane, out to $5''$ in radius. According to Vasterberg et al. (1991), the dominant knot is bluer, $\Delta(B - r) = -0.10$, than the surrounding stellar population.

Because of the presence of the dust lane, we need to move to longer wavelengths to obtain the best two-dimensional model for the light distribution in the central regions of NGC 3311, as the effect of dust absorption is weaker at those wavelengths. In the next Sections, we combine the analysis of the V band photometry with the archive 2MASS Ks band data.

6.2.2 Ks band photometry - 2MASS archive data

We retrieve a $9' \times 7'$ image with a pixel scale of $1''$ pixel^{-1}, centered on the galaxy NGC 3311 in the core of the Hydra I cluster, from the 2MASS archive (http://irsa.ipac.caltech.edu/cgi-bin/2MASS/LGA/). This image includes both NGC 3311 and NGC 3309. The 2MASS archive images are already reduced and flux calibrated, with a zero point for the Ks band photometry $ZP_{Ks} = 19.91$ with 2-3% uncertainty (Jarrett et al., 2003).

The 2MASS Ks data are shallower than the ESO/MPI V band data. We can reliably measure surface brightness down to a value of 19 mag arcsec^{-2} in the Ks band, corresponding to a distance of $53''$, while the V band surface photometry can be measured reliably down to 23 mag arcsec^{-2}, corresponding to a distance of $81''$; the extracted profiles in Ks and V band plotted in Fig. 6.8 show that the background noise starts to dominate at these radii. These surface brightness limits are computed from the noise in the co-added images and the background level, using the photometric zero point in the different bands. Therefore, we expect the surface brightness parameters to be noisier for the Ks band image than for the V band. An average background level value is estimated and subtracted off before the surface photometry analysis is carried out in both V and Ks band.

6.3 Surface photometry for NGC 3311 and NGC 3309 in V and Ks bands

6.3.1 Isophote fitting

We use the *ELLIPSE* task in IRAF on the V and Ks images to perform the isophotal analysis of NGC 3311 and NGC 3309. We produce the P.A., ellipticity and average surface brightness profiles for NGC 3311 and NGC 3309; those for NGC 3311 are shown in Fig. 6.2; in addition the isophotes shape parameter profiles are also computed and shown in Fig. 6.3.

The V band average surface brightness profiles extends out to $81''$ from the galaxy center; the Ks band profile extends to $53''$, see also Sect. 6.2.2. The half-light radius R_e evaluated from the light-

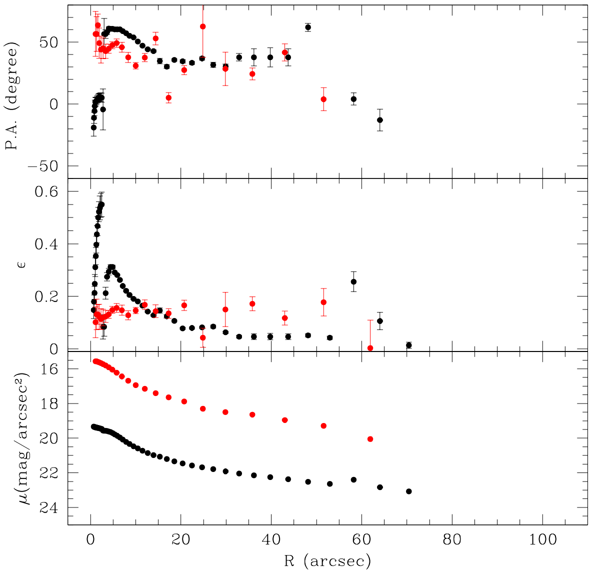

Figure 6.2: Plots of the isophotes' major axis P.A., ellipticity and average surface brightness profiles obtained with *ELLIPSE* for the V (black full dots) and Ks (red full dots) band images of NGC 3311.

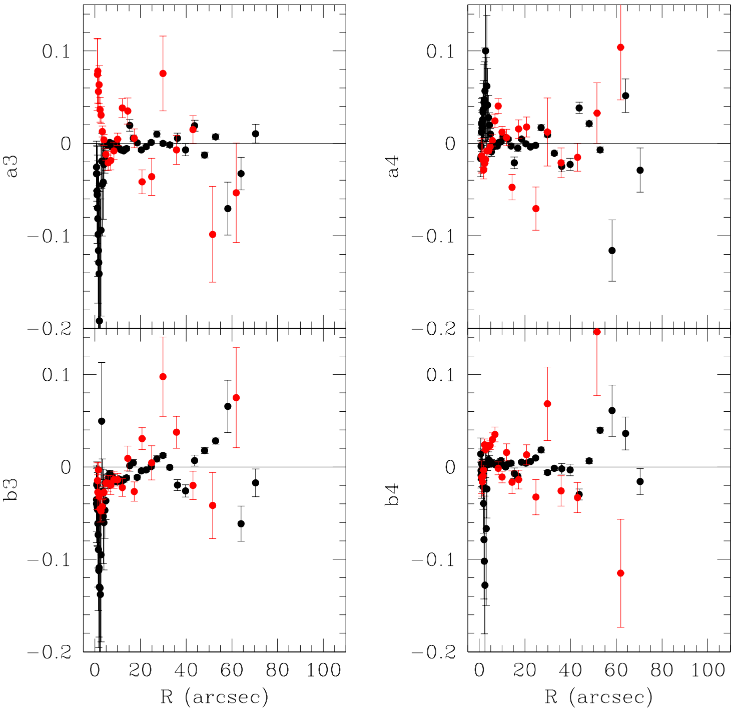

Figure 6.3: Plots of the isophote shape parameter (a_3, a_4, b_3, b_4) profiles obtained with *ELLIPSE* for NGC 3311 V (black full dots) and Ks (red full dots) band images.

growth curve are $R_{eV} = 27'' \pm 2''$ ($\sim$ 6.5 kpc), $R_{eK} = 53'' \pm 2''$ ($\sim$ 12.8 kpc), in the V and Ks bands respectively. At $R \leq 10''$, the presence of a dust-lane is seen in the V band ellipticity, P.A. and shape parameter (a_3, a_4, b_3, b_4) profiles because of the large spread in the measured values. Between $5''$ and $15''$ the V band isophotes twist by about 20 degrees; a twist of the NGC 3311 isophotes was also reported by Vasterberg et al. (1991), but the P.A. variation was not quantified. At radii $R > 15''$, both ellipticity and P.A. profiles are nearly constant and with average values $\epsilon \simeq 0.05$ and $P.A. \simeq 36^\circ$. This behavior suggests that the V, Ks band isophotes are almost round and coaxial. Furthermore, the shape parameter profiles are about zero at $R > 15''$, thus the V, Ks isophotes do not deviate significantly from a regular elliptical shape.

6.3.2 Analysis of the V, Ks surface profiles

We now concentrate on the description of the average surface brightness profiles extracted by *ELLIPSE* in the V, Ks band. They are shown in Figure 6.4, plotted as function of the $R^{1/4}$ semi-major axis radius. We discuss their properties in turn. The Ks band $\mu_K(R)$ shows the presence of a core at $R < 3''$ and then follows an $R^{1/4}$ law at larger radii. The V band average profile $\mu_V(R)$ flattens for $R < 5''$, and deviates from the $R^{1/4}$ law at larger radii as the V band surface brightness profile shows an up-turn curvature which signals additional light at $R > 20''$ with respect to the $R^{1/4}$ law.

We wish to investigate the distribution of light in the V band at large radii in detail. We extracte the surface brightness profile along P.A.= 36° for the kinematic major axis and a second profile at P.A.= 126°, along the minor axis; these profiles are shown in Figure 6.5. The profile extracted at P.A.= 126° shows the light of NGC 3309 at $R > 50''$ distance from NGC 3311. Any two-dimensional model of the NGC 3311 light must be carried out simultaneously with NGC 3309, as the outer regions of the two elliptical galaxies overlap along the LOS.

The folded profile of NGC 3311 along the major axis shows an excess of light in the North-East quadrant in the radial range $20'' < R < 95''$, with the largest excess of about 1 mag at $R = 60''$. We note that the additional light indicated by the folded profile along the major axis for NGC 3311 is superposed to the azimuthally averaged light halo that causes the up-turn in the $R^{1/4}$ semi-major axis radius plot, shown in Figure 6.4.

6.3.3 Two-dimensional model for the light distribution in NGC 3311 and NGC 3309 in V, Ks bands

We perform the two-dimensional model of the light distribution in the V, Ks bands with the GALFIT program (Peng et al., 2002). The light from foreground stars and nearby galaxies is accurately masked with the exception of NGC 3309, whose continuum is modeled simultaneously to the NGC 3311 light. We also mask the Southern region of NGC 3311, where the CCD gaps overlap and the ADU counts in the background are lower than other sky regions on average.

As a first step and according with the morphological classification in NED (NGC 3311 cD2 and

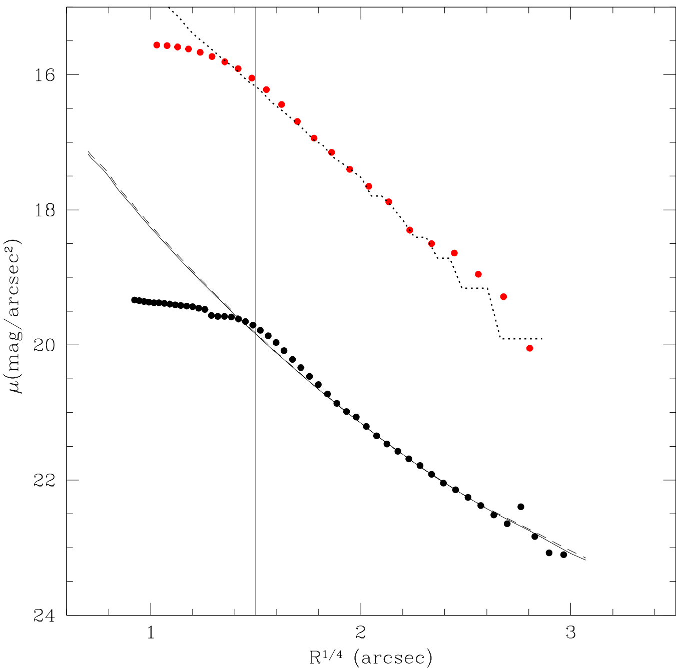

Figure 6.4: The average surface brightness profile in V (black full dots) and Ks (red full dots) band from the ELLIPSE fit plotted against the $R^{1/4}$ semi-major axis radius. The vertical black line indicates the radius of the central masked area. The dotted line through Ks ELLIPSE profile shows the profile from the two-dimensional GALFIT fit to the Ks light distribution, see Sect. 6.3.3. The long and dashed lines through the V ELLIPSE profile show the surface brightness profile of the two-dimensional GALFIT fit to the V band light. The dashed line is for the GALFIT model computed with the light excess masked, see Sect. 6.3.3.

NGC 3309 E3), the light of both galaxies is fit using a single Sersic law (Sersic, 1968). The results show that the light distribution of NGC 3309 is reproduced by a single Sersic profile with $n_V = 2.7$ in V and $n_{Ks} = 2.0$ in Ks; see a summary of the GALFIT parameters in Table 6.1.

In case of NGC 3311, the fit to the V, Ks light distribution with a single Sersic law is poor, due to the presence of a core, a dusk lane and additional light in the central regions ($R \leq 5''$), as shown by the unsharp masking in Sect. 6.3 and the average surface brightness profile in Sect. 6.3.2. When the center is masked with a circle of 5″ radius, the fit to NGC 3311 light distribution gives a better χ^2 for both Ks and V band. Because of the central mask, the center of the two-dimensional GALFIT model is determined a priory with a Gaussian fit to the central parts of NGC 3311. In the Ks band, the galaxy light distribution in NGC 3311 is well described by a single De Vaucouleurs law at $R \geq 5''$ (see Fig. 6.4, dotted line); the GALFIT two-dimensional model of the Ks band light distribution and the residuals are shown in Figure 6.6. In the V band, the light distribution is modeled with a Sersic law and index $n_{V1} = 7.1$, see the continuum line in the Fig. 6.4. Here the larger n is driven by the positive curvature in the radial profile, as described in Section 6.3 and shown in Fig. 6.4. The GALFIT two-dimensional model for the V band distribution and the residuals are shown in Figure 6.7. The surface brightness profiles in Ks, V band extracted along the major and minor axis of NGC 3311 are shown in

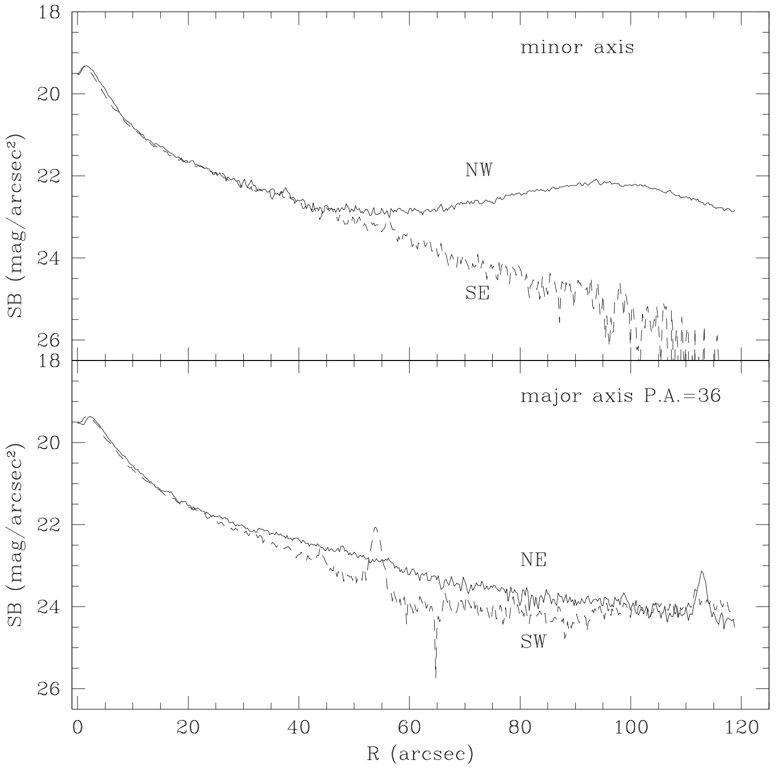

Figure 6.5: *Upper panel*: V band profile extracted at P.A.= 126° along the minor axis. *Lower panel*: V band profile extracted along P.A.= 36°. The folded profile along the major axis illustrates the excess of light in the North East quadrant of the NGC 3311 halo, in the range of radii $20'' < R < 95''$, with the maximum excess of about one magnitude at $R = 60''$. Along the minor axis, we see the contribution from the outer region of NGC 3309. The P.A.= 36° coincides with the kinematics major axis, see Ventimiglia et al. (2010b).

Fig. 6.8, with the corresponding profiles from the GALFIT two dimensional light distribution models. The best GALFIT two-dimensional models for the Ks and V band light distributions for NGC 3311 require very different Sersic n indices, $n_{Ks} = 4$ and $n_{V1} = 7.1$, with the larger n in the V band, which signals more light at large radii than the De Vaucouleurs law. Is the halo light in NGC 3311 becoming bluer in the outer parts? The $(B - V)$ aperture photometry profile by Vasterberg et al. (1991) is nearly constant and equal to ~ 1.1, with no evidence of bluer color gradient, in the same radial interval - 10" to 100" - of the current V band data. As already discussed in Sect. 6.2.2, the outer halo is not detected in the Ks 2MASS data because of the large background noise.

We investigate whether the excess of light in the North-East quadrant of NGC 3311 changes the Sersic fit determined by GALFIT to the light distribution of NGC 3311. The light excess in the North-East quadrant is detected when folding the light profile along P.A.= 36° (see Sect. 6.3.2 and Fig. 6.5). When the light excess is masked, the index of the Sersic law is $n_{V2} = 6.98$, see the dashed line in Figure 6.4. The Sersic index n_{V2} is consistent with the n_{V1} derived previously and only a few percent smaller. The final values of the parameters for the best fit GALFIT model to the Ks, V bands are given in Table 6.1.

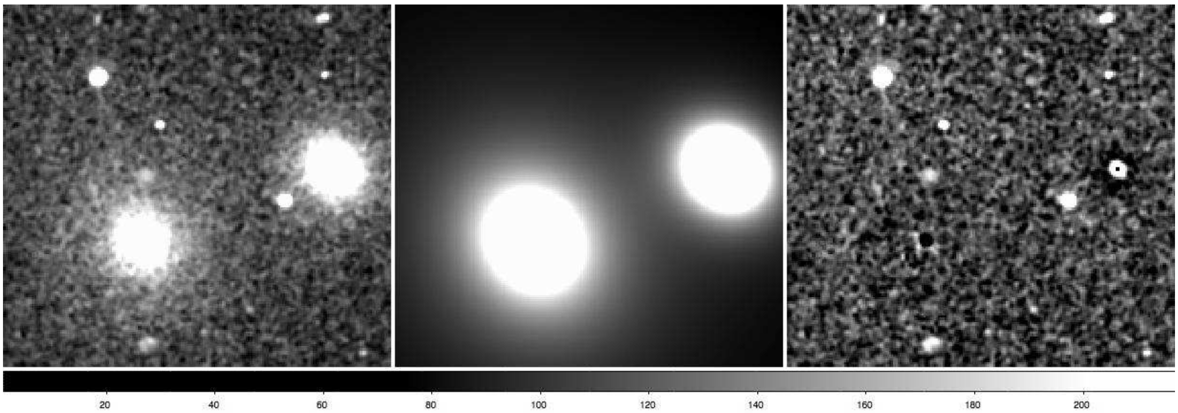

Figure 6.6: *Left panel*: Ks band image of the central core of the Hydra I cluster, $3'.6 \times 2'.0$. The two main galaxies are NGC 3311 (center) and NGC 3309 (upper right). *Central panel*: model, obtained with GALFIT for NGC 3311 and NGC 3309. *Right panel*: residual image. It has been obtained by subtracting the model (central panel) from the Ks band image of the cluster (left panel). North is up and East to the left.

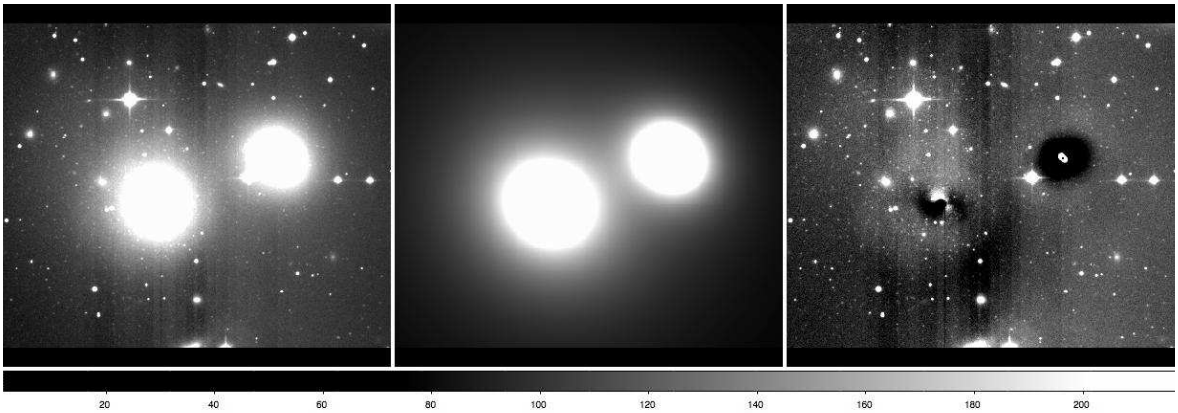

Figure 6.7: *Left panel*: V band image of the central core of the Hydra I cluster, $6'.3 \times 4'.2$. The two main galaxies are NGC 3311 (center) and NGC 3309 (upper right). *Central panel*: 2D model from GALFIT of NGC 3311 and NGC 3309 in the V band. *Right panel*: residual image obtained by subtracting the model (central panel) from the V band image of the cluster (left panel). North is up and East to the left.

Table 6.1: Parameters for the two-dimensional GALFIT fit for NGC 3309 and NGC 3311

Parameter		Ks band	V band		Ks band	V band
Comp. type	NGC 3309	Sersic	Sersic	NGC 3311	De Vauc.	Sersic
m_{ToT}		8.72	14.92		8.0	12.92
R_e		$11''.30$	$18''.00$		$44''.21$	$355''.56$
n		2.0	2.68		4.0	6.9
b/a		0.87	0.88		0.89	0.90
P.A.		50.6	54.5		39.76	54.65

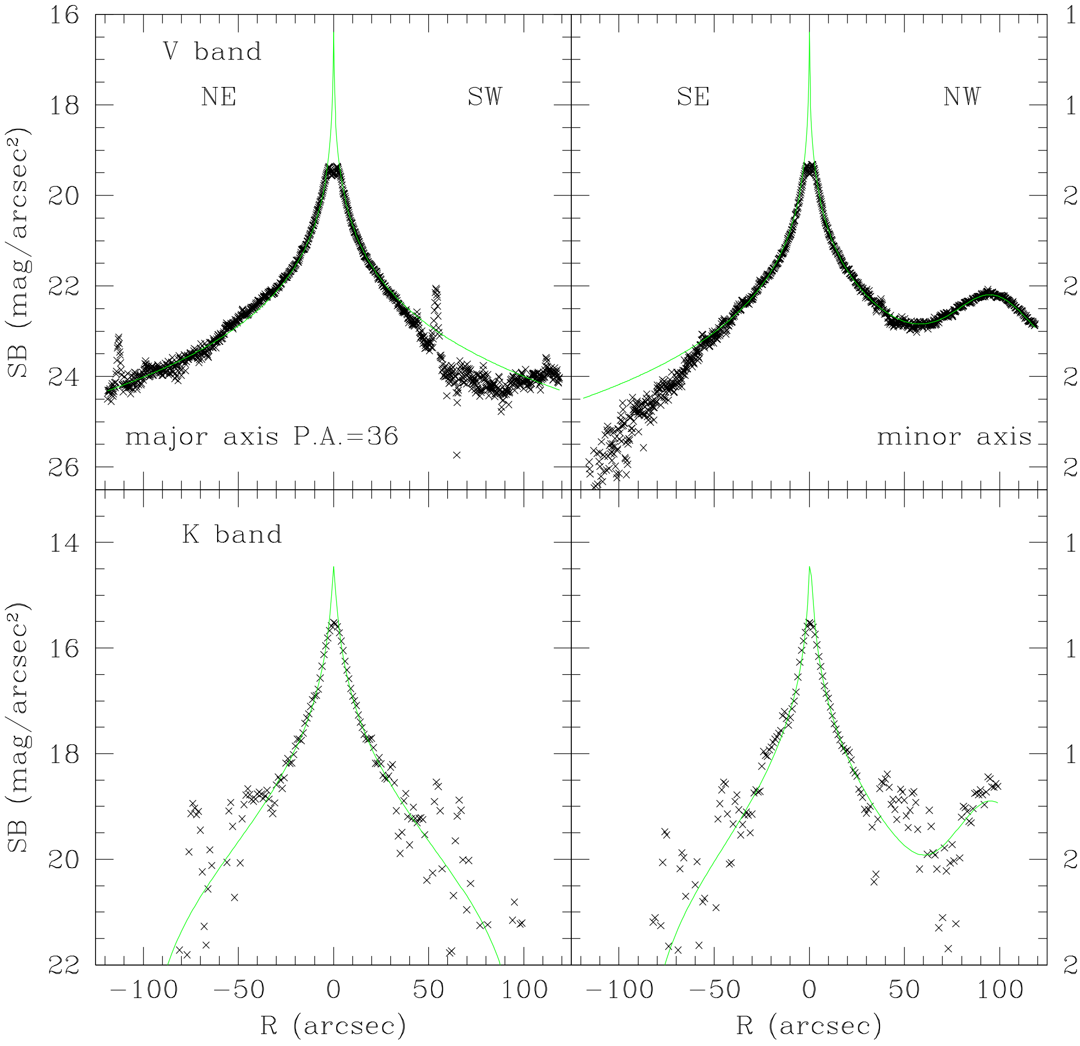

Figure 6.8: The upper panels show the V band profiles, along the major and minor axis. The lower panels display the Ks band profiles, along the major and minor axis. Crosses are the data points from V, Ks band images and the continuous green curves are from the GALFIT two dimensional light distribution models, see Sect. 6.3.3.

6.3.4 Morphology of the light excess in the NE quadrant of NGC 3311

The residual image obtained by subtracting the two-dimensional GALFIT model to the V band image shows an excess of light with respect to a symmetric light distribution, in the North-East quadrant of NGC 3311, as previously illustrated by the analysis of the folded light profiles at P.A.= 36° (see Figure 6.5). The morphology of the excess resembles of thick “C” from 20″ to 80″ in radius with a peak luminosity at about 60″ and a fainter luminosity in the South-West quadrant. As discussed in Sect. 6.2.2, the archive NIR image is not deep enough to sample the faint surface brightness regions at large radii, where the light excess is situated.

We can compute the ratio between the flux in the V band image and the two-dimensional GALFIT model for NGC 3311 in the V band. In a rectangular area of $100'' \times 50''$ centered on the peak of the light excess, the average flux ratio is $I_{Vband}/I_{GALFIT} = 1.09 \pm 0.08$, and we estimate an upper limit to the fraction of light in the excess of the order of 10% of the NGC 3311 halo light in this region. We then carry out the surface photometry in the area covered by the light excess with polyphot, and the luminosity in the excess amounts to $L_{excess} \simeq 3.3(\pm 1.8) \times 10^9 L_\odot$.

6.4 Long slit spectroscopy of the NGC 3311 halo: contribution from the excess of light in the North-East quadrant

Deep long slit spectroscopic observations of the NGC 3311 halo were carried out by Ventimiglia et al. (2010b) with FORS2 on VLT-UT1, in visitor mode. These $4655 - 5955$ Å spectra include absorption lines from H_β, MgI ($\lambda\lambda 5167, 5173, 5184$ Å) and Fe I ($\lambda\lambda 5270, 5328$ Å) and were acquired with a long-slit $1''.6$ wide and $6'.8$ long, GRISM 1400+V, an instrumental dispersion of 0.64 Å pixel^{-1} and a spectral resolution of $\sigma = 90$ km s^{-1}. The long slit was centered on the dwarf galaxy HCC 26 at $\alpha = 10h36m45.85s$ and $\delta = -27d31m24.2s$ (J2000), with a position angle of P.A.=142°; HCC 26 is seen in projection onto the NGC 3311 halo. Eight exposures of 1800 sec each were taken (in total 4 hrs). In addition to the deep spectra, the standard star G dwarf star HD102070 and spectrophotometric standard star EG 274 were also observed with the same set up. Standard reduction steps were then applied to these data; for further details on the observational set-up and data reduction we refer to Ventimiglia et al. (2010b).

Ventimiglia et al. (2010b) used the deep two-dimensional spectrum to measure the velocity dispersion and LOS velocity profiles for the halo of NGC 3311 at several radial distances from the galaxy center. Our immediate goal is different here: we wish to detect a secondary component in the spectrum, in addition to the main absorption features from the continuum emitted by the NGC 3311 halo. We expect these secondary absorption lines to come from the light excess, and to be about 10% of those associated with the NGC 3311 halo at $v_{Hy,halo} = 3921$ km s^{-1}, and at a different LOS velocity.

We extract the light profile along the slit and identify those regions where the continuum is bright enough to provide a suitable S/N. We identify a region of $\sim 22''.5$ wide (95 pixels), North-West of HCC 26 as indicated by the back section along the slit in Fig. 6.12. All signal in this region is co-added to reach a $S/N \simeq 20$ in the continuum of the extracted single spectrum. We are aware that co-adding all the signal from an extended portion of the slit we may cause a broadening of the absorption lines, but this does not affect our goal, which is the detection of a secondary component at a different LOS from the NGC 3311 halo light at $v_{Hy,halo}$.

The stellar kinematics is measured from the extracted one-dimensional spectrum in the wavelength range $4800 < \lambda < 5800$ Å using a “penalized pixel-fitting” method (PPXF, Cappellari and Emsellem, 2004). In the PPXF method, stellar template stars from the MILES library (Sanchez-Blazquez et al., 2007) are combined to fit the one-dimensional extracted spectra;

the velocity and the velocity dispersion are measured simultaneously. The best PPFX fit to the co-added spectrum provides a stellar template, a LOS velocity and velocity dispersion values which are consistent with those measured by Ventimiglia et al. (2010b) for NGC 3311. From the photometry carried out in Section 6.2, we set an upper limit to the luminosity in the excess of light equals to $\sim$ 10% of the light in the region sampled by the long slit. To be able to detect the weak kinematic signal from the excess of light, we need to subtract the main NGC 3311 halo contribution. We achieve this by taking the PPFX best stellar template fit from the MILES library to the original extracted science spectrum, multiply it by 0.9 and subtract it off; the residual spectrum is shown in Figure 6.9. Clearly, the S/N of the residual spectrum is not high enough for a direct pixel fitting, although the main absorption features are readily identified, and we must now use a different approach. We use the *RV.FXCOR* task in IRAF to identify the velocity components in the residual spectrum; this task implements the Fourier cross-correlation technique by Tonry and Davis (1979), which makes use of template stars. To be able to detect the weak signal from the excess of light, we compute the Fourier cross-correlation between the residual spectrum and the 1D extracted spectrum of the G dwarf star HD102070 (G8III), in the wavelength interval $4800 < \lambda < 5800$ Å. The computed cross correlation function is shown in Fig. 6.10. In the lower panel, the region centered on the two strongest peaks show the presence of two components at different velocities: the strongest peak is at 5054 km s^{-1} and a second weaker peak at 3931 km s^{-1}. The results from the Fourier cross-correlation on the residual spectrum in the NGC 3311 halo provide evidence for a second component at $\Delta V = +1100$ km s^{-1} relative velocity with respect to the NGC 3311 systemic velocity V_{sys} at this position. From the results of the two-dimensional photometry, we conclude that the light excess in the North-East quadrant of

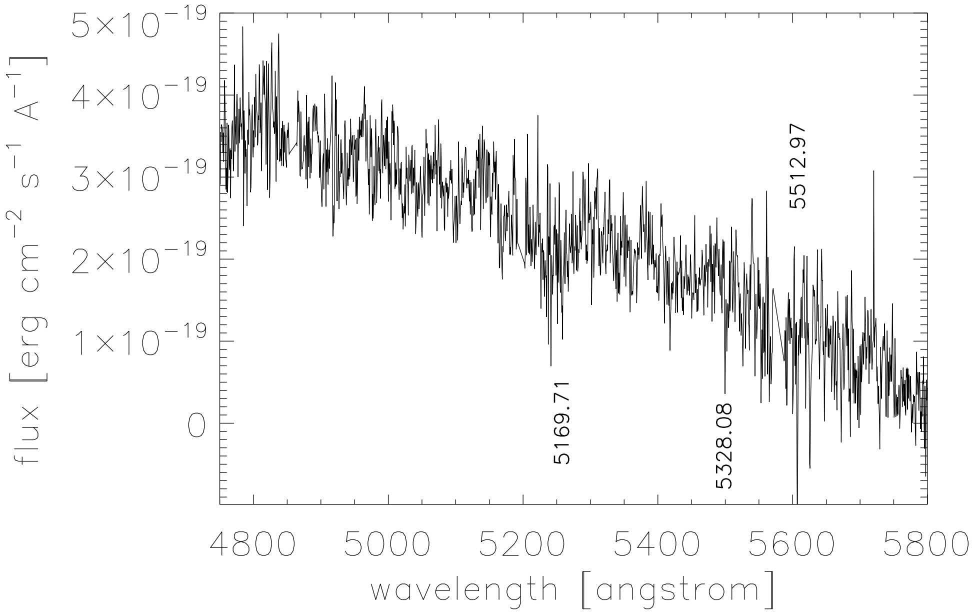

Figure 6.9: The flux calibrated spectrum extracted in the region with the light excess. The rest frame wavelengths of the strongest absorption lines are indicated in the plot.

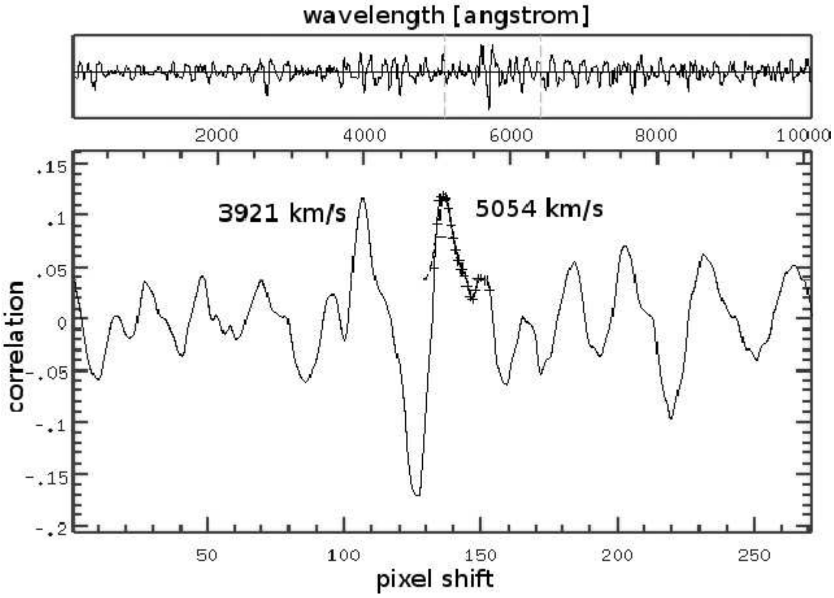

Figure 6.10: *Upper panel*: Plot of the Fourier cross-correlation function computed using the residual spectrum and the G dwarf star HD102070 spectrum. The result of the Fourier cross-correlation indicates the presence of two sets of absorption lines features at different velocities in the residual spectrum. The strongest peak in the Fourier cross-correlation is at $V_{LOS,1}$ = 5054 km s^{-1} and the second weaker peak is at $V_{LOS,2}$ = 3931 km s^{-1}. *Lower panel*: Region of the Fourier cross-correlation function (in pixel scale) centred on the two main peaks.

NGC 3311 is at a LOS velocity of 5054 km s^{-1}.

6.5 Correlation among substructures in the Hydra I diffuse light, PNs and galaxies distributions

6.5.1 Light excess and PNs substructure

As we move towards smaller cluster-centric radii, we ask whether there are additional correlations among substructures in the PNs and galaxies distributions with those in the halo light of NGC 3311. Our aim is to reach a better understanding of the relevance of cluster substructures for the origin of the diffuse light.

In Ventimiglia et al. (2010a), we identified different velocity components in the PN LOSVD and describe their spatial distribution. We summarize the velocity components in the PN LOSVD in the Hydra I core briefly in turn:

- there is a broad central velocity component in the PN LOSVD peaked at about 3100 km s^{-1}with $\sigma \simeq 500$ km s^{-1}, which is consistent with the kinematics of the extended stellar halo around NGC 3311. The spatial distribution of these PNs follows the spatial distribution of the bright galaxies in the Hydra I core and the NGC 3311 halo light.
- A narrow “bluer” velocity component, near 1800 km s^{-1}, whose PNs have an elongated

distribution along the North/South direction. There is no clear association with galaxies in a $6.8' \times 6'.8$ field centred on NGC 3311.

- A second "redder" velocity component, at $\simeq$ 5000km s^{-1}. These PNs show a strong spatial and velocity correlations with an assembly of dwarf galaxies, that is located within a central 100×100 kpc^2 region of the cluster core, centred on NGC 3311.

In the current work we use two dimensional photometry to quantify the main radial profile and substructures in the NGC 3311 halo light distribution. In the V band, the main halo component of NGC 3311 is represented by a Sersic law with a large $n \sim 7.0$ value, that indicates the presence of an extended halo out to $\simeq 90'' = 20$ kpc. The PNs associated with the broad velocity component correlate in space , i.e. round circular distribution around NGC 3311, and in velocity with the halo light, whose kinematics is provided by the the long slit measurements $V_{sys} = 3800$ km s^{-1} and $\sigma_{halo} = 460$ km $s^{-1}$from Ventimiglia et al. (2010b). There are no other Hydra I galaxies at these velocities within a 100 kpc distance from NGC 3311's center.

Once the main symmetric halo component is subtracted off, we detect a light excess in the North-East quadrant of NGC 3311 whose V_{LOS} measurement is 5054 km s^{-1}, see Sect. 6.4. We plot the PNs associated with the blue and red components of the PN LOSVD on the residual image in the V band of the central $6'.5 \times 4'.20$ around NGC 3311, obtained as difference from the V band images and the GALFIT two-dimensional models for NGC 3311 and NGC 3309; the plot is shown in Figure 6.11. In the whole region covered by the light excess, there are nine PNs associated with the red-peak velocity component and only three PNs with the blue-peak component of the PN LOSVD. We speculate that the nine PNs at $V > 4450$ km s^{-1} are associated with the stellar population of the light excess, as they are coincident in sky position and LOS velocity.

6.5.2 Differences in the α parameter

Ventimiglia et al. (2010a) derived a very low *luminosity specific PN number* or α parameter for the NGC 3311 halo light. They argued that the α parameter of the NGC 3311 stellar halo is a factor $4 - 6$ lower than the α parameter value $\log \alpha_{Tot} = -7.34$ determined from the (FUV-V) color vs $\log \alpha_{1.0}$ relation shown in Fig. 12 of Coccato et al. (2009), and corrected to $\log \alpha_{Tot}$ by using Fig.8 of (Buzzoni et al., 2006). They identified two possible explanations: either the stellar population in the halo of NGC 3311 is unusually PN poor, or the ram pressure stripping of PNs by the hot X-ray emitting gas in the halo of NGC 3311 is sufficiently large to severely shorten the lifetime of PNs (Villaver and Stanghellini, 2005).

In this study we can explore the *luminosity specific PN number* for the substructures and the halo light. In a window of $100'' \times 50''$ centered on the peak of the light excess, we find $3/4$ PNs associated with the light excess, because they are on the same sky position, distance and LOS velocity. In a similar region of the sky, we count six PNs associated with the NGC 3311 halo light, from Ventimiglia et al. (2010a). For the light excess we calculate $\alpha_{excess} = 6 \times \alpha_{halo}$, a value which is in agreement with those of red and old stellar population, as predicted by the (FUV-V) color vs log $\alpha_{1.0}$ relation. The implication is that the effect of the hot environment on the PN evolution is not acting on the PNs associated with the light excess.

If the ram pressure stripping is effective during the PN lifetime, it acts similarly on the halo PNs and the light excess PNs, as the stars associated with the light excess cover 100 kpc distance in 10^8 yrs, while a PN lifetime of about $\sim 10^4$ yr. Our estimate of a normal PN number for the light excess indicates that this light is most likely beyond the Hydra-I core, and outside the hot X-ray halo, therefore the ram pressure stripping of PN is not taking place.

6.5.3 Light excess and substructures in the galaxy distribution

Ventimiglia et al. (2010a) discussed that while there are no galaxies in the Hydra core at small cluster-centric radii ($< 100 kpc$), several dwarf galaxies at high velocities $V_{LOS} > 4450$ km s^{-1}are present. In Table 6.2 we list the sky coordinates, apparent total V band magnitude, and LOS velocities from Misgeld et al. (2008) for these dwarf galaxies.

These dwarfs are associated with a well defined substructure both in velocity and spatial distribution, see Fig. 6.12. The substructure traces by these dwarfs occurs at the same sky position and velocity as the light excess.

Table 6.2: Names, position, magnitude in V band and LOS velocities (Misgeld et al., 2008) for the dwarf galaxies in the NGC 331 field.

Galaxy	α(2000) [h:m:s]	δ(2000) [∘:’:”]	M_V [mag]	v [km s^{-1}]
HCC 19	10:36:52.573	-27:32:16.34	16.91	5735±55
HCC 22	10:36:40.373	-27:32:57.68	18.23	4605±37
HCC 23	10:36:48.911	-27:30:01.49	18.07	4479±44
HCC 24	10:36:50.140	-27:30:46.20	17.75	5270±32
HCC 27	10:36:45.700	-27:30:31.30	18.48	5251±89

The total luminosity of the five DWs is $\sim 1.1 \cdot 10^9 L_\odot$, and amounts to about one third of the total luminosity in the excess of light.

The association between the light excess and the dwarf galaxies may result because of these dwarfs are falling through the cluster core, and their halo light was unbound during any previous close pericenter passages with NGC 3311. As we discuss in Sect. 6.5.2, the light excess is beyond the Hydra I core now, and it is made up by stars being now on slightly different orbits than the dwarfs galaxies they were once bound to.

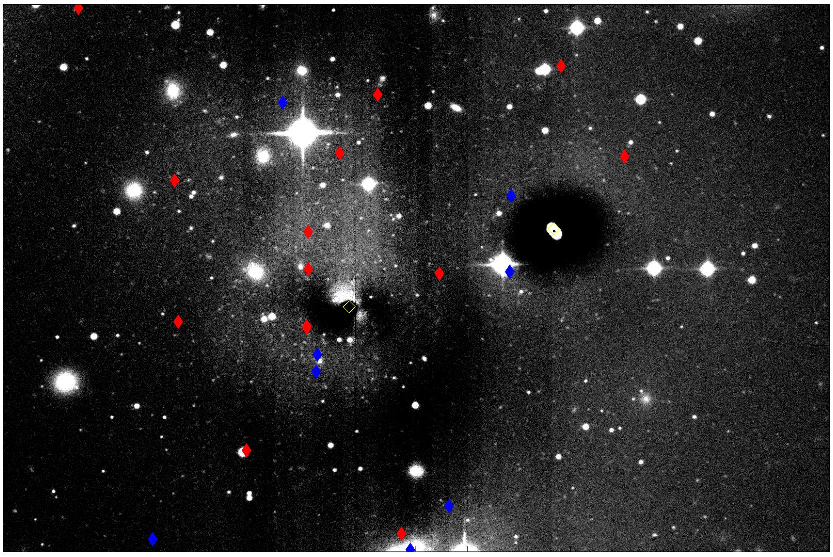

Figure 6.11: PNs contributing to the blue peak at 1800 km s^{-1}(blue diamonds) and to the red peak at 5000 km s^{-1}in the PN LOSVD (red diamonds) on top of the residual V band image of Hydra I. The green and gray triangles are at the position of NGC 3311 (center) and NGC 3309 (upper right), respectively. The FOV is $6'.5 \times 4'.20$. North is up and East is to the left.

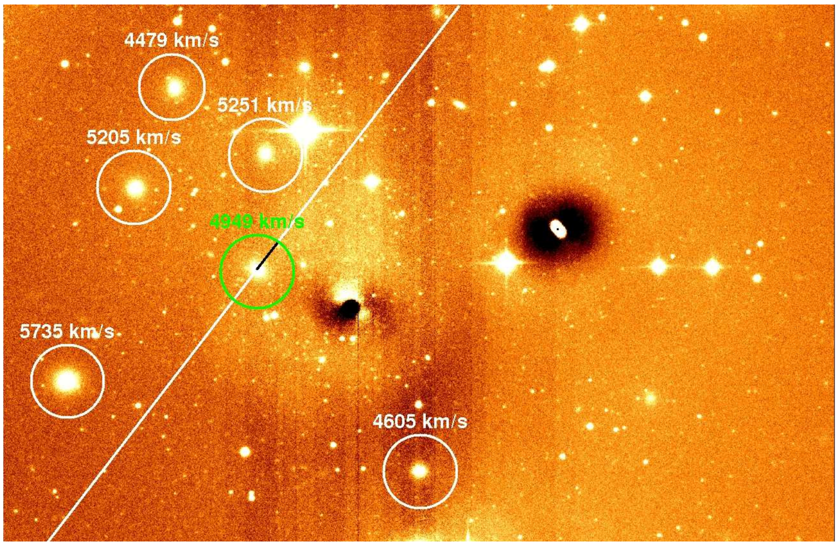

Figure 6.12: Residual image obtained by subtracting the model of NGC 3311 and NGC 3309 (central panel in Fig. 6.7) to the V band image of the central core of the cluster (left panel in Fig. 6.7). In the image we see the excess of light centered on NGC 3311 and spanning from North to South-East. In the white circles are shown the DWs that are superposed, along the line of sight, onto the excess of light. Their velocities are shown as well. In the green circles is the DW galaxy HCC 26. The white line is at the position of the long-slit data Ventimiglia et al. (2010b), centered on HCC 26 and with a P.A. = 142°, that were used to measure the kinematics of the excess of light and the characteristics of HCC 26. The black part of the long-slit is the one used to measure the excess of light velocity. The FoV is $6'.5 \times 4'.2$; North is up and East to the left.

6.6 Summary and conclusions

In the current work we extend our investigation on the substructures present in the projected phase-space of galaxies and PNs associated with the diffuse light in the Hydra I core further. The aim is to correlate them with the structures in the light distribution around NGC 3311.

We use V band imaging data obtained at the ESO/MPI 2.2m telescope and 2MASS archive Ks data to derive the structural parameters of the light distribution of NGC 3311 and NGC 3309. In case of NGC 3309, the light profile is reproduced by a single Sersic fit, with $n_{Ks} = 2.0$ in the K band and $n_V = 2.68$ in the V band. The light distribution in NGC 3311 is characterized by several components, that are more easily detected in the V band. The central regions of NGC 3311 are affected by a dust lane and bright luminous regions, which are then masked by a $10''$ circular aperture. The galaxy's light in the 2MASS Ks band is reproduced by a De Vacouleurs profile, and by a Sersic $n_V = 7.0$ profile in the V band. The large value of the Sersic index n in the V band indicates a bright halo and a characteristic up-turn of the radial surface brightness profile in a $\mu(R)$ vs $R^{1/4}$ diagram at large radii. Furthermore, the analysis of the extracted profiles indicates a light excess in the North-East quadrant of the galaxy NGC 3311 halo: this light is in addition to the extended halo traced by the surface brightness profile up-turn. The total luminosity in the light excess is $3.3(\pm 1.8) \times 10^9 L_\odot$.

We then measure the LOS of this outer component by studying the weaker absorption lines in a deep long-slit spectrum acquired in the region of the light excess. We carry out the Fourier cross-correlation between a residual spectrum, where 90% of the contribution from the best fit kinematic model spectrum of the NGC 3311 is subtracted off, and a standard G8III template star spectrum; we detect clearly two velocity components along the same LOS, with the stronger peak at a redder velocity of 5054 km $s^{-1}$and a second weaker peak which we identify with the NGC 3311 halo.

We conclude that in a region within 100 kpc radius from NGC 3311, the PNs in the red velocity peak at 5000km s^{-1}, the dwarf galaxies at $V_{LOS} > 4400$ km s^{-1} and the excess of light occupy the same location in velocity and space, and are physically associated. The light excess is made up of stars unbound during previous close passages of the dwarfs in the Hydra I core, and are now on slightly different orbits from the galaxy they were bound to previously.

As the case investigated here, stars can be unbound as galaxies fall through the cluster cores, and they can be seen as structures in the diffuse light at this location. While the current study proves that stars are added to the diffuse light at redshift zero, we cannot conclude that this is the main mechanism for the halo formation, as the contributed light is only a small fraction, about 10%, of the whole halo light around NGC 3311. Two-dimensional photometry and deep spectroscopy aimed at the determination of the Lick indices and stellar abundance are instrumental in addressing the issue of the main galaxy progenitors for the ICL.

6.7 Acknowledgements

The authors wish to thank the ESO VLT staff for their support during the observations and the referee for a constructive report. This research has made use of the 2MASS archive data and the NASA/IPAC Extragalactic Database (NED) which is operated by the Jet Propulsion Laboratory, California Institute of Technology, under contract with the National Aeronautics and Space Administration.

Chapter 7

HCC 26: the characteristics of one of the dwarf galaxies in the core of the Hydra I cluster

Giulia Ventimiglia, Ortwin Gerhard, Magda Arnaboldi, Lodovico Coccato

2010, in preparation[1]

7.1 Introduction

In Chapter 6 of this work we discussed the photometry of the central core of Hydra I. The V band image shows a faint excess of light in the North-East part of the central cD galaxy of the cluster, NGC 3311. The velocity of the excess is $v_{excess} = 5054\,\mathrm{km\,s^{-1}}$, $\sim 1400\,\mathrm{km\,s^{-1}}$ higher than the mean velocity of the Hydra I cluster. In the central 100×100 kpc^2 of the cluster, apart from NGC 3311 and NGC 3309, no galaxies with velocity within 1.5σ of the systemic velocity of Hydra I are observed. This region is populated only by galaxies with similar velocity as the excess of light. Most of them are dwarf galaxies (DWs) positioned in projection on top of the excess. In Chapter 4 of this thesis we investigated the kinematics of the intracluster Planetary Nebulas (PNs) in the same core area of Hydra I. The observed PN line of sight velocity distribution shows a multi-peaked structure. One of the peaks is at the same velocity as the excess. The group of DWs and many of the PNs contributing to this peak fall on top of the excess. We concluded that we are seeing a small group of galaxies, unbound light kinematically related to the group and the PNs associated with it. We are now interested in understanding how this diffuse light has formed. V band photometric data for all the DWs and LSS data - the same used to measure the kinematics of NGC 3311 along its major axis and the kinematics of the excess of light - for one of them, HCC 26, are available. In this chapter we analyze these data

---

[1] The results presented in this chapter are the preliminary version of a forthcoming paper focused on the DW galaxy HCC 26. The study of the indices, age and metallicity of HCC 26 were done by L. Coccato.

with the aim of understanding if the above mentioned DWs have signs of tidal disruption and/or their characteristics give us any hint on how the diffuse light, observed in the North-East part of the halo of NGC 3311 has formed.

7.2 The dwarf galaxies in the core of the Hydra I cluster: photometric characteristics

7.2.1 Observational set up, data reduction and 2D modeling

Johnson V band images of Hydra I were acquired with the Wide Field Imager (WFI) on the ESO/MPI 2.2 m telescope, for a total exposure time of 0.5 hrs. All the information about the observational set up and the data reduction are described in Chapter 6 of this thesis. The best fit models for the 2D light distribution of the 6 DWs were obtained using the GALFIT program (Peng et al., 2002). For each galaxy the fit was performed considering a boxy region centered on the galaxy with size roughly twice its dimensions. The light from foreground stars was properly masked and the background light due to the light of the halo of NGC 3311 was fitted and subtracted.

7.2.2 Results

All the galaxies are well described by a Sersic profile. The parameters of the fits are summarized in Table 7.1. Their values are in good agreement with those previously found by Misgeld et al. (2008).

Galaxy	α(2000) [h:m:s]	δ(2000) [$\circ$:’:”]	m_V [mag]	R$_e$ [arcsec]	n	P.A. [N=0, E=90] [degree]	v [km/s]
HCC 19	10:36:52.573	-27:32:16.34	16.91	4.43	1.66	-87	5735±55
HCC 22	10:36:40.373	-27:32:57.68	18.23	2.19	0.87	87	4605±37
HCC 23	10:36:48.911	-27:30:01.49	18.07	3.79	1.02	11	4479±44
HCC 24	10:36:50.140	-27:30:46.20	17.75	3.58	1.47	-71	5270±32
HCC 26	10:36:45.85	-27:31:24.2	18.00	3.50	1.15	61	4949*±10
HCC 27	10:36:45.700	-27:30:31.30	18.48	2.82	0.98	-1	5251±89

Table 7.1: Position, magnitude in V band, effective radius, index n of Sersic profile, position angle, as obtained by a 2-dimensional fit with the GALFIT task, on the residual V-band image for the 6 DW galaxies in the central (100 kpc)^2 of the Hydra I cluster. Velocities are from Misgeld et al. (2008) (* except for HCC 26. For this object velocity was determined from FORS2 data in this work, see Sec. 7.3 for more details.)

The photometry of the 6 DWs in the core of the Hydra I cluster does not show any peculiar characteristics. The shape of the galaxies’ isophotes is regular with no clear sign of tidal tails or other features indicating disruption. The total luminosity of the 6 galaxies amounts to $\sim 3.1 \cdot 10^9 L_\odot$, about 1/3 of the total luminosity of the excess of light on which they lie.

7.3 HCC 26

We now focus on HCC 26. For this galaxy we have LSS spectroscopic data. We will use them to study the kinematics, the age and the metallicity of the object. HCC 26 is particularly interesting in our study because it falls in the middle of the region where we detected the excess of light.

7.3.1 Kinematics

Observational set up and data reduction

The LSS data were acquired with FORS2 on VLT-UT1. The slit, $1''.6$ wide, was centered on HCC 26, at $\alpha = 10h36m45.85s$ and $\delta = -27d31m24.2s$ (J2000). The GRISM used is the 1400V+18. With this set up the spectral resolution is $\sigma = 90\,\mathrm{km\,s^{-1}}$. The data reduction was carried out in IRAF. After the standard operations of bias subtraction, flat-fielding and background subtraction HCC 26's spectrum was extracted, rectified and flux calibrated. The 1D spectrum was obtained by summing over a region $\sim 6''.8$ wide along the spatial direction, where HCC 26's light dominates. The spectrum covers the wavelength range from 4600 Å to 5800 Å. For further details regarding both the observational set up and the data reduction we refer to Chapter 2 of this work.

Results

HCC 26's stellar kinematics was measured from the galaxy 1D spectrum using the "penalized pixel fitting" method (PPXF, Cappellari and Emsellem, 2004). The velocity, velocity dispersion and Gauss-Hermite moments were computed simultaneously.

We find a mean velocity for HCC 26 of $4946 \pm 4\,\mathrm{km\,s^{-1}}$ and a velocity dispersion $15\ \mathrm{km\,s^{-1}}$. Errors are calculated performing Monte Carlo simulations. The galaxy velocity was previously obtained by Christlein and Zabludoff (2003) using Las Campanas LSS data. The value they found is 4195 km/s, about 300 km/s lower than ours. The better agreement with the mean velocity of the other DWs ($v_{DWsmean} = 5068\,\mathrm{km\,s^{-1}}$, see Tab. 7.1) and with the excess of light ($v_{excess} = 5054\,\mathrm{km\,s^{-1}}$), and more importantly the larger S/N of our spectrum (S/N≥20), significantly higher than theirs (S/N=8), give us confidence on the reliability of our value. The measurement of the dispersion of the galaxy is instead very difficult, because the recovered number is significantly smaller than the FORS2 instrumental resolution, $\sim 90\,\mathrm{km\,s^{-1}}$. We consider our value not conclusive and set an upper limit to the velocity dispersion of $\sim 90\,\mathrm{km\,s^{-1}}$.

In Fig. 7.1 HCC 26's spectrum is shown in black and the PPXF best fit in red. The spectrum is characterized by several strong absorption lines. Among these we distinguish H_β at 4941.48 Å and magnesium lines at 5254.23 Å, 5258.08 Å, 5269.68 Å, respectively.

The stellar template that fits HCC 26 spectrum is typical for a G8III star. We use this information to estimate the color for HCC 26 to be (B-V) ~ 0.7 (Scheffler and Elsasser, 1990).

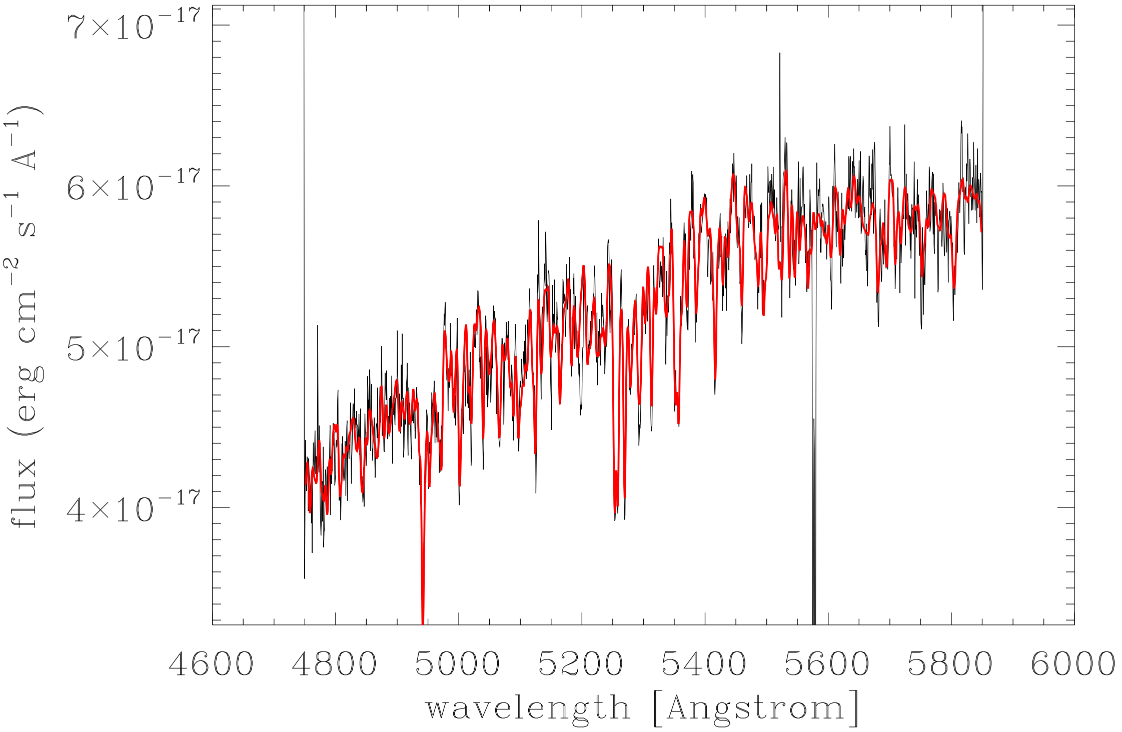

Figure 7.1: HCC 26's spectrum. The black line is the calibrated spectrum of HCC 26. The red line is the fit to the spectrum obtained by using the PPXF method.

7.3.2 Age and metallicity

We also evaluated HCC 26's Lick indices and metallicity.

A set of Lick spectrophotometric standard stars for correction to the Lick system were taken from the ESO archive. We chose them so as to have an instrumental set up as similar as possible to the set up for HCC 26. The 7 Lick stars were observed with FORS2 on UT1 with a 1′′.0 slit and with the Grism 1400V+18.

We measured the H_β, Mg_2, Mg_b, [MgFe]′ and ⟨Fe⟩ line-strength indices as defined by Faber et al. (1985) and Worthey et al. (1994) ($\langle Fe \rangle = (Fe\,I + FeII)/2$ and $[MgFe]' = \sqrt{Mgb \cdot (0.72\ Fe_{5270} + 0.28\ Fe_{5335})}$). Spectra were convolved with a Gaussian function to match the spectral resolution of the Lick system (FWHM = 8.4 Å at 5100 Å, Worthey and Ottaviani, 1997). Measurements were also corrected for the galaxy intrinsic broadening, following the procedure described in Kuntschner et al. (2006). Correcting coefficients C_I for each line strength index I were determined by comparing (i) the "intrinsic" values (I_0, in Angstrom) measured on the optimal stellar template; and (ii) the line-of-sight-velocity-distribution "modified" values (I_{LOSVD}) measured on the best fit model (i.e. the optimal template convolved with the galaxy LOSVD). Corrected galaxy line strength indices (in angstrom) are then given by:

$$I_{correct} = C_I \cdot I_{measured} = \frac{I_0}{I_{LOSVD}} \cdot I_{measured} \tag{7.1}$$

No focus correction was applied because atmospheric seeing was the dominant effect during observations. Errors on line-strength indices were determined via Monte Carlo simulations, which accounted for the errors on radial velocity measurement also. The measured values are $H_\beta = 1.77 \pm 0.22$, $\mathrm{Mg}_b = 2.40 \pm 0.27$, $[\mathrm{MgFe}]' = 2.30 \pm 0.16$, $\langle \mathrm{Fe} \rangle = 2.29 \pm 0.17$. From them we also calculated $[\mathrm{MgFe}] = \sqrt{\mathrm{Mg}_b \cdot < \mathrm{Fe} >} = 2.34 \pm 0.2$.

Luminosity-weighted age, [Z/H] and [α/Fe] of the stellar population are determined from the fit of single stellar population models by Thomas et al. (2003) to the line-strength indices Hβ, Mgb, $\langle$Fe$\rangle$ and [MgFe]. The measured age is $12^{-3.5}_{+1}$ Gyrs, the metallicity $[Z/H] = -0.5 \pm 0.15$ and $[\alpha/\mathrm{Fe}] = -0.06 \pm 0.15$. Errors on ages, [Z/H] and [α/Fe] were computed by means of Monte Carlo simulations.

7.4 HCC 26: comparison with dwarf galaxy samples in nearby clusters

Our data indicate that HCC 26 falls, in projection, in the middle of the region where we detected the excess of light and it has a velocity compatible with that of the excess, the other DWs on top of the excess, and the PNs contributing to the red peak in the PN LOSVD (see Sec. 7.3.1).

What can we learn from the characteristics of this galaxy about the whole group of DWs and about the core of Hydra I? Does HCC 26 have the characteristics of a typical DW galaxy? If not, could this galaxy be the remains of a spiral galaxy that has lost its disk? Can the observed excess of light be the disrupted disk of this galaxy? Do we see any evidence suggesting that HCC 26 has undergone some disruption process?

To answer these questions we compared HCC 26's characteristics with those of other DWs and bulges of spirals in the local Universe.

7.4.1 Lick indices and stellar population parameters

In Fig. 7.2 are shown the Lick indices for HCC 26 (red asterisk), a group of 24 DWs in the Virgo cluster and the field (black crosses, Michielsen et al., 2008) and a sample of 14 bulges of disc galaxies (light blue crosses, Morelli et al., 2008) in nearby clusters. Fig. 7.3 displays HCC 26's magnitude versus age and magnitude versus metallicity compared to the same sample of DWs and bulges. The B magnitude for HCC 26 was calculated from the V-band image, using (B-V) ~ 0.7 from Sec. 7.3.1.

Analyzing the plots in Fig. 7.2 and 7.3 we learn that from the Hβ versus [MgFe] and the Mgb/ $< \mathrm{Fe} >$ versus Hβ relations we have an indication that HCC 26 has Lick indices that are more typical for a DW galaxy than for the bulge of a spiral galaxy. In the first plot HCC 26 falls $\sim 1.5\sigma$ out of the relation for bulges, and $\sim 1\sigma$ out in the second plot. This is consistent with the age and metallicity values of HCC 26, which tend to be higher (lower) that the age (Z) for bulges, but

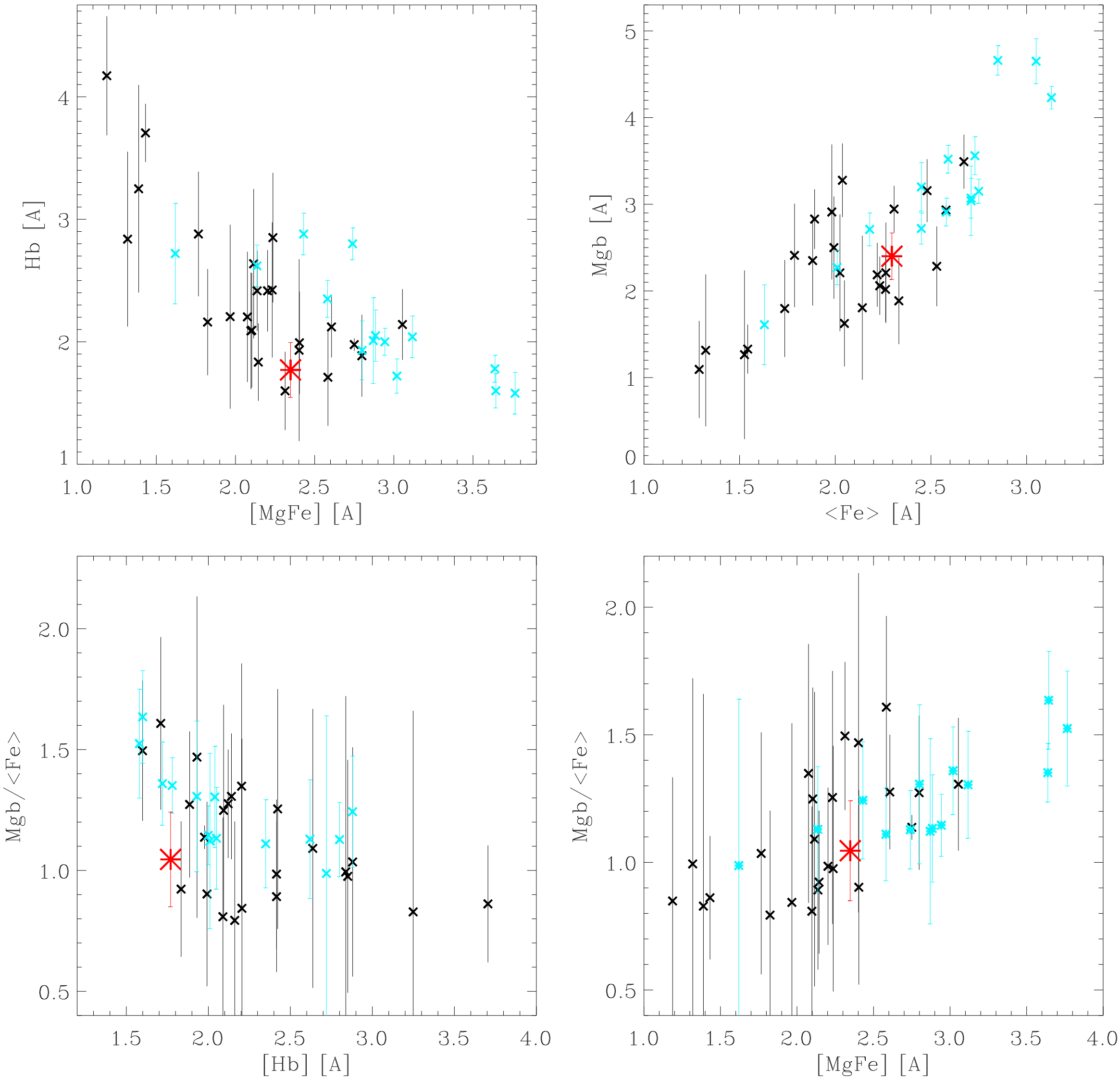

Figure 7.2: Comparison of Lick indices for HCC 26 with dwarfs and bulges of spirals *Upper left panel*: Hβ versus [MgFe]. *Upper right panel*: Mgb versus < Fe >. *Lower left panel*: Mgb/ < Fe > versus Hβ. *Lower right panel*: Mgb/ < Fe > versus [MgFe]. The red asterisks show the index values found for HCC 26. Black crosses denote indices for the 24 DWs in the Virgo cluster studied by Michielsen et al. (2008). Light blue crosses represent the indices calculated for the the bulges from the 14 cluster disk galaxies studied by Morelli et al. (2008).

are typical for DWs. This is without taking into account the fact that the galaxy falls in the very faint end of the plot. On the other hand, from the Mgb versus < Fe > and Mgb/ < Fe > versus [MgFe] relations HCC 26 has index values that are somewhat in the middle between the values typical for DWs and for bulges. The same can be said about the α/Fe value.

We conclude that the lick indices and stellar population analysis of HCC 26 indicate that the galaxy has the characteristics of a dwarf galaxies, but the evidence is not so strong.

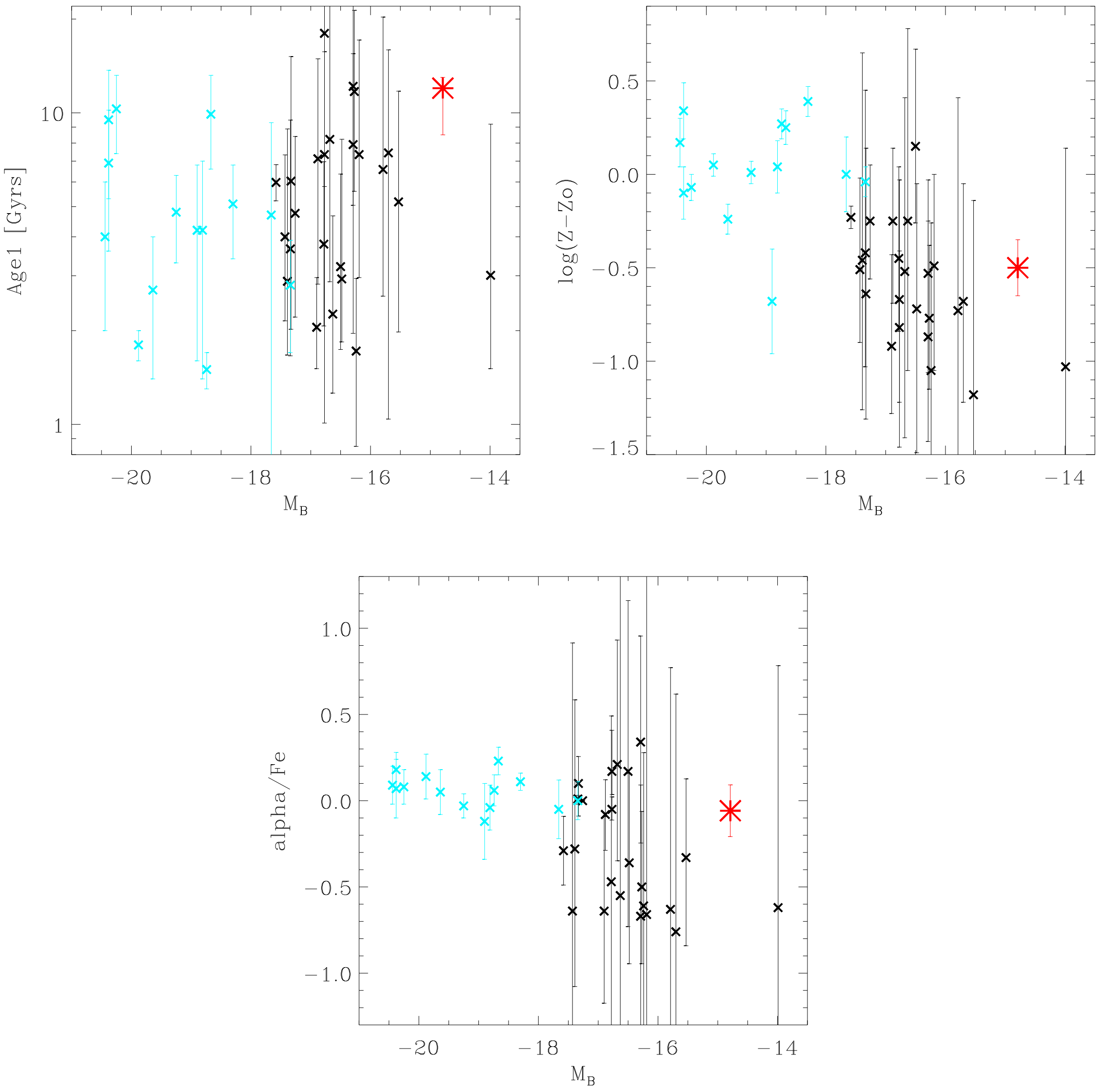

Figure 7.3: Stellar population of HCC 26 compared to dwarfs and bulges of spiral galaxies *Upper left panel*: Age versus B magnitude. *Upper right panel*: metallicity versus B magnitude. *Lower panel*: α/Fe versus B magnitude. The symbols are the same as in Fig. 7.2.

7.4.2 Structural parameters and fundamental plane

The position of HCC 26 on the Σ_e vs r_e (Kormendy relation, Kormendy, 1977), Σ_e vs M_B and r_e vs M_B planes (total B magnitude M_B, effective radius r_e and effective surface brightness Σ_e) compared with the sample of 24 DWs in Virgo and a group of DWs galaxies (grey squares) and bulges (blue squares) from Bender et al. (1992) is displayed in Fig. 7.4. To estimate the effect of tidal stripping on the structural parameters we assume a simple isothermal sphere model for the light distribution of HCC 26, where $L(r) \propto r$ and the outer shells are sequentially stripped. If HCC 26 was is the past 4 times more luminous than it is now, as suggested by the ratio of the luminosity in the excess of light and the luminosity of the six DWs superposed on it, then this galaxy should have moved in the Σ_e vs r_e, Σ_e vs M_B and r_e vs M_B planes along the arrows shown in Fig.7.4.

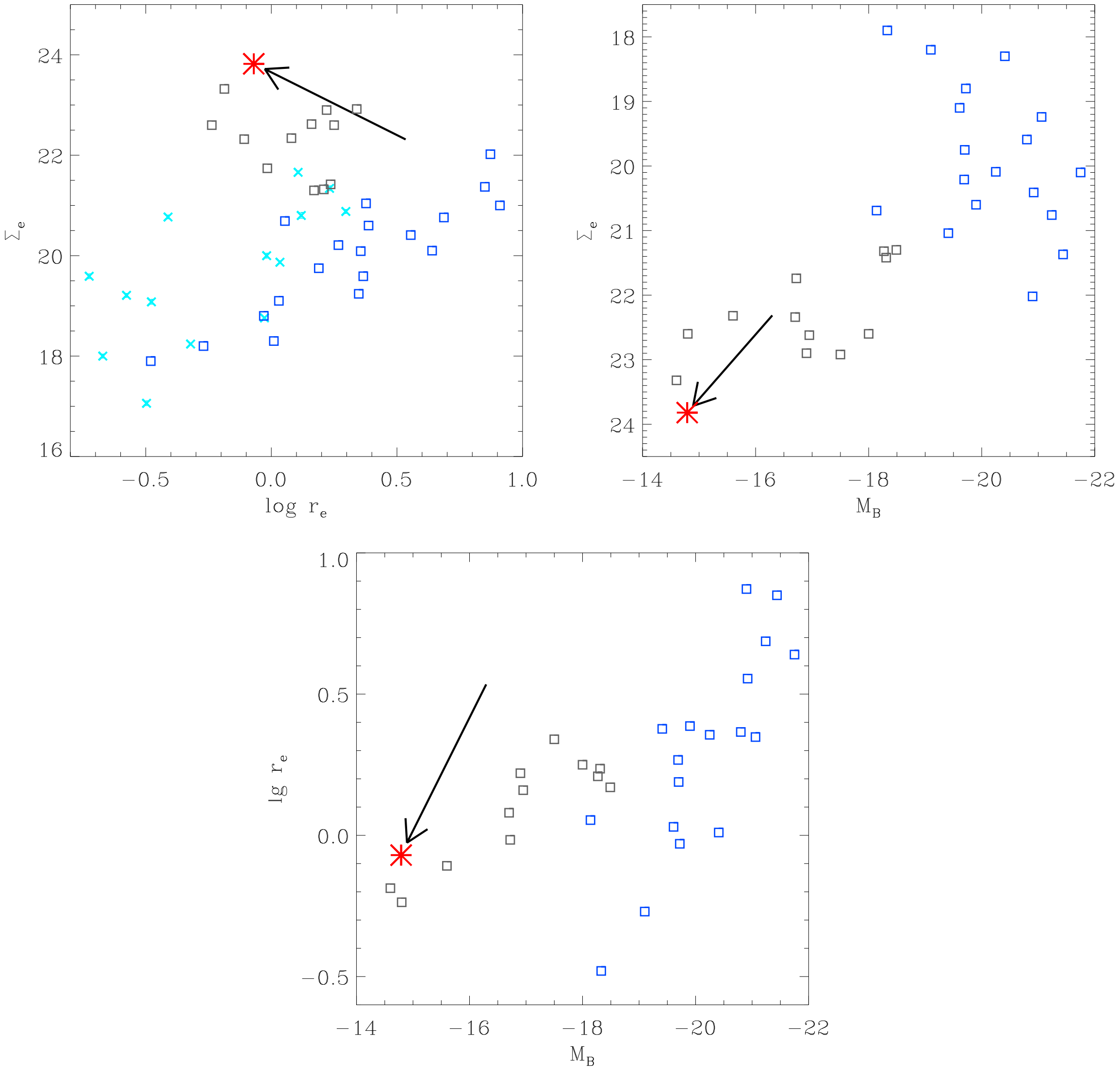

Figure 7.4: Kormendy, Σ_e vs M_B and r_e vs M_B relations for HCC 26 compared to dwarfs and bulges of spiral galaxies *Left upper panel*: effective surface brightness in B band vs effective radius. *Right upper panel*: effective surface brightness in B band versus B magnitude. *Central lower panel*: effective radius versus B magnitude. The red asterisks show HCC 26. Light blue crosses represent the 24 DWs in the Virgo cluster studied by Michielsen et al. (2008). Blue squares denote bulges from Bender et al. (1992) and grey squares show DWs from the same catalog.

To complete HCC 26's analysis, we finally investigated its position on the Fundamental Plane

(FP). We calculated k_1, k_2, k_3, as described in Eq.1.11, which we rewrite here:

$$k_1 = \frac{1}{\sqrt{2}}\log(r_e\sigma_0^2);\ k_2 = \frac{1}{\sqrt{6}}\log\left(\frac{\Sigma_e\sigma_0^2}{r_e}\right);\ k_3 = \frac{1}{\sqrt{3}}\log\left(\frac{\sigma_0^2}{\Sigma_e r_e}\right)$$

In this case k_1 is proportional to the logarithm of the total mass of the system, k_2 depends on its SB and k_3 on its M/L ratio (Bender et al., 1992). We compared the position of HCC 26 on the k_3 vs k_1 and k_2 vs k_1 planes to those of the galaxies in Bender's catalog. The catalog comprises giant ellipticals (green squares), bulges (blue squares), bright DWs (grey squares) and DW spheroidals (magenta squares), see Fig 7.5.

As discussed in Sec. 7.3.1 we consider our velocity dispersion measurement for HCC 26 from the LSS data not reliable. We decided therefore to compute it using the virial theorem:

$$\sigma_v^2 = \frac{0.4\,G\,L}{3\,r_e}\cdot\frac{M}{L} \tag{7.2}$$

where from the V band magnitude found for HCC 26 we calculated $L = 1.3\ 10^8\ L_\odot$ and we assumed $M/L \sim 5$. This value is typical for a DW with HCC 26's magnitude (Geha, 2003). The resulting velocity dispersion is $\sigma_v \sim 20\ \mathrm{km\,s^{-1}}$. This value is consistent with the one obtained from the absorption line kinematics. This suggests that at the present HCC 26 is probably in virial equilibrium. In Fig.7.5 we show the position of HCC 26 on the FP for three different velocity dispersion values, i.e. the measured value (15 $\mathrm{km\,s^{-1}}$, red asterisk), the value from the virial theorem (20 $\mathrm{km\,s^{-1}}$, orange asterisk), and the upper limit given by the FORS2 instrumental resolution (90 $\mathrm{km\,s^{-1}}$, yellow asterisk).

From the diagrams shown we conclude that the photometric characteristics of HCC 26 give fairly convincing evidence that this galaxy is a DW. Even if it had in the past 4 times the luminosity it has now it can not have originated from the bulge of a disk galaxy. Moreover, in the k_2 vs k_1 plane, for all three velocity dispersion values the DW falls in the region typical for DWs. In the k_3 vs k_1 plane the measured velocity dispersion and the one calculated from the virial theorem put HCC 26 among DWs, while the velocity dispersion of $\sigma = 90\ \mathrm{km\,s^{-1}}$ requires a M/L ratio for HCC 26, i.e. a dark matter halo, too high for a DW of this luminosity.

7.5 Summary and conclusions

In this chapter we presented the analysis of the DW galaxy HCC 26. We have focused on this object, since it is particularly interesting for the scientific case presented in this thesis. HCC 26 is a member of a group of DW galaxies that populate the central $100 \times 100\ \mathrm{kpc}^2$ of the Hydra I cluster. In Chap. 6 of this work we detected an excess of light, with respect to a symmetric distribution, in the North-East part of the halo of NGC 3311. The excess has the same velocity as the group of DWs in the core of the cluster to which HCC 26 belongs and also as the PNs contributing to the redder peak in the PN

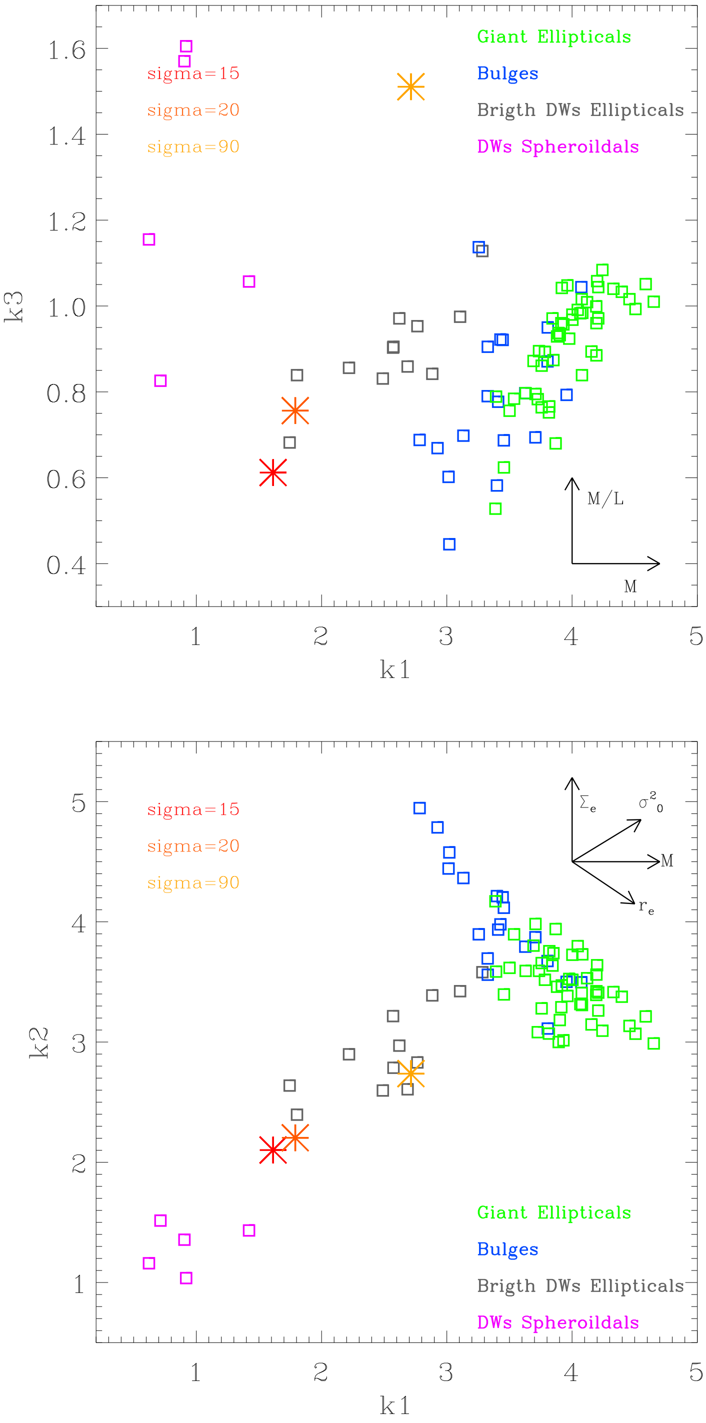

Figure 7.5: *Upper panel*: k_1 versus k_3. *Lower panel*: k_1 versus k_2. The squares represents the values for the sample of galaxies in Bender et al. (1992). The red, orange and yellow asterisks represent the values found for HCC 26 (see text for more details).

LOSVD (see Chap. 5). Both the DWs and the PNs fall, in projection, on top of the excess of light. We are therefore seeing a small group of galaxies separated in velocity with respect to the main galaxy population of the cluster, diffuse light kinematically linked to the group, and the PNs associated with it.

We are interested in understanding the origin of the unbound light. We studied the 6 DW galaxies from photometric data, and spectroscopic data for HCC 26. The aim was to see if from the characteristics of these galaxies was possible to understand the origin of the detected diffuse light. In particular, we tried to verify whether the photometric characteristics of the DWs present any sign of disruption and if HCC 26 is a real DW galaxy or if it is, perhaps, the bulge of a disk galaxy that has lost its disk, whose stripped light is now part of the observed diffuse light.

From our analysis we find that the photometry of the 6 DWs does not show any clear sign of tidal tails or other disruption features in the light distribution of the galaxies. The shape of the galaxies' isophotes appear regular. The light in the excess is currently about 3 times that in the DWs. The stellar population and structural properties of HCC 26 are consistent with the characteristics of a typical DW galaxy and there are indications that it is in virial equilibrium and does not show signs of disruption at the present time.

One possible scenario that could explain the sum of the evidences is that the observed group of DWs was damaged by a recent close passage through the dense core of the cluster. The DWs could have, during this close interaction, lost their outer shells. Considering the relative velocity and distance between HCC 26 and NGC 3311, the high speed encounter hypothesis is valid. In such a case the tidal force acting on HCC 26 would induce stars to get unbound from the galaxy only outside $\sim 3r_e$, while the central regions should remain unaffected. In this picture the resulting unbound stars could have had time to fill the space between the group members if sufficient time has passed since the interaction at the pericenter, $\sim$ 200 Myrs. In this time the DWs should have moved $\sim$ 200 kpc behind the cluster core, and might now be located near the apocenter of their orbits. This would also explain why the galaxies do not show any disruption feature at the present time.

This scenario needs, of course, to be more quantitatively confirmed. Moreover, in the near future we are also planning to perform a spectroscopic follow-up of all the above-mentioned DWs. We hope that the study of their kinematics, age and metallicity will give us a clear picture of the group as a whole and thus on how the diffuse light we observe in the North-East part of the halo of NGC 3311 has formed.

Chapter 8

Summary and conclusions

This thesis work is dedicated to the study of the kinematics of the intracluster light (ICL) component in the core of the Hydra I cluster.
ICL consists of stars that fill up the cluster space between galaxies and are now not bound to any cluster member. Numerical simulations predict that the ICL is formed by stars lost by galaxies in tidal stripping and mergers events (Murante et al., 2007) that happen during structure formation. It comprises of the order of 10-30% of the total optical light emitted by a cluster depending on the dynamical status and history of the hosting system (Feldmeier et al., 2004; Zibetti et al., 2005). Its amount can reach higher values in very massive and dynamically evolved clusters like Coma, where it has been estimated to be 50% of the total star light in the core (Bernstein et al., 1995). ICL has a very faint SB, of the order of 1% of the night sky, and its observation is very challenging. Deep photometric studies have revealed that ICL occurs in the form of extended halos around BCGs, tidal tails and plumes and diffuse light between galaxies (Mihos et al., 2005). Once this component has been created it remains on the orbits on which it formed, conserving the color and chemical characteristics of the objects from which it has been lost. So, in the cases where it is possible to detect it, the study of the ICL can give information both about the evolution mechanisms acting on single galaxies and on the kinematics status of clusters as a whole.
Hydra I is a medium compact cluster in the Southern hemisphere at a distance of ~50 Mpc. In its central region it is dominated by a pair of non-interacting giant elliptical galaxies, NGC 3311 and NGC 3309. NGC 3309 is a regular giant elliptical (E3) and NGC 3311 is the BCG of the cluster and is a cD galaxy with an extended halo (Vasterberg et al., 1991). The cluster velocity and velocity dispersion as measured from a deep spectroscopic sample of cluster galaxies are $\overline{v}_{\mathrm{Hydra\ I}} = 3982 \pm 148\,\mathrm{km\,s^{-1}}$ and $\sigma_{\mathrm{Hydra\ I}} = 724\,\mathrm{km\,s^{-1}}$, respectively (Christlein and Zabludoff, 2003). The virial radius of the cluster is $r_{200} = 1$ Mpc. Within this radius Hydra I has a mass of M(≤1 Mpc)=$10^{14}\mathrm{M}_{\odot}$ (Hayakawa et al., 2004, 2006).

By investigating the kinematics of the core of Hydra I, the central $\sim 100 \times 100$ kpc^2 around NGC 3311, our aim was to answer mainly three questions. The first two are related to ICL and

BCGs:

(i) What is the relation between the ICL and the cD halo of BCGs? Is the cD envelope made of stars dynamically bound to the BCG itself or are these part of the ICL and therefore responding to the cluster potential?

(ii) From the study of the ICL kinematics what can we learn about the mechanisms involved in the build-up of the cD halo of BCGs?

These two questions are important in the framework of modern extragalactic astronomy because one of the challenging issues in the field of galaxy evolution and ICL is the formation of BCG galaxies. These objects have special characteristics if compared to Hubble sequence galaxies. They stay at the center of clusters, at the bottom of their potential well, are brighter than normal ellipticals of the same size and often have extended halos, commonly called cD halos. Cosmological N-body and hydrodynamical simulations predict that the origin of intracluster stars is strongly related to BCG formation. The main mechanisms responsible for stars to be unbound from galaxies could be merging leading to the formation of cD galaxies and tidal stripping processes (Sommer-Larsen et al., 2005; Murante et al., 2007; Rudick et al., 2009). For the moment however, the relation between the ICL and the cD halos remains unclear. It is not understood yet whether the cD envelope is simply the central part of the cluster's diffuse light component, or if it is distinct from it and part of the host galaxy (Gonzalez et al., 2005). To answer this question by using LSS absorption line spectroscopy is difficult due to the low surface brightness of the cD halos. Most of the kinematical studies have been limited to the central regions (within ~ 1 R_e) of BCGs (Fisher et al., 1995; Carter et al., 1999; Hau et al., 2004). Only in few cases the data have allowed to explore the halo dominated areas. Unfortunately, these studies have not provided an unanimous picture. In NGC 6166 in Abell 2199 (Kelson et al., 2002) for example, the velocity dispersion profile in the outer halo of the galaxy, at a distance of ~ 60 kpc from the galaxy center, rises to nearly cluster values, indicating the passage from the galaxy-bound stars to the ICL component. In the central Coma BCGs (Coccato et al., 2010a), instead, the velocity dispersion profiles of NGC 4889 and NGC 4874 remain flat, indicating in this cases that the stars also at R ~ $4R_e$ are still bound to the central BCGs and that there is not a measurable contribution of ICL in their halos. More extreme is the case of M87 in Virgo (Doherty et al., 2009), in which the measured dispersion profile falls steeply to the outer edge. These discordant results suggest that further observations are needed to increase the statistics and to better understand the problem.

The third question we tried to address is related to the ICL and clusters as a whole:

(iii) What can the study of the ICL tell us about the kinematic status of a cluster in general? Is the ICL a relaxed and well mixed component or is it un-mixed and reveals the presence of substructures?

This question arises, because in the current cosmological scenario clusters are formed in a hierarchical way. Small mass virialized systems are formed first and bigger structures of the size of clusters are formed later by assembly of galaxies or groups of galaxies. Among others one observational evidence strongly supporting this scenario is the presence in many clusters of subcluster components, related to recent accretion events (Dressler and Shectman, 1988).

Hydra I was chosen as a target to address these questions, because from X-rays observations it appears to be the prototype of a relaxed and evolved system. The X-ray emission of the hot ICM of the cluster is smooth and has no spatial substructures. This makes Hydra I a good candidate for the study of the relation between the central cD galaxy of the cluster, NGC 3311, and the ICL. If the cluster is dynamically evolved, as suggested by X-rays, we expect ICL to form a well mixed and relaxed component.

In this work the study of the ICL in the core of Hydra I was performed using three different types of data. First we analyzed the kinematics of NGC 3311, along a P.A.∼ 63° (major axis direction), using long-slit spectroscopic data. Then using the Multi-Slit Imaging Spectroscopy (MSIS) technique we detected the Planetary Nebulas (PNs) associated with the central ICL component, and finally we used photometric data to study the distribution of light around NGC 3311.

The main results of this work can be summarized in the following five points. The first three are related to the kinematics of the ICL in the core of the cluster. The last two concern the physical characteristics of the sample of PNs detected with the MSIS.

- *The stellar halo of NGC 3311 is dominated by the central intracluster stars of the cluster, and the transition from predominantly galaxy-bound stars to cluster stars occurs in the radial range from 4 to 12 kpc from the center of the galaxy*.

The study of the kinematics of NGC 3311 along its major axis was performed by combining Gemini GMOS-South and VLT-FORS2 deep LSS data. Absorption line spectra reach out to ∼25 kpc in the halo of this galaxy.

In Hydra I the situation is similar to the one of NGC 6166 in Abell 2199 (Kelson et al., 2002), but more extreme. The velocity dispersion of NGC 3311 increases more rapidly from a value of σ_0=150 km s^{-1} at the center to σ_{out}=450 km s^{-1} at R ∼12 kpc. Farther out the dispersion remains roughly constant around this value, which is 60% of the velocity dispersion of the Hydra I galaxies (724 km s^{-1}).

With these characteristics, NGC 3311 is far from being a typical elliptical galaxy. We calculated for this galaxy its position on the V/σ, X-ray luminosity L_X and total absolute B-band magnitude B_T vs velocity dispersion σ planes. Its position on these planes was estimated for three different values of velocity dispersion, at R=0, R=4 kpc and R=12 kpc. The comparison of the obtained values with those calculated for a sample of early-type galaxies from Coccato et al. (2009, 2010b) showed that NGC 3311 falls in the middle of the other early-type galaxies distribution only when the central velocity dispersion value is used. In the other cases it deviates strongly, with a much larger σ than expected for its L_X or B_T. This shows that the properties of NGC 3311's halo are different from that of a typical galaxy-bound halo.

We concluded that NGC 3311 is a small galaxy, because of its central low dispersion value, and that its halo is dynamically hot with the galaxy being dominated by the central intracluster star component of the cluster already at small radii. This interpretation is supported not only by the trend of the velocity dispersion profile, but also by the large amount of dark matter inferred from X-rays around NGC 3311 ($\sim 10^{12} M_\odot$ within 20 kpc, Hayakawa et al., 2004). Previous works from Hau et al. (2004) and Loubser et al. (2008) already indicated NGC 3311's rising velocity dispersion profile, to a radius of $\sim 5-7$ kpc, and Hau et al. (2004) already suggested that the observed trend indicates the response of the stars to the Hydra I cluster potential, but now we have shown this conclusively.

- *The diffuse light in the central* 100×100 *kpc*^{2} *of the Hydra cluster, around NGC 3311, is still un-mixed and reveals the presence of substructures in the cluster core. This indicates that the build-up of the hot intracluster halo of NGC 3311 is still on-going.*

To understand whether the central region of Hydra I is relaxed, as suggested by X-ray observations, or it contains substructures, we wanted to further investigate the kinematics of the ICL component in the core of the cluster. The kinematics of very low surface brightness regions is very difficult with traditional absorption line spectroscopy, given the low S/N we can achieve with this technique. The study of the kinematics is easier if observations of single stellar indicators associated with the galaxy light and tracing its underlying kinematics are performed. Planetary Nebulas (PNs) are the best tracers for this purpose. They are post-AGB stars at the end of their lives. They consist of a central white dwarf star surrounded by an envelope of low density gas. The gas re-emits more than 15% of the light of the central star in the [OIII] λ5007 forbidden line. The detection of this emission line makes the identification of PNs possible. At the distance of the Hydra I cluster the flux from the [OIII] λ5007 Å line of the brightest PNs is a few 10^{-18}erg s^{-1}. To detect them is possible only by using the Multi-Slit Imaging Spectroscopy technique (MSIS, Gerhard et al., 2005). The MSIS is a blind search technique that combines the use of a mask of parallel slits, a narrow band filter centered at the redshifted [OIII] emission line and a dispersing element. The technique allows to measure velocity, position and magnitude of all the emission line objects that happens to lie behind the MSIS mask slits.

In Chapter 3 of this thesis we described the data reduction of the MSIS data, the selection criteria of the PN candidates, defined as unresolved emission sources without measurable continuum, and the evidence for these stars to be associated with the ICL in the Hydra I cluster. Together with PNs, two other categories of objects were identified in the MSIS images: [OII] emitters at z~0.37 and Lyα galaxies at z~3.12. We do not investigated in detail the properties of these objects, but their main physical characteristics are summarized in Chapter 4 of this work. The most relevant result is that almost all the detected background galaxies are in the velocity range between 1000 km s^{-1} and 2800 km s^{-1}. From this we concluded that any possible contamination to the PN sample by background galaxies with undetectable continuum must be mainly restricted to the this velocity range.

In total we identified 56 intracluster PNs in the central $100{\times}100$ kpc^2 of the cluster. From the LSS results if the ICL around NGC 3311 forms a relaxed diffuse component, we expect the line-of-sight velocity distribution (LOSVD) of the PNs in the core of the cluster to be the superposition of two Gaussians. The first cold component should consist of PNs spatially concentrated on the central core of the galaxy with a velocity dispersion similar to the values measured for NGC 3311 at 0≤R≤5 kpc. The second component should be hotter, with a higher velocity dispersion value as measured at R≥12 kpc and spatially associated with the halo of the BCG. The presence of any additional structure in the observed PN LOSVD will indicate that the stellar population in the core of the cluster is not relaxed.

Results are partially different from our expectations. The first evidence is that no subcomponent of PNs with velocity dispersion $\sim 150-250\,\mathrm{km\,s^{-1}}$ is seen, associated with the central ∼ 5 kpc of NGC 3311. This is mainly due to the high SB of the galaxy at its center. The observed PN LOSVD shows, instead, three separated peaks. The main peak is centered at a velocity of $\sim 3000\,\mathrm{km\,s^{-1}}$, within 1σ the systemic velocity of the cluster. This component is, in accordance with our expectation, related to the PNs associated with the hot halo of NGC 3311. We confirmed this result simulating the LOSVD, as observed through our observational set up, for a sample of PNs at the distance of the galaxy. The simulated stars were distributed in velocity according to a Gaussian centered at the systemic velocity of NGC 3311 and with a velocity dispersion of $\sim 470\,\mathrm{km\,s^{-1}}$, i.e. the value measured from the absorption line spectroscopy at R≥12 kpc. The comparison of the simulated LOSVD with the main peak of the observed PN LOSVD showed that the two distributions are approximately consistent. The investigation of the phase-space distribution of the galaxies in the central 20 arcmin square (150×150 kpc^2) of the cluster (Christlein and Zabludoff, 2003; Misgeld et al., 2008) showed a lack of galaxies with velocities within 1σ the velocity dispersion of the cluster in the 100×100 kpc^2 region around NGC 3311. Outside this region these galaxies are homogeneously distributed in the cluster. This evidence suggests a scenario, in which the missing galaxies were disrupted by the gravitational field of NGC 3311 and the surrounding cluster dark matter, with their light now contributing to the hot intracluster halo of NGC 3311.

The other two secondary peaks detected in the PN LOSVD are a blue component centered at a velocity of $\sim 1800\,\mathrm{km\,s^{-1}}$, about $1900\,\mathrm{km\,s^{-1}}$ bluer than the systemic velocity of the cluster, and a red component centered at $\sim 5000\,\mathrm{km\,s^{-1}}$, at a velocity about $1300\,\mathrm{km\,s^{-1}}$ redder than Hydra I systemic velocity. These two additional peaks show that the ICL component is still un-mixed and reveal the presence of real substructures in the core of the cluster. We concluded that the diffuse light is not relaxed and the build-up of the intracluster hot cD halo of NGC 3311 is still on-going.

The possible origin of the secondary peaks in the PN LOSVD is discussed below.

- *V-band photometric data around NGC 3311 reveals the presence of an excess of light, with respect to a symmetric distribution, in the North-East part of the halo of this galaxy. The excess has a velocity compatible with the PNs contributing to the red peak of the PN LOSVD and a group of dwarf galaxies (DWs) falling through the central core of the Hydra I cluster at* $\sim 1100\,\mathrm{km\,s^{-1}}$. *Our hypothesis is that the light in the excess consists of stars stripped from the group of DWs in a recent close passage to the dense cluster core.*

Once discovered that the ICL in the core of Hydra I does not form a relaxed and well mixed component, we were interested in investigating the origin of the substructures related to the two secondary velocity peaks in the PN LOSVD: the blue component at $\sim$ 1800 km s^{-1} and the red component at $\sim$ 5000 km s^{-1}. With this in mind we studied the light distribution in the core of Hydra I. The aim was to identify the light possibly associated with the above-mentioned substructures. The 2D analysis of the surface photometry of the two central galaxies of the cluster both in Ks and V band was performed. The Ks-band images are from 2MASS archive data and the V-band image are from deeper WFI data. We found that the surface brightness profile of NGC 3309 is well described by a Sersic law with an exponent $n = 2.7$. The analysis of NGC 3311 was more complicated. The central 5 arcsec^2 $\sim$ 1.2 kpc of the galaxy are dominated by the presence of a dust lane, well visible in the V-band image. The galaxy SB profile is well described by a de Vaucouleur law roughly from R=1.2 kpc to R=5 kpc, while in the outer regions the light distribution is better fitted by a Sersic law with index $n \sim 7.0$. This model is consistent with the results obtained in the earlier study of the absorption line kinematics of the galaxy that describe NGC 3311 as dominated by a central cold component from the center to a radius of R=5-6 kpc and by a dynamically hot cD halo further out.

But the most interesting discovery from the study of the photometry of the core of Hydra I was the presence of an excess of light, with respect to a symmetric light distribution, around NGC 3311 in the North-East side of its halo. This has the shape of a thick “C” extending from 20$''$ to 80$''$ from the center of NGC 3311 from North-East to South-East. The amount of light in this excess is ~10% of the total light emitted in the region. Despite the low luminosity, we measured, from FORS2 long-slit data, its kinematics. The excess has a mean velocity $\sim$ 5054 km s^{-1}, $\sim$ 1400 km s^{-1} higher than the systemic velocity of the cluster. This value is similar to the velocity of the PNs contributing to the red peak in the PN LOSVD. Most of them fall in projection of top of the excess of light. By analyzing also the phase-space galaxy distribution we found that in the central 100×100 kpc^2 of Hydra I, apart from the two main cD galaxies, NGC 3311 and NGC 3309, no galaxies with velocity within 1.5σ of the systemic velocity of the cluster are observed. This region is mainly populated by dwarf galaxies (DWs) at the same velocity as the excess of light and positioned in projection on top of it. Currently, the diffuse light contains three times as much light as the DWs.

The evidence retrieved suggest the existence of a kinematics link between the reddest peak in the PN LOSVD, the excess of light and DWs in the core of the cluster. Our hypothesis is that we are seeing a small group of galaxies, separated in velocity from the cluster main component, associated diffuse light and the related PN. The group was probably disrupted in a close passage near the dense cluster core, and is now behind NGC 3311. The absence of tidal features in the group member galaxies (none were detected in the photometric study) could mean that these had time to come back to equilibrium after losing their outer envelops. To confirm this hypothesis further investigation is needed. We are planning to perform a spectroscopic follow-up of the above-mentioned DWs. The aim is to measure the velocity dispersions of these objects so to put them on the fundamental plane and to study their ages and metallicities. This will show us if the galaxies have kinematic signs of tidal disruption and constrain further how and from what kind of stars the IGL we observe in the North-East part of the halo of NGC 3311 formed. For the moment, we analyzed the physical characteristics of only one of these DWs, for which LSS data are available, HCC 26. Unfortunately, the low resolution of the data do not allow us to draw any definitive conclusion abot its intrinsic dynamics (see Chapter 7).

The origin of the peak at $1800\,\mathrm{km\,s^{-1}}$ in the PN LOSVD remains unclear. There is an indication of a possible correspondence between the PNs in this peak and 8 galaxies in the cluster with a velocity slower than $2800\,\mathrm{km\,s^{-1}}$. Among these galaxies there is the spiral NGC 3312. This galaxy, according to McMahon et al. (1992), should be at the center of a foreground group. Unfortunately, due to the small area covered by the MSIS survey and the statistically small number of detected PNs, it was not possible to confirm this connection. The realization of a second MSIS survey in the region connecting NGC 3311 to NGC 3312 would help to solve the problem.

- *The number density of the PNs detected in the core of Hydra I is ~4 times lower for the light seen than expected.*

In parallel to the investigation of the kinematics of the core of the Hydra I cluster, we have also analyzed the characteristics of the detected PN sample. The number density of PNs (N_{PN}) is related to the total bolometric luminosity of the parent stellar population (L_{Bol}), by the simple relation:

$$N_{PN} = \alpha * L_{Bol}$$

where α is the so called luminosity-specific PN number. This parameter is empirically related to the color of the light of the considered galaxy. A list of values are given in Table 6 of Buzzoni et al. (2006). Knowing the α parameter of a given system and its total bolometric luminosity it is possible to predict the number of observed PNs and vice versa.

We computed the expected number of PNs in NGC 3311 using the α parameter calculated by Buzzoni et al. (2006) for the red and old central galaxy of the Fornax cluster, NGC 1399. The total bolometric light was calculated in circular apertures around NGC 3311 from V-band images of the core of Hydra I (Chapter 6). In this calculations the central 5 kpc of the galaxy were eliminated because in this region the SB of the galaxy is too high to allow the detection of the [OIII] emission line from PNs.

We found that the number of PNs observed is lower than expected by a factor of 4. We proposed two possible scenarios to explain this evidence. The first is that the stellar population of the halo of NGC 3311 is unusually PN poor. The second is that the PN lifetime in this galaxy is significantly shortened by ram pressure effects. The density of the ISM in the central $5'$ around NGC 3311 is $\sim 6 \times 10^{-3}\,\mathrm{cm^{-3}}$, and the typical velocity of a star is $\sqrt{3} \times 450\,\mathrm{km\,s^{-1}} \simeq 800\,\mathrm{km\,s^{-1}}$. In these conditions ram pressure, due to the fast movement of PNs in the hot ISM, might significantly affect their visibility (Villaver and Stanghellini, 2005).

The second hypothesis would also explain the lack of PNs associated to NGC 3309. In our PN sample, in fact, we saw only one star that has a position and a velocity compatible with an object bound to the second brightest galaxy of the Hydra I cluster. If this lack of PNs was due to the distance of the galaxy, so that also its brightest PNs were too faint to be detected with the MSIS observational setup, then the elliptical should have a distance of ∼70 Mpc, significantly out of the cluster. We know from X-ray observations that this is not the case (Hayakawa et al., 2004).

- *The luminosity function of the PNs detected with the MSIS is consistent with that expected at a distance of ∼50 Mpc.*

The PN luminosity function (PNLF), defined as the luminosity distribution of their [OIII] λ5007 lines, has a sharp cutoff at its bright end at a fixed intrinsic magnitude of $M^*_{5007} = -4.51$. This makes PNs useful as distance indicators.

Since the MSIS allowed us to measure not only the positions and velocity, but also the fluxes of the detected emission line objects, we were able to recover the luminosity function of the observed stars. But the MSIS is a blind search technique and the detected sources are not previously centered on the MSIS mask slits. The measured fluxes are dimmed in relation to the distance of the object from the slit center.

We used a technique to take into account this statistical flux loss, and convolved with the errors on magnitudes and the sample incompleteness at faint magnitudes, and we performed all the appropriate corrections necessary to use the observed MSIS PNLF as a distance indicator (Gerhard et al. 2010, in preparation, Ciardullo et al., 1998). A preliminary analysis in the Hydra I cluster suggests that the observed PNLF is consistent with a population of stars at a distance of ∼ 50 Mpc.

The study of the PNLF bright cutoff in BCG galaxies has potential for understanding the stellar population in such systems. The results obtained with the MSIS could give important hints in explaining the discrepancy with the prediction from stellar population evolution models, that predict a trend of the PNLF bright cutoff with the age of the parent stellar population (Marigo et al., 2004; Ciardullo et al., 2004). This study could be complementary to that of the PNLF in the Galaxy and other late type galaxies in the local Universe, for which the PN population has been better studied.

In the current cosmological scenario structure formation happens in a hierarchical *bottom-up* way, with small mass virialized systems forming first and then enlarging by accretion and merging events. Clusters, being the most massive virialized systems in the Universe, are the last to form. Their growth continue to happen also at z=0 through the accretion of new galaxies or group of galaxies from the filaments that surrounds them and that link them to the *cosmic web*. During these events different mechanisms influence the life of the involved galaxies. Galaxies falling toward the cluster center experience a more and more dense environment and can interact between each other, with the ICM and with the global cluster potential. The more accredited mechanisms responsible for galaxy evolution are tidal interactions, mergers and ram-pressure stripping, to mention only a few. These processes can completely change galaxy properties, from morphology to gas content to star formation activity. In this framework a particular role is played by BCGs. Simulations suggest that the formation of these objects, that sit at the bottom of cluster potential wells at their centers, is related to the overall cluster formation history. All the above mentioned processes that involve galaxy evolution and BCG formation can also be responsible for stars to be lost from galaxies and contribute to the build-up of the ICL component. When, during a cluster life, ICL is created and which are the mechanisms that more contribute to its formation and under which conditions the play a significant role, is still matter of debate. Numerical simulations indicate that massive galaxies mainly contribute to the build-up of the ICL component (Puchwein et al., 2010). According to their predictions, most of it is produced at $z < 1$ during the merger history that leads to the formation of BCGs, or other massive galaxies in clusters while smaller galaxies and tidal stripping mechanisms are responsible only for a minor fraction of the ICL in the outskirts (Murante et al., 2007; Dolag et al., 2009). The direct study of ICL properties, when possible, can give useful hints both for the identification of the processes involved in galaxy interactions and BGC formation and in the investigation of the characteristics of clusters as whole.

In this framework two are the conclusions that can be drawn from this thesis work: (i) A possible interpretation of the retrieved evidences is that in dynamically evolved clusters, as X-ray observations suggest for Hydra I, the stars in the outer halo of their BCGs are not bound to the galaxy itself, but have had enough time to start feeling the cluster potential and contribute to the ICL component. This indicates that possibly the kinematics of BCGs' halos is strongly related to the dynamical status of the histing cluster. Such hypothesis is supported by the fact that in other cluster, whose dynamical status is significantly different than in Hydra I, different situations were observed. In Coma, that is in a middle evolutionary state with the two BCGs of the cluster probably involved in a second close passage, the velocity dispersion profiles of the two interacting galaxies are flat. In Virgo, that is considered to be a dynamically young system, the halo of M 87 has a decreasing velocity dispersion profile. The analysis of the kinematics of BCG halos in different systems will help to confirm this scenario. (ii) From our results we learned that the halo formation can be related to accretion processes. The study confirms that accretion of stars from galaxies falling in the cluster core is a possible ICL formation mechanism. These events can happen at redshift $z=0$ and leave their mark by the presence of substructures of diffuse light where they occur. However, from our analysis we can not genarelize this result and conclude that the formation of the halo of NGC 3311 has happened only though galaxy stripping. To really investigate this topic the study of NGC 3311 halo stellar population is needed. This is going to be done in the next future (Coccato et al. 2011, in preparation). Moreover, the studies of various systems suggest that other mechanisms, like merger and stripping from different galaxies, may play a major role in ICL formation.

Our work contributes to the study of the ICL at $z=0$ and the proceses involved in galaxies' and BCGs' formation. Similar studies in other systems in the local Universe that investigate ICL's and BCGs' properties in relation to the whole cluster dynamical state will help to increase the statistics and give more general answers to the questions we tried to answer in this thesis. For the moment the studied systems have provided different results and a clear picture is difficult to be drawn. It will be also extremely interesting to explore the group environment to understand if in less massive systems the mechanisms leading ICL formation are similar as in clusters. This will be an important step in the study of the formation of diffuse stellar components, since the group environment has not been deeply explored yet. An analysis similar to the one performed for Hydra I is already in progress for the Centaurus cluster and the HGC 90 compact group. MSIS, LSS and photometric data for these systems are available.

Acknowledgments

I want to thank my supervisors Ortwin Gerhard and Magda Arnaboldi for the knowledge they transmitted to me and for the support in the work of these years. I also want to thank the Max Planck Institut für Extraterrestrische Physik and the European Southern Observatory Hemisphere for hosting me and for proving a scientifically very stimulating environment. A special acknowledgment goes to Lodovico Coccato, Enrica Iodice and Ken Freeman for the fruitful discussions and the technical help and to all our big group members, Inma, Lucia, Payel, Stefanie, Emily, Marilena, Kanak, Xufen, Jens, Arianna.

I also want to say a big thank you to all my friends old an new: Betta and Rattonzo, Paolina and Andrè, Lodovicolo, Daria, Erica and her beautiful *puffi*, *la fratenita'*, Giò, Lucy and Marchito, Anna, Luca and Cristina, Angela, Nico, Lollo and Samuele, Giulianina and Achille. A thought goes as well to the people in Catania, especially *I Cantoni*, Suor Concettina and Roberto that have loved me although the distance and to all my huge family, Chiara, Michelozzo, zio Nino and zia Gida in particular. Thank you for your endless patience and affection through the years.

And finally a huge thank you goes to my parents Egle and Michele (I really miss you) and my husband Thomas. I need to add no words, you already know how much I love you all.

Bibliography

Abdelsalam, H. M., Saha, P., and Williams, L. L. R. (1998). Nonparametric Reconstruction of Abell 2218 from Combined Weak and Strong Lensing. *AJ*, 116:1541–1552.

Abell, G. O. (1958). The Distribution of Rich Clusters of Galaxies. *ApJS*, 3:211–288.

Adami, C., Slezak, E., Durret, F., Conselice, C. J., Cuillandre, J. C., Gallagher, J. S., Mazure, A., Pelló, R., Picat, J. P., and Ulmer, M. P. (2005). Large scale diffuse light in the Coma cluster: A multi-scale approach. *A&A*, 429:39–48.

Aguerri, J. A. L., Gerhard, O. E., Arnaboldi, M., Napolitano, N. R., Castro-Rodriguez, N., and Freeman, K. C. (2005). Intracluster Stars in the Virgo Cluster Core. *AJ*, 129:2585–2596.

Ajiki, M., Taniguchi, Y., Fujita, S. S., Shioya, Y., Nagao, T., Murayama, T., Yamada, S., Umeda, K., and Komiyama, Y. (2003). A Subaru Search for Lyα Emitters at Redshift 5.7. *AJ*, 126:2091–2107.

Allen, S. W., Schmidt, R. W., and Fabian, A. C. (2001). The X-ray virial relations for relaxed lensing clusters observed with Chandra. *MNRAS*, 328:L37–L41.

Arnaboldi, M., Aguerri, J. A. L., Napolitano, N. R., Gerhard, O., Freeman, K. C., Feldmeier, J., Capaccioli, M., Kudritzki, R. P., and Méndez, R. H. (2002). Intracluster Planetary Nebulae in Virgo: Photometric Selection, Spectroscopic Validation, and Cluster Depth. *AJ*, 123:760–771.

Arnaboldi, M., Doherty, M., Gerhard, O., Ciardullo, R., Aguerri, J. A. L., Feldmeier, J. J., Freeman, K. C., and Jacoby, G. H. (2008). Expansion Velocities and Core Masses of Bright Planetary Nebulae in the Virgo Cluster. *ApJL*, 674:L17–L20.

Arnaboldi, M., Freeman, K. C., Okamura, S., Yasuda, N., Gerhard, O., Napolitano, N. R., Pannella, M., Ando, H., Doi, M., Furusawa, H., Hamabe, M., Kimura, M., Kajino, T., Komiyama, Y., Miyazaki, S., Nakata, F., Ouchi, M., Sekiguchi, M., Shimasaku, K., and Yagi, M. (2003). Narrowband Imaging in [O III] and Hα to Search for Intracluster Planetary Nebulae in the Virgo Cluster. *AJ*, 125:514–524.

Arnaboldi, M. and Gerhard, O. (2010). JD2 - Diffuse Light in Galaxy Clusters. *Highlights of Astronomy*, 15:97–110.

Arnaboldi, M., Gerhard, O., Aguerri, J. A. L., Freeman, K. C., Napolitano, N. R., Okamura, S., and Yasuda, N. (2004). The Line-of-Sight Velocity Distributions of Intracluster Planetary Nebulae in the Virgo Cluster Core. *ApJL*, 614:L33–L36.

Arnaboldi, M., Gerhard, O., Okamura, S., Kashikawa, N., Yasuda, N., and Freeman, K. C. (2007). Multi-Slit Imaging Spectroscopy Technique: Catalog of Intracluster Planetary Nebulae in the Coma Cluster. *Pub. Astron. Soc. Japan*, 59:419–425.

Balogh, M. L., Morris, S. L., Yee, H. K. C., Carlberg, R. G., and Ellingson, E. (1999). Differential Galaxy Evolution in Cluster and Field Galaxies at z˜0.3. *ApJ*, 527:54–79.

Baria, P., Brito, W., and Martel, H. (2009). The Fate of Dwarf Galaxies in Clusters and the Origin of Intracluster Stars. *Journal of Astrophysics and Astronomy*, 30:1–36.

Barnes, J. E. (1988). Encounters of disk/halo galaxies. *ApJ*, 331:699–717.

Bauer, F. E., Fabian, A. C., Sanders, J. S., Allen, S. W., and Johnstone, R. M. (2005). The prevalence of cooling cores in clusters of galaxies at z˜ 0.15-0.4. *MNRAS*, 359:1481–1490.

Bautz, L. P. and Morgan, W. W. (1970). On the Classification of the Forms of Clusters of Galaxies. *ApJL*, 162:L149+.

Bender, R. (1990). Unraveling the kinematics of early-type galaxies - Presentation of a new method and its application to NGC4621. *A&A*, 229:441–451.

Bender, R., Burstein, D., and Faber, S. M. (1992). Dynamically hot galaxies. I - Structural properties. *ApJ*, 399:462–477.

Bernardi, M., Hyde, J. B., Sheth, R. K., Miller, C. J., and Nichol, R. C. (2007). The Luminosities, Sizes, and Velocity Dispersions of Brightest Cluster Galaxies: Implications for Formation History. *AJ*, 133:1741–1755.

Bernstein, G. M., Nichol, R. C., Tyson, J. A., Ulmer, M. P., and Wittman, D. (1995). The Luminosity Function of the Coma Cluster Core for -25<M/R<-9.4. *AJ*, 110:1507–+.

Bernstein, J. P. and Bhavsar, S. P. (2001). Models for the magnitude-distribution of brightest cluster galaxies. *MNRAS*, 322:625–630.

Best, P. N., von der Linden, A., Kauffmann, G., Heckman, T. M., and Kaiser, C. R. (2007). On the prevalence of radio-loud active galactic nuclei in brightest cluster galaxies: implications for AGN heating of cooling flows. *MNRAS*, 379:894–908.

Binggeli, B., Sandage, A., and Tammann, G. A. (1988). The luminosity function of galaxies. *ARA&A*, 26:509–560.

Biviano, A., Murante, G., Borgani, S., Diaferio, A., Dolag, K., and Girardi, M. (2006). On the efficiency and reliability of cluster mass estimates based on member galaxies. *A&A*, 456:23–36.

Böhringer, H. (2004). X-ray Studies of the Intracluster Medium in Clusters of Galaxies - Characterizing Galaxy Clusters as Giant Laboratories. *Journal of Korean Astronomical Society*, 37:361–369.

Böhringer, H., Burwitz, V., Zhang, Y., Schuecker, P., and Nowak, N. (2005a). Chandra Reveals Galaxy Cluster with the Most Massive Nearby Cooling Core: RXC J1504.1-0248. *ApJ*, 633:148–153.

Böhringer, H., Matsushita, K., Churazov, E., Ikebe, Y., and Chen, Y. (2002). The new emerging model for the structure of cooling cores in clusters of galaxies. *A&A*, 382:804–820.

Böhringer, H., Matsushita, K., Finoguenov, A., Xue, Y., and Churazov, E. (2005b). Metal abundances in the ICM as a diagnostics of the cluster history. *Advances in Space Research*, 36:677–681.

Böhringer, H., Pratt, G. W., Arnaud, M., Borgani, S., Croston, J. H., Ponman, T. J., Ameglio, S., Temple, R. F., and Dolag, K. (2010). Substructure of the galaxy clusters in the REXCESS sample: observed statistics and comparison to numerical simulations. *A&A*, 514:A32+.

Böhringer, H., Pratt, G. W., Finoguenov, A., and Schuecker, P., editors (2007). *Heating versus Cooling in Galaxies and Clusters of Galaxies*.

Böhringer, H. and Werner, N. (2010). X-ray spectroscopy of galaxy clusters: studying astrophysical processes in the largest celestial laboratories. *A&A Rev.*, 18:127–196.

Borgani, S. (2006). Cosmology with clusters of galaxies. *ArXiv Astrophysics e-prints*.

Borgani, S. and Guzzo, L. (2001). X-ray clusters of galaxies as tracers of structure in the Universe. *Nature*, 409:39–45.

Boselli, A., Boissier, S., Cortese, L., and Gavazzi, G. (2008). The Origin of Dwarf Ellipticals in the Virgo Cluster. *ApJ*, 674:742–767.

Briel, U. G., Henry, J. P., and Boehringer, H. (1992). Observation of the Coma cluster of galaxies with ROSAT during the all-sky survey. *A&A*, 259:L31–L34.

Brough, S., Collins, C. A., Burke, D. J., Lynam, P. D., and Mann, R. G. (2005). Environmental dependence of the structure of brightest cluster galaxies. *MNRAS*, 364:1354–1362.

Buote, D. A. and Lewis, A. D. (2004). The Dark Matter Radial Profile in the Core of the Relaxed Cluster A2589. *ApJ*, 604:116–124.

Butcher, H. and Oemler, Jr., A. (1978a). The evolution of galaxies in clusters. I - ISIT photometry of C1 0024+1654 and 3C 295. *ApJ*, 219:18–30.

Butcher, H. and Oemler, Jr., A. (1978b). The evolution of galaxies in clusters. II - The galaxy content of nearby clusters. *ApJ*, 226:559–565.

Buzzoni, A., Arnaboldi, M., and Corradi, R. L. M. (2006). Planetary nebulae as tracers of galaxy stellar populations. *MNRAS*, 368:877–894.

Calcáneo-Roldán, C., Moore, B., Bland-Hawthorn, J., Malin, D., and Sadler, E. M. (2000). Galaxy destruction and diffuse light in clusters. *MNRAS*, 314:324–333.

Cappellari, M. and Emsellem, E. (2004). Parametric Recovery of Line-of-Sight Velocity Distributions from Absorption-Line Spectra of Galaxies via Penalized Likelihood. *Publ. Astr. Soc. Pac.*, 116:138–147.

Carter, D., Bridges, T. J., and Hau, G. K. T. (1999). Kinematics, abundances and origin of brightest cluster galaxies. *MNRAS*, 307:131–148.

Castro-Rodríguez, N., Aguerri, J. A. L., Arnaboldi, M., Gerhard, O., Freeman, K. C., Napolitano, N. R., and Capaccioli, M. (2003). Narrow band survey for intragroup light in the Leo HI cloud. Constraints on the galaxy background contamination in imaging surveys for intracluster planetary nebulae. *A&A*, 405:803–812.

Castro-Rodriguéz, N., Arnaboldi, M., Aguerri, J. A. L., Gerhard, O., Okamura, S., Yasuda, N., and Freeman, K. C. (2009). Intracluster light in the Virgo cluster: large scale distribution. *A&A*, 507:621–634.

Cavaliere, A. and Fusco-Femiano, R. (1976). X-rays from hot plasma in clusters of galaxies. *A&A*, 49:137–144.

Christlein, D. and Zabludoff, A. I. (2003). Galaxy Luminosity Functions from Deep Spectroscopic Samples of Rich Clusters. *ApJ*, 591:764–783.

Ciardullo, R. (2003). Planetary Nebulae as Extragalactic Distance Indicators (invited review). In S. Kwok, M. Dopita, & R. Sutherland, editor, *Planetary Nebulae: Their Evolution and Role in the Universe*, volume 209 of *IAU Symposium*, pages 617–+.

Ciardullo, R., Feldmeier, J. J., Krelove, K., Jacoby, G. H., and Gronwall, C. (2002). A Measurement of the Contamination in [O III] λ5007 Surveys of Intracluster Stars and the Surface Density of z=3.13 Lyα Galaxies. *ApJ*, 566:784–793.

Ciardullo, R., Jacoby, G. H., Feldmeier, J. J., and Bartlett, R. E. (1998). The Planetary Nebula Luminosity Function of M87 and the Intracluster Stars of Virgo. *ApJ*, 492:62–+.

Ciardullo, R., Jacoby, G. H., Ford, H. C., and Neill, J. D. (1989). Planetary nebulae as standard candles. II - The calibration in M31 and its companions. *ApJ*, 339:53–69.

Ciardullo, R., Mihos, J. C., Feldmeier, J. J., Durrell, P. R., and Sigurdsson, S. (2004). The Systematics of Intracluster Starlight. In P.-A. Duc, J. Braine, & E. Brinks, editor, *Recycling Intergalactic and Interstellar Matter*, volume 217 of *IAU Symposium*, pages 88–+.

Ciardullo, R., Sigurdsson, S., Feldmeier, J. J., and Jacoby, G. H. (2005). Close Binaries as the Progenitors of the Brightest Planetary Nebulae. *ApJ*, 629:499–506.

Coccato, L., Arnaboldi, M., Gerhard, O., Freeman, K. C., Ventimiglia, G., and Yasuda, N. (2010a). Kinematics and line strength indices in the halos of the Coma Brightest Cluster Galaxies NGC 4874 and NGC 4889. *ArXiv e-prints*.

Coccato, L., Gerhard, O., and Arnaboldi, M. (2010b). Distinct core and halo stellar populations and the formation history of the bright Coma cluster early-type galaxy NGC 4889. *MNRAS*, pages L97+.

Coccato, L., Gerhard, O., Arnaboldi, M., Das, P., Douglas, N. G., Kuijken, K., Merrifield, M. R., Napolitano, N. R., Noordermeer, E., Romanowsky, A. J., Capaccioli, M., Cortesi, A., de Lorenzi, F., and Freeman, K. C. (2009). Kinematic properties of early-type galaxy haloes using planetary nebulae. *MNRAS*, 394:1249–1283.

Cortese, L., Marcillac, D., Richard, J., Bravo-Alfaro, H., Kneib, J., Rieke, G., Covone, G., Egami, E., Rigby, J., Czoske, O., and Davies, J. (2007). The strong transformation of spiral galaxies infalling into massive clusters at z ˜ 0.2. *MNRAS*, 376:157–172.

Da Rocha, C., Ziegler, B. L., and Mendes de Oliveira, C. (2008). Intragroup diffuse light in compact groups of galaxies - II. HCG 15, 35 and 51. *MNRAS*, 388:1433–1443.

De Lucia, G. (2007). How 'Heredity' and 'Environment' Shape Galaxy Properties. In N. Metcalfe & T. Shanks, editor, *Cosmic Frontiers*, volume 379 of *Astronomical Society of the Pacific Conference Series*, pages 257–+.

De Lucia, G. and Blaizot, J. (2007). The hierarchical formation of the brightest cluster galaxies. *MNRAS*, 375:2–14.

De Lucia, G., Poggianti, B. M., Aragón-Salamanca, A., Clowe, D., Halliday, C., Jablonka, P., Milvang-Jensen, B., Pelló, R., Poirier, S., Rudnick, G., Saglia, R., Simard, L., and White, S. D. M. (2004). The Buildup of the Red Sequence in Galaxy Clusters since z ˜ 0.8. *ApJL*, 610:L77–L80.

De Lucia, G., Springel, V., White, S. D. M., Croton, D., and Kauffmann, G. (2006). The formation history of elliptical galaxies. *MNRAS*, 366:499–509.

De Propris, R., Colless, M., Driver, S. P., Couch, W., Peacock, J. A., Baldry, I. K., Baugh, C. M., Bland-Hawthorn, J., Bridges, T., Cannon, R., Cole, S., Collins, C., Cross, N., Dalton, G. B., Efstathiou, G., Ellis, R. S., Frenk, C. S., Glazebrook, K., Hawkins, E., Jackson, C., Lahav, O., Lewis, I., Lumsden, S., Maddox, S., Madgwick, D. S., Norberg, P., Percival, W., Peterson, B., Sutherland, W., and Taylor, K. (2003). The 2dF Galaxy Redshift Survey: the luminosity function of cluster galaxies. *MNRAS*, 342:725–737.

de Rijcke, S., Michielsen, D., Dejonghe, H., Zeilinger, W. W., and Hau, G. K. T. (2005). Formation and evolution of dwarf elliptical galaxies. I. Structural and kinematical properties. *A&A*, 438:491–505.

de Vaucouleurs, G. (1948). Recherches sur les Nebuleuses Extragalactiques. *Annales d'Astrophysique*, 11:247–+.

de Vaucouleurs, G., de Vaucouleurs, A., Corwin, Jr., H. G., Buta, R. J., Paturel, G., and Fouque, P. (1991). *Third Reference Catalogue of Bright Galaxies*.

Dekel, A. and Silk, J. (1986). The origin of dwarf galaxies, cold dark matter, and biased galaxy formation. *ApJ*, 303:39–55.

Desroches, L., Quataert, E., Ma, C., and West, A. A. (2007). Luminosity dependence in the Fundamental Plane projections of elliptical galaxies. *MNRAS*, 377:402–414.

Doherty, M., Arnaboldi, M., Das, P., Gerhard, O., Aguerri, J. A. L., Ciardullo, R., Feldmeier, J. J., Freeman, K. C., Jacoby, G. H., and Murante, G. (2009). The edge of the M 87 halo and the kinematics of the diffuse light in the Virgo cluster core. *A&A*, 502:771–786.

Dolag, K., Murante, G., and Borgani, S. (2009). Dynamical difference between the cD galaxy and the stellar diffuse component in simulated galaxy clusters. *ArXiv e-prints*.

Dolag, K., Murante, G., and Borgani, S. (2010). Dynamical difference between the cD galaxy and the diffuse, stellar component in simulated galaxy clusters. *MNRAS*, 405:1544–1559.

Dopita, M. A., Jacoby, G. H., and Vassiliadis, E. (1992). A theoretical calibration of the planetary nebular cosmic distance scale. *ApJ*, 389:27–38.

Dopita, M. A., Massaglia, S., Bodo, G., Arnaboldi, M., and Merluzzi, P. (2000). Do the Nuclei of Elliptical Galaxies Eat Planetary Nebulae? In J. H. Kastner, N. Soker, & S. Rappaport, editor, *Asymmetrical Planetary Nebulae II: From Origins to Microstructures*, volume 199 of *Astronomical Society of the Pacific Conference Series*, pages 423–+.

Douglas, N. G., Arnaboldi, M., Freeman, K. C., Kuijken, K., Merrifield, M. R., Romanowsky, A. J., Taylor, K., Capaccioli, M., Axelrod, T., Gilmozzi, R., Hart, J., Bloxham, G., and Jones, D. (2002). The Planetary Nebula Spectrograph: The Green Light for Galaxy Kinematics. *Publ. Astr. Soc. Pac.*, 114:1234–1251.

Dressler, A. (1978). A comprehensive study of 12 very rich clusters of galaxies. I - Photometric technique and analysis of the luminosity function. *ApJ*, 223:765–775.

Dressler, A. (1980). Galaxy morphology in rich clusters - Implications for the formation and evolution of galaxies. *ApJ*, 236:351–365.

Dressler, A. and Gunn, J. E. (1983). Spectroscopy of galaxies in distant clusters. II - The population of the 3C 295 cluster. *ApJ*, 270:7–19.

Dressler, A., Lynden-Bell, D., Burstein, D., Davies, R. L., Faber, S. M., Terlevich, R., and Wegner, G. (1987). Spectroscopy and photometry of elliptical galaxies. I - A new distance estimator. *ApJ*, 313:42–58.

Dressler, A., Oemler, Jr., A., Butcher, H. R., and Gunn, J. E. (1994). The morphology of distant cluster galaxies. 1: HST observations of CL 0939+4713. *ApJ*, 430:107–120.

Dressler, A., Oemler, Jr., A., Couch, W. J., Smail, I., Ellis, R. S., Barger, A., Butcher, H., Poggianti, B. M., and Sharples, R. M. (1997). Evolution since Z = 0.5 of the Morphology-Density Relation for Clusters of Galaxies. *ApJ*, 490:577–+.

Dressler, A. and Shectman, S. A. (1988). Evidence for substructure in rich clusters of galaxies from radial-velocity measurements. *AJ*, 95:985–995.

Dubinski, J. (1998). The Origin of the Brightest Cluster Galaxies. *ApJ*, 502:141–+.

Durrell, P. R., Ciardullo, R., Feldmeier, J. J., Jacoby, G. H., and Sigurdsson, S. (2002). Intracluster Red Giant Stars in the Virgo Cluster. *ApJ*, 570:119–131.

Edge, A. C. and Frayer, D. T. (2003). Resolving Molecular gas in the Central Galaxies of Cooling Flow Clusters. *ApJL*, 594:L13–L17.

Eke, V. R., Cole, S., Frenk, C. S., and Patrick Henry, J. (1998). Measuring Omega_0 using cluster evolution. *MNRAS*, 298:1145–1158.

Ettori, S. (2005). Brief history of metal accumulation in the intracluster medium. *MNRAS*, 362:110–116.

Ettori, S., Allen, S. W., and Fabian, A. C. (2001). BeppoSAX observations of three distant, highly luminous clusters of galaxies: RXJ1347-1145, Zwicky 3146 and Abell 2390. *MNRAS*, 322:187–194.

Faber, S. M., Dressler, A., Davies, R. L., Burstein, D., and Lynden-Bell, D. (1987). Global scaling relations for elliptical galaxies and implications for formation. In S. M. Faber, editor, *Nearly Normal Galaxies. From the Planck Time to the Present*, pages 175–183.

Faber, S. M., Friel, E. D., Burstein, D., and Gaskell, C. M. (1985). Old stellar populations. II - an analysis of K-giant spectra. *ApJS*, 57:711–741.

Faber, S. M. and Jackson, R. E. (1976). Velocity dispersions and mass-to-light ratios for elliptical galaxies. *ApJ*, 204:668–683.

Fabian, A. C. (1994). Cooling Flows in Clusters of Galaxies. *ARA&A*, 32:277–318.

Fabian, A. C. and Nulsen, P. E. J. (1977). Subsonic accretion of cooling gas in clusters of galaxies. *MNRAS*, 180:479–484.

Fabian, A. C., Sanders, J. S., Taylor, G. B., Allen, S. W., Crawford, C. S., Johnstone, R. M., and Iwasawa, K. (2006). A very deep Chandra observation of the Perseus cluster: shocks, ripples and conduction. *MNRAS*, 366:417–428.

Faltenbacher, A. and Mathews, W. G. (2005). On the dynamics of the satellite galaxies in NGC 5044. *MNRAS*, 362:498–504.

Fasano, G., Poggianti, B. M., Couch, W. J., Bettoni, D., Kjærgaard, P., and Moles, M. (2000). The Evolution of the Galactic Morphological Types in Clusters. *ApJ*, 542:673–683.

Feldmeier, J. J., Ciardullo, R., Jacoby, G. H., and Durrell, P. R. (2003). Intracluster Planetary Nebulae in the Virgo Cluster. II. Imaging Catalog. *ApJS*, 145:65–81.

Feldmeier, J. J., Ciardullo, R., Jacoby, G. H., and Durrell, P. R. (2004). Intracluster Planetary Nebulae in the Virgo Cluster. III. Luminosity of the Intracluster Light and Tests of the Spatial Distribution. *ApJ*, 615:196–208.

Feldmeier, J. J., Mihos, J. C., Morrison, H. L., Rodney, S. A., and Harding, P. (2002). Deep CCD Surface Photometry of Galaxy Clusters. I. Methods and Initial Studies of Intracluster Starlight. *ApJ*, 575:779–800.

Felten, J. E., Gould, R. J., Stein, W. A., and Woolf, N. J. (1966). X-Rays from the Coma Cluster of Galaxies. *ApJ*, 146:955–958.

Fisher, D., Illingworth, G., and Franx, M. (1995). Kinematics of 13 brightest cluster galaxies. *ApJ*, 438:539–562.

Fitchett, M. and Merritt, D. (1988). Dynamics of the Hydra I galaxy cluster. *ApJ*, 335:18–34.

Forman, W., Jones, C., Cominsky, L., Julien, P., Murray, S., Peters, G., Tananbaum, H., and Giacconi, R. (1978). The fourth Uhuru catalog of X-ray sources. *ApJS*, 38:357–412.

Freeman, K. C., Arnaboldi, M., Capaccioli, M., Ciardullo, R., Feldmeier, J., Ford, H., Gerhard, O., Kudritzki, R., Jacoby, G., Méndez, R. H., and Sharples, R. (2000). Intracluster Planetary Nebulae in the Virgo Cluster. In F. Combes, G. A. Mamon, & V. Charmandaris, editor, *Dynamics of Galaxies: from the Early Universe to the Present*, volume 197 of *Astronomical Society of the Pacific Conference Series*, pages 389–+.

Furusho, T., Yamasaki, N. Y., Ohashi, T. S. R., Kagei, T., Ishisaki, Y., Kikuchi, K., Ezawa, H., and Ikebe, Y. (2001). ASCA Temperature Maps of Three Clusters of Galaxies: Abell 1060, AWM 7, and the Centaurus Cluster. *Pub. Astron. Soc. Japan*, 53:421–432.

Gal-Yam, A., Maoz, D., Guhathakurta, P., and Filippenko, A. V. (2003). A Population of Intergalactic Supernovae in Galaxy Clusters. *AJ*, 125:1087–1094.

Garilli, B., Maccagni, D., and Andreon, S. (1999). Composite luminosity function of cluster galaxies. *A&A*, 342:408–416.

Geha, M. (2003). *Internal dynamics, structure and formation of dwarf elliptical galaxies*. PhD thesis, UNIVERSITY OF CALIFORNIA, SANTA CRUZ.

Geller, M. J. and Beers, T. C. (1982). Substructure within clusters of galaxies. *Publ. Astr. Soc. Pac.*, 94:421–439.

Gerhard, O., Arnaboldi, M., Freeman, K. C., Kashikawa, N., Okamura, S., and Yasuda, N. (2005). Detection of Intracluster Planetary Nebulae in the Coma Cluster. *ApJL*, 621:L93–L96.

Gerhard, O., Arnaboldi, M., Freeman, K. C., and Okamura, S. (2002). Isolated Star Formation: A Compact H II Region in the Virgo Cluster. *ApJL*, 580:L121–L124.

Gerhard, O., Arnaboldi, M., Freeman, K. C., Okamura, S., Kashikawa, N., and Yasuda, N. (2007). The kinematics of intracluster planetary nebulae and the on-going subcluster merger in the Coma cluster core. *A&A*, 468:815–822.

Gerhard, O. E. (1981). N-body simulations of disc-halo galaxies - Isolated systems, tidal interactions and merging. *MNRAS*, 197:179–208.

Gerhard, O. E. (1993). Line-of-sight velocity profiles in spherical galaxies: breaking the degeneracy between anisotropy and mass. *MNRAS*, 265:213–+.

Giacconi, R., Murray, S., Gursky, H., Kellogg, E., Schreier, E., and Tananbaum, H. (1972). The Uhuru catalog of X-ray sources. *ApJ*, 178:281–308.

Giavalisco, M. (2002). Lyman-Break Galaxies. *ARA&A*, 40:579–641.

Gladders, M. D. and Yee, H. K. C. (2000). A New Method For Galaxy Cluster Detection. I. The Algorithm. *AJ*, 120:2148–2162.

Gnedin, O. Y. (2003). Tidal Effects in Clusters of Galaxies. *ApJ*, 582:141–161.

Gonzalez, A. H., Zabludoff, A. I., and Zaritsky, D. (2005). Intracluster Light in Nearby Galaxy Clusters: Relationship to the Halos of Brightest Cluster Galaxies. *ApJ*, 618:195–213.

Gonzalez, A. H., Zabludoff, A. I., Zaritsky, D., and Dalcanton, J. J. (2000). Measuring the Diffuse Optical Light in Abell 1651. *ApJ*, 536:561–570.

Gonzalez, A. H., Zaritsky, D., and Zabludoff, A. I. (2007). A Census of Baryons in Galaxy Clusters and Groups. *ApJ*, 666:147–155.

Gronwall, C., Ciardullo, R., Hickey, T., Gawiser, E., Feldmeier, J. J., van Dokkum, P. G., Urry, C. M., Herrera, D., Lehmer, B. D., Infante, L., Orsi, A., Marchesini, D., Blanc, G. A., Francke, H., Lira, P., and Treister, E. (2007). Lyα Emission-Line Galaxies at z = 3.1 in the Extended Chandra Deep Field-South. *ApJ*, 667:79–91.

Gunn, J. E. and Gott, III, J. R. (1972). On the Infall of Matter Into Clusters of Galaxies and Some Effects on Their Evolution. *ApJ*, 176:1–+.

Hansen, S. M., McKay, T. A., Wechsler, R. H., Annis, J., Sheldon, E. S., and Kimball, A. (2005). Measurement of Galaxy Cluster Sizes, Radial Profiles, and Luminosity Functions from SDSS Photometric Data. *ApJ*, 633:122–137.

Hau, G. K. T., Hilker, M., Bridges, T., Carter, D., Dejonghe, H., de Rijcke, S., and Quintana, H. (2004). The stellar kinematics of the giant halos of Brightest Cluster Galaxies. In A. Diaferio, editor, *IAU Colloq. 195: Outskirts of Galaxy Clusters: Intense Life in the Suburbs*, pages 491–495.

Hausman, M. A. and Ostriker, J. P. (1978). Galactic cannibalism. III - The morphological evolution of galaxies and clusters. *ApJ*, 224:320–336.

Hayakawa, A., Furusho, T., Yamasaki, N. Y., Ishida, M., and Ohashi, T. (2004). Inhomogeneity in the Hot Intracluster Medium of Abell 1060 Observed with Chandra. *Pub. Astron. Soc. Japan*, 56:743–752.

Hayakawa, A., Hoshino, A., Ishida, M., Furusho, T., Yamasaki, N. Y., and Ohashi, T. (2006). Detailed XMM-Newton Observation of the Cluster of Galaxies Abell 1060. *Pub. Astron. Soc. Japan*, 58:695–702.

Henize, K. G. and Westerlund, B. E. (1963). Dimensions of Diffuse and Planetary Nebulae in the Small Magellanic Cloud. *ApJ*, 137:747–+.

Herrmann, K. A., Ciardullo, R., Feldmeier, J. J., and Vinciguerra, M. (2008). Planetary Nebulae in Face-On Spiral Galaxies. I. Planetary Nebula Photometry and Distances. *ApJ*, 683:630–643.

Hilker, M. (2002). Globular Cluster Systems in the Hydra I Galaxy Cluster. In D. P. Geisler, E. K. Grebel, & D. Minniti, editor, *Extragalactic Star Clusters*, volume 207 of *IAU Symposium*, pages 281–+.

Hilker, M. (2003). Globular Clusters in Nearby Galaxy Clusters. In M. Kissler-Patig, editor, *Extragalactic Globular Cluster Systems*, pages 173–+.

Hogg, D. W., Cohen, J. G., Blandford, R., and Pahre, M. A. (1998). The O II Luminosity Density of the Universe. *ApJ*, 504:622–+.

Hu, E. M., Cowie, L. L., and McMahon, R. G. (1998). The Density of Ly alpha Emitters at Very High Redshift. *ApJL*, 502:L99+.

Hubble, E. and Rosseland, S. (1936). Astronomy. (Scientific Books: The Realm of the Nebulae; Theoretical Astrophysics). *Science*, 84:509–510.

Jacoby, G. H. (1980). The luminosity function for planetary nebulae and the number of planetary nebulae in local group galaxies. *ApJS*, 42:1–18.

Jacoby, G. H. (1989). Planetary nebulae as standard candles. I - Evolutionary models. *ApJ*, 339:39–52.

Jacoby, G. H., Branch, D., Ciardullo, R., Davies, R. L., Harris, W. E., Pierce, M. J., Pritchet, C. J., Tonry, J. L., and Welch, D. L. (1992). A critical review of selected techniques for measuring extragalactic distances. *Publ. Astr. Soc. Pac.*, 104:599–662.

Jacoby, G. H. and Ciardullo, R. (1999). Chemical Abundances of Planetary Nebulae in the Bulge and Disk of M31. *ApJ*, 515:169–190.

Jarrett, T. H., Chester, T., Cutri, R., Schneider, S. E., and Huchra, J. P. (2003). The 2MASS Large Galaxy Atlas. *AJ*, 125:525–554.

Jerjen, H. and Tammann, G. A. (1997). Studies of the Centaurus cluster. III. Luminosity functions of individual Hubble-types as compared to Virgo and Fornax. *A&A*, 321:713–723.

Jordán, A., Peng, E. W., Blakeslee, J. P., Côté, P., Eyheramendy, S., Ferrarese, L., Mei, S., Tonry, J. L., and West, M. J. (2009). The ACS Virgo Cluster Survey XVI. Selection Procedure and Catalogs of Globular Cluster Candidates. *ApJS*, 180:54–66.

Kaastra, J. S. and Mewe, R. (2000). Coronal Plasmas Modeling and the MEKAL code. In M. A. Bautista, T. R. Kallman, & A. K. Pradhan, editor, *Atomic Data Needs for X-ray Astronomy*, pages 161–+.

Kapferer, W., Schindler, S., Knollmann, S. R., and van Kampen, E. (2010). The evolution of an intra-cluster and intra-group stellar population. Their contribution to the stellar mass, their age, and their dynamics. *A&A*, 516:A41+.

Kelson, D. D., Zabludoff, A. I., Williams, K. A., Trager, S. C., Mulchaey, J. S., and Bolte, M. (2002). Determination of the Dark Matter Profile of A2199 from Integrated Starlight. *ApJ*, 576:720–737.

Khochfar, S. and Burkert, A. (2003). The Importance of Spheroidal and Mixed Mergers for Early-Type Galaxy Formation. *ApJL*, 597:L117–L120.

Koester, B. P., McKay, T. A., Annis, J., Wechsler, R. H., Evrard, A. E., Rozo, E., Bleem, L., Sheldon, E. S., and Johnston, D. (2007). MaxBCG: A Red-Sequence Galaxy Cluster Finder. *ApJ*, 660:221–238.

Kofman, L. A., Gnedin, N. Y., and Bahcall, N. A. (1993). Cosmological constant, COBE cosmic microwave background anisotropy, and large-scale clustering. *ApJ*, 413:1–9.

Kormendy, J. (1977). Brightness distributions in compact and normal galaxies. II - Structure parameters of the spheroidal component. *ApJ*, 218:333–346.

Kormendy, J., Fisher, D. B., Cornell, M. E., and Bender, R. (2009). Structure and Formation of Elliptical and Spheroidal Galaxies. *ApJS*, 182:216–309.

Kravtsov, A. V. and Yepes, G. (2000). On the supernova heating of the intergalactic medium. *MNRAS*, 318:227–238.

Krick, J. E. and Bernstein, R. A. (2007). Diffuse Optical Light in Galaxy Clusters. II. Correlations with Cluster Properties. *AJ*, 134:466–493.

Kudritzki, R., Méndez, R. H., Feldmeier, J. J., Ciardullo, R., Jacoby, G. H., Freeman, K. C., Arnaboldi, M., Capaccioli, M., Gerhard, O., and Ford, H. C. (2000). Discovery of Nine Lyα Emitters at Redshift z˜3.1 Using Narrowband Imaging and VLT Spectroscopy. *ApJ*, 536:19–30.

Kuntschner, H., Emsellem, E., Bacon, R., Bureau, M., Cappellari, M., Davies, R. L., de Zeeuw, P. T., Falcón-Barroso, J., Krajnović, D., McDermid, R. M., Peletier, R. F., and Sarzi, M. (2006). The SAURON project - VI. Line strength maps of 48 elliptical and lenticular galaxies. *MNRAS*, 369:497–528.

Laine, S., van der Marel, R. P., Lauer, T. R., Postman, M., O'Dea, C. P., and Owen, F. N. (2003). Hubble Space Telescope Imaging of Brightest Cluster Galaxies. *AJ*, 125:478–505.

Lee, M. G., Park, H. S., and Hwang, H. S. (2010). Detection of a Large-Scale Structure of Intracluster Globular Clusters in the Virgo Cluster. *Science*, 328:334–.

Lewis, A. D., Buote, D. A., and Stocke, J. T. (2003). Chandra Observations of A2029: The Dark Matter Profile Down to below 0.01r_{vir} in an Unusually Relaxed Cluster. *ApJ*, 586:135–142.

Liedahl, D. A., Osterheld, A. L., and Goldstein, W. H. (1995). New calculations of Fe L-shell X-ray spectra in high-temperature plasmas. *ApJL*, 438:L115–L118.

Lin, Y. and Mohr, J. J. (2004). K-band Properties of Galaxy Clusters and Groups: Brightest Cluster Galaxies and Intracluster Light. *ApJ*, 617:879–895.

Liu, F. S., Mao, S., Deng, Z. G., Xia, X. Y., and Wen, Z. L. (2009). Major dry mergers in early-type brightest cluster galaxies. *MNRAS*, 396:2003–2010.

Loubser, S. I., Sánchez-Blázquez, P., Sansom, A. E., and Soechting, I. K. (2009). Stellar populations in the centres of brightest cluster galaxies. *MNRAS*, 398:133–156.

Loubser, S. I., Sansom, A. E., Sánchez-Blázquez, P., Soechting, I. K., and Bromage, G. E. (2008). Radial kinematics of brightest cluster galaxies. *MNRAS*, 391:1009–1028.

Lugger, P. M. (1986). Luminosity functions for nine Abell clusters. *ApJ*, 303:535–555.

Marigo, P., Girardi, L., Weiss, A., Groenewegen, M. A. T., and Chiosi, C. (2004). Evolution of planetary nebulae. II. Population effects on the bright cut-off of the PNLF. *A&A*, 423:995–1015.

Martin, C. L., Sawicki, M., Dressler, A., and McCarthy, P. (2008). A Magellan IMACS Spectroscopic Search for Lyα-emitting Galaxies at Redshift 5.7. *ApJ*, 679:942–961.

Mastropietro, C., Moore, B., Mayer, L., Debattista, V. P., Piffaretti, R., and Stadel, J. (2005). Morphological evolution of discs in clusters. *MNRAS*, 364:607–619.

Mateo, M. L. (1998). Dwarf Galaxies of the Local Group. *ARA&A*, 36:435–506.

Matteucci, F. and Vettolani, G. (1988). Chemical abundances in galaxy clusters - A theoretical approach. *A&A*, 202:21–26.

Mayer, L., Mastropietro, C., Wadsley, J., Stadel, J., and Moore, B. (2006). Simultaneous ram pressure and tidal stripping; how dwarf spheroidals lost their gas. *MNRAS*, 369:1021–1038.

McGee, S. L. and Balogh, M. L. (2010). Constraints on intragroup stellar mass from hostless Type Ia supernovae. *MNRAS*, 403:L79–L83.

McIntosh, D. H., Guo, Y., Hertzberg, J., Katz, N., Mo, H. J., van den Bosch, F. C., and Yang, X. (2008). Ongoing assembly of massive galaxies by major merging in large groups and clusters from the SDSS. *MNRAS*, 388:1537–1556.

McMahon, P. M., van Gorkom, J. H., Richter, O., and Ferguson, H. C. (1992). H I imaging of NGC 3312 and NGC 3314a - A foreground group to the Hydra cluster? *AJ*, 103:399–404.

McNeil, E. K., Arnaboldi, M., Freeman, K. C., Gerhard, O. E., Coccato, L., and Das, P. (2010). Counter-dispersed slitless-spectroscopy technique: planetary nebula velocities in the halo of NGC 1399. *A&A*, 518:A44+.

Menci, N. and Cavaliere, A. (2000). The history of cosmic baryons: X-ray emission versus star formation rate. *MNRAS*, 311:50–62.

Mendel, J. T., Proctor, R. N., Rasmussen, J., Brough, S., and Forbes, D. A. (2009). The anatomy of the NGC5044 group - II. Stellar populations and star formation histories. *MNRAS*, 396:2103–2123.

Méndez, R. H., Riffeser, A., Kudritzki, R., Matthias, M., Freeman, K. C., Arnaboldi, M., Capaccioli, M., and Gerhard, O. E. (2001). Detection, Photometry, and Slitless Radial Velocities of 535 Planetary Nebulae in the Flattened Elliptical Galaxy NGC 4697. *ApJ*, 563:135–150.

Mendez, R. H. and Soffner, T. (1997). Improved simulations of the planetary nebula luminosity function. *A&A*, 321:898–906.

Merritt, D. (1984). Relaxation and tidal stripping in rich clusters of galaxies. II. Evolution of the luminosity distribution. *ApJ*, 276:26–37.

Merritt, D. (1985). Relaxation and tidal stripping in rich clusters of galaxies. III - Growth of a massive central galaxy. *ApJ*, 289:18–32.

Michielsen, D., Boselli, A., Conselice, C. J., Toloba, E., Whiley, I. M., Aragón-Salamanca, A., Balcells, M., Cardiel, N., Cenarro, A. J., Gorgas, J., Peletier, R. F., and Vazdekis, A. (2008). The relation between stellar populations, structure and environment for dwarf elliptical galaxies from the MAGPOP-ITP. *MNRAS*, 385:1374–1392.

Mieske, S., Hilker, M., and Infante, L. (2005). The distance to Hydra and Centaurus from surface brightness fluctuations: Consequences for the Great Attractor model. *A&A*, 438:103–119.

Mihos, J. C. (2004). Interactions and Mergers of Cluster Galaxies. *Clusters of Galaxies: Probes of Cosmological Structure and Galaxy Evolution*, pages 277–+.

Mihos, J. C., Harding, P., Feldmeier, J., and Morrison, H. (2005). Diffuse Light in the Virgo Cluster. *ApJL*, 631:L41–L44.

Misgeld, I., Hilker, M., and Mieske, S. (2009). The early-type dwarf galaxy population of the Centaurus cluster. *A&A*, 496:683–693.

Misgeld, I., Mieske, S., and Hilker, M. (2008). The early-type dwarf galaxy population of the Hydra I cluster. *A&A*, 486:697–709.

Moore, B., Katz, N., Lake, G., Dressler, A., and Oemler, A. (1996). Galaxy harassment and the evolution of clusters of galaxies. *Nature*, 379:613–616.

Moore, B., Lake, G., and Katz, N. (1998). Morphological Transformation from Galaxy Harassment. *ApJ*, 495:139–+.

Morelli, L., Pompei, E., Pizzella, A., Méndez-Abreu, J., Corsini, E. M., Coccato, L., Saglia, R. P., Sarzi, M., and Bertola, F. (2008). Stellar populations of bulges in 14 cluster disc galaxies. *MNRAS*, 389:341–363.

Murante, G., Arnaboldi, M., Gerhard, O., Borgani, S., Cheng, L. M., Diaferio, A., Dolag, K., Moscardini, L., Tormen, G., Tornatore, L., and Tozzi, P. (2004). The Diffuse Light in Simulations of Galaxy Clusters. *ApJL*, 607:L83–L86.

Murante, G., Giovalli, M., Gerhard, O., Arnaboldi, M., Borgani, S., and Dolag, K. (2007). The importance of mergers for the origin of intracluster stars in cosmological simulations of galaxy clusters. *MNRAS*, 377:2–16.

Mushotzky, R. F. and Loewenstein, M. (1997). Lack of Evolution in the Iron Abundance in Clusters of Galaxies and Implications for the Global Star Formation Rate at High Redshift. *ApJL*, 481:L63+.

Naab, T. and Burkert, A. (2003). Statistical Properties of Collisionless Equal- and Unequal-Mass Merger Remnants of Disk Galaxies. *ApJ*, 597:893–906.

Napolitano, N. R., Pannella, M., Arnaboldi, M., Gerhard, O., Aguerri, J. A. L., Freeman, K. C., Capaccioli, M., Ghigna, S., Governato, F., Quinn, T., and Stadel, J. (2003). Intracluster Stellar Population Properties from N-Body Cosmological Simulations. I. Constraints at z = 0. *ApJ*, 594:172–185.

Navarro, J. F., Frenk, C. S., and White, S. D. M. (1997). A Universal Density Profile from Hierarchical Clustering. *ApJ*, 490:493–+.

Neill, J. D., Shara, M. M., and Oegerle, W. R. (2005). Tramp Novae between Galaxies in the Fornax Cluster: Tracers of Intracluster Light. *ApJ*, 618:692–704.

Oemler, Jr., A. (1974). The Systematic Properties of Clusters of Galaxies. Photometry of 15 Clusters. *ApJ*, 194:1–20.

Okamura, S., Yasuda, N., Arnaboldi, M., Freeman, K. C., Ando, H., Doi, M., Furusawa, H., Gerhard, O., Hamabe, M., Kimura, M., Kajino, T., Komiyama, Y., Miyazaki, S., Nakata, F., Napolitano, N. R., Ouchi, M., Pannella, M., Sekiguchi, M., Shimasaku, K., and Yagi, M. (2002). Candidates for Intracluster Planetary Nebulae in the Virgo Cluster Based on the Suprime-Cam Narrow-Band Imaging in [O III] and Hα. *Pub. Astron. Soc. Japan*, 54:883–889.

O'Sullivan, E., Forbes, D. A., and Ponman, T. J. (2001). A catalogue and analysis of X-ray luminosities of early-type galaxies. *MNRAS*, 328:461–484.

Ouchi, M., Shimasaku, K., Akiyama, M., Sekiguchi, K., Furusawa, H., Okamura, S., Kashikawa, N., Iye, M., Kodama, T., Saito, T., Sasaki, T., Simpson, C., Takata, T., Yamada, T., Yamanoi, H., Yoshida, M., and Yoshida, M. (2005). The Discovery of Primeval Large-Scale Structures with Forming Clusters at Redshift 6. *ApJL*, 620:L1–L4.

Ouchi, M., Shimasaku, K., Akiyama, M., Simpson, C., Saito, T., Ueda, Y., Furusawa, H., Sekiguchi, K., Yamada, T., Kodama, T., Kashikawa, N., Okamura, S., Iye, M., Takata, T., Yoshida, M., and Yoshida, M. (2008). The Subaru/XMM-Newton Deep Survey (SXDS). IV. Evolution of Ly alpha Emitters from z=3.1 to 5.7 in the 1 deg2 Field: Luminosity Functions and AGN. *ApJS*, 176:301–330.

Peacock, J. (1999). Book Review: Cosmological physics / Cambridge U Press, 1999. *Nature*, 399:322–+.

Peebles, J. E. (1993). Book Review: Principles of physical cosmology / Princeton U Press, 1993. *Physics Today*, 46:87–+.

Peng, C. Y., Ho, L. C., Impey, C. D., and Rix, H. (2002). Detailed Structural Decomposition of Galaxy Images. *AJ*, 124:266–293.

Peterson, J. R. and Fabian, A. C. (2006). X-ray spectroscopy of cooling clusters. *Phys. Rep.*, 427:1–39.

Pierini, D., Zibetti, S., Braglia, F., Böhringer, H., Finoguenov, A., Lynam, P. D., and Zhang, Y. (2008). Diffuse stellar emission in X-ray luminous galaxy clusters at z ˜ 0.3. I. Is the diffuse optical light boosted and rejuvenated in merging clusters? *A&A*, 483:727–739.

Poggianti, B. M. (2004). Evolution of galaxies in clusters. In R. Dettmar, U. Klein, & P. Salucci, editor, *Baryons in Dark Matter Halos*.

Poggianti, B. M., Bridges, T. J., Komiyama, Y., Yagi, M., Carter, D., Mobasher, B., Okamura, S., and Kashikawa, N. (2004). A Comparison of the Galaxy Populations in the Coma and Distant Clusters: The Evolution of k+a Galaxies and the Role of the Intracluster Medium. *ApJ*, 601:197–213.

Poggianti, B. M., von der Linden, A., De Lucia, G., Desai, V., Simard, L., Halliday, C., Aragón-Salamanca, A., Bower, R., Varela, J., Best, P., Clowe, D. I., Dalcanton, J., Jablonka, P., Milvang-Jensen, B., Pello, R., Rudnick, G., Saglia, R., White, S. D. M., and Zaritsky, D. (2006). The Evolution of the Star Formation Activity in Galaxies and Its Dependence on Environment. *ApJ*, 642:188–215.

Pointecouteau, E., Arnaud, M., and Pratt, G. W. (2005). The structural and scaling properties of nearby galaxy clusters. I. The universal mass profile. *A&A*, 435:1–7.

Pracy, M. B., De Propris, R., Driver, S. P., Couch, W. J., and Nulsen, P. E. J. (2004). The dwarf galaxy population in Abell 2218. *MNRAS*, 352:1135–1144.

Pratt, G. W. and Arnaud, M. (2002). The mass profile of ¡ASTROBJ¿A1413¡/ASTROBJ¿ observed with XMM-Newton: Implications for the M-T relation. *A&A*, 394:375–393.

Pratt, G. W. and Arnaud, M. (2005). XMM-Newton observations of three poor clusters: Similarity in dark matter and entropy profiles down to low mass. *A&A*, 429:791–806.

Puchwein, E., Springel, V., Sijacki, D., and Dolag, K. (2010). Intracluster stars in simulations with active galactic nucleus feedback. *MNRAS*, 406:936–951.

Purcell, C. W., Bullock, J. S., and Zentner, A. R. (2007). Shredded Galaxies as the Source of Diffuse Intrahalo Light on Varying Scales. *ApJ*, 666:20–33.

Rafferty, D. A., McNamara, B. R., and Nulsen, P. E. J. (2008). The Regulation of Cooling and Star Formation in Luminous Galaxies by Active Galactic Nucleus Feedback and the Cooling-Time/Entropy Threshold for the Onset of Star Formation. *ApJ*, 687:899–918.

Rauch, M., Haehnelt, M., Bunker, A., Becker, G., Marleau, F., Graham, J., Cristiani, S., Jarvis, M., Lacey, C., Morris, S., Peroux, C., Röttgering, H., and Theuns, T. (2008). A Population of Faint Extended Line Emitters and the Host Galaxies of Optically Thick QSO Absorption Systems. *ApJ*, 681:856–880.

Read, J. I., Wilkinson, M. I., Evans, N. W., Gilmore, G., and Kleyna, J. T. (2006). The tidal stripping of satellites. *MNRAS*, 366:429–437.

Reiss, D. J., Germany, L. M., Schmidt, B. P., and Stubbs, C. W. (1998). The Mount Stromlo Abell cluster supernova search. *AJ*, 115:26–+.

Reiss, D. J. and Hola, R. (1998). Supernova 1998fb in Anonymous Galaxy. *IAU Circular*, 7077:1–+.

Renzini, A. and Buzzoni, A. (1986). Global properties of stellar populations and the spectral evolution of galaxies. In C. Chiosi & A. Renzini, editor, *Spectral Evolution of Galaxies*, volume 122 of *Astrophysics and Space Science Library*, pages 195–231.

Richer, M. G., López, J. A., García-Díaz, M. T., Clark, D. M., Pereyra, M., and Díaz-Méndez, E. (2010). The Evolution of the Kinematics of Nebular Shells in Planetary Nebulae in the Milky Way Bulge. *ApJ*, 716:857–865.

Richstone, D. O. (1976). Collisions of galaxies in dense clusters. II - Dynamical evolution of cluster galaxies. *ApJ*, 204:642–648.

Richtler, T., Dirsch, B., Gebhardt, K., Geisler, D., Hilker, M., Alonso, M. V., Forte, J. C., Grebel, E. K., Infante, L., Larsen, S., Minniti, D., and Rejkuba, M. (2004). The Globular Cluster System of NGC 1399. II. Kinematics of a Large Sample of Globular Clusters. *AJ*, 127:2094–2113.

Rines, K., Finn, R., and Vikhlinin, A. (2007). An Extremely Massive Dry Galaxy Merger in a Moderate Redshift Cluster. *ApJL*, 665:L9–L13.

Rood, H. J. and Sastry, G. N. (1971). ”Tuning Fork” Classification of Rich Clusters of Galaxies. *Publ. Astr. Soc. Pac.*, 83:313–+.

Rosati, P., Borgani, S., and Norman, C. (2002). The Evolution of X-ray Clusters of Galaxies. *ARA&A*, 40:539–577.

Rudick, C. S., Mihos, J. C., Frey, L. H., and McBride, C. K. (2009). Tidal Streams of Intracluster Light. *ApJ*, 699:1518–1529.

Rudick, C. S., Mihos, J. C., Harding, P., Feldmeier, J. J., Janowiecki, S., and Morrison, H. L. (2010). Optical Colors of Intracluster Light in the Virgo Cluster Core. *ApJ*, 720:569–580.

Rudick, C. S., Mihos, J. C., and McBride, C. (2006). The Formation and Evolution of Intracluster Light. *ApJ*, 648:936–946.

Sanchez-Blazquez, P., Peletier, R. F., Jimenez-Vicente, J., Cardiel, N., Cenarro, A. J., Falcon-Barroso, J., Gorgas, J., Selam, S., and Vazdekis, A. (2007). MILES library of empirical spectra (Sanchez-blazquez+, 2006). *VizieR Online Data Catalog*, 837:10703–+.

Sandage, A. and Bedke, J. (1994). *The Carnegie Atlas of Galaxies. Volumes I, II.*

Sarazin, C. L. (1988). *X-ray emission from clusters of galaxies*.

Sato, K., Yamasaki, N. Y., Ishida, M., Ishisaki, Y., Ohashi, T., Kawahara, H., Kitaguchi, T., Kawaharada, M., Kokubun, M., Makishima, K., Ota, N., Nakazawa, K., Tamura, T., Matsushita, K., Kawano, N., Fukazawa, Y., and Hughes, J. P. (2007). X-Ray Study of Temperature and Abundance Profiles of the Cluster of Galaxies Abell 1060 with Suzaku. *Pub. Astron. Soc. Japan*, 59:299–317.

Schaerer, D. (2007). Primeval galaxies. *ArXiv e-prints*.

Schechter, P. (1976). An analytic expression for the luminosity function for galaxies. *ApJ*, 203:297–306.

Scheffler, H. and Elsasser, H. (1990). *Physik der Sterne und der Sonne*.

Sersic, J. L. (1968). *Atlas de galaxias australes*.

Shapley, A. E., Steidel, C. C., Pettini, M., and Adelberger, K. L. (2003). Rest-Frame Ultraviolet Spectra of z˜3 Lyman Break Galaxies. *ApJ*, 588:65–89.

Smail, I., Edge, A. C., Ellis, R. S., and Blandford, R. D. (1998). A statistical analysis of the galaxy populations of distant luminous X-ray clusters. *MNRAS*, 293:124–+.

Sommer-Larsen, J., Romeo, A. D., and Portinari, L. (2005). Simulating galaxy clusters - III. Properties of the intracluster stars. *MNRAS*, 357:478–488.

Spergel, D. N., Bean, R., Doré, O., Nolta, M. R., Bennett, C. L., Dunkley, J., Hinshaw, G., Jarosik, N., Komatsu, E., Page, L., Peiris, H. V., Verde, L., Halpern, M., Hill, R. S., Kogut, A., Limon, M., Meyer, S. S., Odegard, N., Tucker, G. S., Weiland, J. L., Wollack, E., and Wright, E. L. (2007). Three-Year Wilkinson Microwave Anisotropy Probe (WMAP) Observations: Implications for Cosmology. *ApJS*, 170:377–408.

Stanford, S. A., Elston, R., Eisenhardt, P. R., Spinrad, H., Stern, D., and Dey, A. (1997). An IR-Selected Galaxy Cluster at ζ=1.27. *AJ*, 114:2232–+.

Steidel, C. C., Giavalisco, M., Dickinson, M., and Adelberger, K. L. (1996a). Spectroscopy of Lyman Break Galaxies in the Hubble Deep Field. *AJ*, 112:352–+.

Steidel, C. C., Giavalisco, M., Pettini, M., Dickinson, M., and Adelberger, K. L. (1996b). Spectroscopic Confirmation of a Population of Normal Star-forming Galaxies at Redshifts Z gt 3. *ApJL*, 462:L17+.

Takamiya, M., West, M., Côté, P., Jordán, A., Peng, E., and Ferrarese, L. (2009). *IGCs in the Virgo Cluster*, pages 361–+.

Tamura, T., Makishima, K., Fukazawa, Y., Ikebe, Y., and Xu, H. (2000). X-Ray Measurements of the Gravitational Potential Profile in the Central Region of the Abell 1060 Cluster of Galaxies. *ApJ*, 535:602–614.

Teodorescu, A. M., Méndez, R. H., Saglia, R. P., Riffeser, A., Kudritzki, R., Gerhard, O. E., and Kleyna, J. (2005). Planetary Nebulae and Stellar Kinematics in the Flattened Elliptical Galaxy NGC 1344. *ApJ*, 635:290–304.

Thomas, D., Maraston, C., and Bender, R. (2003). Stellar population models of Lick indices with variable element abundance ratios. *MNRAS*, 339:897–911.

Thuan, T. X. and Kormendy, J. (1977). Photographic measurements of the diffuse light in the Coma cluster. *Publ. Astr. Soc. Pac.*, 89:466–473.

Tonry, J. and Davis, M. (1979). A survey of galaxy redshifts. I - Data reduction techniques. *AJ*, 84:1511–1525.

Toomre, A. and Toomre, J. (1972). Galactic Bridges and Tails. *ApJ*, 178:623–666.

Tran, K., van Dokkum, P., Franx, M., Illingworth, G. D., Kelson, D. D., and Schreiber, N. M. F. (2005). Spectroscopic Confirmation of Multiple Red Galaxy-Galaxy Mergers in MS 1054-03 (z = 0.83)1,. *ApJL*, 627:L25–L28.

Vasterberg, A. R., Lindblad, P. O., and Jorsater, S. (1991). An optical study of the cD galaxy NGC3311 and the giant elliptical galaxy NGC3309 in the cluster Hydra I. *A&A*, 247:335–347.

Ventimiglia, G. and Arnaboldi, M. (2010). A Survey of Lyα Galaxies at $z \sim 3.1$. *VA*, in press.

Ventimiglia, G., Arnaboldi, M., and Gerhard, O. (2008). Intracluster Planetary Nebulae in the Hydra I cluster. *Astronomische Nachrichten*, 329:1057–+.

Ventimiglia, G., Arnaboldi, M., and Gerhard, O. (2010a). The unmixed kinematics and origins of diffuse stellar light in the core of the Hydra I cluster (Abell 1060). *A&A*, in press.

Ventimiglia, G., Gerhard, O., Arnaboldi, M., and Coccato, L. (2010b). The dynamically hot stellar halo around NGC 3311: a small cluster-dominated central galaxy. *A&A*, 520:L9+.

Verhamme, A., Schaerer, D., Atek, H., and Tapken, C. (2008). 3D Lyα radiation transfer. III. Constraints on gas and stellar properties of z ˜ 3 Lyman break galaxies (LBG) and implications for high-z LBGs and Lyα emitters. *A&A*, 491:89–111.

Vílchez-Gómez, R. (1999). Optical diffuse light in clusters of galaxies. In J. I. Davies, C. Impey, & S. Phillips, editor, *The Low Surface Brightness Universe*, volume 170 of *Astronomical Society of the Pacific Conference Series*, pages 349–+.

Villaver, E. and Stanghellini, L. (2005). The Survival of Planetary Nebulae in the Intracluster Medium. *ApJ*, 632:854–858.

Voit, G. M. (2005). Tracing cosmic evolution with clusters of galaxies. *Reviews of Modern Physics*, 77:207–258.

von der Linden, A., Best, P. N., Kauffmann, G., and White, S. D. M. (2007). How special are brightest group and cluster galaxies? *MNRAS*, 379:867–893.

Wetzel, A. R. and White, M. (2010). What determines satellite galaxy disruption? *MNRAS*, 403:1072–1088.

White, P. M., Bothun, G., Guerrero, M. A., West, M. J., and Barkhouse, W. A. (2003). Extraordinary Diffuse Light in Hickson Compact Group 90. *ApJ*, 585:739–749.

White, S. D. M., Navarro, J. F., Evrard, A. E., and Frenk, C. S. (1993). The baryon content of galaxy clusters: a challenge to cosmological orthodoxy. *Nature*, 366:429–433.

Williams, B. F., Ciardullo, R., Durrell, P. R., Vinciguerra, M., Feldmeier, J. J., Jacoby, G. H., Sigurdsson, S., von Hippel, T., Ferguson, H. C., Tanvir, N. R., Arnaboldi, M., Gerhard, O., Aguerri, J. A. L., and Freeman, K. (2007). The Metallicity Distribution of Intracluster Stars in Virgo. *ApJ*, 656:756–769.

Willman, B., Governato, F., Wadsley, J., and Quinn, T. (2004). The origin and properties of intracluster stars in a rich cluster. *MNRAS*, 355:159–168.

Worthey, G., Faber, S. M., Gonzalez, J. J., and Burstein, D. (1994). Old stellar populations. 5: Absorption feature indices for the complete LICK/IDS sample of stars. *ApJS*, 94:687–722.

Worthey, G. and Ottaviani, D. L. (1997). H gamma and H delta Absorption Features in Stars and Stellar Populations. *ApJS*, 111:377–+.

Yamasaki, N. Y., Ohashi, T., and Furusho, T. (2002). Chandra Observation of the Central Galaxies in the A1060 Cluster of Galaxies. *ApJ*, 578:833–841.

Zabludoff, A. I., Huchra, J. P., and Geller, M. J. (1990). The kinematics of Abell clusters. *ApJS*, 74:1–36.

Zibetti, S., White, S. D. M., Schneider, D. P., and Brinkmann, J. (2005). Intergalactic stars in z˜ 0.25 galaxy clusters: systematic properties from stacking of Sloan Digital Sky Survey imaging data. *MNRAS*, 358:949–967.

Zwicky, F. (1951). The Coma Cluster of Galaxies. *Publ. Astr. Soc. Pac.*, 63:61–+.

Zwicky, F., Herzog, E., Wild, P., Karpowicz, M., and Kowal, C. T. (1961). *”Catalogue of Galaxies and of Clusters of Galaxies”, Volume I-VI*.